



HIGHLIGHTS 2002



European Synchrotron Radiation Facility



Highlights 2002

Contents

Pages

Introduction

2

Scientific Highlights

3

Macromolecular Crystallography

4

Soft Condensed Matter

17

Surface and Interface Science

25

X-ray Absorption and Magnetic Scattering

35

High Resolution and Resonance Scattering

49

Materials Science

63

X-ray Imaging

73

Applied and Industrial Research

90

Methods and Instrumentation

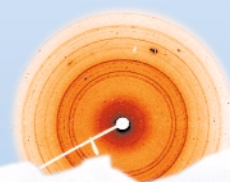
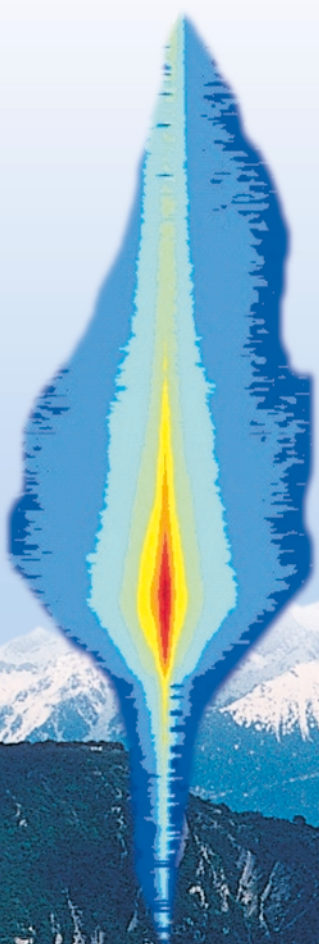
94

The X-ray Source

104

Facts and Figures

112



Introduction

The signing of the Memorandum of Understanding of the Partnership for Structural Biology stands out among the many significant events of 2002 in terms of its potential impact on the ESRF – and on its neighbouring institutes. After almost two years of discussion and preparation the MoU was signed on 15 November by the Directors (or their representatives) of the European Molecular Biology Laboratory (EMBL), the ESRF, the Institut de Biologie Structurale (IBS), and the Institut Laue-Langevin (ILL). The opening ceremony was attended by a number of local and national dignitaries including Prof B. Bigot, *Directeur du Cabinet de la Ministre déléguée à la Recherche et aux Nouvelles Technologies*. The four partner institutes will now work to combine their expertise in state-of-the-art molecular biology to tackle crucial problems in research related to issues of human health.



PSB opening ceremony.

The ESRF's contribution to the partnership involves three components. First, our scientists will take a substantial part in the execution of the ambitious joint scientific programme. The ESRF will make a major financial commitment to the laboratory/office building, to be situated between the EMBL building and the ESRF's Experimental Hall. The third, and most striking of the ESRF's contribution is the new ID23 beamline complex. Two new highly-automated beamlines for high-throughput macromolecular structure determination are under construction; the first station will be commissioned towards the end of 2003, with the second following about one year later. The ID23 beamline represents a major increase of our capacity in this critical area of research and will allow a series of specific PSB investigations to supplement our current user, in-house and industrial research programmes. We look forward to a continued expansion of the PSB's activities, as our site becomes an internationally leading centre for structural and functional biology.



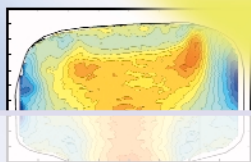
Inauguration of FaME38.

We also made progress on other important research collaborations. The Facility for Materials Engineering (FaME 38) was inaugurated on 26 November 2002. This joint ILL-ESRF initiative, involving a number of U.K. universities, has the objective of providing scientific and technical support for engineering and materials science investigations at our complementary facilities. Another important milestone was the signature of the EIROforum charter, uniting the seven major European intergovernmental research organisations (CERN, EFDA-JET, EMBL, ESA, ESO, ESRF, ILL) in a number of joint actions to promote European science. This event took place at the launch of the EC's 6th Framework Programme in Brussels on 11-13 November 2002; the ESRF presence was marked by an impressive stand presenting the full range of our activities.



Signature of the EIROforum charter.

Closing this "international" chapter, we would like to note that an extension of the agreement between the ESRF and the Czech Republic was signed on 20 September 2002 during a visit by Professor Jungwirth, representing the Institute of Physics of the Czech Academy of Sciences. Furthermore, the Austrian Academy of Science became a new associate of the ESRF and the Portuguese government renewed its agreement with the ESRF, both from January 2003. These agreements testify to the scientific success and attractiveness of the ESRF, as do the 750 refereed publications produced during 2002, describing research carried out at the ESRF.

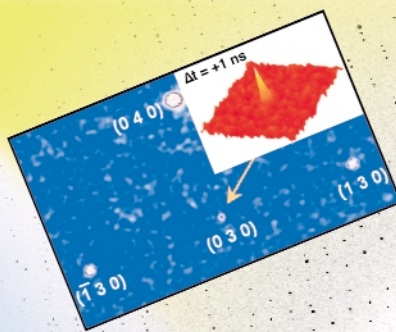


In 2002, over 5300 hours of X-ray beam were delivered to the beamlines with an availability of 98% if we disregard the 1% necessarily used for refills. The mean time between failures reached a record 57.8 hours – this statistic is especially meaningful, as the most sensitive experiments on the beamlines often require long periods of stable uninterrupted beam. The programme of Machine upgrades to improve performance and reliability is mirrored by a continuous refurbishment and renewal programme on the beamlines. Of particular importance is the refinement of beamline optics. The Optics Group has been responsible for many advances in focusing techniques, notably the supermirror Kirkpatrick-Baez system that can now provide a focal spot of less than 100 by 100 nanometres at an X-ray energy of 20 keV. These devices will have many applications on a large number of beamlines.

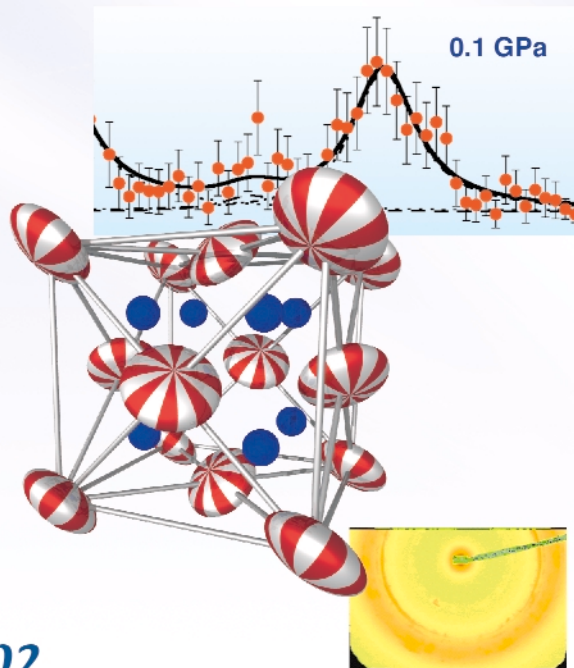
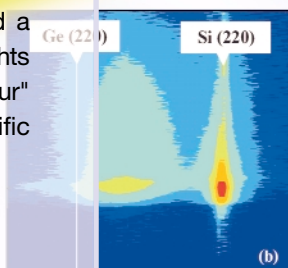
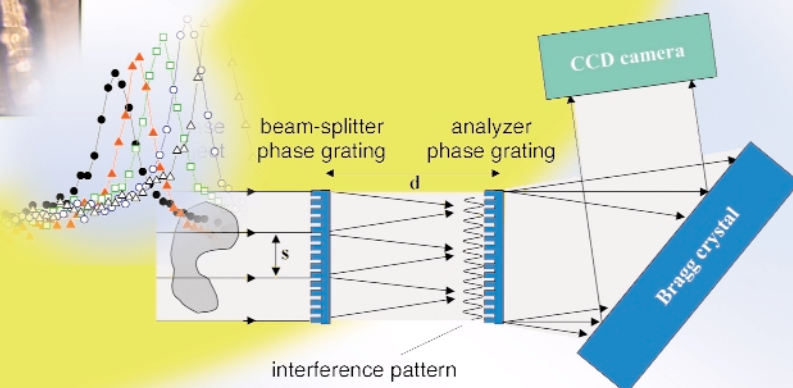
Other noteworthy changes during the last year include the creation of the Industrial and Commercial Unit, to further focus our commercial activities, and the Communication Unit, to strengthen our communication interactions, both internal and external. The new ESRF web site, born of a strong multi-divisional collaboration, came on-line towards the end of 2002 and will allow improved presentation of the ESRF and its activities towards the scientific community and the wider public.

In this short introduction it is not possible to mention all of the events and developments that took place during the last year. So let us end by thanking all of those who contributed to the ESRF's scientific success – staff, users, scientific collaborators, and delegations. In the following pages you will find a comprehensive summary of the Scientific Highlights of the year 2002 which should provide a "flavour" of the remarkably diverse range of scientific phenomena investigated at the ESRF.

W.G. Stirling, P. Elleaume, H. Krech, F. Sette
(January 2003)



Scientific Highlights



Highlights 2002



Macromolecular Crystallography

Introduction

Macromolecular crystallography (MX) at the ESRF has continued to thrive during 2002. Four beamlines (ID14-1, -2, -4; and ID29) have been available to the User Community with approximately 400 experimental sessions involving a total of around 1600 visitors to the beamlines being supported. Such levels of support could not have been achieved without the wholehearted commitment of the MX Group staff and their EMBL colleagues who together form the Joint Structural Biology Group, and the excellent backup of the ESRF User Office. Furthermore, ID13, the microfocus beamline, also contributes with a share of its beam time to macromolecular structure determination where an exceedingly small focus is required. In addition the Collaborating Research Group (CRG) beamlines continue to provide excellent support for their User Communities. The joint operation of BM14 by the Spanish and UK consortia has now been successfully concluded and the Spanish consortium will move to the newly rebuilt facilities on BM16 during 2003, with the UK consortium taking over sole responsibility for BM14. The French CRG beamline FIP (BM30) continues to enhance its performance with particular advances in the field of automation.

Technical enhancements of the MX Group beamlines continued apace with the major focus on improving the automation of both beamline alignment and data collection and also of crystal screening protocols. The policy of beamline upgrade and refurbishment has also continued with the rebuilding and commissioning of ID14-3 which will re-enter user operation in Spring 2003. The remodelling of ID14-3 is designed to produce the first fully-automatic MX beamline at the ESRF. Achieving this goal has necessitated the adoption of many new ideas for instrument control and X-ray beam diagnostics as well as the development of sophisticated and reliable



Highlights 2002

software and hardware. S. Arzt and J. McCarthy in their article (page 15) describe the scope and intentions of efforts currently underway in this area and it is expected that many of the developments arising from these will be deployed on the other MX Group beamlines starting in 2003.

Construction of the ID23 beamline complex has also been started with the lead hutches erected and control cabins installed. ID23 was designed for construction in two stages.

The first, the experimental facility, due to be available at the end of 2003, will consist of a MAD beamline with tuneability between 5 and 25 keV. We envisage that this beamline will also benefit from efforts elsewhere in the ESRF. Moreover, like ID14-3, it will provide a highly-automated environment.

Apart from providing a further platform for MX at the ESRF, the ID23 beamline also forms a crucial part of the Partnership for Structural Biology (PSB) collaboration. This joint enterprise will greatly augment and extend the structural biology programme of the ESRF, introducing better access to the expertise in molecular biology of the EMBL and IBS, and the neutron scattering capabilities of the ILL. Together, the four laboratories making up the PSB provide a resource, unique in Europe, for structural biology and genomics research, where industry will also play a major role. In their keynote addresses at the opening ceremony of the PSB, Prof. Fotis Kafatos, Director General of the EMBL, Prof. R. Douce, Director of IBS, and Prof. D. Stuart of Oxford University stressed the importance of the PSB to European structural biology research. A fuller account of the organisation and aims of the PSB is given in the General Introduction to these Highlights.

The Block Allocation Group (BAG) system has now been in operation for several years and has brought about a marked increase in the effectiveness with which ESRF beam-time is utilised by the MX User Community. The standard of publications arising from the use of the ESRF for MX remains extremely high. In this chapter, the editors have undertaken the task of reflecting this excellence by choosing to present highlight contributions that reflect the broad range of science carried out at the beamlines.

The outer membrane mitochondrial monoamine oxidase B (MOA B) plays a key role in the breakdown of neurotransmitters, is implicated in many neurological disorders and has long been a target for drug therapy. The three-dimensional structure of MAO B as determined by Mattevi *et al.* (page 6) reveals an apparently novel method of membrane insertion for protein molecules and also provides the basis for future studies with the aim of designing novel drugs.

Membrane-bound proteins play an increasingly large part in the structural biology studied at the ESRF. Here they are also represented by the work of Hunte and Lange (page 7) who report on the crystal structure of the electron transfer complex of Cytochrome c and the Cytochrome bc₁ complex from yeast. Since the structure was obtained at physiological ionic strength there is evidence that the complex represents the true native electron transfer complex and therefore sheds significant light on the mechanism and regulation of the electron transfer process.

Blood clotting is essential to the maintenance of healthy blood circulation system. Gros *et al.* (page 8) used data from ESRF beamlines to determine the structure of the complex between glycoprotein Ib α and the blood protein von Willebrand factor (VWF) as amino acid mutations in either of the two moieties involved in the complex can cause bleeding disorders. The crystal structure of the complex described here allows both for the construction of a model for the mechanism of the adhesion of blood platelets at sites of bleeding (one of the first steps in clotting) as well as providing a framework for the structure-based design of novel therapeutic agents designed to treat diseases such as thrombosis.

Phosphate is a vital component of many cellular processes. In *E. coli* the uptake of phosphate is regulated by the signal transduction system based around PhoR and PhoB. M. Coll *et al.* have determined the interactions present at a key point of the signal transduction specific pathway namely the binding of PhoB to its specific DNA target (page 9).

R Fourme *et al.*, using the high-energy physics beamline ID30, have undertaken studies on the effect of high pressures on protein and virus samples and structures (page 14). As well as a clear proof of principle the experiments described in this article offer tantalising glimpses of the possible exploitation of this technique to explore protein sub-states, to probe protein-protein interactions as a function of pressure and even, in favourable cases, to improve the quality of the diffraction patterns obtainable from crystals of macromolecules.

In-house research has also continued to develop in the last year. The work carried out by ESRF staff and their collaborators is represented here in three contributions.

D. Bourgeois, E. Fioravanti *et al.*, using the technique of kinetic crystallography, have investigated the enzymatic reaction of the *M. tuberculosis* thymidylate kinase (page 10). They demonstrate the essential role played by a Mg²⁺ ion in catalysis and propose that potential anti-tuberculosis agents could be designed with this in mind. A. Imberty, E. Mitchell *et al.* have determined the structure of fucose binding lectin PA-III from *P. aeruginosa*, which is one of the major causes of mortality in cystic fibrosis sufferers (page 11). It is hoped that the structural information obtained from their analysis of the PA-III-fucose complex will provide a basis for design of efficient anti-bacterial compounds. Finally E. Hough *et al.* have determined the structure of the bovine lysosomal α -mannosidase defects in which cause the lysosomal storage disorder α -mannosidosis (page 12). Using a range of biophysical techniques including the determination of the three-dimensional structure of the enzyme using data collected at the ESRF these authors have been able to provide many insights into the molecular basis of the bovine and human forms of this disease.

Finally 2002 saw the departure of Peter Lindley as Director of Research. The MX group would like to thank him for the support and encouragement received during his tenure and wish him good luck in his "retirement" - don't work too hard!

Structure of the Outer-Membrane Mitochondrial Monoamine Oxidase B

Human monoamine oxidases A and B (MAO A and B) are the most intensively investigated flavin-dependent amine oxidases. This is due to their roles in the metabolism of neurotransmitters such as serotonin and dopamine [1,2]. MAO A and MAO B are separate gene products of ~70% sequence identity with both isoforms containing 8 α -S-cysteinyl-FAD coenzymes as the sole redox cofactors and retaining different but partly overlapping substrate and inhibitor specificities. MAOs are implicated in a large number of neurological disorders such as Parkinson's disease and depression and have been important targets for drug therapy over the past 40 years [1]. The three-dimensional structures of both MAO A and MAO B are therefore of interest. However, both enzymes are bound to the outer mitochondrial membrane through a C-terminal polypeptide segment and this feature has made structural investigation by X-ray crystallography more difficult.

Despite these difficulties, we recently solved the crystal structure of human MAO B using the single isomorphous replacement method combined with multicrystal 12-fold averaging based on two crystal forms grown from different detergent crystallisation conditions. All diffraction data were measured on ESRF beamlines.



Fig. 1: Three-dimensional structure of human MAO B. The FAD-cofactor is in ball-and-stick representation and the membrane binding region is formed by the protruding α -helix. The figure shows the two cavities found in the substrate-binding domain.

The crystal structure (Figure 1) reveals that MAO B has a two-domain topology similar to that observed in other flavoenzymes. In both crystal forms, the enzyme crystallises as a dimer, which indicates that this oligomeric arrangement probably occurs also in the physiological membrane environment. The 60-residue C-terminal tail (residues 460-520) forms an extended segment that traverses the protein surface and then folds into an α -helix. This helix protrudes from the basal

face of the structure with its axis approximately parallel to the molecular two-fold axis, in an orientation suited to anchor the protein to the outer mitochondrial membrane. In addition to this transmembrane helix, two apolar loops located at different positions in the sequence form two hydrophobic patches on the protein surface which are also probably involved in membrane binding. Thus MAO B, which is one of the very few known structures of a monotonically inserted membrane protein appears to have a different method of membrane insertion than those of other monotonically inserted proteins such as prostaglandin synthase and squalene cyclase.

A second prominent feature of MAO B structure is the presence of two adjacent cavities in the interior of the protein (Figure 1). The largest cavity is directly in front of the flavin ring and forms the substrate-binding site occupied by the pargyline inhibitor (Figure 2). For the substrate to enter this cavity, it must first pass through an "entrance cavity" situated near the point where the protein surface intersects with the surface of the outer mitochondrial membrane. This observation raises the intriguing possibility that the anionic membrane surface may function in the electrostatic steering of the positively-charged amine substrate to the entrance cavity binding site. In the substrate cavity, two tyrosyl side chains form an "aromatic sandwich" by facing each other in perpendicular orientations to the flavin, generating an "aromatic cage" that may form the recognition site for the substrate amino group.

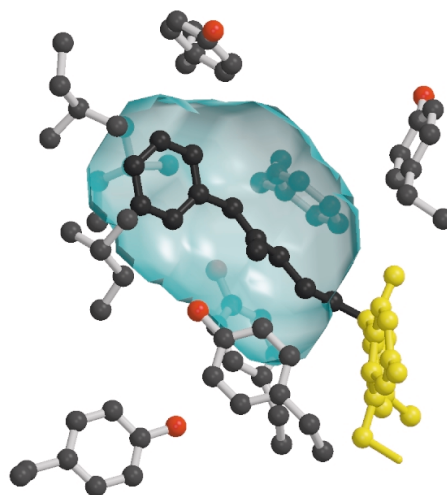


Fig. 2: The active site of MAO B. The figure shows the inhibitor pargyline bound in the substrate cavity.

The features revealed by the three-dimensional structure of MAO B provide a framework for future studies aimed at the investigation of MAO A and MAO B substrate specificities, the functional significance of membrane association and the possible exploitation of the entrance cavity as a site for drug binding.

References

- [1] A.M. Cesura, A. Pletscher, *Prog. Drug Res.* **38**, 171-297 (1992).

[2] J.C. Shih, K. Chen, M.J. Ridd, *Annu. Rev. Neurosci.* **22**, 197-217 (1999).

Principal Publication and Authors

C. Binda (a), P. Newton-Vinson (b), F. Hubalek (b), D.E. Edmondson (b), A. Mattevi (a), *Nat. Struct. Biol.* **9**, 22-26 (2002).

(a) Department of Genetics and Microbiology, University of Pavia (Italy)

(b) Department of Biochemistry, Emory University School of Medicine, Atlanta (USA)

Structure of the Electron-transfer Complex of Cytochrome *c* and Cytochrome *bc*₁ Complex from Yeast

Electron transfer processes are of great importance in many metabolic pathways of living organisms. They are essential for respiration, a process in which energy gained from oxidation of nutrients is converted to ATP. Energy conversion is achieved by coupling the transfer of electrons along a chain of proteins to the translocation of protons across a lipid membrane. The resulting electrochemical proton gradient can then be used for ATP synthesis. In the respiratory chain of eukaryotic cells electron transfer involves four multisubunit complexes that are embedded in the inner mitochondrial membrane. Electrons are transferred between two of these, namely the cytochrome *bc*₁ complex and the cytochrome *c* oxidase, via reversible docking of the small soluble protein cytochrome *c* (CYC).

We crystallised the complex of cytochrome *c* and cytochrome *bc*₁ complex (QCR) from the yeast *Saccharomyces cerevisiae* with the help of an antibody Fv fragment. The molecular structure of this entity was determined at 2.97 Å resolution by molecular replacement using the previously determined high resolution structure of QCR [1] as search model (Figure 3). This is the first structure of a complex of redox partners from the mitochondrial respiratory chain.

CYC binds to the cytochrome *c*₁ subunit of the cytochrome *bc*₁ complex. The resulting complex between the two is stabilised by hydrophobic interactions surrounding the heme crevices thereby creating a small, compact contact site (Figure 4). A central cation- π interaction is an important and conserved feature of CYC binding [2] and peripheral

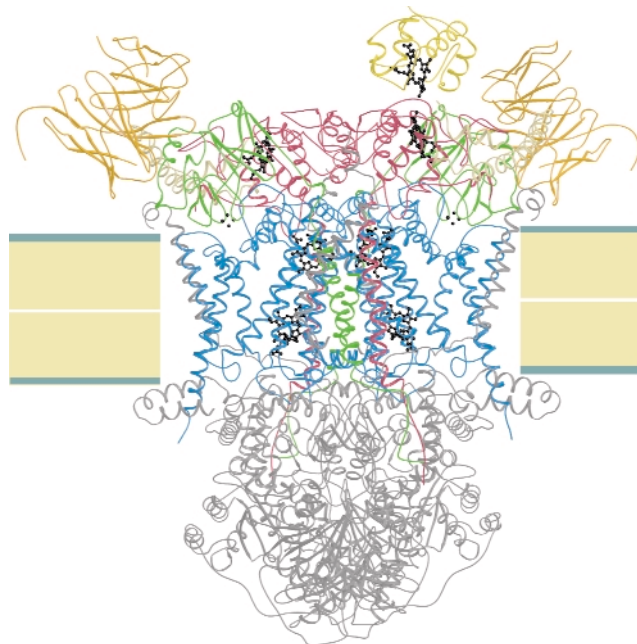


Fig. 3: The three-dimensional structure of the electron-transfer complex between cytochrome *c* (yellow) and QCR with bound antibody Fv fragment (orange). Cytochrome *c* binds only to one of two possible binding sites of the homodimeric *bc*₁ complex. The catalytic cytochrome *b*, cytochrome *c*₁ and Rieske protein of the *bc*₁ complex are coloured in blue, red and green, respectively. The relative position of the inner mitochondrial membrane is indicated.

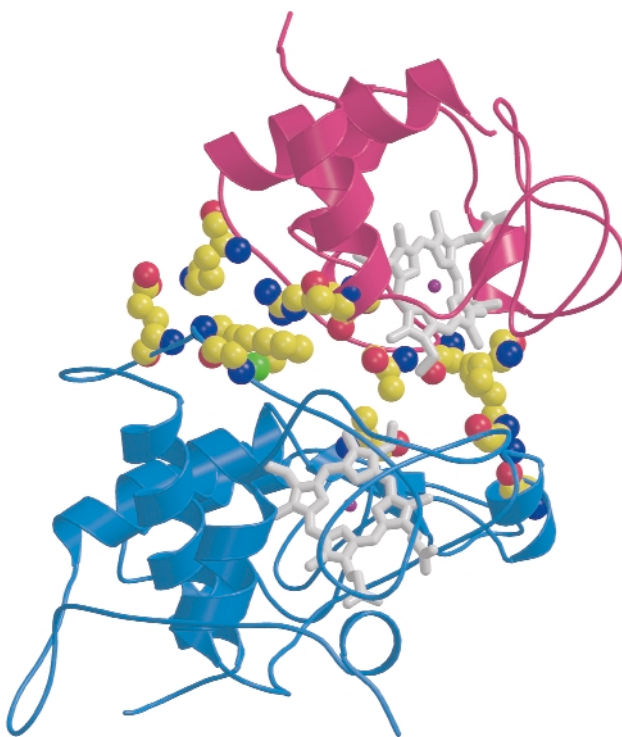


Fig. 4: Close-up view showing binding interactions between cytochrome *c* (purple) and the cytochrome *c*₁ subunit (blue) of the *bc*₁ complex. Side chains of amino acid residues involved in stabilising interactions are shown in a space-filling representation.

patches with highly-conserved complementary charges further stabilise the enzyme-substrate complex using long-range electrostatic forces that may also serve to ensure the orientation of CYC. The close spatial arrangement of the hemes suggests a direct and rapid heme-to-heme electron transfer at a rate of $\sim 8 \times 10^6 \text{ sec}^{-1}$. CYC reduction by QCR is highly dependent on ionic strength with an optimum activity at physiological ionic strength [2]. As the crystals of the complex were obtained at physiological ionic strength, and as the size and characteristics of the contact site are optimal for the formation of a transient complex allowing fast electron transfer, there is strong indication that the structure represents the true native electron transfer complex. Remarkably, CYC binds only to one of the two possible binding sites of the homodimeric complex and binding is correlated with the presence of ubiquinone at the site of quinone reduction. This suggests a regulated binding of ubiquinone and CYC which act as electron acceptors for the two-electron oxidation of the substrate ubiquinol.

References

- [1] C. Hunte, J. Köpke, C. Lange, T. Roßmanith and H. Michel, *Structure* **8**, 669-684 (2000).
 [2] C. Hunte, S. Solmaz and C. Lange, *Biochim. Biophys. Acta* **1555**, 21-28 (2002).

Principal Publication and Authors

C. Lange and C. Hunte, *Proc. Natl. Acad. Sci. USA* **99**, 2800-2805 (2002).
Dept. Molecular Membrane Biology, MPI, Frankfurt (Germany)

Crystal Structure Reveals Blood Platelet Adhesion Complex

Integrity of the blood circulation is crucial to survival. Therefore, blood loss from damaged vessels should be stopped rapidly. An essential first step in the arrest of bleeding is the adhesion of blood platelets to sites of vascular damage. In rapidly-flowing blood, this depends on the interaction between the glycoprotein Ib α (GpIb α), located at the platelet surface, and the multimeric blood protein von Willebrand Factor (VWF) immobilised at sites of vessel damage. The importance of the interaction between GpIb α and VWF is highlighted by the familial bleeding disorders von Willebrand's disease and the Bernard-Soulier syndrome that are caused by mutations in GpIb α and VWF. The interaction between GpIb α and VWF also plays a pivotal role in the onset of thrombosis, a condition in which undesired platelet-aggregates are

formed that can block blood vessels causing heart- and brain-infarctions.

We used data sets collected at beamlines **ID14-1** and **ID14-2** to determine crystal structures of the VWF-binding domain of GpIb α and of its complex with the VWF-A1 domain at resolutions of 1.9 Å and 3.1 Å, respectively. For the structure determination of the complex we crystallised the mutant proteins A1(R543Q) and GpIb α (M239V). These mutations are related to bleeding disorders and enhance complex formation.

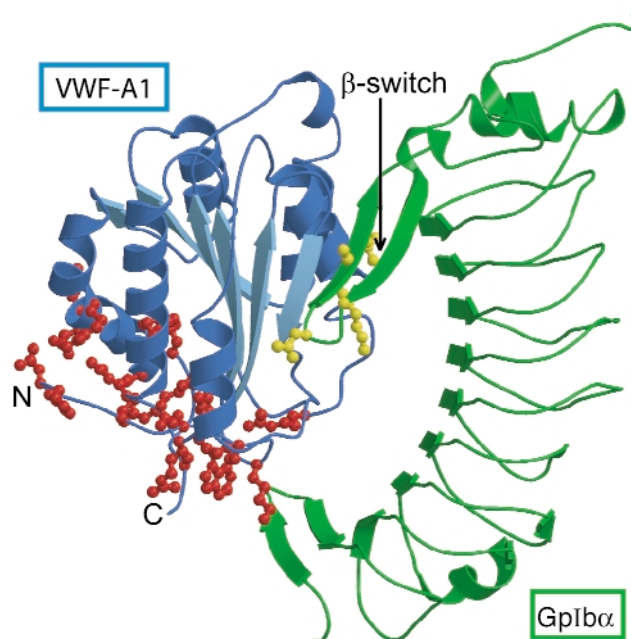


Fig. 5: Schematic representation of the complex of GpIb α (green) and the VWF-A1 domain (blue). Amino acids in VWF-A1 and GpIb α with known mutations that enhance complex formation are shown in red and yellow, respectively. The amino- and carboxy-termini of A1 are labelled.

The VWF-binding domain of GpIb α displays an elongated curved shape (Figure 5). The crystal structure of the complex shows that the globular A1 domain interacts with the concave face of GpIb α with two sites of close interaction. Interaction at the larger contact site near the top of the A1 domain depends on conformational changes in a surface-exposed loop of GpIb α . This loop, which we call β -switch, is flexible in free GpIb α , whereas in the complex it forms a β -hairpin that binds to the central β -sheet of A1. Mutation M239V and in fact all other mutations in GpIb α that cause stronger binding to VWF are located in the β -switch. Because the activating mutations introduce residues known to stabilise β -hairpin conformations (valine in the strand region or glycine in the turn region) enhanced complex formation probably results from stabilisation of the β -hairpin conformation of the β -switch, which primes GpIb α for binding to A1. The second, smaller contact site, located at the base of A1 appears to require the dislodging of the termini of the A1 domain uncovering the

site of interaction. Mutations in A1 that cause increased binding to GpIb α are all located at the base of A1 and probably induce the uncovering of the minor binding site by destabilising the conformation of its termini.

We propose that dislodging of the termini of the A1 domain under physiological conditions may be caused by pulling forces exerted on the immobilised VWF molecule by the rapidly flowing blood, thus providing activation in the platelet adhesion process. The two sites of interaction between GpIb α and VWF-A1 identified in this study present primary targets for development of drugs for the treatment or prevention of thrombosis.

Principal Publication and Authors

E.G. Huizinga (a), S. Tsuji (b), R.A.P. Romijn (b), M.E. Schiphorst (b), Ph.G. de Groot (b), J.J. Sixma (b) and P. Gros (a), *Science* **297**, 1176–1179 (2002).

(a) *Crystal and Structural Chemistry, Utrecht University (The Netherlands)*

(b) *Department of Haematology, University Medical Center Utrecht (The Netherlands)*

Tandem DNA Recognition by the Two-component Response Regulator PhoB

Two-component systems are signal transduction pathways widely used by bacteria to sense and respond to environmental changes. In *Escherichia coli*, PhoR and PhoB constitute a two-component system which controls phosphate uptake. In this system, PhoR is the sensor histidine kinase and PhoB is the response regulator. The former is a transmembrane receptor that senses phosphate levels. When phosphate is low, PhoR autophosphorylates on a histidine residue and transfers the phosphate group to an invariant aspartate located in a conserved regulator domain of PhoB. Upon phosphorylation, the effector domain of PhoB properly binds to the *pho* box, its specific DNA target sequence, and is able to activate the expression of at least 39 genes implicated mainly in the transport and metabolism of phosphorus compounds [1].

We have used synchrotron radiation to solve the three-dimensional crystal structure of the PhoB effector domain (PhoB^E) in complex with *pho* box DNA at 2.5 Å resolution (Figure 6). The protein presents a winged-helix fold consisting of a central three α -helix bundle packed against two β -sheets located at each terminus. Helices α 2 and α 3 form a modified helix-turn-helix motif where the turn has been replaced by a loop, called the

transactivation loop because mutational studies indicate that it is implicated in transcription activation [1]. Finally, the turn located at the C-terminal β -hairpin constitutes the wing. In the complex crystal structure, two PhoB^E protomers are bound in tandem to the same face of the *pho* box DNA, covering 22 base-pairs and smoothly bending it by 40°. Interestingly, the C-terminal β -sheet of the upstream protomer (blue in Figure 6) interacts with the N-terminal β -sheet of the downstream one, directing the head-to-tail DNA binding. DNA recognition elements comprise helices α 3, which penetrate the major grooves, and β -hairpin wings, which interact with the minor grooves. Both β -hairpin wings compress the minor grooves by inserting Arg219, which is tightly sandwiched between the DNA sugar backbones.

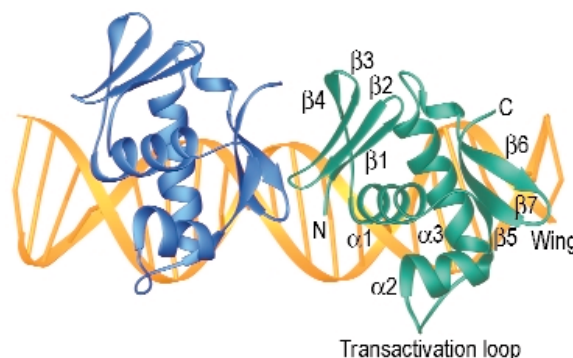


Fig. 6: Ribbon representation of the PhoB^E in complex with the *pho* box DNA. Two PhoB^E protomers are bound in tandem along 22 base pairs of DNA.

Our findings clarify crucial aspects of the mode of action of PhoB and its homologues, which constitute the OmpR-PhoB family response regulators. Firstly, the protein-DNA complexes are arranged head to tail in the crystal, giving rise to a pseudocontinuous DNA helix, and protein-protein interactions between all neighbouring molecules along this helix are identical. Thus, we have a reliable model of the structure of multiple PhoB^E molecules bound to promoters that contain several adjacent *pho* boxes (Figure 7). Secondly, the transactivation loops protrude laterally, and are thus able to contact the σ^{70} subunit to trigger transcription initiation. Finally, none of the secondary structure elements implicated in DNA binding in PhoB are blocked by the regulator domain in the unphosphorylated and

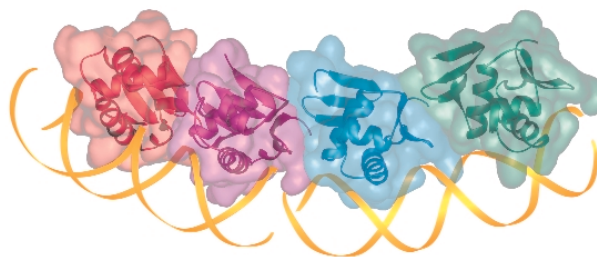


Fig. 7: Structure of a tetramer of PhoB^E bound to two consecutive *pho* boxes, superimposed with the transparent molecular surface of the protomers, as formed by crystallographic contacts in the crystal structure.

inactive full-length structure of the PhoB counterpart DrrD from *Thermotoga maritima* [2]. Using this full-length structure as a guide, it is possible to model the interaction between the two domains of full-length, inactive PhoB when complexed to DNA. In this model, severe clashes occur between receiver domains from adjacent PhoB monomers bound in tandem to the DNA. We thus propose that the mechanism for PhoB inhibition is based on steric impediments that prevent the tandem DNA binding needed for transcriptional activation, rather than the blocking of the DNA binding surface by the regulator domain as it occurs in the response regulator NarL, which belongs to a different family [3].

References

- [1] K. Makino, M. Amemura, T. Kawamoto, S. Kimura, H. Shinagawa, A. Nakata and M. Suzuki, *J. Mol. Biol.* **259**, 15-26 (1996).
- [2] D.R. Buckler and A.M. Stock, *Structure* **10**, 153-164 (2002).
- [3] I. Baikalov, I. Schroder, M. Kaczor-Grzeskowiak, K. Grzeskowiak, R.P. Gunsalus and R.E. Dickerson, *Biochemistry* **35**, 11053-11061 (1996).

Principal Publication and Authors

A.G. Blanco, M. Sola, F.X. Gomis-Rüth and M. Coll, *Structure* **10**, 701-713 (2002).
Institut de Biologia Molecular de Barcelona CSIC (Spain)

Mycobacterium tuberculosis Thymidylate Kinase: Structural Studies of Intermediates Along the Reaction Pathway

Tuberculosis is the primary cause of human mortality from infectious agents, with one-third of the world's population

infected. In the absence of an effective vaccine, the need for new drugs against tuberculosis has become a priority. Kinases responsible for the activation of nucleoside to nucleotide triphosphates, the building blocks of RNA and DNA, represent promising targets. Of special interest is thymidylate kinase (TMPK), an enzyme essential to cell survival, catalysing the phosphorylation of deoxythymidine-5'-monophosphate (TMP) to deoxythymidine-5'-diphosphate (TDP). Like other TMPKs, *Mycobacterium tuberculosis* TMPK (TMPK_{Mtub}) is a homodimer in solution ($M_r = 44$ kDa) with each monomer being composed of nine α -helices surrounding a five-stranded β -sheet core [1]. The active site includes the usual P-loop (a phosphate binding loop) and LID region (a highly flexible stretch of residues covering the ATP binding site). However, subtle sequence deviations from other TMPKs [1] confer unique properties to TMPK_{Mtub}, suggesting that inhibitors could specifically target this enzyme.

In order to clarify the phosphorylation mechanism employed by TMPK_{Mtub}, we have used kinetic crystallography and investigated the sequence of structural changes that take place upon the binding of substrates and catalysis.

Crystallisation of TMPK_{Mtub} using sodium malonate as precipitating agent and initiation of catalysis in the crystal by diffusion of ATP allowed us to elucidate the structures of (i) the apo-TMPK_{Mtub} (Figure 8a), (ii) the complex TMPK_{Mtub}-TMP (Figure 8b), (iii) the complex TMPK_{Mtub}-TMP-Mg²⁺ (Figure 8c) and (iv) the complex TMPK_{Mtub}-TDP-ADP-Mg²⁺ (Figure 8e). In addition, crystals grown in the presence of ammonium sulphate show a magnesium ion and a sulphate ion in the ATP binding site and provide a good mimic of the complex TMPK_{Mtub}-TMP-ATP-Mg²⁺ (Figure 8d, [1]).

Overall, a series of snapshots along the reaction pathway is obtained, revealing a closure of the active site in the process of going from an empty to a fully-occupied state. This suggests an induced-fit mechanism typical of NMPKs. These results also demonstrate that in TMPK_{Mtub} the LID closure is specifically coupled to the transient binding of an unusual magnesium ion

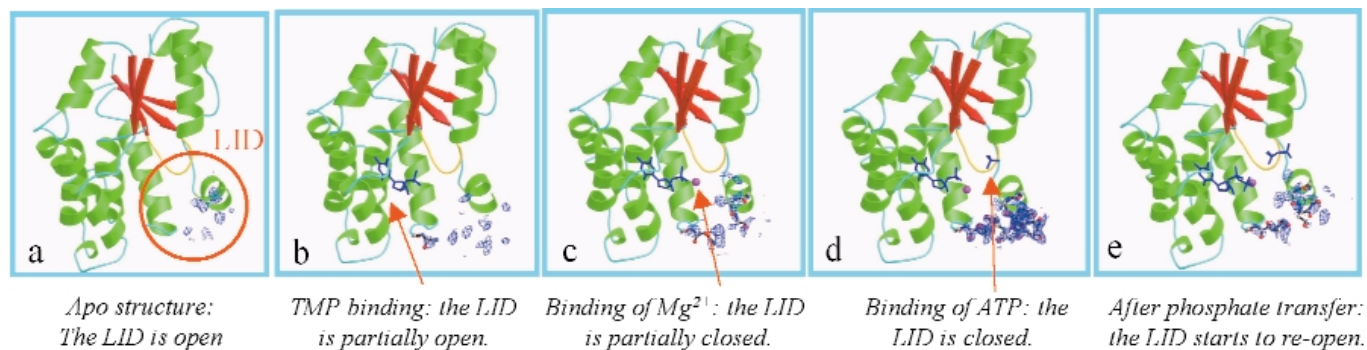


Fig. 8: Omit maps calculated by omitting 17 residues (149-165) in the LID region and contoured at 1.2 σ . (a) apo-TMPK_{Mtub}; (b) TMPK_{Mtub}-TMP complex; (c) TMPK_{Mtub}-TMP-Mg²⁺ complex; (d) TMPK_{Mtub}-TMP-Mg²⁺-sulphate complex; (e) TMPK_{Mtub}-TDP-Mg²⁺-ADP complex. A clear ordering of the LID is seen in going from (a) to (d). After catalysis, the LID starts to open again (e).

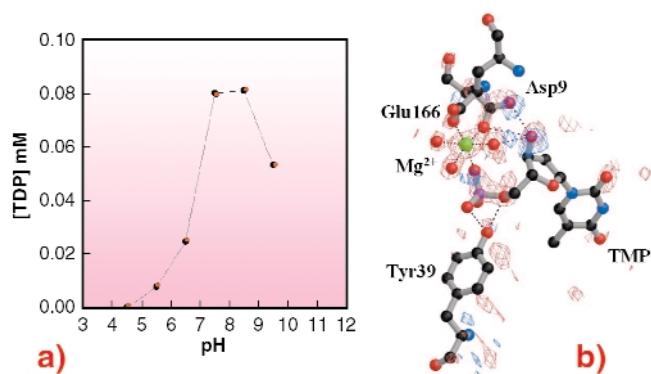


Fig. 9: (a) pH dependence curve of the $\text{TMPK}_{\text{Mtub}}$ catalytic activity. The TDP production (on the vertical axis) is represented as a function of pH (horizontal axis); (b) $\text{TMPK}_{\text{Mtub}}$ active site. Difference electron density map contoured at $\pm 3.5 \sigma$ (blue, positive; red negative) and calculated between data collected from a crystal of $\text{TMPK}_{\text{Mtub}}$ soaked in 30 mM ATP at pH 4.6 and data collected from a non-soaked crystal at pH 6.0. The peaks show the disappearance of the Mg^{2+} ion and its coordinated water molecules, the displacements of the phosphate and 3'-OH moieties of TMP and the swinging motion of Asp 9.

coordinating TMP in the active site. To clarify the role of this ion, crystals were soaked in ATP at acidic pH, where the enzyme is inactive (**Figure 9a**). In such conditions there is no Mg^{2+} bound to the enzyme. The overall geometry of the TMP binding site is disrupted and no formation of TDP occurs (**Figure 9b**), revealing that the presence of the metal ion is indispensable in bringing together the α -phosphate of TMP and the γ -phosphate of ATP for efficient phosphoryl transfer.

The essential role of Mg^{2+} in driving catalysis in $\text{TMPK}_{\text{Mtub}}$ suggests that structure-based design of inhibitors for the enzyme should focus on possibilities to destabilise this ion. The low pH structure shows that the 3'-hydroxyl group of the TMP substrate participates in binding Mg^{2+} . Potential inhibitors designed to contain a 3'-hydroxyl group substituent without hydrogen bonding capability may therefore prevent the binding of the metal ion and abolish the catalytic activity of $\text{TMPK}_{\text{Mtub}}$.

Reference

[1] I. Li de la Sierra, H. Munier-Lehmann, A.M. Gilles, O. Bâzu and M. Delarue, *J. Mol. Biol.* **311**, 87-100 (2001).

Principal Publication and Authors

E. Fioravanti (a,b), A. Haouz (c), T. Ursby (d), H. Munier-Lehmann (c), M. Delarue (c) and D. Bourgeois (a,b), *to be published*.

(a) LCCP, UMR 9015, IBS, Grenoble (France)

(b) ESRF

(c) Institut Pasteur, Paris (France)

(d) MAX-lab, Lund University, Lund (Sweden)

Structural Basis for Oligosaccharide-mediated Adhesion of *Pseudomonas aeruginosa* in the Lungs of Cystic Fibrosis Patients

The galactose- and fucose-binding (PA-IL and PA-IIL) lectins of *Pseudomonas aeruginosa* contribute to the virulence of this pathogenic bacterium, which is a major cause of morbidity and mortality in cystic fibrosis (CF) patients via chronic lung colonisation. CF gene mutations increase cell surface fucosylation and CF patients also display modifications in their respiratory and salivary mucins with a higher percentage of sialylated and sulphated oligosaccharides [1]. These cystic fibrosis mucins and cell surface glycoconjugates carry fucose as the terminal sugar residue. Since the *P. aeruginosa* lectins have been characterised to reveal an outstandingly high affinity of PA-IIL for fucose, they can serve as targets for binding by PA-IIL [2].

Precise three-dimensional knowledge of the lectin sugar-binding site should allow the unusually high affinity to be understood and allow a better design of new anti-bacterial-adhesion prophylactics. With this aim in mind, the crystal structure of the PA-IIL:fucose complex has been determined using the single-wavelength anomalous diffraction (SAD) technique on beamline **ID14-1** using the anomalous signal from holmium at 0.934 Å wavelength. Non-isomorphous native data collected on beamline **ID14-2** were obtained to 1.3 Å resolution and the holmium structure used as a molecular replacement model for phasing in the asymmetric unit.

The PA-IIL crystals contain a tetramer with each monomer binding two calcium ions and a fucose molecule (**Figure 10**). The calcium binding pocket is

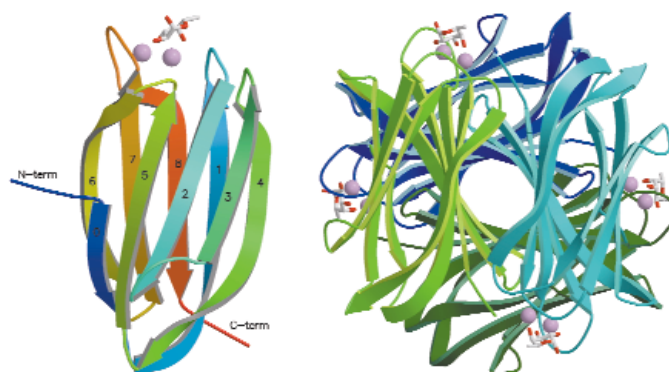


Fig. 10: Structure of the PA-IIL-fucose complex with stick representation of fucose and calcium ions as space-filling models: (left) Monomer with numbering of β -strands in agreement with the greek-key motif (1 to 5); (right) The tetramer making up the asymmetric unit.

made up of five acidic groups (Glu95, Asp99, Asp101, Asp 104 and Glu114), the side chain oxygen of Asn103 and a carbonyl oxygen (Asn21) with two of the acid groups (Asp101 and Asp104) bridging between the calcium ions. In each monomer the calcium ions are just 3.75 Å apart and mediate the binding of fucose in a unique and sturdy carbohydrate-recognition mode (Figure 11). The fucose residue itself locks onto both calcium ions, with three of the fucose hydroxyl groups participating in both the coordination of the calcium ions and in hydrogen bonds with acidic groups forming the calcium binding site.

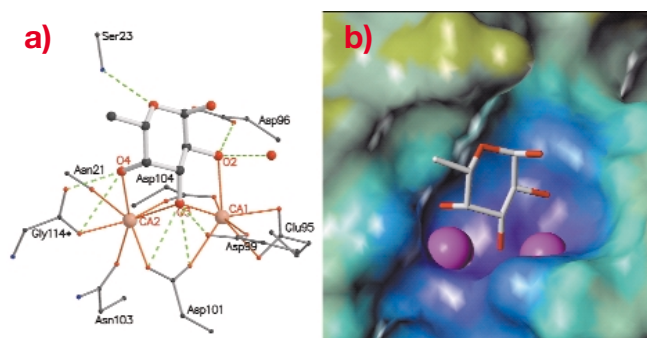


Fig. 11: Interactions of PA-IIL with calcium ions and fucose.
 (a) Stick representation of the amino acids involved in binding. Ca^{2+} coordination bonds are shown as solid orange lines; hydrogen bonds as dashed green lines. Colour coding: red, oxygen; blue, nitrogen; black, carbon; pink, Ca^{2+} .
 (b) Electrostatic surface representation of the PA-IIL binding site with Ca^{2+} as large pink spheres and fucose as a stick model.

In contrast with most lectins that display only weak affinity for monovalent sugar ligands, the PA-IIL-fucose interaction has an association constant in the micromolar range. The unusual ternary complex formed by the two Ca^{2+} ions, the side chains of amino acids that coordinate them, and the sugar provides the basis for such strong affinity. In order for sugars to bind to Ca^{2+} ions as found in the structure of PA-IIL, they must have a particular stereochemical arrangement of three carbohydrate hydroxyl groups. L-fucose, L-galactose, D-mannose and D-arabinose all have the necessary stereochemistry and all of them are recognised by PA-IIL, albeit with diverse affinities [2]. Subsequent modelling studies, based on the fucose complex structure, and binding studies have demonstrated that the preferred ligands of this bacterial lectin belong to the Lewis a series. Such structure-based knowledge could be used for the design of efficient anti-bacterial compounds and, furthermore, the unusually high affinity interaction of this novel binding mode suggests that PA-IIL may be a useful target for oligosaccharide-based therapeutics.

References

- [1] Lamblin *et al.*, *Glycoconj. J.* **18**, 661-684 (2001).
- [2] N. Garber, U. Guempel, N. Gilboa-Garber and R.J. Doyle, *FEMS Microbiol. Lett.* **48**, 331-334 (1987).

Principal Publication and Authors

E. Mitchell (a), C. Houles (b), D. Sudakevitz (c), M. Wimmerova (b), C. Gautier (b), S. Pérez (b), A.M. Wu (d), N. Gilboa-Garber (c) and A. Imberty (b), *Nature Struct. Biol.* **9**, 918-921 (2002).

(a) ESRF

(b) CERMAV – CNRS, Université Joseph Fourier, Grenoble (France)

(c) Bar-Ilan University, Faculty of Life Sciences, Ramat Gan (Israel)

(d) Institute of Molecular and Cellular Biology, Chang-Gung University (Taiwan)

Structure of the Bovine Lysosomal α -Mannosidase, the Enzyme Involved in the Lysosomal Storage Disease α -Mannosidosis

Lysosomal α -mannosidase (LAM) is a member of the glycosyl hydrolase family GH38. It hydrolyses all known α -mannosidic linkages in lysosomes. Lysosomes are cellular particles, which are responsible for the breakdown of cellular end products. They have an internal pH of 4.5 and are thus much more acidic than the rest of the cell. Errors in lysosomal processes lead to a number of inherited lysosomal storage diseases, many of which are very serious. These include α -mannosidosis, which is a rare disease in humans, cattle, cats and guinea pig. Lack of LAM activity causes swelling of the lysosomal vacuoles, and apparently leaking of the unhydrolysed sugars from these vacuoles causes the symptoms of the disease; mental retardation, skeletal changes, hearing loss and reduced immunity in humans [1, 2]. Two protein level α -mannosidosis mutations have been identified in cattle and six in humans.

We isolated the natural lysosomal α -mannosidase directly from bovine kidneys [2] (10 kg of kidneys yielding 5-20 mg of the enzyme). The LAM protein is a ~250 kDa homodimer which is both glycosylated and proteolytically cleaved during its maturation and transport to lysosomes. The protein was crystallised in a fully-glycosylated form in a large hexagonal unit cell with cell dimensions $a = b = 117.88$ Å, $c = 582.04$ Å. Data were collected to 2.7 Å resolution at beamline ID14-4. We solved the structure in $P6_122$ space group by molecular replacement with a distant relative, the *Drosophila melanogaster* Golgi II α -mannosidase. The asymmetric unit of the crystal contains a single

monomer and the crystallographic packing offered two possible LAM dimers. The correct dimer was identified by electron microscopy.

The N-terminal active site domain is a distorted 7-stranded α/β barrel and the active site is formed on the top of the barrel. Following the barrel domain, the structure consists of a 3-helix bundle, two further small β domains and a large 17 stranded β -domain (**Figure 12**). All known LAMs have a conserved glycosylation site following the 3-helix bundle. In our bovine LAM (bLAM) structure this site contains a high mannose type glycan, which rests against the 3-helix bundle. Two GlcNAc and eight mannose residues are visible in the electron density map. The bLAM structure also contains several salt bridge networks. As these networks are not conserved in related enzymes functioning at neutral pH, it seems likely that these networks are involved in stability and activation of the enzyme at the lysosomal pH (~ 4.5), which is close to the pK_a of aspartic and glutamic acids.

Mutations in the LAM amino acid sequence that cause α -mannosidosis in humans are scattered throughout the structure. Only the mutation H72L is in the active site itself, where it affects a metal-coordinating residue. Two others (T355P and P356R) are located at the start of an α -helix in the active-site domain and presumably disturb the initiation of the helix and folding of the domain. Three further mutations (W714R, R750W and L809P) are located in the 17-stranded β -domain. Of these, R750W is possibly the most interesting, since it mediates an interaction between three domains.

Both mutations causing α -mannosidosis in cattle [2] are related to the active site of the enzyme. The R220H mutation in Galloway cattle affects R220, which is hydrogen-bonded both to an important residue in the catalysis, D196, as well as to the substrate mimic Tris. H220 would be able to form hydrogen bonds to D196 and to Y380 as R220 does, but the hydrogen-bonding to Tris and presumably to the substrate would be broken. This mutation will thus most likely affect the substrate binding and also the chemistry of D196. Another mutation, F320L, causes α -mannosidosis in Angus cattle and is also known to affect the stability of the enzyme. In the structure, the aromatic ring in A:F320 stacks against Y84 in a loop which is involved in dimer formation. Its mutation to Leucine would presumably weaken monomer-monomer interactions in the physiological dimer. However, this mutation might also affect catalysis since it follows another active-site residue, D319, in the amino acid sequence.

Our structure determination helps to explain how particular mutations on the LAM amino acid sequence can result in α -mannosidosis and represents the first step in understanding the biological mechanism behind

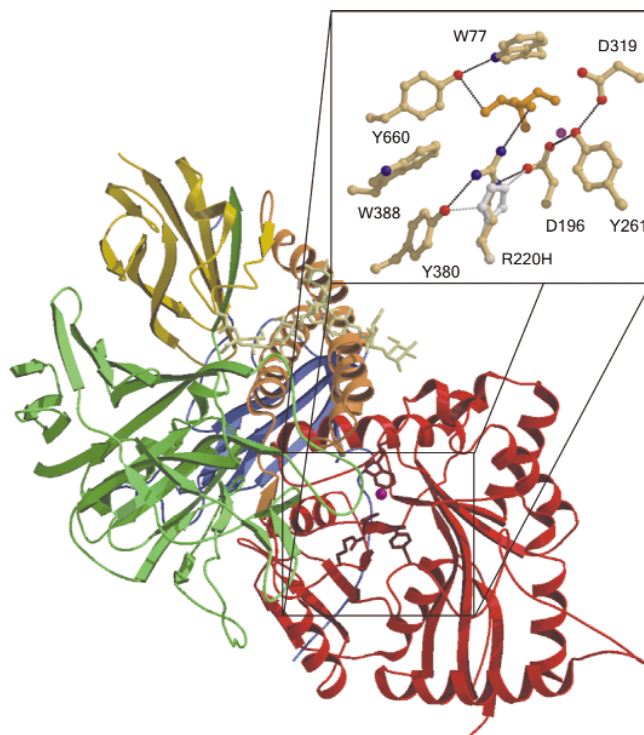


Fig. 12: The three-dimensional structure of bovine α -mannosidase. The N-terminal active-site domain is shown in red, the three-helix bundle in brown and the two small β domains in blue and khaki. The large 17-stranded β -domain is shown in lime green. The high-mannose sugar found at the glycosylation site at the end of the three-helix bundle is shown in stick representation. The insert shows, in ball-and-stick representation, the residues involved in substrate binding and catalysis (the substrate mimic, Tris, is shown in brown) and demonstrates how the R220H mutation would lead to a loss of a hydrogen bond to the substrate.

the disease. It also provides a first structure of a mammalian enzyme in this class of glycoside hydrolases and provides an interesting new way of low pH activation.

References

- [1] T. Berg, H.M. Riise, G.M. Hansen, D. Malm, L. Tranebjaerg, O.K. Tollersrud and Ø. Nilssen, *Am. J. Hum. Genet.* **64**, 77-88 (1999).
- [2] O.K. Tollersrud, T. Berg, P. Healy, G. Evjen, U. Ramachandran and Ø. Nilssen, *Eur. J. Biochem.* **246**, 410-419 (1997).

Authors

P. Heikinheimo (a), R. Helland (a), H-K. Schrøder Leiros (a), I. Leiros (a), S. Karlsen (a), G. Evjen (a), R. Ravelli (b), G. Schoehn (b,c), R. Ruigrok (b), O-K. Tollersrud (a), S. McSweeney (b,d) and E. Hough (a).

(a) Universitetet i Tromsø, Tromsø (Norway)

(b) EMBL, Grenoble (France)

(c) IBS, Grenoble (France)

(d) ESRF

Protein and Virus Crystallography under High Hydrostatic Pressure

The potential of pressure as a thermodynamic variable in macromolecular crystallography remains largely unexplored although the pioneering work [1] on the structure of tetragonal crystals of hen egg-white lysozyme (tHEWL) compressed at 1 kbar in a polycrystalline beryllium cell was carried out as far back as 1987. This work was followed only recently by the publication of the 1.5 kbar structure of another small monomeric protein, sperm whale metmyoglobin, pressurised in a similar cell. A different device, a diamond anvil cell (DAC), has also been used to measure the compressibility of HEWL crystals although without follow-up data collection [2].

On beamline **ID30**, the combination of a DAC, ultra-short wavelength undulator radiation and a large imaging plate has allowed us to extend the field of high-pressure macromolecular crystallography in terms of both the accessible pressure range (increased by one order of magnitude with respect to the pressure range of beryllium cells), and the data quality obtainable. Experimental procedures were established and the first results obtained on crystals of tHEWL and Cu, Zn superoxide dismutase (SOD), a dimeric protein [3]. Compressibility measurements were achieved up to 8.2 kbar on tHEWL crystals and beyond 10 kbar for SOD crystals. Diffraction data from tHEWL crystals at 7 kbar were then collected and analysed demonstrating that high-pressure data can be of very similar quality (resolution 1.6 Å, completeness 0.93, multiplicity 7.2, R_{merge} (I) 0.057) to that expected from experiments carried out at ambient pressure. tHEWL structures at normal pressure and 7 kbar were then refined in parallel at 1.6 Å resolution and a detailed comparison was made (example in [Figure 13](#), article in preparation).

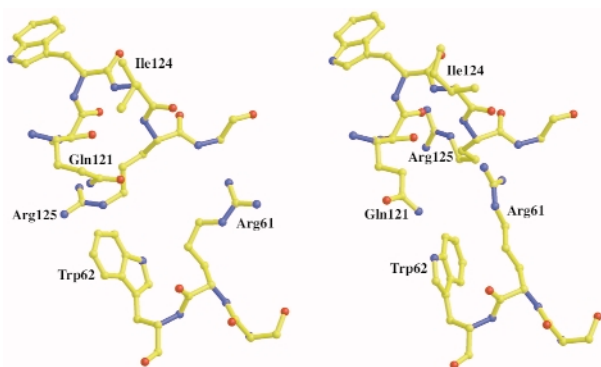


Fig. 13: A representation of a molecular contact region in lysozyme at ambient pressure (left) and at a pressure of 7 kbar (right). Several residues in the 7 kbar structure take new positions to accommodate the closer contacts induced by pressure between symmetry-related molecules in the crystal.

We then applied the same methodology to crystals of cowpea mosaic virus (CPMV) particles, the first example of a crystallised macromolecular assembly studied at high pressure. CPMV is a member of the Comovirus family, a group of icosahedral plant viruses similar to mammalian Picornaviruses. The refined 2.8 Å crystal structure at atmospheric pressure was available [4]. Single oscillation images of a cubic crystal of CPMV were recorded at several pressures between 1 bar and 4.4 kbar at which point the crystal no longer diffracted. The initial crystal at 1 bar, 1.1 and 2.0 kbar was disordered and diffracted only to low resolution with the space group tentatively assigned as P23. At 3.3 kbar, however, the diffraction pattern extended to 2.6 Å with a high signal-to-noise ratio ([Figure 14](#)) and was indexed in space group I23. In this particular case, pressure induces a first order transition, with long-range three-dimensional order most likely reached through small rotations and translations of virus particles. The ordering effect of high pressure observed for CPMV was not unexpected, as an increase of pressure at constant temperature leads to a decrease of the entropy of the compressed system.

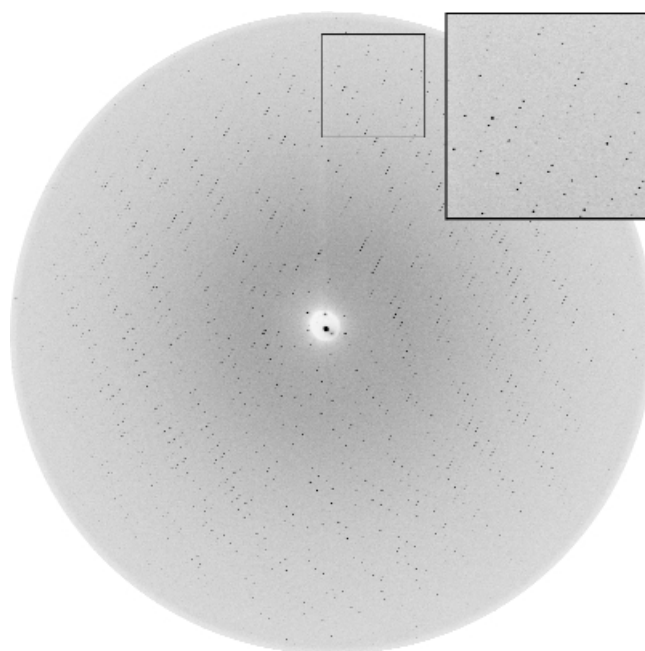


Fig. 14: An oscillation image (0.3°) from an I23 form CPMV crystal at 3.3 kbar ($\lambda = 0.3305$ Å; crystal-to-detector distance 1400 mm). The resolution is limited by the detector edge to 2.7 Å. The insert shows an enlargement of the diffraction quality at the edge of the image. Using such images from 8 crystals, a merged data set at 2.7 Å resolution has been obtained.

The type of disorder in CPMV at atmospheric pressure appears to be unusual, and further experiments on other systems are required. If it turns out that improvement of crystal, and hence data quality, under high pressure is a more general phenomenon, the consequences might be quite important for macromolecular crystallography. Besides this possible outcome, the demonstration that accurate structural information on macromolecular

structures can be obtained at high pressure opens avenues such as the exploration of protein sub-states, the study of interactions between macromolecules and between subunits and the detection of the onset of pressure-induced denaturation.

References

- [1] C.E. Kundrot and F.M. Richards, *J. Mol. Biol.* **193**, 157 (1987).
- [2] A. Katrusiak and Z. Dauter, *Acta Cryst.* **D52**, 607 (1996).
- [3] R. Fourme, R. Kahn, M. Mezouar, E. Girard, C. Hoerentrup, T. Prangé and I. Ascone, *J. Synchrotron Rad.* **8**, 1149 (2001).
- [4] T. Lin, Z. Chen, R. Usha, C.V. Stauffacher, J.B. Dai, T. Schmidt and J.E. Johnson, *Virology* **265**(1), 20 (1999).

Principal Publication and Authors

R. Fourme (a), I. Ascone (b), R. Kahn (c), M. Mezouar (d), P. Bouvier (d), E. Girard (c), T. Lin (e) and J.E. Johnson (e), *Structure* **10**, 1409 (2002).

(a) Synchrotron SOLEIL, Saint Aubin (France)

(b) LURE, Orsay (France)

(c) IBS, Grenoble (France)

(d) ESRF

(e) Scripps Research Institute, La Jolla (USA)

Beamline Automation – Why and How?

Progress report by J.E. McCarthy and S. Arzt (ESRF)

The advent of recombinant gene technology and protein expression systems combined with the publication of genome sequences for many organisms, including *H. sapiens* and many of his pathogens, has led to a surge in the number of macromolecular structures to be studied. X-ray crystallography is the dominant technique used in the determination of the three-dimensional structures of macromolecules and third-generation synchrotron sources such as the ESRF are already proving of great benefit in the rapid collection of X-ray data from macromolecular single crystals. In the current era of structural genomics it is important that the structure-determination process occurs as rapidly as possible and modern synchrotron macromolecular crystallography (MX) has evolved into an efficient pipeline of sample screening and subsequent data collection, reduction and phasing at the beamline [1]. However, when carried out manually, this process has many bottlenecks, which will become increasingly evident as crystal production becomes more efficient. Automation is therefore an essential step in ensuring that

macromolecular structure solution becomes a very high throughput process.

Automation of a synchrotron MX experiment may be divided into two areas; data collection and data processing, and beamline alignment and stability. Data collection automation should include processes for sample mounting/dismounting, aligning and screening, whilst automation of data processing needs to address image indexing and integration, data reduction, phasing, map calculation and model building. Beamline alignment automation should ensure that the users have access to a beam that is stable in both intensity and position during their experiments, without having to carry out manual alignment procedures. All of the aspects described above have been addressed in the automation program currently being undertaken at the ESRF by the JSBG.

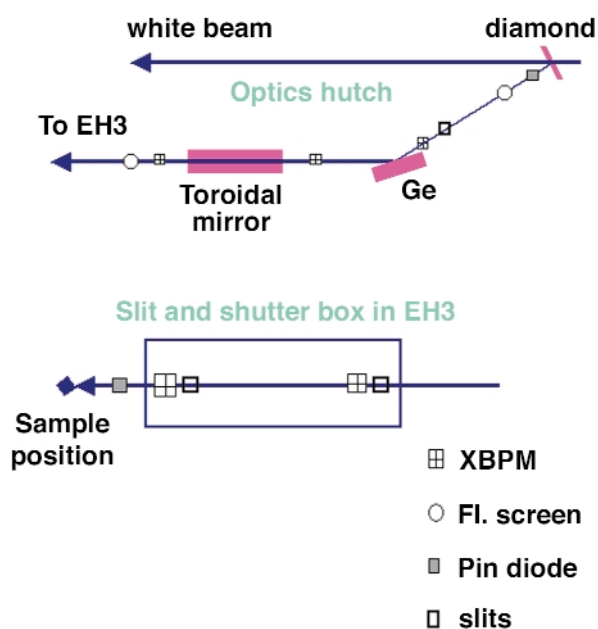


Fig. 15: Outline of automation diagnostics on the refurbished beamline ID14-3. Information concerning the X-ray beam position will be constantly monitored using the XBPMs. This will be used along with monitored values of all motor and encoder positions for constant feedback and auto-regulation of the beamline components.

For beamline alignment, a system of X-ray beam position monitors (XBPMs) will be used to constantly track both the position and intensity of the X-ray beam. The positions of the XBPMs and other diagnostic tools are shown in Figure 15 for the newly refurbished ID14-3 beamline. The monitored values will be stored in a database along with motor and encoder positions, and will be used for constant feedback and auto-regulation of the beamline components.

Mounting and alignment of pre-cryocooled samples into the X-ray beam will be done using an automatic sample

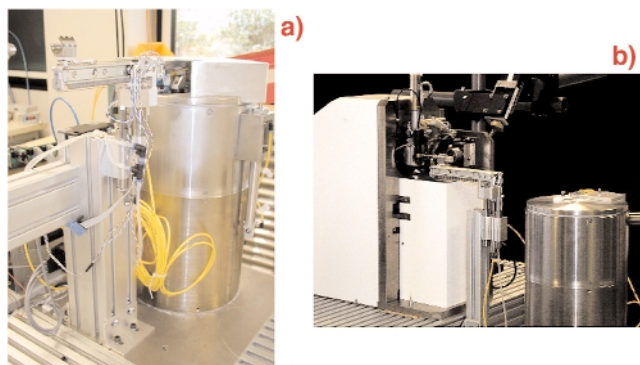


Fig. 16: (a) The automatic sample changer and (b) the micro-diffractometer.

changer and micro-diffractometer (**Figure 16**), both developed by the JSBG. The sample changer will allow storage and automatic mounting/dismounting of up to 50 crystal samples. The micro-diffractometer allows visual monitoring of the X-ray beam and can automatically centre micro-crystals accurately in the X-ray beam. Prototypes of both the sample changer and the micro-diffractometer have been successfully tested and will be installed on selected ESRF MX beamlines within the coming year.

Automatic screening of crystals as well as data processing will be handled by the DNA project [2], an inter-facility project involving scientists from ESRF, SRS Daresbury and the MRC-LMB. The system

characterises each sample by analysing test images to determine crystal and data quality. If these are acceptable, a strategy for optimum data collection is proposed then followed (including integration etc), otherwise the sample changer is activated to mount a new crystal and the screening procedure repeated. In this way, the DNA software will supervise simultaneously data collection and processing. Automation of information management uses PXWEB, a Web-based database combining information from the ESRF User Office with a local experimental database. Users may enter and access information about the crystal samples, view/edit reports about collected data, monitor current data collections with access to images and reexamine previously collected data.

The ESRF's first fully-automated MX beamlines, **ID14-3** and **ID23**, are under construction and are expected to take users during 2003.

References

- [1] E.P. Mitchell, *Nucl. Instr. and Meth. A.* **467-468**, 1372-1374 (2001).
- [2] A.G.W. Leslie, H.R. Powell, G. Winter, O. Svensson, D. Spruce, S. McSweeney, D. Love, S. Kinder, E. Duke and C. Nave, *Acta Cryst. D* **58**, 1924-1928 (2002).

Principal Publication and Authors

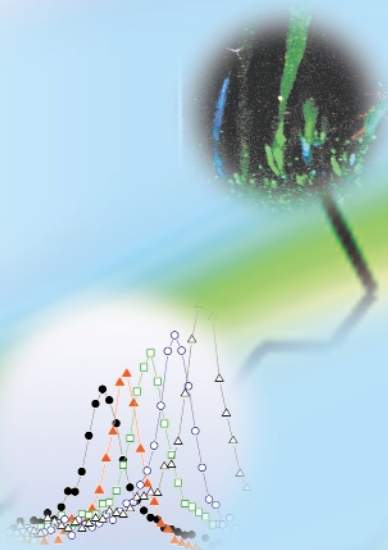
J.E. McCarthy and S. Arzt.
ESRF

Introduction

Soft condensed matter science accounts for about 15% of User activities at the ESRF. It is a broad discipline that addresses questions concerning the microstructure, kinetics, dynamics and rheology of complex and nano-structured materials (polymers, colloids, fluids, liquid crystals, etc.) in 3D and under reduced dimensionality. Many experiments are concerned with the structure determination of thin organic films and membranes or diffraction from fibres, small unit cell systems and biological entities. They also involve studies of *in situ* processing, site-selective chemistry and tailoring of molecular assemblies. This research is carried out at several beamlines and has been supported since January 2002 by a newly formed Soft Condensed Matter Group (www.esrf.fr/UsersAndScience/Experiments/SCMatter/), comprising the insertion device beamlines ID02, ID10A, ID10B and ID13. Similar activities are pursued at the CRG beamlines BM02, BM26 and BM32. The borders with neighbouring disciplines such as life sciences, surface- and interface physics, chemistry and materials science have become increasingly transparent. This is aided by constant progress at beamlines (availability of micrometre and submicrometre-sized and/or coherent X-ray beams, two-dimensional detectors with high spatial and temporal resolution, advanced sample environments) and the large variety of available measuring techniques. Key techniques are single crystal diffraction as well as small-angle and wide-angle scattering (μ SAXS/WAXS) with microbeams at ID13, time-resolved small-angle and wide-angle scattering (SAXS/WAXS) and ultra small-angle scattering (USAXS) at ID02, high-resolution diffraction and reflectometry (XRD, XRR) and X-ray photon correlation spectroscopy (XPCS) at ID10A, and grazing-incidence diffraction (GID), X-ray reflectometry (XRR) and grazing-incidence small-angle scattering (GISAXS) at ID10B.

In 2002, the main technical developments at ID02 were commissioning of the bypass SAXS camera for experiments requiring special detectors, as well as improvements in photon flux and sensitivity of the SAXS detector (resulting in a combined gain of five). Moreover, a new rheometer was added to the list of sample environments, allowing low stress level and transient rheological measurements together with combined small- and wide-angle (SAXS and WAXS) scattering. Selected scientific highlights include studies of millisecond range structural transformations in micellar solutions [1], microdomain ordering in block copolymers [2] and work tracing the mineral lyotropic liquid-crystalline phase of magnetic nanorods [3]. The interference effect

Soft Condensed Matter



Highlights 2002

in the muscle myosin diffraction was further exploited to shed new light on the mechanism of muscle contraction [4]. Other noteworthy examples include the elucidation of the counter-ion distribution in spherical polyelectrolyte brushes by anomalous SAXS (collaboration between the Polymer Institut at U. Karlsruhe/Germany and ID02), and probing the evolution of microstructure and dynamics (collaboration with ID10A) in attractive colloidal systems.

The ID10A beamline keeps its multipurpose character, accepting experiments from the soft condensed matter, surface and interface, methods and instrumentation and hard condensed matter communities. An example of activities in the latter discipline is a study of the motional ordering of a charge-density wave in the sliding state [5]. Another speciality of ID10A lies in the field of slow dynamics studied by means of photon correlation spectroscopy (XPCS) with coherent X-ray beams. In the domain of soft condensed matter, two-dimensional detection has been used to investigate very slow dynamics and ageing phenomena in non-ergodic glassy materials. Fast, zero-dimensional detection has been used to study layer-displacement fluctuations in smectic membranes [6]. We can identify two main poles of interest for in-house research. The first concerns investigating the structure and dynamics of colloidal suspensions, from glassy systems (highly-concentrated colloidal suspensions, colloid-polymer mixtures and polymer gels) to charged or magnetically-interacting systems. The second concerns the study of (surface) dynamics in "simple" or complex liquids. Recent work on the critical viscosity at the free surface of a liquid crystal is featured in the following highlights section.

The ID10B (Troika II) beamline is the only beamline at the ESRF that routinely provides all surface diffraction techniques for the study of liquid surfaces and interfaces and length-scales from sub-nm to 100 nm (in some cases even up to 1000 nm). A recent upgrade of the deflector stage allows us now to reach a momentum transfer of $Q_z = 8 \text{ nm}^{-1}$ in a reflectivity experiment on a liquid surface.

In 2003 the beamline will install a system to focus the X-ray beam vertically thus providing a significant gain in flux. In-house research is predominantly focused on structural studies of liquid and complex fluid (colloid, sol, gel) interfaces, two-dimensional assemblies of molecules and macromolecules formed at such interfaces and the interaction of these monomolecular films with supporting media [7]. Interaction of antimicrobial peptides with prokaryotic and eukaryotic cell membranes mimicked by different phospholipid monolayers is presented as an example in this year's highlights [8].

On ID13 a second experimental hutch has been commissioned for μ SAXS/ μ WAXS with a dedicated Kirkpatrick-Baez optics. A new in-vacuum undulator optimised for about 13 keV now complements the original tuneable undulator. The use of sub- μm optics, like waveguide or Fresnel optics was further explored for different materials including semiconductors, biopolymers and polymers. Thus scanning μ WAXS with a waveguide beam of about 100 nm across Kevlar fibres and modelling the data with Monte Carlo methods could evidence differences in rotational disorder [9]. Micro-deformation remained a very active field and several polymeric materials have been studied, when subjected to various deformation tests (e.g. cold drawing [10] or stress oscillation during static loading). Furthermore, μ SAXS craze field scanning in deformed industrial samples was performed and modelled. A micro-hardness setup has been commissioned and allowed us to perform *in situ* μ WAXS experiments during indentation [11]. The microgoniometer has been available on a regular basis for protein crystallography experiments. Several small unit cell experiments were performed using the detector rotating-arm. The flexibility of this setup has also been demonstrated in μ SAXS experiments on single cell nuclei.

The following selected highlights reflect both the wide variety of subjects and the specific strengths of individual beamlines. The first contribution shows how the beam from a bending magnet beamline (BM26) can be used to illustrate the

self-organisation of colloidal hard sphere particles into a crystalline structure. In the second contribution the superior brilliance of an insertion device beamline (ID10A) is used to produce a coherent X-ray beam thus enabling the study of the critical behaviour of the viscosity of a liquid crystal at the nematic-smecticA phase transition in 8OCB. In a beautiful experiment at ID02 high-resolution SAXS and WAXS were used to illustrate the hierarchical self-organisation of nanotubes. The interaction of antimicrobial peptides with prokaryotic and eukaryotic cell membranes mimicked by different phospholipid monolayers was studied by reflectivity and grazing-incidence techniques at ID10B. Finally, micro-SAXS at ID13 was used to unravel the (twisted plywood) diffraction pattern of collagen fibrils in fish scales.

- [1] S. Schmölzer *et al.*, *Phys. Rev. Lett.* **88**, 258301-1 (2002).
- [2] A. Böker *et al.*, *Phys. Rev. Lett.* **89**, 135502-1 (2002).
- [3] B.J. Lemaire *et al.*, *Phys. Rev. Lett.* **88**, 125507-1 (2002).
- [4] G. Piazzesi *et al.*, *Nature* **415**, 659 (2002).
- [5] R. Danneau *et al.*, *Phys. Rev. Lett.* **89**, 106404-1 (2002).
- [6] I. Sikharulidze *et al.*, *Phys. Rev. Lett.*, **88**, 115503-1 (2002).
- [7] B. Struth *et al.*, *Phys. Rev. Lett.* **88**, 025502-1 (2002).
- [8] O. Konovalov *et al.*, *European Biophysics Journal*, **31**, 428 (2002).
- [9] S. Roth *et al.*, *Macromolecules*, *in press*.
- [10] M.C. Garcia-Gutiérrez *et al.*, *Macromolecules* **35**, 7320 (2002).
- [11] A. Gourrier *et al.*, *Macromolecules* **35**, 8072 (2002).

Glass Microspheres Generate Perfect Aperiodic Order

Self-organisation of colloidal hard spheres into crystalline structures provides an important model of atomic crystal growth and attracts significant attention as a technique for inexpensive, large-scale fabrication of photonic materials [1]. A crystal is said to be perfect when the positions of the "atoms" (in the present case the micro-spheres) are correlated throughout the whole crystal despite their thermal motion. In reality, however, most crystals are not perfect [2]. Although local order may be apparent, various defects or strain fields can easily destroy order on a large scale. Moreover, the colloidal spheres are non-identical as there is slight variation in their sizes, which may also affect the long-range order. To date, confocal optical microscopy has provided essential information on the local order in colloidal crystals, while order on a large scale was rarely addressed. The latter can be determined by diffraction techniques from the width δq of the reciprocal lattice reflections. Colloidal crystals are a particularly challenging subject for X-ray studies because the sub-micrometre "atoms" are more than three orders of magnitude larger than the wavelength λ (in this work the silica spheres had a diameter of 224 nm and $\lambda = 0.124$ nm). For crystals possessing positional order over distances Λ as large as 10^3 lattice periods, the width δq of the diffraction peaks is smaller than one millionth part of the X-ray wavevector $k_0 = 2\pi/\lambda = 50$ nm⁻¹. The results obtained at beamline **BM26B** "DUBBLE CRG" demonstrate that such a resolution is readily achievable in a small-angle X-ray diffraction experiment on a single colloidal crystal.

The apparent width of the reflections $\sim 3 \times 10^{-3}$ nm⁻¹ on the detector (Figure 17) is limited by the instrumental resolution rather than by the crystal order in the transverse direction. Rocking the crystal by a tiny angle around one of the low-index orientations is found to lead to significant modification of the pattern, which does allow for accurate determination of the width δq of the reflections in the longitudinal direction (along the beam). In our small-angle diffraction geometry (maximum diffraction angle 2θ in Figure 17 is $\sim 0.5^\circ$), the curvature of the relevant part of the Ewald sphere is extremely small. However, due to the smallness of δq , it is clearly visible in (c) and (d) yielding an asymmetric diffraction pattern. The brightest reflections are found along a circle where the Ewald sphere is intersected by a plane of reciprocal lattice nodes. Detailed analysis of the data shows that in fact $\delta q < 5 \times 10^{-5}$ nm⁻¹ suggesting long-range interplanar positional order throughout the sample thickness. Sample translations revealed only small modifications of the diffraction pattern within the same single crystal. This result indicates high (within 0.1°) orientational correlation over distances larger than a millimetre suggesting high rigidity of the hexagonal planes.

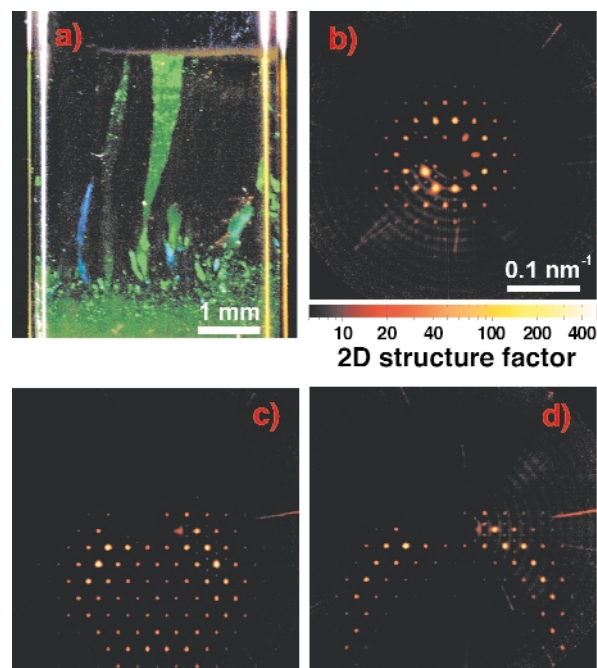


Fig. 17: (a) Bragg reflections of light from colloidal crystals in a flat capillary (cross section 0.2 x 4 mm²); (b-d) two-dimensional structure factors (X-ray diffraction intensity divided by the single sphere form factor) obtained from the large crystal in the middle of the capillary in (a). In (b) the incident beam is normal to the hexagonal planes. The sample is tilted by 0.2° in (c) and by 0.3° in (d).

The crystal was found to possess a randomly-stacked hexagonal close-packed (rhcp) structure. Due to irregular stacking, some features of the reciprocal lattice of an rhcp crystal are smeared out into Bragg scattering rods while periodicities common to all layers lead to sharp Bragg spots, which are both clearly visible in the structure factor profile (Figure 18). The intensity modulation along the rods is also typical for rhcp crystals [2].

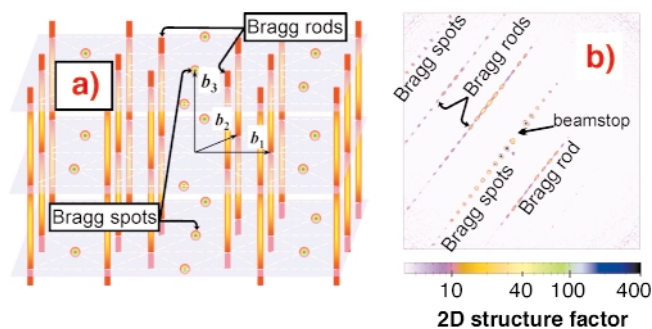


Fig. 18: (a) Reciprocal lattice of rhcp crystals. The shadowed planes are to guide the eye. (b) Sets of Bragg spots and Bragg rods in the structure factor measured with X-rays propagating along the hexagonal crystal planes.

In summary, various order parameters of single colloidal crystals are determined by small-angle X-ray diffraction with a resolution of $10^{-6}k_0$. The glass microspheres are found to organise themselves into flat hexagonal layers, which are randomly stacked. Despite the lack of

periodicity, perfect interplanar positional order is demonstrated.

References

- [1] Y.A. Vlasov *et al.*, *Nature* **414**, 289 (2001).
 [2] A. Guinier, *X-ray Diffraction in Crystals, Imperfect Crystals and Amorphous Bodies*, Dover Publications (1994).

Principal Publication and Authors

A.V. Petukhov (a), D.G.A.L. Aarts (a), I.P. Dolbnya (b), E.H.A. de Hoog (a), K. Kassapidou (a), G.J. Vroege (a), W. Bras (b) and H.N.W. Lekkerkerker (a), *Phys. Rev. Lett.* **88**, 208301 (2002); *ibid* **90**, 028304 (2003).

(a) Van't Hoff Laboratory for Physical and Colloidal Chemistry, Utrecht (The Netherlands)

(b) DUBBLE CRG, ESRF

Structure and Dynamics at the Free Surface of a Liquid Crystal

The liquid crystal state was first observed in 1888 by the Austrian botanist Frederich Reinitzer. Academic interest in liquid crystals grew enormously a decade later once the similarities between the normal-to-superconductor transition and the nematic-to-smectic phase transition were brought to light [1]. A liquid consisting of elongated molecules is said to be in the nematic phase when the molecules are randomly arranged but aligned to point along the same direction. This changes in the smectic A (SmA) phase, where the molecules rearrange into a layered structure with the molecules standing normal to the layers. It is well known that SmA ordered clusters are formed in the nematic phase when the phase transition is approached from above. The size of these clusters is characterised by two correlation lengths ξ_{\parallel} and ξ_{\perp} (\parallel parallel, \perp perpendicular to the molecules). We have probed the SmA ordering at the free surface of the liquid crystal compound 8OCB by X-ray scattering. The experiment was performed at ID10B and the growth of the SmA layering peak upon approaching the phase transition temperature T_{NA} is shown in Figure 19 (inset). From the width of the peak, the correlation length ξ_{\parallel} can be extracted as shown in Figure 19. A diverging behaviour $\xi_{\parallel} \propto (T/T_{NA})^{-\nu_{\parallel}}$ with critical exponent $\nu_{\parallel} = 0.70$ is evident and the best power-law fit determines $T_{NA} = 337.74$ K. The second exponent ν_{\perp} is 0.58.

The structural change from a nematic phase to a layered smectic structure has also consequences for the dynamic properties of the liquid. In the nematic phase the viscosity is anisotropic and one needs three viscosity coefficients

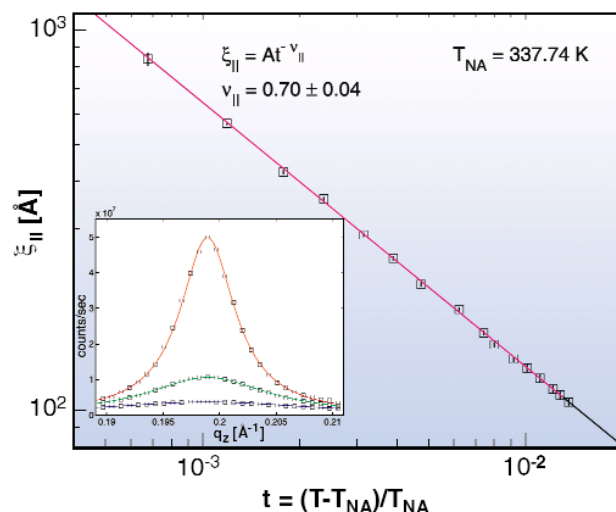


Fig. 19: Critical behaviour of the smectic order correlation length ξ_{\parallel} .

η_{1-3} for its description. η_{1-2} remain finite at the N-to-SmA transition while η_3 is predicted to show critical behaviour. To verify this we have investigated the free surface of 8OCB by X-ray photon correlation spectroscopy (XPCS) at beamline ID10A, applying a coherent X-ray beam. The surface of a liquid is covered by thermally-activated capillary waves and with XPCS the dispersion relation $\omega(q)$ can be measured [2]. The results for 8OCB are shown in Figure 20 (inset) for three different temperatures. In all three cases a linear dependence $\omega(q) \propto q$ is observed indicating that the capillary wave is over-damped [2]. The viscosity coefficient η_3 can be deduced from the slope of the dispersion relation. The result is plotted in Figure 20 vs. reduced temperature t and a critical, diverging behaviour is apparent. The solid line is a power-law fit to the data yielding a critical exponent of $x=0.95$. Previously it was predicted [3] that there is a relation between the dynamic exponent x and the static exponents ν_{\parallel} and ν_{\perp} such that $x=3\nu_{\parallel}-2\nu_{\perp}$. Our measurements yield the first experimental evidence for the validity of this relationship.

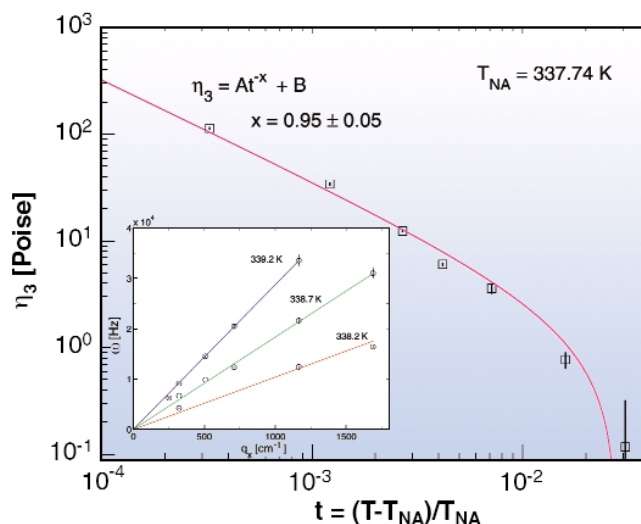


Fig. 20: Critical behaviour of the viscosity coefficient η_3 determined by XPCS.

In summary, we have used the fact that X-ray scattering can yield information on both the static and the dynamic behaviour of a system to obtain new insight into the connection between structural and dynamic properties at the free surface of a liquid crystal.

References

- [1] P.G. de Gennes, *Solid State Commun.* **10**, 753 (1972).
- [2] T. Seydel, A. Madsen, M. Tolan, G. Grübel and W. Press, *Phys. Rev. B* **63**, 073409 (2001).
- [3] K.A. Hossain, J. Swift, J.-H. Chen and T.C. Lubensky, *Phys. Rev. B* **19**, 432 (1979).

Principal Publication and Authors

A. Madsen (a), J. Als-Nielsen (b) and G. Grübel (a), *Phys. Rev. Lett.* (2002) *in print*; A. Madsen (a), B. Struth (a) and G. Grübel (a), to be published.

(a) ESRF

(b) Niels Bohr Institute, University of Copenhagen (Denmark)

Supramolecular Organisation of Biomimetic Nanotubes

Controlled self-assembly of molecules into well-defined nanoscale structures is a challenging task, which has wide-ranging applications in biotechnology and materials science. These nanoscale structures can be realised by using naturally occurring proteins such as tobacco mosaic virus (TMV) [1]. Biological entities like viruses or microtubules, are perfectly monodisperse thanks to the perfection achieved by mother nature in protein self-assembly. In general, such level of perfection is hard to obtain in artificial systems. However, an alternative route has become feasible, based on synthetic molecules that can be programmed to self-organise in a tailored fashion. The design of such systems requires the understanding of the interrelationship between the molecular structure and the self-assembly process to nanostructures [2]. New strategies have developed using inorganic materials, lipids and amphiphilic compounds. One of the most promising approaches is based on the *de novo* synthesis of oligopeptide that self-organises in well-defined fibres.

In this context, the Lanreotide octapeptide developed by Beaufour-Ipsen laboratory that forms a therapeutic gel (autogel®) is an illustrative example. At a lower Lanreotide concentration than in the gel, monodisperse nanotubes are spontaneously formed (Figure 21). This work concerns the elucidation of supramolecular and molecular organisation

by small and wide angle X-ray scattering (SAXS and WAXS, respectively), carried out on ID02, and the complementary techniques of electron microscopy and vibrational spectroscopies. The exceptionally well-aligned WAXS pattern (Figure 22) reveals that the organisation within the nanotubes wall is crystalline with low mosaicity ($< 0.1^\circ$). This diffraction pattern acquired with a Lanreotide derivative can be unambiguously interpreted in terms of a 2D curved crystal and it is quite similar to the pattern recorded for Tobacco Mosaic Viruses [1]. The Patterson function of the nanotubes wall, calculated from the diffuse scattering, indicates a 20.7 Å alternation of aliphatic and aromatic residues that form beta-amyloid like fibres. The nanotubes are constituted by 26 of these fibres and consequently their diameter is very monodisperse as evidenced by SAXS (Figure 22). High-resolution SAXS further reveals the hexagonal packing of these tubes.

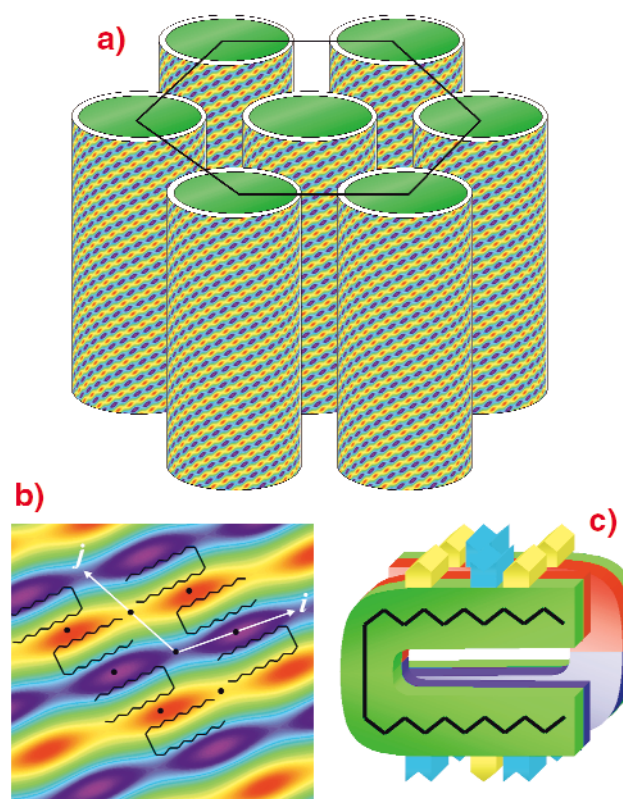


Fig. 21: a) hexagonal packing of the nanotubes, b) close-up of electron density and c) molecular conformation within the fibre.

A multidisciplinary approach involving high-resolution X-ray fibre diffraction and molecular spectroscopies (FTIR, FT-Raman) is essential to solve the Lanreotide nanotube structure at different hierarchical levels. The complete picture demonstrates a systematic segregation between aliphatic and aromatic residues at the origin of the nanotube organisation. High-resolution small-angle X-ray scattering revealed the nanotube sizes (diameter, wall thickness) and their packing. The controlled supramolecular organisation will be a promising route in the future for designing *de novo* molecules that can self-assemble into nanotubes with tuneable diameter.

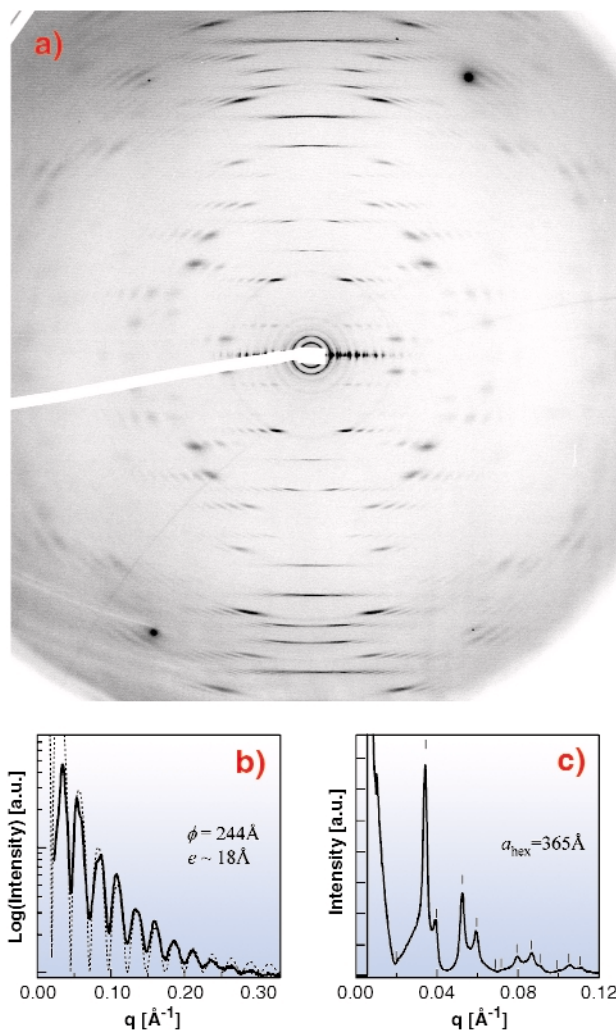


Fig. 22: (a) Fibre diffraction of the nanotube, (b) SAXS demonstrating the tube monodispersity and (c) high-resolution SAXS showing the hexagonal packing of the nanotubes.

References

- [1] A. Klug, *Angew. Chem. Int. Ed. Engl.* **22**, 565-636 (1983).
- [2] J.-M. Lehn, *Angew. Chem. Int. Ed. Engl.* **29**, 1304-1319 (1990).

Authors

F. Artzner (a), C. Valery (a), M. Paternostre (a,b)
 T. Narayanan (c)
 (a) UMR 8612 CNRS, Faculté de pharmacie de Chatenay-Malabry (France)
 (b) URA 2096 CNRS, CEA Saclay (France)
 (c) ESRF

Lipid Discrimination in Phospholipid Monolayers by the Antimicrobial Frog-skin Peptide, PGLa

Every organism must contend with invaders and thus have an active system of defence and offence. A broad spectrum of molecular mechanisms has evolved in nature to perform these functions. Important contributors to a fast response are small peptides consisting of 20-40 amino acids. The activity of these peptides does not seem to be correlated to specific receptors, rather they act by perturbing the barrier function of cell membranes. However, the molecular mechanism of their action is still a matter of debate. An understanding of how these peptides distinguish between bacterial and mammalian cell membranes would allow the design of novel peptide antibiotics, which could selectively kill bacteria. Interest in this research area has grown, since the number of bacterial strains being resistant to conventional antibiotics has been increasing dramatically in recent years.

Using X-ray reflectivity (XRR) and grazing-incidence diffraction (GID) techniques on **ID10B**, we studied the effects of the antimicrobial peptide, peptidyl-glycylleucine-carboxamide (PGLa), on lipid monolayers formed at the air/water interface. This peptide, consisting of 21 amino acid residues, is found in the skin secretion of the South African clawed frog, *Xenopus laevis*. Monolayers composed of the negatively-charged phospholipid distearoyl-phosphatidylglycerol (DSPG) mimicked a bacterial cell membrane, whereas a mammalian cell membrane was mimicked by the zwitterionic distearoyl-phosphatidylcholine (DSPC).

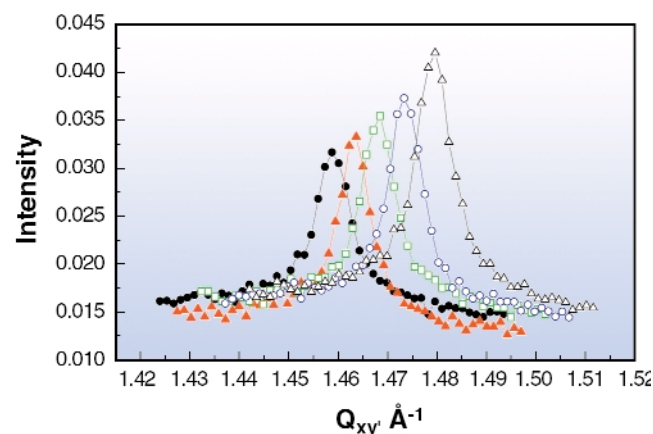


Fig. 23: Grazing-incidence diffraction of a DSPG monolayer at different surface pressures: (●) 20 mN/m, (▲) 25 mN/m, (□) 30 mN/m, (○) 35 mN/m, (Δ) 40 mN/m.

The Bragg peaks of the GID spectra (**Figure 23**), recorded from the monolayer of DSPG molecules, are characteristic for a two-dimensional (2D) ordering of the lipids in the monolayer plane. These peaks disappear completely from

the spectra at any surface pressure upon addition of peptides to the monolayer (molar ratio of lipid:peptide studied: 2.5:1, 5:1, 25:1), which indicates destruction of the initial order of the 2D lattice. The XRR measurements, which give information about the electron-density profile normal to the monolayer surface, demonstrate that, in addition to the loss of the lateral arrangement, the film also loses its structure across the layer. In contrast, XRR and GID measurements performed on monolayers of DSPC and DSPC/PGLa showed that there is no interaction between the lipid and peptide molecules, *i.e.* the structure of the DSPC monolayer stays intact upon addition of the peptide. Therefore, these two types of molecules do not mix at a molecular level at the air/water interface, but form two independent phases. A sketch of the molecular organisation for a monolayer of the pure lipids and in the presence of PGLa is presented in **Figure 24**.

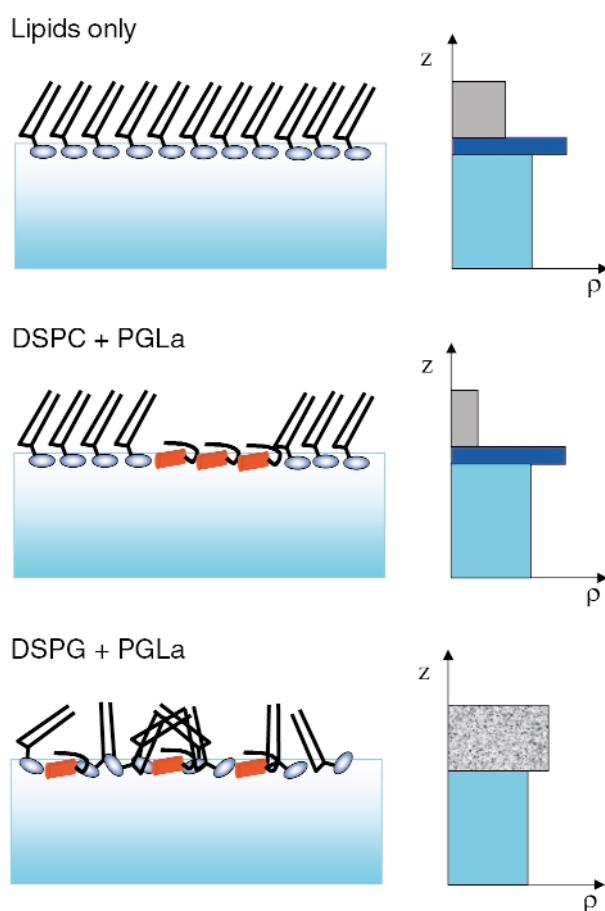


Fig. 24: Models of the organisation of the lipid monolayer in the absence and presence of the frog skin antimicrobial peptide, PGLa. Diagrams on the right illustrate variation of the electron density (ρ) versus coordinate (z).

Both diffraction techniques clearly show that the antimicrobial peptide PGLa does not interact with DSPC. In contrast, PGLa was shown to interact strongly with DSPG monolayers leading to destruction of the 2D packing of these lipids, subsequently forming a disordered homogeneous molecular mixture of lipids and peptides. This would naturally result in a perturbation of the membrane functionality. Hence, the electrostatic

interaction between the positively-charged peptides and these negatively-charged lipid molecules, which are the predominant components in bacterial membranes, is an important step in the discrimination between bacterial and mammalian cell membranes by antimicrobial peptides.

Principal Publication and Authors

O. Konovalov (a), I. Myagkov (b), B. Struth (a), K. Lohner (c), *European Biophysics Journal* **31**, 428, (2002).

(a) ESRF

(b) Research Institute for Physical Problems, Zelenograd (Russia)

(c) Institut für Biophysik und Röntgenstrukturforschung, Austrian Academy of Sciences, Graz (Austria)

Twisted Plywood Pattern of Collagen Fibrils in Fish Scales

The mineralised collagen fibril represents the building unit of several calcified tissues, such as tooth, bone and calcified tendons. Different patterns of fibril arrays have been described [1]. The results of a number of morphological and structural investigations performed on various mineralised tissues have indicated a close structural relationship between the nanocrystalline carbonated apatite and collagen molecular packing as collagen acts as a template for the deposition of the mineral phase [1,2]. We have shown that the local distribution and orientation of collagen fibrils and apatite crystals in mineralised tissues can be successfully investigated by means of micro-small-angle X-ray scattering (μ SAXS) [3]. Here we describe the use of μ SAXS on **ID13** to study the distribution and orientation of collagen and apatite in fish scales.

A typical scale from a teleost fish (*Leuciscus cephalus*) is shown in **Figure 25**. These scales grow and are mineralised continuously throughout life. The annuli, some of which are labelled with arrows in the figure, mark the pauses of growth in winter. μ SAXS patterns with a 7 μ m beam were obtained from a single scale by step-scanning over areas as large as 600 x 600 μ m. After every step a 2D- μ SAXS pattern was obtained with a CCD detector.

The μ SAXS patterns from most of the examined areas exhibit a distribution of intensity of the collagen reflections according to five directions of preferential orientation, at 36° from each other (**Figure 26**). The data suggest that this pattern is due to a plywood arrangement of collagen fibrils in successive layers parallel to the surface of the scale. The fibrils are strictly aligned in each layer and the alignment

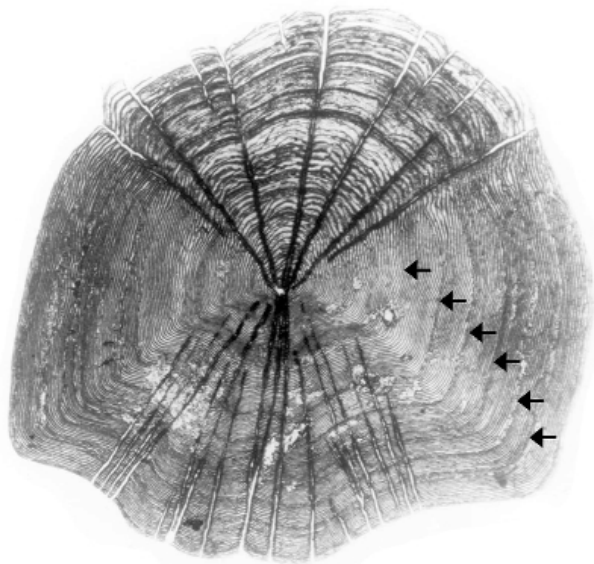


Fig. 25: Optical micrograph of a typical scale from *Leuciscus cephalus*. The annuli are indicated by arrows.

rotates by 36° in successive layers, according to a discontinuous twist that generates a symmetric plywood pattern. Evidence for a preferred alignment of c-axes of the

hexagonal apatite crystallites parallel to the collagen fibrils was obtained from the 002 reflection. These are the very first diffraction data, which unambiguously confirm the presence of these peculiar structures, and suggest that this kind of investigation represents a powerful tool to study plywood arrangements in biological tissues.

References

- [1] S. Weiner and H.D. Wagner *Annu. Rev. Mater. Sci.* **28**, 271 (1998).
- [2] A. Ascenzi, A. Benvenuti, A. Bigi, E. Foresti, M.H.J. Koch, F. Mango, A. Ripamonti, and N. Roveri, *Calcif. Tissue Int.* **62**, 266-273 (1998).
- [3] A. Bigi, M. Burghammer, R. Falconi, M.H.J. Koch, S. Panzavolta and C. Riekell, *J. of Struct. Biol.* **136**, 137 (2001).

Authors

A. Bigi (a), S. Panzavolta (a), M. Burghammer (b), C. Riekell (b), R. Falconi (a), M.H.J. Koch (c),
 (a) *University of Bologna (Italy)*
 (b) *ESRF*
 (c) *EMBL, Hamburg Outstation, Hamburg (Germany)*

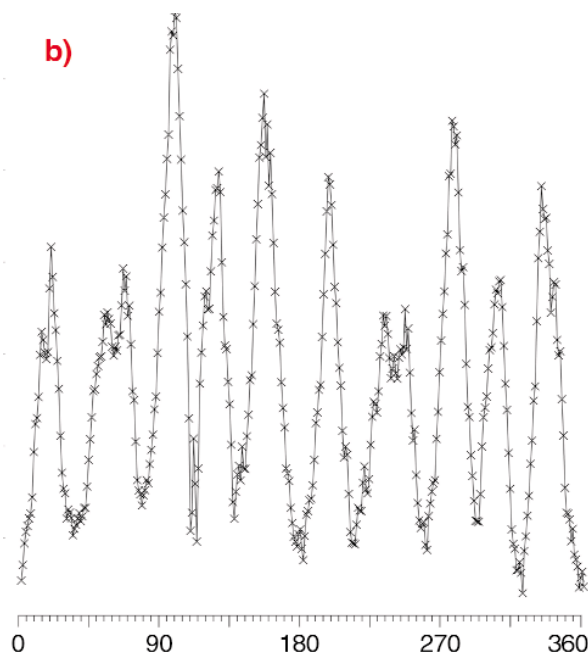
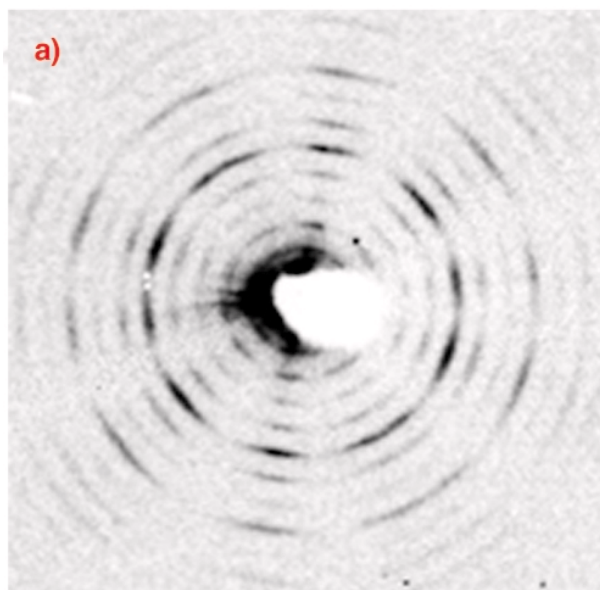
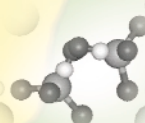


Fig. 26: Micro X-ray small-angle scattering pattern recorded from a decalcified scale. The reflections correspond to the orders of collagen (periodicity: 64 nm). The reflections are preferentially oriented along 5 preferential directions. The relative integrated intensity distribution along the Debye ring of the sixth order collagen reflection is reported in b) as a function of azimuthal angle.

Surface and Interface Science



Introduction

Surfaces and Interfaces is an area of interest at the ESRF not only in the group formed by ID01, ID03 and ID32 but also in many other beamlines. Diffraction techniques are mostly used to investigate structural aspects of relevant interfaces. As nano-objects are currently of great interest we present here three contributions on semiconductor quantum dots. The first one shows how the anomalous scattering effect helps to differentiate strain and intermixing. The second contribution deals with Ge dots grown through a Si_3N_4 layer revealing how the strain is relaxed when the dot dimensions increase. The third one concentrates on SiC crystallites in a Si matrix.

Two examples of solid liquid interfaces are then presented. One of them shows that at the interface of KDP crystals in contact with water, there are two molecular layers that resemble ice more than liquid water due to the strong interactions at the interface. In the second, the evolution of adsorbed S atoms on Au(111) in an electrochemical cell containing alkanethiols was investigated as a function of the cell potential.

Finally an example of gas/solid interfaces is also described. CO chemisorbed on Ni(111) was investigated over 9 decades in pressure. At atmospheric pressure the CO layer is compressed, stiff and incommensurate with the substrate lattice.



Highlights 2002

Liquid Order at a Solid-liquid interface

In all the areas where one encounters solid-liquid interfaces, e.g. crystal growth, lubrication, catalysis and electrochemistry, a proper understanding of the physical and chemical phenomena requires structural knowledge of the interface at an atomic scale. For a long time suitable experimental techniques were not available and the main ideas were derived from theoretical models. Such studies show that a liquid at the interface of a crystal exhibits crystal-induced ordering in the first three to four layers. The ordering is predicted to be strongest in the perpendicular direction (layering). Using the intense and high-energy X-ray beams that are available at the ESRF one can now determine this ordering experimentally from surface X-ray diffraction (SXRD) data.

SXRD probes the atomic structure of an interface by measuring diffracted intensities along so-called crystal truncation rods (CTRs) [1]. These rods are tails of diffuse intensity connecting the bulk Bragg peaks in the direction perpendicular to the surface (Figure 27). Their exact shape is determined by the interface atomic structure. A partly-ordered liquid at the interface will contribute to the diffraction signal from the substrate with a magnitude that depends on the ordering. If the liquid layer is completely disordered parallel to the interface, it only contributes to the specular rod (labelled as the (00)-rod) – it does not contribute to rods with an in-plane momentum transfer. If the liquid layer at the interface is partially ordered owing to the periodic potential of the surface, it contributes most strongly to rods with small in-plane momentum transfer. Thus, the amount of ordering in the liquid can be determined by measuring various rods with different in-plane momentum transfer. Figure 27 shows a schematic drawing of a crystal covered with a partly-ordered liquid layer and of the varying contribution of the ordered liquid to the different rods in reciprocal space.

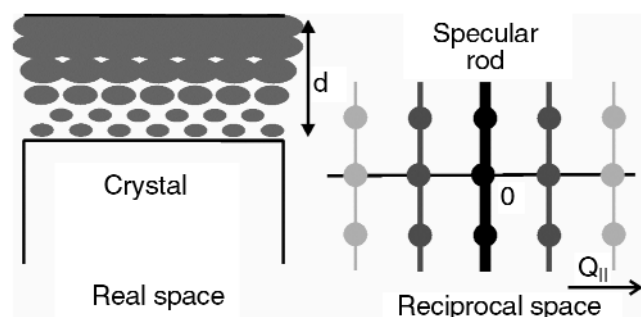


Fig. 27: Schematic drawing of a crystal covered with a partly-ordered liquid layer of thickness d . The contribution of the (partially) ordered liquid to the substrate diffraction rods is strongest in the specular rod and diminishes at higher parallel momentum transfer ($Q_{||}$) in reciprocal space.

The interface structure of KDP (potassium-dihydrogen-phosphate, KH_2PO_4) crystals with water was measured [2] on beamlines ID3 and ID32. KDP crystals can be grown with high quality and are technologically important, e.g. in laser systems for harmonic generation and opto-electrical switching. Grown from aqueous solution, two different faces are observed on the morphology of KDP crystals, the {101} and {100} face. The surface structure of the {101} face was found previously to terminate in a potassium layer [3].

Such measurements are not easy because the modulation due to the liquid is weak, while the signal-to-background ratio is poor – much poorer than data taken from a crystal in vacuum because the liquid gives a strong background. For this reason the reported results to date concern mainly the layering of the liquid perpendicular to the surface, as derived from the specular rod [4]. In order to measure the lateral ordering components as well, one needs to reduce the background as much as possible. One way to achieve this is to use ultra-thin water layers. AFM and ellipsometry measurements indicate that in a humid environment KDP crystals are covered with such an ultra-thin water layer. It is possible to control the thickness of the water layer using a temperature-controlled 'environment cell' in which the relative humidity can be set to 100%.

Extensive data sets were measured under a variety of conditions. An example showing two rods is presented in Figure 28, for data obtained at 45°C. An indication of the effect of the ordering of the liquid layer on the diffracted intensity is obtained by comparing the measured structure

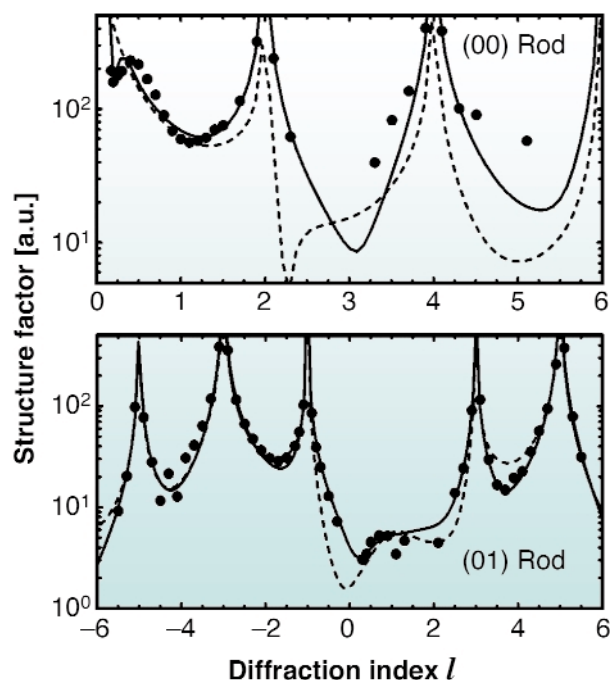


Fig. 28: The data for the (00) (= specular) and (10) crystal truncation rods, plotted as a function of l . The solid line is the best fit using the model described in the text. The dashed line is calculated using a model that ignores the water layer.

factors with the ones calculated using the earlier model (dashed curves), in which the effects of the liquid were ignored. As expected, large differences were found for the specular rod and smaller differences for the (10) rod, indicating ordering in the water layer.

In order to determine the structure of the liquid, a model is needed that describes all features of the interface shown in Figure 27. Thus the model must contain a crystalline part describing the KDP crystal surface and a liquid part describing both the ordering properties as well as the thickness of the water layer. A potassium terminated KDP surface is used to model the crystalline part. The liquid part of the interface is modelled with planes of oxygen atoms parallel to the surface. Oxygen atoms are used instead of water molecules because X-rays are largely insensitive to hydrogen atoms. The strength of the ordering of each layer is fitted through anisotropic Debye-Waller parameters for the oxygen atoms. A small in-plane Debye-Waller parameter corresponds to a layer with high lateral ordering that will contribute to all rods. Bulk liquid layers that only contribute to the specular rod, are modelled by giving these a large in-plane Debye-Waller parameter (>1000). As demonstrated by the solid curves in Figure 28, the model describes the data well, including the Kiessig fringe near $l = 0.4$ of the (00)-rod that shows that the total liquid film thickness is 22 Å.

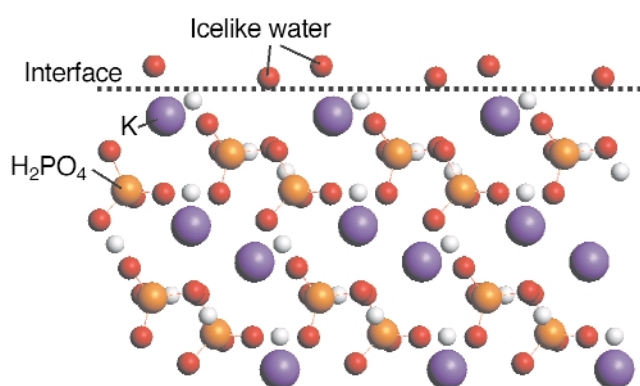


Fig. 29: Schematic side view of the KDP {101} surface, including the two well-ordered water layers represented by O atoms. The first O layer is located close to the extrapolated position of a next K layer.

The structure of the crystalline part fully agrees with that found earlier. Somewhat surprisingly, we find the first two water layers near the crystal surface to be well-ordered. Subsequent layers rapidly lose their order; the third layer has both lateral and perpendicular order, the fourth layer only perpendicular. Figure 29 shows the interface structure including the two well-ordered water layers. The two atoms are in close contact with the topmost crystal layer, with which the atoms apparently have quite a strong interaction. Our data show that these layers show a more ice-like than liquid-like behaviour.

A convenient way to visualise the results is with a projection of the electron density distribution on the z-axis.

The in-plane order of the water layer can be taken into account using an additional term in the density distribution depending on the in-plane momentum transfer and in-plane Debye-Waller parameters. The electron density distribution for the specular rod is the 'genuine' distribution, including the diffuse part of the liquid layer. The profile for the other rods shows the part of the electron density that corresponds to this particular Fourier component in the liquid. Figure 30 shows the electron density profiles across the interface. The double peak at 14–15 Å corresponds to the oxygen atoms. In all cases, we see the two well-ordered oxygen peaks near the surface. The (10) and (20) profiles show in addition a weak contribution from the third water layer. The density for the (00) rod clearly shows the entire diffuse water layer with a density close to that of a saturated solution, as expected.

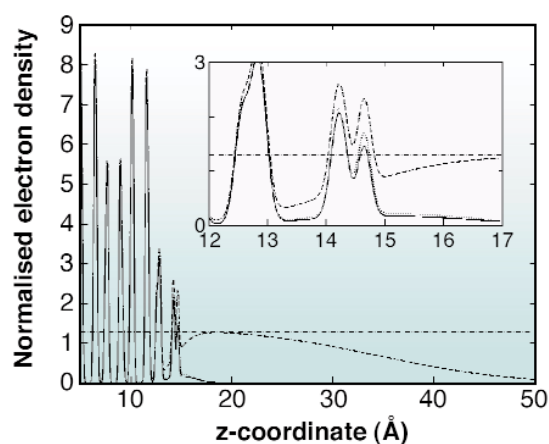


Fig. 30: Electron density distribution across the interface. The electron density is normalised to the electron density of water. The density distribution is shown for three parallel momentum transfers, (00) (dashed line), (10) (dotted line) and (20) (solid line). In addition, the dash-dotted line gives the electron density of a saturated KDP solution. The double peak at 14.5 Å represents the ice-like layer.

In general, the observations agree with earlier theoretical studies that predicted a stronger perpendicular than lateral ordering. The highly ordered first two water layers were unexpected for this crystal in contact with its growth solution. These layers must arise from the strong interactions with the ionic surface, similar to the hydration layers around isolated ions, and deserve further theoretical investigation.

References

- [1] I.K. Robinson, *Phys. Rev. B* **33**, 3830–3836 (1986).
- [2] M.F. Reedijk, J. Arsic, F.F.A. Hollander, S.A. de Vries and E. Vlieg, *Phys. Rev. Lett.* (2003) *accepted*.
- [3] S.A. de Vries, P. Goedtkindt, S.L. Bennett, W.J. Huisman, M.J. Zwanenburg, D.-M. Smilgies, J.J. De Yoreo, W.J.P. van Enkevort, P. Bennema and E. Vlieg, *Phys. Rev. Lett.* **80**, 2229–2232 (1998).
- [4] W.J. Huisman, J.F. Peters, M.J. Zwanenburg, S.A. de Vries, T.E. Derry, D.L. Abernathy and J.F. van der Veen, *Nature* **390**, 379–381 (1997).

Authors

E. Vlieg, M.F. Reedijk.

Dept. of Solid State Chemistry, University of Nijmegen
(The Netherlands)

Anomalous X-ray Diffraction on InAs/GaAs Quantum Dot Systems

In recent years, a vast variety of self-organised systems of 2D and even 1D nanocrystals were grown by heteroepitaxy. In almost all of these systems, materials with slightly different lattice parameter are grown epitaxially on top of each other. X-ray diffraction is the most appropriate tool for the characterisation of crystalline nanostructures. There are, however, difficulties in separating their structure and composition.

Here we introduce a method to overcome this problem via contrast variation using anomalous diffraction at the GaAs/InAs (200) reflection. As GaAs crystallises in the zinc-blend structure, the structure amplitude F_{hkl} for the (200) reflection is $F_{200} = f_{\text{Ga}} - f_{\text{As}}$, where $f_{\text{Ga,As}}$ denote the scattered amplitude from the corresponding atom. The atomic scattering factor is a complex number that describes the scattering from an atom as a driven oscillator, taking into account the shift in phase, ϕ , with respect to the exciting wave field. ϕ is of importance close to an absorption edge, when electrons of a shell are in resonance, and scatter with a phase-shift.

It becomes clear that once the absolute values of the scattering factors and their phases are equal, the scattered amplitude is completely annihilated. $|f_{\text{Ga}}| = |f_{\text{As}}|$ is fulfilled at the two energies, above and below the K-edge of As. The corresponding calculated intensity for the (200) reflection of GaAs and InAs is depicted in Figure 31.

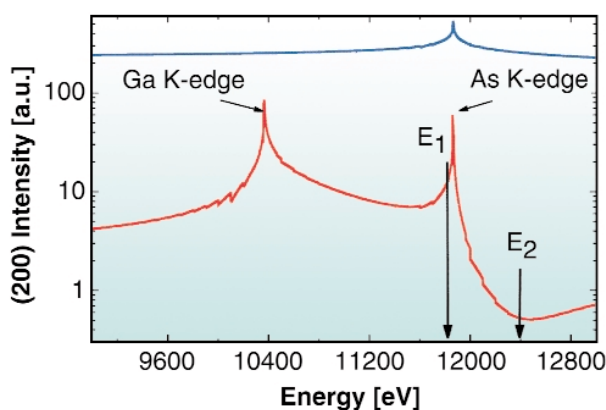


Fig. 31: Calculated (200) intensity for GaAs (red line) and InAs (blue line).

To demonstrate and exploit the expected effect on the scattered intensity around the (200) surface reflection, a grazing incidence X-ray diffraction (GID) experiment was performed at beamline ID1. The sample consisted of a (001)-GaAs substrate covered with InAs dots grown by MBE in the Stranski-Krastanow growth mode. The two chosen energies, where $E_1 = 11.8$ keV and $E_2 = 12.38$ keV, are marked with an arrow in Figure 31. Radial scans along $\langle 100 \rangle$ through the (200) reflection, together with fits are presented in Figure 32. As expected, a tremendous change in the scattered intensity of the GaAs substrate is found, whereas the diffraction from the InAs quantum dots is less influenced.

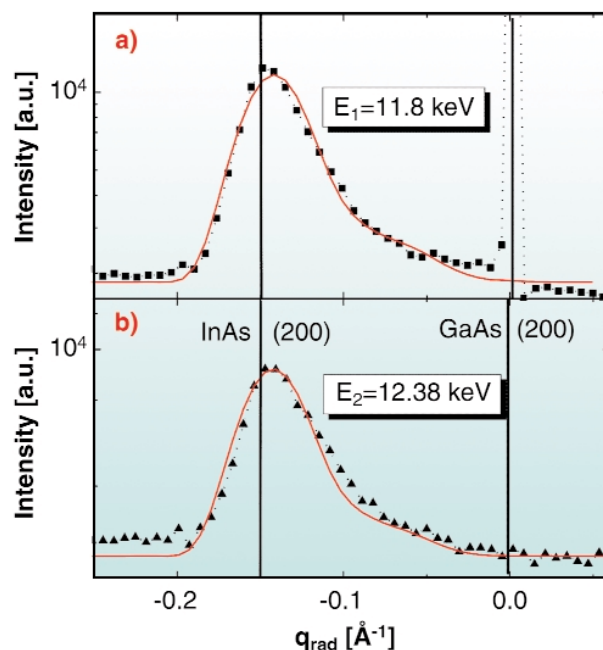


Fig. 32: Radial scan through (200) InAs dot and GaAs substrate reflection at (a) 11.8 keV and (b) 12.38 keV. Red lines are simulations.

In order to fit the diffraction curves, we developed a model for the diffraction from coherently-grown InAs dots on a GaAs (001) substrate. The composition was allowed to vary with the height over the substrate from pure GaAs to $\text{Ga}_x\text{In}_{1-x}$ with $0 < x < 1$ and the condition of a monotonic decay of the gallium content with increasing height. Accordingly, the lattice parameter was allowed to relax monotonically from a_{GaAs} towards a_{InAs} . To exploit the fact that the Ga-containing parts of the dot change their scattering contribution at the two energies by a factor of 20, whereas the InAs intensity contribution changes only by a factor of 1.3, both scans were fitted simultaneously (red lines in Figure 32). The effect of the Ga interdiffusion into the dot causes a weakening of the scattering contribution from the dot material at 12.38 keV. Therefore the measured intensity is directly linked to this compositional change.

The resulting interdiffusion and lattice parameter profile as a function of the height z above the substrate surface

is shown in **Figure 33**. The red line describes the decay of the Ga content inside the dots with the dot height whereas the blue line describes the change of the lattice parameter. The fact that these two parameters have a very similar behaviour indicates that the strain energy in this sample was minimised by interdiffusion.

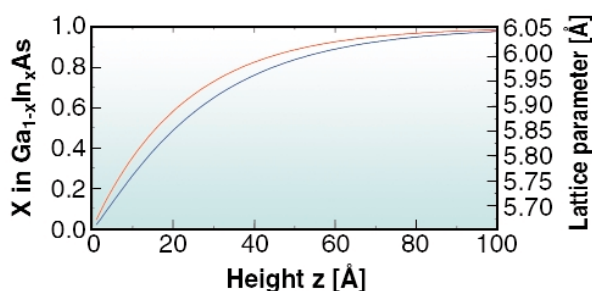


Fig. 33: Material composition (left scale, red line) and lattice parameter in the dots (right scale, blue line) as a function of the height z resulting from the fits in Figure 32.

In summary, we wish to emphasise that contrast maximisation by anomalous diffraction on superstructure reflections is a powerful tool to enhance the scattering contribution from quantum dots on a substrate.

Principal publication and Authors

T.U. Schüllli (a), M. Sztucki (a), V. Chamard (a), D. Schuh (b), T.H. Metzger (a), *Appl. Phys. Lett.* **81**, 448 (2002).

(a) ESRF

(b) Walter Schottky Institut Technische Universität München, Garching (Germany)

GID Study of Germanium Quantum Dots: Small in Size and High in Density

During the last 10 years, semiconductor nanostructures have been investigated extensively in order to study the effect of quantum confinement on the physical properties of semiconducting materials. Group IV (*i.e.* Si and Ge), nanostructures embedded in a dielectric layer can emit light and store carriers suggesting future applications in optoelectronic and non-volatile memory devices.

A major difficulty in the fabrication is that nanometric dimensions and high density of dots have to be achieved in order to make the devices operate at room temperature. Recently germanium dots have been grown by Molecular Beam Epitaxy (MBE) on a silicon (001) surface covered by a thin (1.2 nm-thick) silicon oxide and/or silicon nitride layer. Growth has been performed

on an MBE machine installed on **BM32**, the CRG IF beamline. The experimental procedure, which induces the growth of high-density ($10^{11}/\text{cm}^2$) and nanometric-size germanium dots on silicon oxide and silicon nitride has been described previously [1,2]. Despite the presence of a thin dielectric layer, germanium dots grown by MBE exhibit an epitaxial relationship with the underlying silicon substrate. In order to optimise the growth procedure a systematic characterisation of the density and shape of dots has been performed by Atomic Force Microscopy (AFM) observations in the Surface Science Laboratory of ESRF (see **Figure 34**).

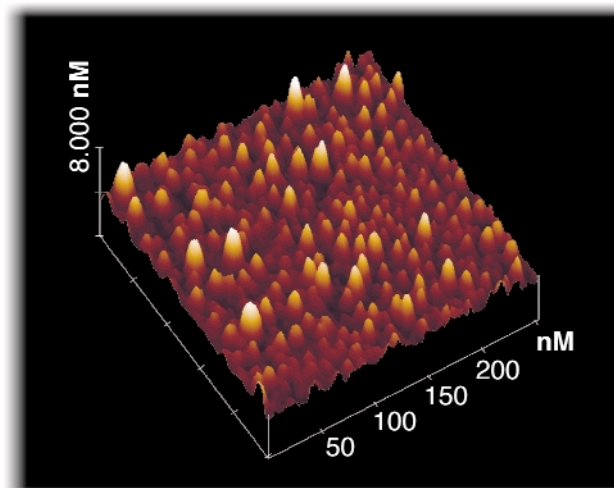


Fig. 34: Image in tapping mode of germanium dots grown on a silicon (001) surface covered by a thin silicon nitride layer.

Grazing-incidence X-ray diffraction (GID) experiments have been performed on the **ID1** beamline in order to investigate the structural properties of germanium dots, such as size, strain and the orientation relationship to the Si (001) substrate [3].

Several samples have been investigated, consisting of germanium dots with a coverage of 2.2 and 6.6 monolayers, grown through a very thin Si_3N_4 layer. After annealing at $\sim 710^\circ\text{C}$, GID measurements were performed at the (220) surface reflection to determine the strain and shape distribution inside the dots.

The radial scans from the (220) germanium to the (220) silicon Bragg peak for the two samples are shown in **Figure 35**. For small dots (a few nm, resulting from 2.2 ML of Ge) only a small asymmetry can be detected close to the silicon Bragg peak (**Figure 35a**) indicating a high degree of pseudomorphic strain inside the dots. Larger dots (~ 12 nm, resulting from 6.6 ML of Ge) exhibit a distribution of in-plane lattice parameter induced by an elastic strain relaxation and/or silicon interdiffusion into the Ge dots (**Figure 35b**).

With the input parameter for the size and shape as obtained from AFM and GID, an atomistic simulation of

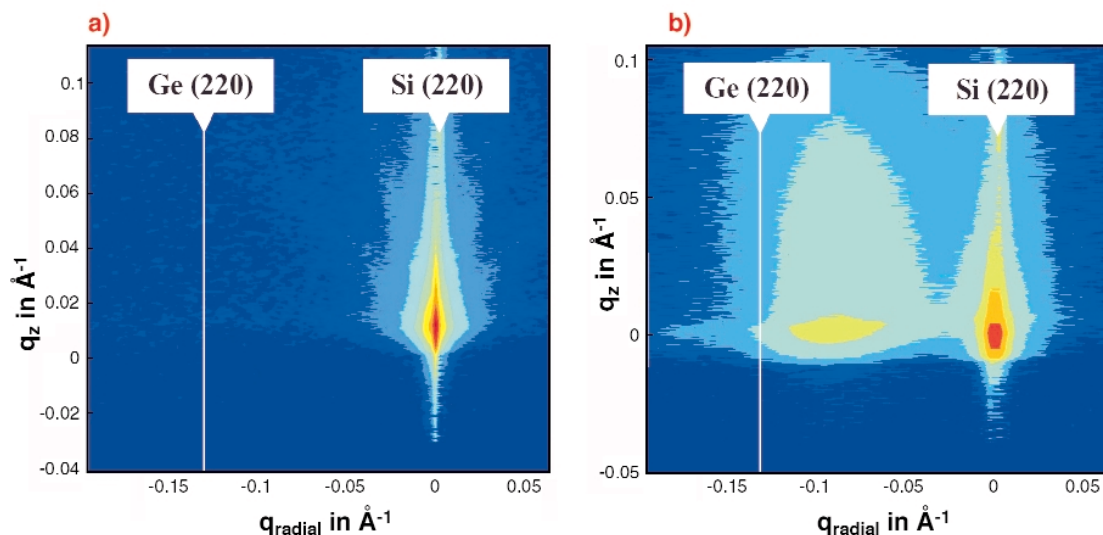


Fig. 35: q_{radial}/q_z reciprocal space maps close to the Si (220) surface reflection:
(a) sample with 2.2 ML of Ge.
(b) sample with 6.6 ML of Ge grown on a silicon (001) surface covered by a thin silicon nitride layer.

the diffraction pattern was performed. Variable fit parameters were the lateral size of a cylindrical dot and its height-dependent strain evolution. Due to the small size of the dots, this method allows to fit reciprocal space maps in an acceptable calculation time even on an atomistic scale. The measured diffuse intensity distribution is presented in Figure 36 together with the fitted model.

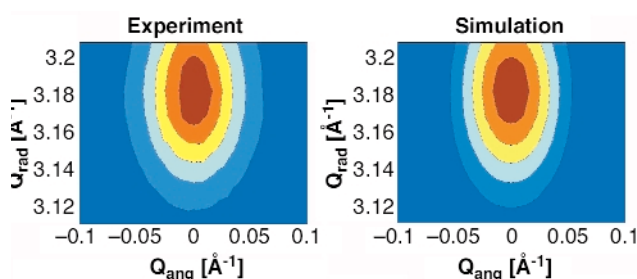


Fig. 36: $q_{\text{angular}}/q_{\text{radial}}$ reciprocal space map at the (220) surface reflection: comparison between experimental results and atomistic simulation.

In conclusion, nanometric size Ge dots have been grown in epitaxy to the silicon (001) surface. The smaller dots are almost fully strained to the silicon. The bigger dots exhibit a large distribution of the in-plane lattice parameter which indicates a high degree of strain relaxation. Further work is clearly necessary in order to determine the mechanism of the strain relaxation, the chemical composition and the critical diameter (size) of dots before the relaxation phenomenon appears.

References

- [1] A. Barski, M. Derivaz, J.L. Rouvière, and D. Buttard, *Appl. Phys. Lett.* **77**, 3541 (2000).
- [2] M. Derivaz, P. Noé, J.L. Rouvière, D. Buttard, D. Sotta, P. Gentil and A. Barski, *Mat. Sci. and Eng. B* **89**, 191 (2002).
- [3] M. Derivaz, P. Noé, R. Dianoux, A. Barski, T. Schüllli, T.H. Metzger, *Appl. Phys. Lett.* **81**, 3843 (2002).

Authors

M. Derivaz (a), P. Noé (a), R. Dianoux (a), A. Barski (a), T. Schüllli (b), T.H. Metzger (b).

(a) CEA Grenoble / DRFMC (France)

(b) ESRF

Structure of Ion-beam Synthesised SiC Nanocrystals in Si

Due to certain physical properties SiC is regarded as a promising semiconductor material for micro- and optoelectronic devices at high temperature and high frequency, and for high-power applications. Thus, improvements of the growth processes are of great technical interest. SiC fabricated by ion-beam synthesis (IBS) can readily be integrated in the well-established Si technology. To this end the SiC crystallites must be confined to a thin surface or interface layer with an epitaxial orientation to the Si host lattice. IBS of SiC in Si is a complex multi-step process depending on the implantation conditions and the thermal treatment. In order to study a representative ensemble of SiC precipitates, various X-ray scattering techniques were used at the materials research station of beamline **BM20** (ROBL-CRG) to reveal structural properties like shape, size and orientation distribution of the SiC nanocrystals.

Using grazing-incidence diffraction (GID) the Si (220) and β -SiC (220) diffraction lines for a Si wafer implanted with C ions in a one-step process has been investigated. The radial scan is shown in Figure 37 for two incident angles. For a penetration depth of 4 nm (lower curve) only the

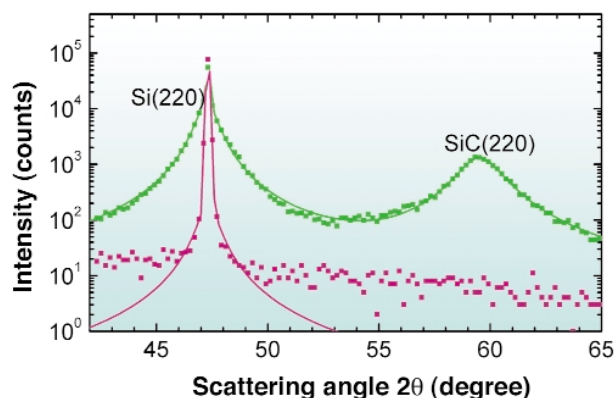


Fig. 37: Si(220) and β -SiC(220) diffraction lines at grazing incidence and grazing exit for a Si wafer implanted with $3.25 \times 10^{17} \text{ cm}^{-2}$ C ions of 45 keV at 500°C and post-annealed at 1200°C for 2 h. The X-rays penetrate 4 nm (magenta) or 1200 nm (green) into the material, respectively.

Si(220) line from the perfect Si crystal surface layer is observed. If the radiation penetrates up to 1200 nm, additionally the β -SiC (220) reflection is found, thus proving that the β -SiC crystallites are located in the buried layer that was intended for the chosen deposition conditions. The analysis of the diffraction curves reveals the detailed structure of the SiC crystallites: the SiC(220) peak is shifted as compared to SiC values tabulated in the ICDD Powder Diffraction File, caused by the crystal lattice strain parallel to the surface. The line profile in the radial direction is influenced by the size of the SiC crystallites and by the strain fluctuation $\delta d/d$, while in angular scans (rocking curves) the line profile is governed by the SiC size and the orientation fluctuation (mosaicity) $\delta\theta$. To extract all of these values, we used the tails of the Si(220) reflection, which can be considered as small-angle scattering from the holes in the Si perfect crystal filled with SiC crystallites (Babinet's principle). The line profile was fitted with a Lorentzian and gives the size of the SiC crystallites not superimposed by other

Growth steps	Particle radius	Lattice strain $\Delta d/d_{\parallel}$ (i.e. $\Delta d/d_{\langle 110 \rangle}$) strain fluctuation $\delta d/d_{\parallel}$	Lattice strain $\Delta d/d_{\perp}$ (i.e. $\Delta d/d_{\langle 002 \rangle}$)
1	7.7 nm	0.0074 0.0310	0.0274
3	6.9 nm	0.0055 0.0170	0.0213

Table 1: Results of diffraction for Si wafers implanted in various steps with $3.25 \times 10^{17} \text{ cm}^{-2}$ C ions of 45 keV at 500°C and post-annealed at 1200°C for 2 h. The particle size is determined from the Si(220) profile. The results for the parallel strain component are extracted from GID measurements on SiC(220) and for the perpendicular component from coplanar beam geometry – they are within technically acceptable limits.

properties. **Table 1** shows results found for Si wafers implanted in one- and multi-step processes and post-annealed. The indices parallel and perpendicular distinguish the direction in the plane and perpendicular to the wafer surface. The orientation fluctuations (mosaicity) are $< 1^\circ$ for in-plane directions and in the range from 2° to 4° for the perpendicular direction. Within these limits the SiC nanocrystallites are aligned with respect to the Si host matrix.

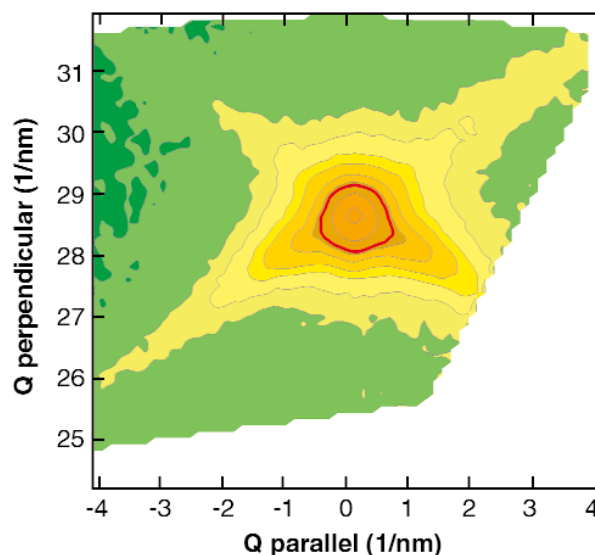


Fig. 38: RSM of the SiC(002) reflection of crystallites formed by implantation of $4 \times 10^{17} \text{ cm}^{-2}$ C ions of 195 keV into Si(001) at 800°C. The red line is the half maximum contour.

We also studied reciprocal space maps (RSM) of the β -SiC (002) reflection in order to gain a complete two-dimensional characterisation of the implanted sample. **Figure 38** shows such an RSM of material implanted with $4 \times 10^{17} \text{ cm}^{-2}$ C ions of 195 keV at 800 °C (and no post-annealing). The adjacent, much stronger Si(004) reflection at $Q_{\parallel} = 0 \text{ nm}^{-1}$ and $Q_{\perp} = 46.3 \text{ nm}^{-1}$ is located outside of the shown area. As the peak intensity of SiC is centred at the same Q_{\parallel} value as the Si host lattice, and as the intensity distribution is narrow, one can conclude a very high degree of alignment of the β -SiC crystallites. Furthermore, the streaks in the Si<111> directions indicate the growth of platelike (oblate) crystallites with facets extended in the {111} planes.

By combining various X-ray scattering techniques (co-planar XRD, in-plane GID) on a versatile 6-circle diffractometer we are able to characterise IBS-manufactured buried SiC nanocrystal layers in Si standard wafers with regards to their depth distribution and their alignment with the Si matrix.

Principal Publication and Authors

F. Eichhorn (a), N. Schell (a, b), A. Mücklich (a), H. Metzger (c), W. Matz (a) and R. Kögler (a), *J. Appl. Phys.* **91**, 1287 (2002).

(a) Forschungszentrum Rossendorf, Institute of Ion Beam Physics and Materials Research, Dresden (Germany)

(b) ROBL-CRG

(c) ESRF

Compressibility of CO Adsorbed on Ni(111) from 10^{-6} mbar to 1.2 bar Ambient CO Pressures Investigated with X-ray Diffraction

Gas molecules adsorbed on solid surfaces have been one of the main topics in surface science in the last two decades. From a fundamental point of view, they make an excellent test case for the investigation of two-dimensional thermodynamic processes such as order-disorder phenomena. From a more practical side, their study is a pre-requisite for the understanding of the microscopic mechanisms underlying heterogeneous catalysis. Most of the experimental work to date was done using electron-based techniques with the surface of the samples in high or ultra high vacuum (UHV) environments so that structural studies on chemisorbed layers could be performed while avoiding attenuation of the electron beams by the gasses. This limitation excluded the possibility of investigating adsorbed layers in equilibrium with their vapour under conditions like those encountered in common industrial reactions where significant adsorption and desorption rates exist. Fortunately, X-rays are not limited by such strong attenuation in the gas phase and so they can be used in crystallographic studies of chemisorbed layers at atmospheric pressures.

We have studied the adsorption of CO at room temperature under equilibrium conditions in the pressure range 10^{-6} mbar - 1.2 bar. The experiments were performed at ID3, the Surface Diffraction Beamline, with X-rays of wavelength 0.74 \AA and a specially-designed UHV/high pressure chamber (base pressure 1×10^{-9} mbar) mounted on a high-precision diffractometer.

At $p = 10^{-3}$ mbar, the commensurate $(\sqrt{7} \times \sqrt{7})R19.1^\circ$ structure [1] was observed. Figure 39 shows that below this pressure, an expansion of the unit cell occurred (and

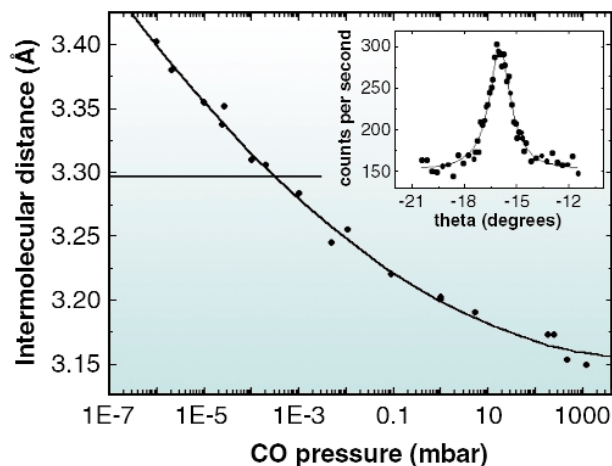


Fig. 39: Inset: rocking scan of a diffraction peak from the adsorbed CO layer taken at $p = 1.2$ bar in the gas phase. Main graph: dependence of the intermolecular distance of adsorbed CO on Ni(111) with the CO pressure in the chamber. The horizontal line marks the nearest neighbour distance for the $(\sqrt{7} \times \sqrt{7})R19.1^\circ$ structure. The continuous line is a polynomial fit to the data.

conversely above this pressure a contraction occurred), as deduced from the magnitudes of the reciprocal lattice vectors from the adlayer, leading to incommensurate structures. Relative to the $\sqrt{7}$ periodicity, the experimentally determined lattice parameter increased by 3.2% at 10^{-6} mbar and decreased by 4.4 % at 1.2 bar. Interestingly, these changes were reversible with the gas pressure. The pressure-induced contraction or expansion of the overlayer results in incommensurate structures with the Ni substrate, as it is the case for the technologically relevant pressure of one atmosphere. This result might be of importance for fundamental studies of catalysis.

The isothermal compressibility of a 2D system in equilibrium with an ideal 3D gas at a pressure P is given by $K = -(kT)^{-1} (\partial a / \partial \ln P)_T$ where k is the Boltzmann constant and a is the molecular area ($a = \sqrt{3}/2 D^2$). By applying the above definition to the continuous curve in Figure 39, the dependence of K with D may be obtained as displayed in Figure 40. As it may be seen, at

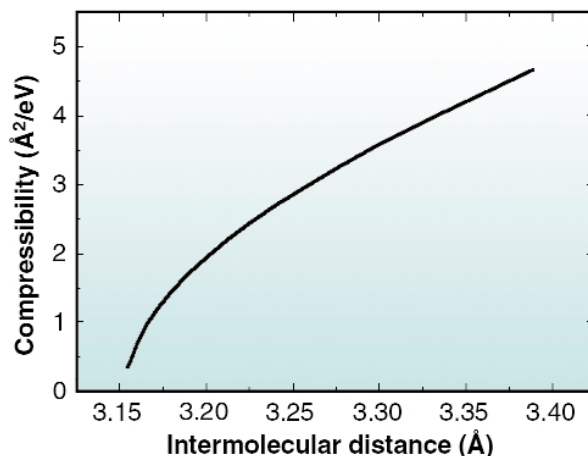


Fig. 40: Compressibility of the adsorbed CO as a function of the nearest neighbour intermolecular distance.

atmospheric pressure the compressibility is about $0.3 \text{ \AA}^2/\text{eV}$, which is about 15 times larger than at low pressures. The above value, which may be compared to that of Pb electrodeposited on Ag(111) ($1 \text{ \AA}^2/\text{eV}$ [2]) and to that of Ar on graphite at 42 K ($35 \text{ \AA}^2/\text{eV}$ [3]), indicates that the CO layer is very stiff at the pressures relevant for catalytic reactions. To our knowledge, the results in Figures 39 and 40 are the only published data of 2D compressibility of a reactive gas over a large pressure range that includes the technologically important pressure of one atmosphere.

In conclusion, we have observed the reversible compression/expansion of adsorbed CO on Ni(111) at room temperature by means of surface X-ray diffraction. The compressibility of the adsorbed layer has been obtained over 9 decades in pressure up to the atmosphere. At pressure values relevant for realistic catalytic conditions, most of the CO molecules sit in low symmetry sites and the layer is stiff.

References

- [1] G. Held, J. Schuler, W. Skalarrek and H.P. Steinruck, *Surf. Sci.*, **398**, 154-171 (1998).
- [2] O. R. Melroy, M. F. Toney, G. L. Borges, M. G. Samant, J. B. Kortright, P. N. Ross and L. Blum, *Phys. Rev. B*, **38**, 10962-10965 (1988).
- [3] C. G. Shaw and S. C. Fain Jr., *Surf. Sci.* **83**, 1-10 (1979).

Principal Publication and Authors

C. Quirós (a), O. Robach (a), H. Isérn (a), P. Ordejón (b) and S. Ferrer (a), *Surf. Sci.* **522**, 161 (2003).

(a) ESRF

(b) Institut de Ciència de Materials de Barcelona, CSIC, Bellaterra (Spain)

Following Adsorption Kinetics at Electrolyte/Metal Interfaces Through Crystal Truncation Scattering: Sulphur on Au(111)

The interaction of sulphur (S) and S-headed organic molecules with metallic surfaces is of interest since S is a poison in heterogeneous catalysis, and S-headed organic molecules, such as alkanethiols, form self-assembled monolayers which could play a role in nanotechnology. The adsorption of these species on Au(111) has been taken as a model system for interfacial science research. In particular, adsorption from aqueous

solutions deserves special interest since many technological processes take place in such an environment. We have made combined *in situ* scanning-tunnelling microscopy (STM), and surface X-ray diffraction (SXRD) studies under electrochemical control for S and S-headed organic molecules on Au(111) at beamline ID32.

In situ STM imaging reveals different S species depending on the potential (E) applied to the Au(111)/electrolyte interface (Figure 41a). When E is shifted from -0.6 V to -0.8 V (Figure 41b), S desorption takes place according to the following pathway:

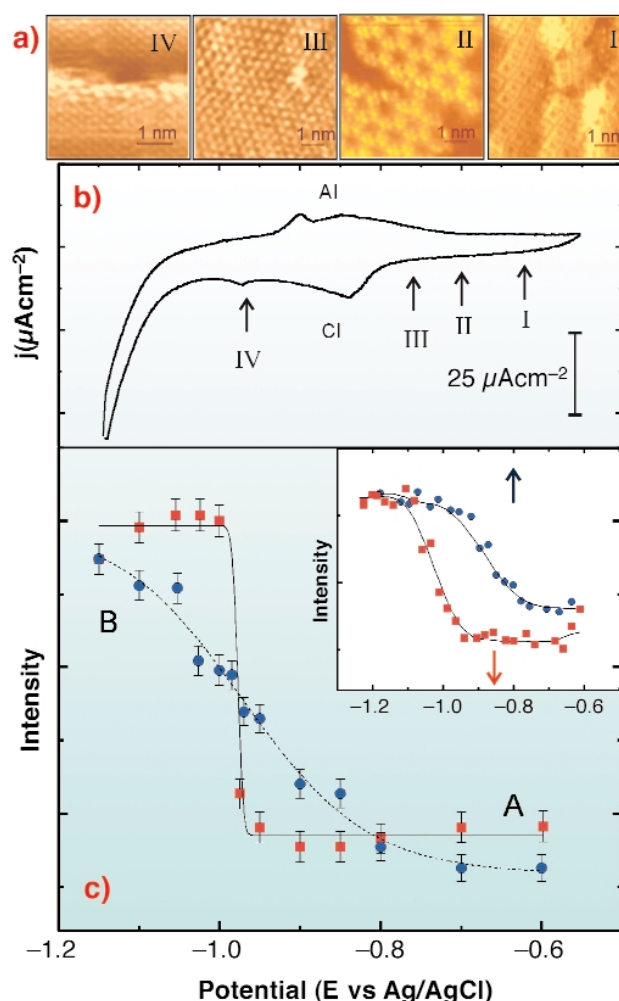
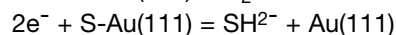
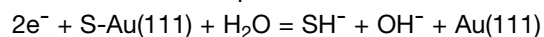


Fig. 41: (a) *In situ* STM images taken at the potentials indicated in (b). (I) S_8 ; (II) S_3 forming a honeycomb array; (III) $\text{S}(\sqrt{3}\times\sqrt{3})\text{R}30^\circ$; (IV) $\text{Au}(1\times 1) + \text{S}$ at steps. (b) Current density (j) vs. applied potential (E) profile for Au(111) in $0.1 \text{ M NaOH} + 10^{-3} \text{ M Na}_2\text{S}$ at 0.001 V/s . (c) Integrated diffraction intensity at $(hkl) = (1\ 0\ 2.5)$ for Au(111) in $0.1 \text{ M NaOH} + 10^{-3} \text{ M Na}_2\text{S}$ as a function of the applied E showing negative (\blacksquare) and positive (\bullet) scan directions. Lines are fitted to the data as a guide for the eye. Inset: the same for hexanethiol/Au(111) in 0.1 M NaOH . Red and blue arrows indicate the position of the electrodesorption and electroadsorption peaks potentials from the voltamogram, respectively.

$S_8 \Rightarrow S_3 \Rightarrow$ monomeric S in $(\sqrt{3} \times \sqrt{3})R30^\circ$ [1]. In this potential range $(\sqrt{3} \times \sqrt{3})R30^\circ$ S, S_3 and S_8 structures can coexist due to slow desorption kinetics. When E is scanned across peak Cl (at -0.84 V) the following reaction could take place:



Thus, the $(\sqrt{3} \times \sqrt{3})R30^\circ$ S lattice is no longer observed, and only the Au(1×1) lattice and S at steps are detected. Potential scan reversal results in S adsorption through the opposite pathway, leading finally to S_8 structures.

The surface structure involves small domains of different sulphur species that arrange in different lattices (Figure 41). This precludes the possibility of observing fractional order diffracted beams. We have performed *in situ* ω -scans for different E at $L = 2.5$ for the (10) crystal-truncation rod (CTR), and simultaneously recorded current density (j) vs. E profiles. We have proved by simulations that the integrated intensity in anti-phase conditions of this CTR is sensitive to the total amount of S in the surface, and therefore, has been used to follow changes in the amount of adsorbed species induced by changes in E, *i.e.* a cyclic diffractogram (CD). Two well-defined regions of almost constant diffraction intensity, separated by a sudden rise at $E = -0.98$ V can be observed, corresponding to potentials where STM shows the presence (A) or absence (B) of adsorbed S on Au(111) terraces (Figure 41c). By repetitive cycling the CD shows that S adsorption/desorption is completely reversible. The fact that the sudden rise in the diffraction intensity takes place at -0.98 V, *i.e.* at E values where chemisorbed S has already been completely transformed into sulphide, suggests that sulphide remains on the Au(111) surface in a physisorbed state. During sulphide re-adsorption diffraction intensity decays to a minimum well before chemisorption (which takes place at Al), also indicating a physisorption step.

The discontinuity in the negative scan of the CD strongly suggests that desorption of the physisorbed layer involves a first order phase transition. Contrary to this, the weak adsorption of the sulphide species from solution increases smoothly with E and the shape of the diffraction intensity plot fits a Langmuir isotherm reasonably well. We have obtained similar results for the hexanethiol/Au(111) interface (inset in Figure 41c): a physisorbed hexanethiolate state is identified. The fact that S and alkanethiolate exhibit the same trend demonstrates that the physisorbed state is mediated by the S head, rather than by hydrocarbon chains, which would only contribute to its stabilisation [2].

In conclusion, the combination of CD, STM and electrochemistry is a powerful tool for the detection of different adsorbed states. It allows us to obtain information of adsorption kinetics for both relatively simple systems and highly-reactive and complex systems such as S and alkanethiols, respectively on Au(111).

References

- [1] C. Vericat, G. Andreassen, M. E. Vela, R. C. Salvarezza, *J. Phys. Chem. B* **104**, 302 (2000).
- [2] C. Vericat, G. Andreassen, M. E. Vela, H. Martin, R. C. Salvarezza, *J. Chem. Phys.* **115**, 6672 (2001).

Principal Publication and Authors

C. Vericat (a), M. E. Vela (a), G. A. Andreassen (a), R. C. Salvarezza (a), F. Borgatti (b), R. Felici (b), T.-L. Lee (c), F. Renner (c), J. Zegenhagen (c), J.A. Martín-Gago (d), *Phys. Rev. Lett.*, *in press*.

(a) INIFTA (Argentina)

(b) INFM-OGG c/o ESRF

(c) ESRF

(d) Instituto Ciencia de Materiales de Madrid-CSIC (Spain)

X-ray Absorption and Magnetic Scattering

Introduction

The activities of the X-ray Absorption and Magnetic Scattering Group are very diverse, covering the structural, magnetic and electronic properties of materials. For this chapter we have selected three main areas: X-ray absorption fine structure, with particular emphasis on chemistry; X-ray magnetic circular dichroism studies with an emphasis on magnetic multilayers and impurities; and X-ray magnetic scattering. Since many of the research interests of the group extend to other beamlines and groups there are also contributions from BM20 (the ROBL CRG beamline) and the Theory Group. There were many other highly-interesting studies done on the Group's beamlines in the past year that we were not able to include here. For interested readers, we have tried to reference some of this work in the short introductions to each section. For example, several articles could equally have illustrated the very high sensitivity of X-ray magnetic circular dichroism to nano-scale magnetism. For instance the study by Gambardella *et al.* [1] of cobalt nano-wires on platinum stepped surfaces (**Figure 42**) revealed new insight into their magnetic properties.

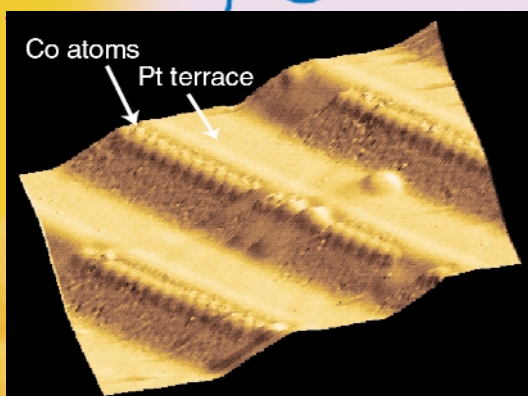


Fig. 42: Scanning Tunneling Microscope (STM) topograph of the Pt(997) surface. Cobalt monatomic chains decorate the platinum step edges (the vertical dimension is enhanced for better contrast). The chains are linearly aligned and have a spacing equal to the terrace width.

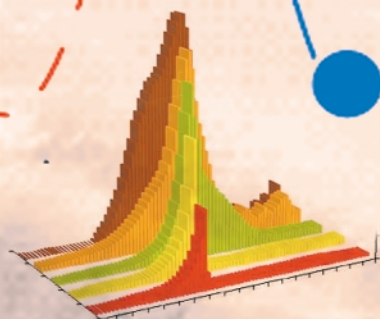
There are also several interesting studies that fall outside the scope of the sections below. In particular, there have been important developments in experimental methods. One such example is spin-resolved X-ray absorption spectroscopy, with a very interesting application to EuO [2]. Another example is an extension of the X-ray resonant Raman scattering technique to allow, through the application of sum rules, the determination of high-order moments in ferromagnetic materials [3].

References

- [1] P. Gambardella *et al.* *Nature* **416**, 301 (2002).
- [2] P. G. Steeneken *et al.* *PRL* **88**, 047201 (2002).
- [3] L. Braicovich *et al.* *PRL* (to be published).



Highlights 2002



Chemistry and EXAFS

Introduction by J. Evans (University of Southampton, UK)

Most chemistry is performed in disordered media, such as in solutions in reaction flasks, within cells and other biological environments and on the surfaces of solid particles, be they in interstellar space, in the stratosphere or within a reactor in a petrochemical process. The last of these examples is effected by a heterogeneous catalyst, with the mediating agent localised on the surface of a solid framework, and the reagents and the resulting products in a second phase (gaseous or liquid). Over 80% of all chemicals require at least one catalytic step in their production (providing a revenue of 1000 – 10000 billion €), and this proportion is increasing with the drive towards atom-efficient and “green” chemical processes.

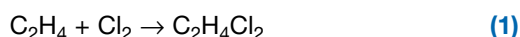
Consequently, understanding the relationships between structure, catalytic activity and selectivity has substantial value beyond its scientific merit. When viewed from the active site, a catalytic reaction can be considered as a cycle of steps (with side reactions) involving transformations between a series of intermediates. The most long-lived of these species is the resting state of the catalyst, but a thorough understanding of the system encompasses all these transformations. All effective catalysts turn over on a sub-second timescale, and thus the structure at the active site will be modified in a split second.

X-ray Absorption Fine Structure (XAFS) provides structural information about the local order of an element in any phase, and thus is the appropriate technique for probing active sites in metal catalysts. In its normal scanning mode, the acquisition time is generally too long to track the rapid processes involved in active catalysts. On ID24, a bent crystal monochromator is used to extract a span of X-radiation sufficient to obtain an XAFS spectrum with a multi-element detector sampling the steps in the spectrum simultaneously. Currently the CCD detector can operate with 150 μ s as

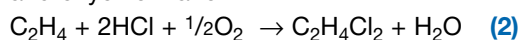
the fastest time resolution. It is thus feasible to track both rapid changes of the resting state under operating conditions and also to monitor transient steps. This report includes two applications on **ID24** involving *in situ* characterisation of alumina-supported catalysts. In one, the X-ray Absorption Near Edge Structure (XANES) is used to probe the oxidation state of the copper sites during the oxychlorination of ethane, whilst the other utilises the Extended X-ray Absorption Fine Structure (EXAFS) to probe the coordination site of rhodium during the reduction of nitric oxide by hydrogen. In both cases, the nature of the metal site is shown to respond rapidly to changes in reaction conditions (temperature and gas composition). Both of these experiments used a continuous flow of gas, and thus will probe changes in the resting state of the metal. In order to probe transients, the system has to be rapidly perturbed, for example by pulsed or modulated gas flow, and these are the basis of future experiments. Transient processes have been successfully studied already on ID24 in the liquid phase, using stopped flow and electrochemical techniques. Characterising transients in chemical reactions is an exciting prospect for the future of ID24.

Chemistry of the Oxychlorination Catalyst: An *In situ*, Time-resolved, Dispersive XANES Study

Nowadays, almost all the world's production of PVC (poly vinyl chloride) is obtained by the polymerisation of vinyl chloride (VCM), which is produced using C_2H_4 , Cl_2 and O_2 as reagents, following the scheme represented in **Figure 43**. Production of VCM is based on the cracking of $C_2H_4Cl_2$, which in its turn is produced by two parallel processes, direct chlorination:



and oxychlorination:



The oxychlorination reaction (2) allows the HCl produced by the cracking of $C_2H_4Cl_2$ (EDC) to be recycled, representing a large scale reaction specifically developed to reduce the raw material consumption (Cl_2) and to avoid the removal from the cycle of unused reagents (HCl), in agreement with the modern requests of chemical industry. Commercial catalysts are produced by impregnation of γ -alumina with $CuCl_2$ (4-8 wt% Cu) following the incipient wetness method [1].

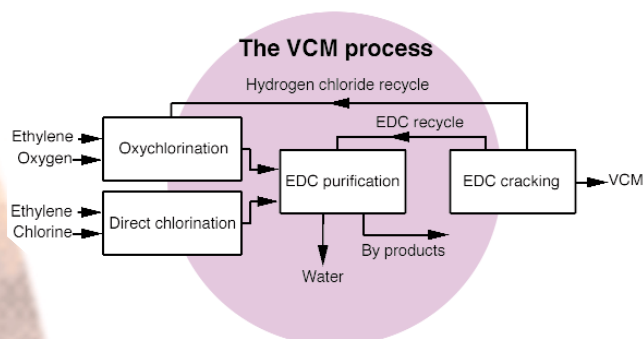


Fig. 43: Schematic representation of the industrial production of vinyl chloride (VCM).

Despite abundant literature on the subject, a significant improvement in the knowledge of the system has been gained only recently [1-3]. By separately feeding in the three reagents, it was shown that the overall ethylene oxychlorination reaction (2) is catalysed by a highly-dispersed $CuCl_2$ phase following a three steps redox mechanism: (i) chlorination of ethylene by reduction of $CuCl_2$ to $CuCl$, (ii) oxidation of $CuCl$ to an oxychloride and (iii) re-chlorination with HCl (closure of the catalytic cycle) [2,3]:

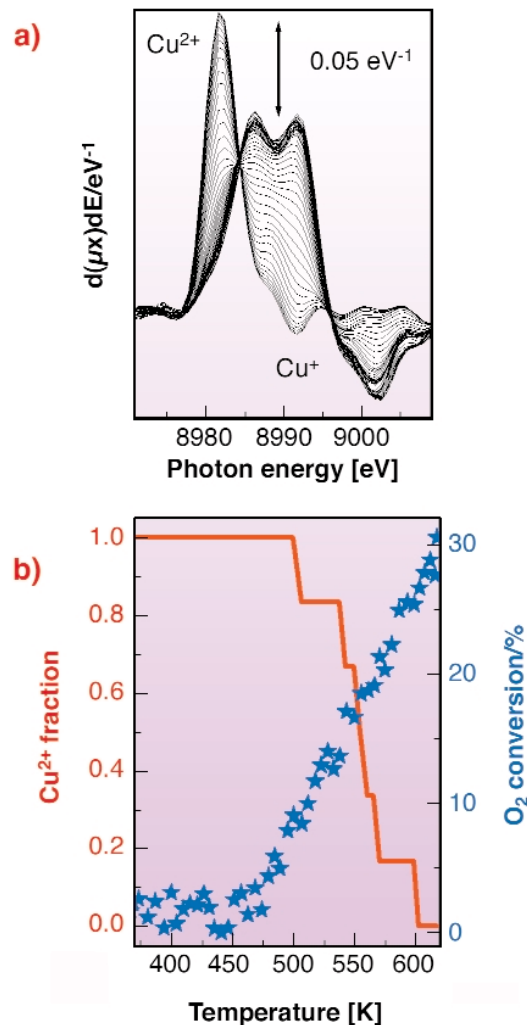
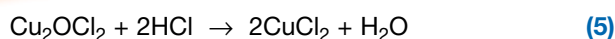
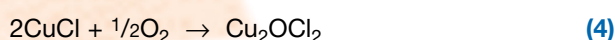
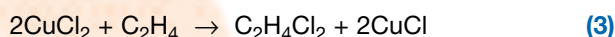


Fig. 44: Part (a): derivative XANES spectra (collected each 30 s) of the catalyst during the heating ramp from 373 to 623 K by 12 K min⁻¹. The presence of two isosbestic points at 8984 and 8995 eV are noticeable. Part (b) Cu²⁺ fraction (red full line, left axis) determined from the spectra reported in part (a) and simultaneous O₂ conversion (blue stars, right axis).

An *in situ*, time-resolved, XANES study, performed on **ID24** has allowed us to determine the $Cu^{2+} \leftrightarrow Cu^+$ transformation occurring on the $CuCl_2/\gamma-Al_2O_3$ catalyst in the ethylene oxychlorination reaction atmosphere within the 373-623 K range. This is shown by the derivative spectra reported in **Figure 44a** and quantified in the red line of **Figure 44b**). The simultaneous determination of the catalysts activity (blue stars in **Figure 44b**), has demonstrated that the catalyst works in the reduced state, and that the rate determining step of the reaction (2) is the oxidation of $CuCl$ according to Equation (4).

This study has also determined the key role of the potassium chloride dopant, added to the industrial catalysts for fixed-bed reactors, by proving that KCl decreases the rate of the reduction step (3), which becomes the rate-determining step for the $KCl/CuCl_2/\gamma-Al_2O_3$ catalyst. This dispersive XANES study, supported by parallel IR investigation supports the thesis that the active phase of the industrial catalyst is a non-stoichiometric mixed chloride K_xCuCl_{2+x} .

References

- [1] G. Leofanti, M. Padovan, M. Garilli, D. Carmello, A. Zecchina, G. Spoto, S. Bordiga, G. Turnes Palomino and C. Lamberti, *J. Catal.* **189**, 91-104 (2000).
- [2] G. Leofanti, A. Marsella, B. Cremaschi, M. Garilli, A. Zecchina, G. Spoto, S. Bordiga, P. Fisticaro, G. Berlier, C. Prestipino, G. Casali, and C. Lamberti, *J. Catal.* **202**, 279-295 (2001).
- [3] G. Leofanti, A. Marsella, B. Cremaschi, M. Garilli, A. Zecchina, G. Spoto, S. Bordiga, P. Fisticaro, C. Prestipino, F. Villain and C. Lamberti, *J. Catal.* **205**, 275-381 (2002).

Principal publication and Authors

C. Lamberti (a,b), C. Prestipino (a,c), F. Bonino (a), L. Capello (a,b), S. Bordiga (a,b), G. Spoto (a), A. Zecchina (b), S. Diaz Moreno (c), B. Cremaschi (d), M. Grilli (d), A. Marsella (d), D. Carmello (d), S. Vidotto (d) and G. Leofanti (d,e), *Angew. Chem. Int. Ed.* **41**, 2341-2344 (2002).

(a) University of Turin (Italy)

(b) INFM UdR of Turin University (Italy)

(c) ESRF

(d) EVC Technological Centre, Porto Marghera, Venezia (Italy)

Dispersive EXAFS Studies of Rapid, Adsorbate-induced, Phase Change in Rh Catalysts and Its Impact on the Selective Reduction of NO to N₂ by H₂

Rhodium is a principal component in modern auto exhaust catalysts due to its capacity to convert the environmentally undesirable NO to benign N₂. Therefore, the fundamental chemistry of Rh in this respect has been much studied [1]. These studies have resulted in the following conundrum: models based on single crystal Rh samples fail to reproduce the activity and selectivity of a highly-dispersed Rh catalyst – in fact the latter consistently produces significant levels of N₂O, whereas this is never observed from the ideal Rh surfaces [1]. This contradictory behaviour points to a major gap in our understanding of these systems and questions the often made assumption that metallic single crystals can be regarded as valid models of their highly-dispersed counterparts.

By using the Laue monochromator configuration [2] available at beamline ID24, we have used time-resolved

energy dispersive EXAFS (EDE) at the Rh K-edge to probe the dynamic behaviour of supported Rh catalysts under feedstocks containing NO.

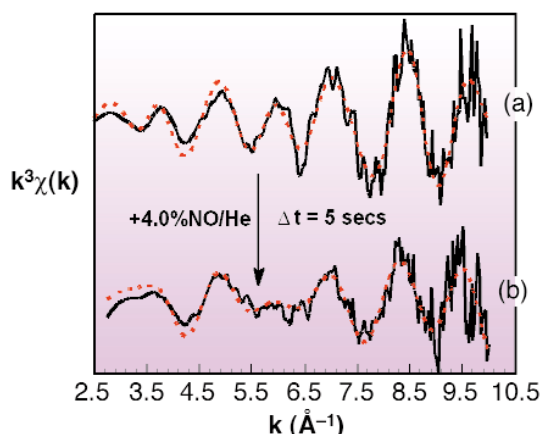


Fig. 45: Rh K-edge derived k^3 -weighted EXAFS data from (a) a reduced 4wt% Rh/Al₂O₃ sample and (b) after exposure to 4% NO/He for ca. 5s. Black and red lines indicate experimental data and theoretical fits respectively.

Figure 45 shows an example of how the metallic Rh nanoparticles structure responds to exposure to NO. Switching from a gas feed of He to one of 4% NO in He resulted in an instantaneous change in the Rh EXAFS signal consistent with a transition from metallic to a new oxidic phase resembling Rh₂O₃. This observation was accompanied by a considerable exotherm. This, together with simultaneously obtained mass spectrometer data, shows that in the nano-regime, molecular dissociation, and the concomitant release of energy, can effect rapid and extreme changes in the structure of the supported phase: no comparable analogy of this behaviour exists on extended metal surfaces.

This observation has a further logical consequence: if a metallic Rh phase is ever to be attained in a reactive environment containing such oxidants (as in a car exhaust with an engine running under “lean burn” conditions), it may only do so as a result of a dynamic equilibrium between these oxidative processes and reactions that may reverse them.

Figure 46a shows the variation in first shell Rh-Rh coordination (N_1^{Rh}) observed during reaction with NO/H₂/He feedstocks of varying composition ($7 > \text{NO} : \text{H}_2 > 0.15$) as a function of temperature. In these cases $N_1^{Rh} = 2$ corresponds to the fully formed oxidic phase, $N_1^{Rh} = 7-8$ indicating fully reduced metallic Rh particles (ca. 20 Å diameter). **Figure 46b** shows the selectivity to N₂O derived simultaneously with the EXAFS data.

This clearly shows that the basic chemistry outlined in **Figure 45** has a pervasive influence on the behaviour of the catalyst. It is only under the most reducing conditions ($\text{NO}/\text{H}_2 < 1$) that a “metallic” Rh phase is ever

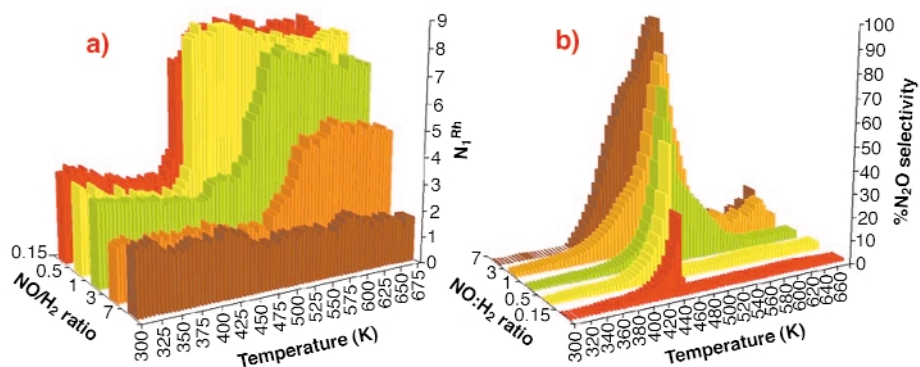


Fig. 46: (a) Variation in N_{1Rh} derived from analysis of EXAFS spectra collected during NO reduction by H_2 over of 5wt% Rh/ γ - Al_2O_3 catalysts as a function of feedstock composition and reaction temperature; (b) Selectivity toward N_2O production as a function of reaction temperature and active feedstock composition in the reduction of NO by H_2 over 5wt% Rh/ γ - Al_2O_3 catalysts.

observed. Moreover, the levels of N_2O produced can be directly correlated with the presence of highly-oxidised Rh, and especially with the collapse of this phase to yield a metallic Rh phase. However when metallic Rh is formed, we see that it produces practically no N_2O – in keeping with the behaviour expected from that of Rh single crystals.

In summary, the application of time-resolved energy-dispersive EXAFS/mass spectrometry has allowed us to show that N_2O production in supported Rh systems results predominantly from an oxidised phase of Rh and its eventual collapse to form metallic Rh. That such an oxidised phase is formed at all is a consequence of an intrinsically enhanced reactivity of nanoscale Rh towards NO – a behaviour that is unique to nanoparticulate Rh and that therefore cannot be modelled through the use of systems of intrinsically lower dispersion.

References

- [1] For instance, V.P. Zhdanov and B. Kasemo, *Surf. Sci. Rep.* **29**, 31 (1997).
- [2] M. Hagelstein, C. Ferraro, U. Hatje, T. Ressler and W. Metz, *J. Synchrotron Rad.* **5**, 1396 (1998).

Principal Publications and Authors

M.A. Newton (a), A.J. Dent (b), S. Diaz-Moreno (c), S.G. Fiddy (c) and J. Evans (a), *Angewandte Chem. Intl. Ed.* **41**, 2587 (2002); T. Campbell (a), A.J. Dent (b), S. Diaz-Moreno (c), J. Evans (a), S.G. Fiddy (c), M.A. Newton (a) and S. Turin (a), *Chem. Comm.*, 304 (2002).

(a) University of Southampton (UK)

(b) SRS Daresbury (UK)

(c) ESRF

EXAFS Applied to Other Fields

The articles above focused on the application of time-resolved X-ray absorption studies to chemical problems. However, X-ray absorption fine structure studies have been applied in many other areas. Below we highlight the problem of neptunium in the environment – studies that are made possible by the unique experimental facilities at **BM20**, the ROBL CRG beamline. The second article concerns the technologically-important colossal magnetoresistance manganese oxides. There has also been work relating to superconductivity [1] and several studies of matter under extreme conditions, whether it be high pressure [2], high temperature [3] or atomic-like systems [4]. A problem in epitaxial semiconductor growth has also recently been addressed at **BM8**, the GILDA CRG beamline [5]. There are also developments in the way of calculating X-ray absorption spectra as can be seen in the final article in this section.

References

- [1] E. Reny *et al.*, *PRB* **66**, 014532 (2002).
- [2] J. Pellicer-Porres *et al.*, *PRB* **65**, 174103 (2002); S. Pascarelli *et al.*, *EPL* (to be published).
- [3] A. Trapananti *et al.*, *PRB* **66**, 014202 (2002).
- [4] A. Kodre *et al.*, *J. Phys. B* **35**, 3497 (2002); A. Mihelic *et al.*, *NIM B* **196**, 194 (2002).
- [5] F. d'Acapito, *PRB* **66**, 205411 (2002).

Reactions of Neptunium with Mackinawite

Microbial activity in waterlogged sediments causes the development of anaerobic conditions. If sulphate is present, this can be exploited by sulphate-reducing bacteria and converted into sulphide, while iron-

reducing bacteria can reduce insoluble iron(III) to soluble iron(II) [1]. The iron(II) reacts with sulphide to form mackinawite (a form of FeS with an open, layered structure; Figure 47), which has a very reactive surface and a large surface area. In such sediments, the fate of trace elements is greatly affected by their potential for reaction with mackinawite, particularly where they can be reduced by and taken up on the mineral surface.

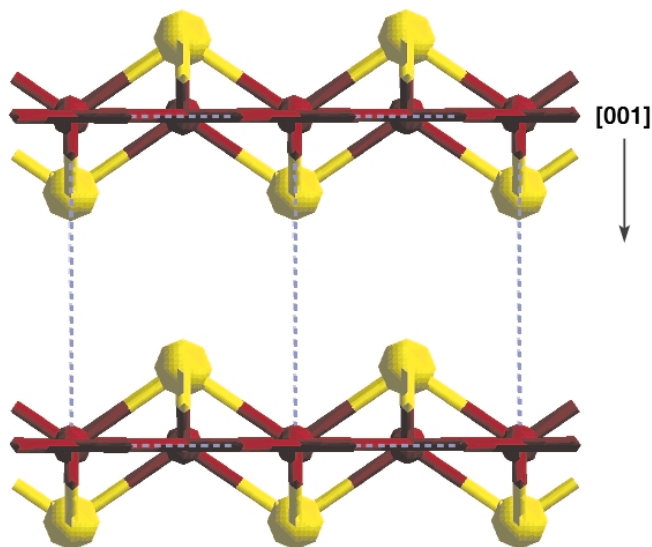


Fig. 47: The layered structure of mackinawite. Sulphur atoms are shown in yellow and iron atoms in red.

Actinide elements, such as uranium, neptunium and plutonium, are released into the environment as a result of nuclear weapons testing, nuclear fuel reprocessing and radioactive waste disposal, and their environmental mobility is therefore of great interest. The uranyl ion, $[\text{UO}_2]^{2+}$, is known to be removed effectively from solution by mackinawite, through partial reduction and precipitation on the mineral surface as an oxide containing both U(IV) and $[\text{UO}_2]^{2+}$ [2]. Neptunium is particularly interesting since it has a long half life (2.16×10^6 years) and is expected generally to be present as the relatively soluble $[\text{NpO}_2]^+$ ion, although, like uranium, in anaerobic conditions it may be reduced to Np(IV), a much less soluble form.

We therefore prepared mackinawite in the laboratory and allowed $[\text{NpO}_2]^+$ to react with it. Because mackinawite is very air-sensitive, and the isotope ^{237}Np is a high specific activity alpha emitter, all the samples had to be prepared in inert atmosphere conditions in a specialised radiochemistry laboratory, then shipped to Grenoble for XAS analysis on the beamline **BM20** (ROBL CRG), the only facility in Europe where such measurements can be made.

Neptunium is very different from uranium in several ways. First, less than 10% of the $[\text{NpO}_2]^+$ in solution is taken up by the surface, compared with over 98% of $[\text{UO}_2]^{2+}$. Second, the XANES spectra for the neptunium samples show that it has been reduced to Np(IV) on reaction with mackinawite and, third, EXAFS analysis

shows that the Np is coordinated directly to the surface sulphur atoms on the mackinawite (Figure 48).

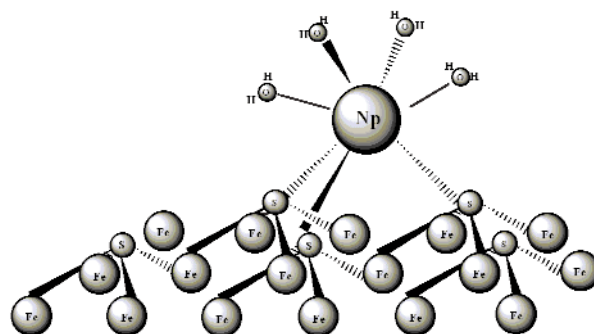


Fig. 48: Possible coordination environment of neptunium on the mackinawite surface.

This experiment illustrates clearly the power of molecular-level spectroscopic analysis of model environmental systems. In the absence of such data, we would have only the empirical observation that $[\text{UO}_2]^{2+}$ was removed from solution much more efficiently than $[\text{NpO}_2]^+$ and would have had to speculate on the reasons for this effect. This XAS experiment allows us to make predictions on the environmental behaviour of radioactive elements with increased confidence.

References

- [1] D.E. Canfield, B. Thamdrup and J. Hansen, *Geochim. Cosmochim. Acta* **57**, 3867-3889 (1993).
- [2] L.N. Moyes, R.H. Parkman, J.M. Charnock, D.J. Vaughan, F.R. Livens, C.R. Hughes and A. Braithwaite, *Environ. Sci. Technol.* **34**, 1062-1068 (2000).

Principal Publication and Authors

L.N. Moyes (a), M.J. Jones (a), W.A. Reed (a), F.R. Livens (a), J.M. Charnock (b), J.F.W. Mosselmans (b), C. Hennig (c), D.J. Vaughan (d) and R.A.D. Patrick (d), *Environ. Sci. Technol.* **36**, 179-183 (2002).
(a) Centre for Radiochemistry Research, Manchester (UK)
(b) CLRC Daresbury Laboratory, Warrington (UK)
(c) Institut für Radiochemie, FZ Rossendorf, Dresden (Germany) and ROBL, ESRF
(d) Williamson Centre for Molecular Environmental Science, Manchester (UK)

X-ray Absorption Study of $\text{LaNi}_{1-x}\text{Mn}_x\text{O}_{3+\delta}$ Perovskites

The recent discovery of colossal magnetoresistance [1] in mixed oxides of manganese has stimulated the research of this property in related compounds. Ferromagnetic oxides with Mn in a mixed-valence state seem to be good candidates to show magnetoresistance. $\text{LaM}_{1-x}\text{Mn}_x\text{O}_3$

(M = Ni, Co) compounds are ferromagnets. Some authors explained their magnetic ordering in terms of interactions between $\text{Ni}^{2+}(\text{Co}^{2+})$ and Mn^{4+} . Other authors claim instead for a homovalent substitution between Mn^{3+} and Ni^{3+} and ascribed these differences to synthetic details. Moreover a recent spectroscopic study on $\text{LaMn}_{1-x}\text{Co}_x\text{O}_3$ compounds suggests a mixture of Mn^{3+} and Mn^{4+} .

We have performed an X-ray-absorption spectroscopy study of $\text{LaNi}_{1-x}\text{Mn}_x\text{O}_{3+\delta}$ series at Mn and Ni K-edges in order to solve the controversy about the electronic state of the transition metals. The measurements were carried out at beamlines **ID26** and **BM29**. The aim of this work is to extract the local geometric structure around each transition metal atom by EXAFS and to study the electronic state and local geometry by XANES. Samples were prepared from different synthetic routes [2] to check their effect on the local and electronic structures.

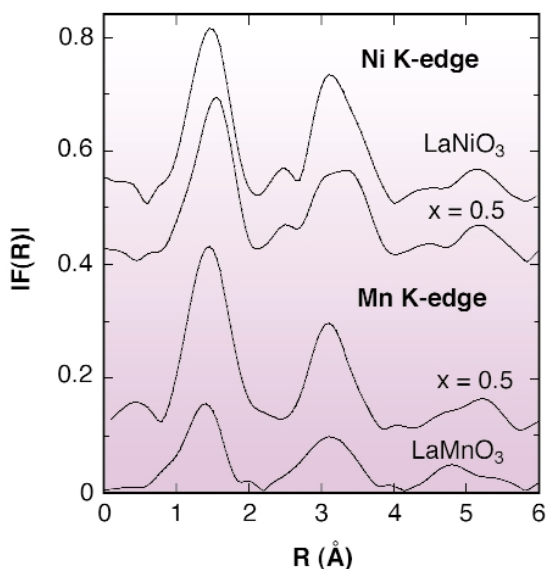


Fig. 49: Modulus of the room temperature Fourier transform of the Mn and Ni K-edge EXAFS spectra for selected $\text{LaNi}_{1-x}\text{Mn}_x\text{O}_{3+\delta}$ samples.

The local structure, determined by EXAFS, shows a tetragonal distorted MnO_6 octahedron in LaMnO_3 . The replacement of Mn by Ni decreases both the tetragonal MnO_6 distortion and the average Mn-O distance. This can be seen in **Figure 49** (Mn K-edge), where the first peak (Mn-O shell) of the Fourier Transform (FT) for the $x = 0.5$ sample is higher than for LaMnO_3 . Samples ($x \geq 0.5$) with the same Mn/Ni ratio and different oxygen content were also studied. The octahedron distortion is smaller in oxidised samples suggesting an increase in holes (oxidation) in the Mn sublattice. Opposite effects were observed in the local structure around the Ni atom. EXAFS shows that the Ni-O distance increases as the Mn content does. **Figure 49** (Ni K-edge) displays the shift of the FT first peak toward higher values for the $x = 0.5$ sample. No changes were observed in the Ni environment in oxidised samples. Therefore, a contraction of the MnO_6 octahedron is coupled to an expansion of the NiO_6 octahedron. This

result is well correlated with the changes in the oxidation states deduced from XANES. The Mn valence state continuously changes from the formal 3+ state in LaMnO_3 to a nearly 4+ state in $\text{LaNi}_{0.5}\text{Mn}_{0.5}\text{O}_3$. Thus, the energy position of the absorption edge for $\text{LaNi}_{0.5}\text{Mn}_{0.5}\text{O}_3$ is close to the position for CaMnO_3 with formal 4+ state (**Figure 50**). The Ni valence state instead shifts from Ni^{3+} in LaNiO_3 to Ni^{2+} in $\text{LaNi}_{0.5}\text{Mn}_{0.5}\text{O}_3$ (inset of **Figure 50**). Therefore, Ni^{2+} and Mn^{4+} are the most suitable ionic approximation for $\text{LaNi}_{0.5}\text{Mn}_{0.5}\text{O}_{3+\delta}$.

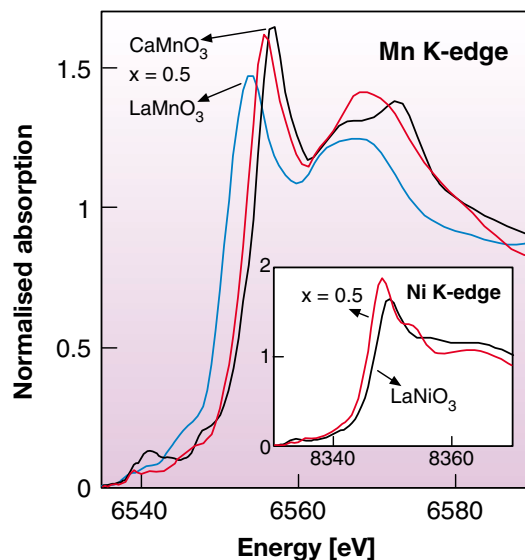


Fig. 50: Normalised Mn K-edge XANES spectra of $\text{LaNi}_{1-x}\text{Mn}_x\text{O}_{3+\delta}$ ($x = 1$ and 0.5) samples compared to CaMnO_3 . Inset: Normalised Ni K-edge XANES spectra of the $\text{LaNi}_{0.5}\text{Mn}_{0.5}\text{O}_{3.08}$ sample compared to LaNiO_3 .

In conclusion, the solid solution cannot be considered as homovalent. The addition of Ni^{3+} to LaMnO_3 would produce an oxidation of the Mn sublattice (coupled to the reduction of Ni^{3+}). In the same way, the incorporation of Mn^{3+} into LaNiO_3 would lead to a reduction of Ni^{3+} (and to an oxidation of Mn^{3+}). Moreover, these results do not seem to depend on synthetic details. Oxygen excess is accommodated as cationic vacancies implying an oxidation of the Mn sublattice.

References:

- [1] J.M.D. Coey, M. Viret, S. von Molnar, *Adv. Phys.*, **48**, 167-293 (1999).
- [2] J. Blasco, M.C. Sánchez, J. Pérez-Cacho, J. García, G. Subías, J. Campo, *J. Phys. Chem. Solids*, **9**, 781- 792 (2002).

Principal Publication and Authors:

M.C. Sánchez (a), J. García (a), J. Blasco (a), G. Subías (b), J. Perez-Cacho (a), *Phys. Rev. B* **65**, 1444091-1444099 (2002).

(a) ICMA-Departamento de Física de la Materia Condensada, CSIC-Universidad de Zaragoza, Zaragoza (Spain)

(b) ESRF

A New Computational Scheme for X-ray Absorption Spectroscopy in Strongly-correlated Systems

Multiple scattering (MS) theory provides an accurate and flexible scheme for the calculation of unoccupied electronic states, which are probed by various synchrotron experiments such as X-ray absorption spectroscopy and resonant X-ray scattering.

The standard theory relies on the single-particle picture: that is, it neglects electron correlation effects. This is a great shortcoming, since core-level X-ray spectra are often strongly modified by electron correlation, in particular by the Coulomb and exchange interaction of the valence electrons with the core hole. In transition metal and rare earth systems, this interaction can give rise to pronounced atomic multiplet and satellite structures in the spectra, which can only be accounted for in a many-electron calculation.

A generalisation of MS theory to many-electron wave functions was developed by Natoli *et al.* [1] and is known as "multichannel" MS theory. The idea is to develop the photo-absorption final state over a basis of corresponding photo-ionisation final states, *i.e.* over the eigenstates of the $N-1$ electron system with one core-hole but without the photo-electron. In a given photo-absorption process, the final state energy and all other conserved quantum numbers can be distributed in different ways between the $N-1$ electron system and the photo-electron; each of these different ways is called a channel. Since the photo-electron is correlated with the $N-1$ other electrons through exchange and Coulomb interaction the channels are coupled.

Within the multichannel MS framework, we have developed a relatively simple method that allows one to take into account atomic multiplet effects due to the interaction between the photo-electron and electrons/holes in sufficiently-localised orbitals. Sufficiently localised means that the wave function is negligibly small beyond the atomic radius. This applies exactly to inner-core shells and well to the $4f$ -shell in rare earths. Whether the same approach may also be used for the interaction with $3d$ -electrons in transition metals is not clear at this point.

Short Outline of the Formalism

The systems' ground state is described by an N -electron wave function, where all N electrons are in core- or sufficiently-localised valence-shells. Electrons in wide valence bands are not explicitly taken into account; their effect on the photo-electron wave function is treated in a mean-field approximation as in standard MS theory. In

the final state of the photo-absorption process $N-1$ electrons remain in localised orbitals and one is promoted to a delocalised (conduction band) orbital.

Atomic multiplet calculations are performed to determine the ground state with energy E_g and the eigenstates of the $N-1$ electron system, $|\alpha\rangle$, with energies E_α . For given total final state energy $E = E_g + \hbar\omega$, N -electron basis states $|\alpha, i, l, m, \sigma\rangle$ are defined as anti-symmetrised product states between $|\alpha\rangle$ and $|\phi_i, l, m, \sigma\rangle$, where ϕ_i stands for a small set of orthogonal orbitals for each orbital quantum number l . With these $|\alpha, i, l, m, \sigma\rangle$, the so-called eigen-channel method [2] is employed for the calculation of the atomic T -matrices and the optical transition matrix elements. Once the latter quantities are known, the MS formalism extends in a straightforward way to the multichannel case [1].

Within the restrictions about the localisation of orbitals stated above, we have shown how the eigen-channel method, so far only used in atomic and nuclear physics, can be applied to X-ray absorption in condensed systems.

Due to the localised character of the core-hole, the most important correlation effects are often local to the absorbing atom. This means that the multichannel nature of the T -matrix needs to be taken into account for this one atom only.

We have shown that in this important case, the MS equations can be solved very efficiently using a partitioning technique. The numerical difficulty of the whole multichannel problem is then reduced to that of a standard MS problem (for the system without absorber) plus a multichannel but purely atomic problem.

Implementation of the formalism in computer code is in progress. First applications include X-ray absorption spectra of light transition metal compounds at the $L_{2,3}$ edges, and magnetic circular dichroism of rare-earth compounds at the rare-earth $X_{2,3}$ ($X = L, M, N$) and ligand K edges. In these cases, standard MS theory fails to reproduce the observed spectra line shapes. The failure is believed to be due to atomic multiplet-like interactions between the photo-electron and the core-hole or the $4f$ electrons, which can be taken into account completely by our new method.

References

- [1] C.R. Natoli, M. Benfatto, C. Brouder, M.F.R. López, and D.L. Foulis, *Phys. Rev. B* **42**, 1944 (1990).
- [2] M. Aymar, C.H. Greene, and E. Luc-Koenig, *Rev. Mod. Phys.* **68**, 1015 (1996).

Principal Publication and Authors

P. Krüger (a) and C.R. Natoli (b), *to be published*.
 (a) ESRF
 (b) INFN, Frascati (Italy)

X-ray Magnetic Circular Dichroism (XMCD)

Introduction by A. Rogalev (ESRF)

X-ray Magnetic Circular Dichroism (XMCD) is considered to be one of the most important discoveries in the field of magnetism in the last two decades. In an XMCD experiment, the quantity studied is the difference in the X-ray absorption spectra recorded with left and right circularly-polarised photons while the sample magnetisation is kept parallel or antiparallel to the direction of the propagation of the incident X-ray beam. The major strength of the XMCD is the capability to deduce from the experimental spectra the orbital-projected magnetic moments both in magnitude and direction with the full benefit of the element selectivity inherent to X-ray absorption spectroscopy.

The physical origin of XMCD can be most easily explained with the so-called two-step model. The first step describes the excitation of a core electron by a circularly-polarised X-ray photon that carries an angular momentum ($+\hbar$ for a right-handed photon and $-\hbar$ for a left-handed photon), the corresponding helicity vector being parallel (right) or antiparallel (left) to the propagation direction. As a consequence of the conservation of angular momentum in the absorption process, the photon's angular momentum is entirely transferred to the photoelectron. Let us consider the photoelectron being excited from a spin-orbit-split core level (e.g., $L_{II,III}$ absorption edges): then part of the angular momentum carried by the photon will be converted into spin *via* spin-orbit coupling. The acquired spin moment is always parallel to the photon propagation direction but its sign depends on the helicity of the incident X-ray photon and on the spin-orbit coupling ($\mathbf{l}+\mathbf{s}$ at the L_{III} and $\mathbf{l}-\mathbf{s}$ at the L_{II}). The magnetic properties of the sample are driving the second step. A polarised photoelectron occupies the states above the Fermi level and, if there is any imbalance in either spin or orbital momentum in the final states, the XMCD spectrum reflects the difference in the density of states with different spin or orbital moments. The sum of the XMCD spectra recorded at the L_{II} and L_{III} edges reflects only a difference in the *orbital moments* of the final states, while the difference is proportional to a spin polarisation of the valence states. This is precisely the content of the magneto-optical sum rules. It is worth mentioning that the summation over two spin-orbit split edges is equivalent to what can be measured for a core level with no spin-orbit interaction. This implies that a dichroic effect at the K-edges is only due to the orbital moments in the valence shell.

The XMCD technique is now widely used to unravel the microscopic origin of magnetism in various ferro- and

ferrimagnetic systems [1]. Furthermore, it has recently been shown that high-quality XMCD spectra could be recorded on paramagnetic systems, including Pauli and van Vleck paramagnets, subjected to high magnetic field [2].

XMCD has also become a remarkable element-specific magnetometry tool for heteromagnetic systems. A particularly outstanding example is presented below for $\text{DyFe}_2/\text{YFe}_2$ magnetic superlattices. The high sensitivity of XMCD also makes it unique for the study of the magnetic properties of reduced-dimensionality structures: thin magnetic films [3] and multilayers [4], magnetic quantum wires and dots [5]. This is nicely illustrated below in the study of magnetic moments of 3d-impurities on alkali films.

References

- [1] M. Besse *et al.*, *EPL* **60**, 608 (2002).
- [2] F. Wilhelm *et al.* *To be published*.
- [3] M. Marangolo *et al.*, *PRL* **88**, 217202 (2002).
- [4] F. Wilhelm, *PRL* **85**, 413 (2000).
- [5] P. Gambardella *et al.*, *Nature* **416**, 301 (2002).

Location of Magnetic Springs in Exchange-coupled Superlattices

Magnetic exchange springs are artificially tailored magnetic domain walls: they develop in a material whose magnetisation is pinned locally, for instance by exchange coupling, but may be rotated by an external magnetic field far from the pinning centre. They are usually present in heterostructures combining a hard magnetic material with a soft one and are of great interest for permanent magnets and for spintronics. In these systems, the magnetisation reversal process is assumed to occur via the development of exchange springs in the soft material before the magnetisation of the hard one is reversed. However, the detailed mechanism remains unclear and is usually more complex, depending on the microstructure, the composition, and other factors.

Typical examples of exchange-spring magnets are $\text{DyFe}_2/\text{YFe}_2$ superlattices composed of alternating layers of a hard ferrimagnet (DyFe_2) and of a soft ferromagnet (YFe_2). Antiferromagnetic interactions at the interfaces in such heterostructures lead to a variety of novel phenomena: magnetic bias and exchange springs [1]. To unravel the mechanisms of magnetisation reversal one needs to know the behaviour of both hard and soft layers separately, which is not possible with conventional

magnetisation measurements since it probes the whole superlattice. X-ray Magnetic Circular Dichroism, being inherently an element-selective technique, allows one to measure the magnetisation of DyFe_2 and YFe_2 layers independently and, therefore, to determine directly the location of magnetic springs. Layer-selective magnetisation curves were recorded at beamline ID12 by monitoring XMCD signals at both the Dy L_3 and the Y L_3 edges as a function of the applied magnetic field.

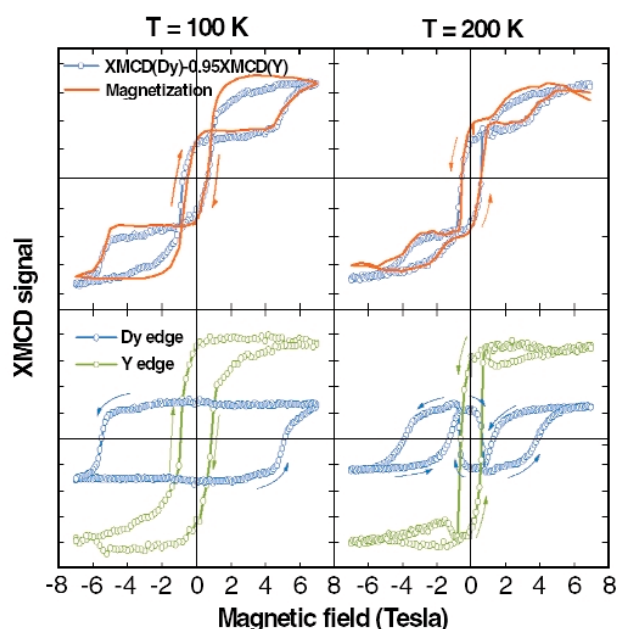


Fig. 51: Magnetisation curves of the $[\text{DyFe}_2(50 \text{ Å})/\text{YFe}_2(200 \text{ Å})]$ superlattice (a) at 100 K and (b) at 200 K. Top: macroscopic magnetisation (in red) superimposed on a linear combination of the hysteresis loops measured with XMCD at the Y and Dy L_3 edges (in blue). Bottom: element-selective magnetisation curves measured at the Dy (blue) and Y (green) L_3 -edges.

For superlattices with rather thick DyFe_2 layers ($>100 \text{ Å}$), the classical reversal process was observed. Whereas for a $[\text{DyFe}_2(50 \text{ Å})/\text{YFe}_2(200 \text{ Å})]$ superlattice, the hysteresis loops show a drastic evolution from a low-temperature regime to a high-temperature regime (Figure 51). At temperatures below 100 K, a first step in magnetisation observed at a positive field is due to the expansion of magnetic springs in the soft layers as evidenced by magnetisation curve of YFe_2 recorded at the Y L_3 edge. A second step occurs at a large negative field and, from the magnetisation measured at the Dy L_3 edge, is attributed to the irreversible switch of the hard layers. However, at 200 K, the superlattice magnetisation exhibits a completely different behaviour that can be unravelled from the compound-selective hysteresis loops. Indeed, it is a superposition of an almost square loop with a negative coercive field in YFe_2 , measured with Y L_3 -XMCD and an atypical loop recorded in DyFe_2 with Dy L_3 -XMCD. The latter is described by three processes: (i) a smooth reversal in positive magnetic field, (ii) a sudden switch back, simultaneously with YFe_2

magnetisation reversal, for a small negative field, (iii) the compression of magnetic walls at larger negative fields. This result unambiguously demonstrates that the magnetic domain walls are located in the hard compound.

The thermal evolution of the reversal process (Figure 52) could be attributed to the thermal variation of the Zeeman and the magnetocrystalline anisotropy energies in the DyFe_2 layers. At high temperatures, it becomes then more favourable that the YFe_2 magnetisation remains along the applied field and the magnetic walls expand, due to interface-exchange coupling, in the hard DyFe_2 layers.

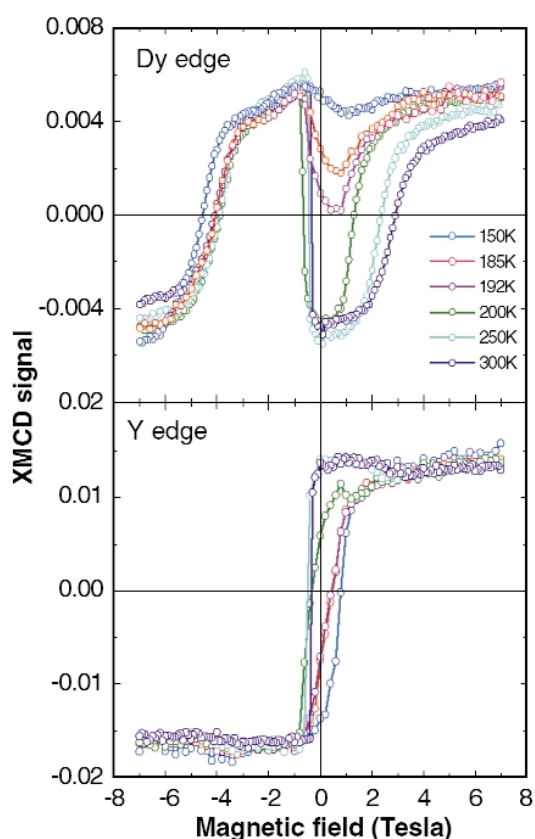


Fig. 52: Temperature variation of the half hysteresis curves (from +7T to -7T) measured with XMCD at the Dy and Y L_3 edges for the $[\text{DyFe}_2(50 \text{ Å})/\text{YFe}_2(200 \text{ Å})]$ superlattice.

These experiments provide direct evidence of the exchange springs penetration into the hard layers, which is in contrast to the generally accepted point of view. This important observation is a first step in the elucidation of the mechanisms of magnetisation reversal and the thermal evolution of coercivity from positive to negative.

References

[1] K. Dumesnil, M. Dutheil, C. Dufour, Ph. Mangin, *Phys. Rev. B* **62**, 1136 (2000).

Principal Publication and Authors

K. Dumesnil (a), C. Dufour (a), Ph. Mangin (b), A. Rogalev (b), *Phys. Rev. B* **65**, 094401 (2002).

(a) *Laboratoire de Physique des Matériaux (UMR 7556), Université Henri Poincaré, Vandoeuvre les Nancy (France)*
 (b) *ESRF*

Magnetic Moment of Single Atoms on Metal Surfaces

The extent to which the d orbitals of a transition metal (TM) atom mix with the conduction electron states of a nonmagnetic host governs fundamental macroscopic properties such as electron transport, magnetic susceptibility, and specific heat. Theoretical predictions as well as experimental studies on bulk TM impurities dissolved into a non-magnetic matrix show that the TM magnetic moments vary, or even disappear, depending on the d -state localisation and host electron density. However, despite extensive study since the work of Friedel and Anderson, the degree of d -state localisation and the magnetic moment of the impurity have remained open questions. Experiments on beamline ID8 have been able to resolve these issues for the first time using a combination of X-ray absorption spectroscopy (XAS) and X-ray magnetic circular dichroism (XMCD). These techniques are sensitive to bulk and, in particular, to surface TM impurities with concentration as low as 3×10^{12} atoms cm^{-2} allowing an unambiguous determination of the impurity valence state, spin (S) and orbital (L) magnetic moment.

The interaction between the localised $3d$ states of Fe, Co, and Ni and a free-electron gas were studied by separately depositing minute amounts of the respective TM onto thick K films condensed onto a Cu(111) substrate at 10 K. The measurements were performed in magnetic fields of 7 T with the sample held at 10 K. The XAS spectra over the $L_{2,3}$ edges and resulting XMCD, recorded using left and right circularly-polarised light, are shown in **Figure 53**. In each case the XAS and XMCD are compared with typical spectra for the bulk case. The lineshapes and relative strengths of the XAS and XMCD features are fingerprints for the atomic d -state configuration. The most striking difference between the impurity and bulk XAS and XMCD spectra is the presence of sharp multiplet features which reveal the TM atomic-like ground states due to strong $3d$ -electron localisation at the impurity sites. Comparison with calculated atomic spectra [1] (bottom inset in **Figure 53b**) indicates that a charge transfer, from the free-electron host, increases the d -valence of the TM adatoms by one electron compared to the atomic case, yielding ground states with predominantly Fe d^7 , Co d^8 , and Ni d^9 character and correspondingly large magnetic moments of 6.6 , 5.6 , and $3.6 \mu_B$, respectively. Further, the XMCD at the L_2 edge of Fe and Co has the opposite sign with respect to the bulk spectra, whereas it is zero for Ni. Application of the XMCD sum rules yields atomic-like values for L of approximately 3, 3, and $2\mu_B$, respectively, in agreement with the predictions of Hund's rules. The consistency of these results strongly supports the XMCD sum rules in the precise context of their derivation, *i.e.* for localised atomic states.

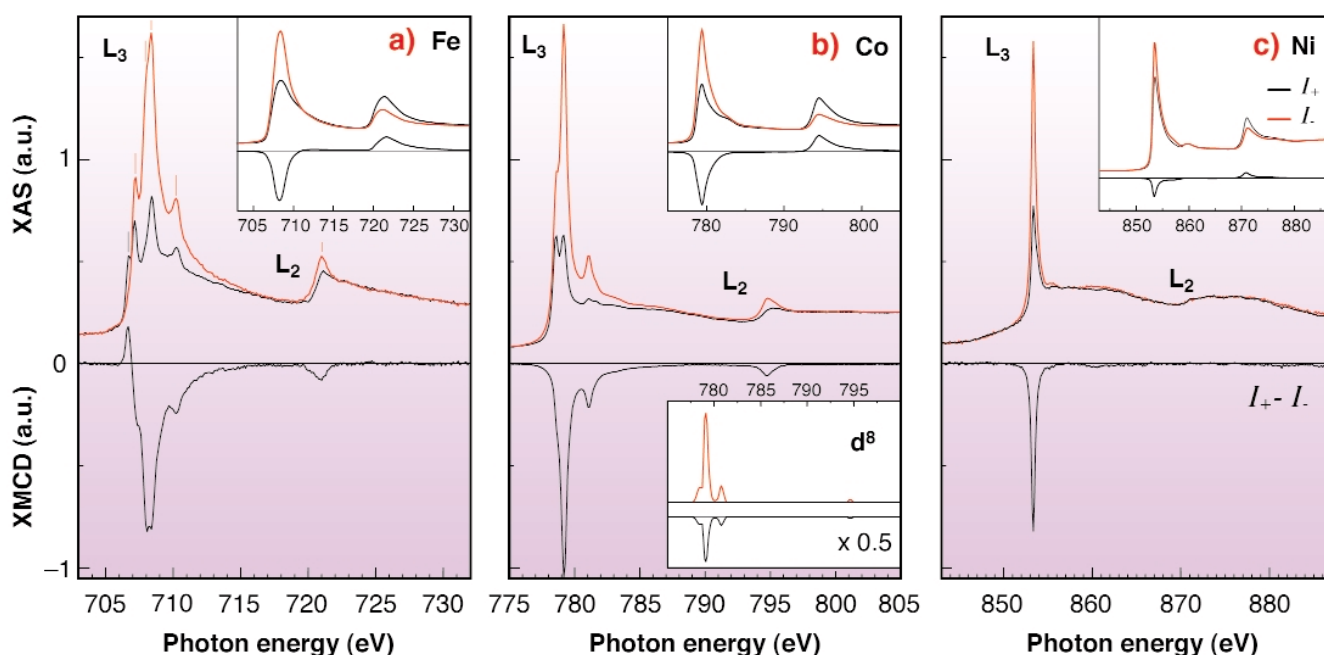


Fig. 53: XAS and XMCD spectra for the $L_{2,3}$ edges recorded with X-ray polarisation vector parallel (black line) and antiparallel (red line) to a 7 T applied magnetic field for (a) Fe, (b) Co, and (c) Ni impurities on K/Cu(111). The top insets show the corresponding bulk spectra. A calculated [1] atomic spectra for a d^8 configuration is shown in the bottom inset in (b).

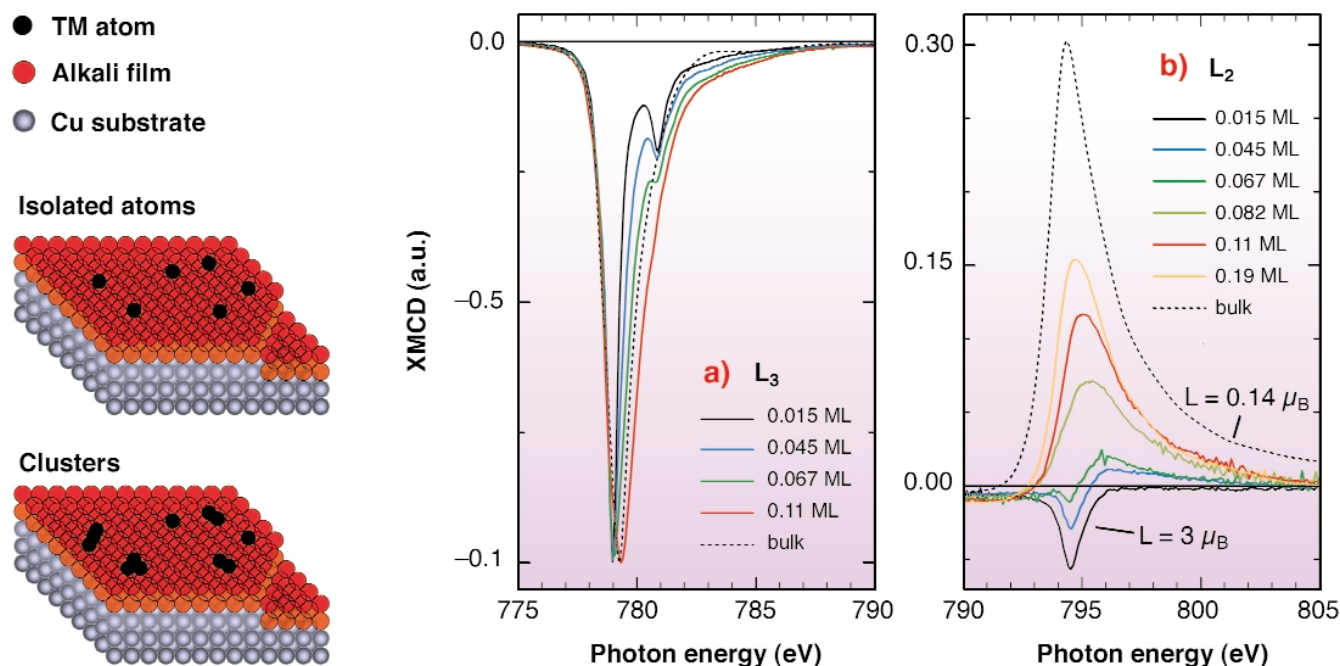


Fig. 54: XMCD spectra recorded at the (a) L_3 and (b) L_2 edge for Co on K/Cu(111) showing changes in the lineshape as isolated Co atoms form clusters with increased coverage. The value of L for bulk Co and isolated adatoms is also indicated.

Figure 54 shows changes in the XMCD lineshape from Co/K/Cu(111) for progressive cluster formation with increasing Co coverage. During cluster growth, atomic configuration mixing and increasing d -state hybridisation result in broader multiplet features in the XAS and hence also the XMCD. At the L_3 edge shown in Figure 54a, the peak broadens, whereas the smaller satellite at 781 eV becomes less well-defined and finally disappears. At the L_2 edge, shown in Figure 54b, the XMCD is negative and changes sign with increasing coverage. These changes imply that L is quenched much faster than S .

In conclusion, the electronic state and magnetic moment of isolated TM atoms on metal surfaces have been investigated for the first time. TM impurities on a simple metal substrate display localised atomic configurations with atomic orbital magnetic moments. The present results conclusively prove that the giant TM magnetic moments in alkali systems [2] originate from the localisation of the $3d$ states. Finally, we emphasise that combined XAS and XMCD experiments have an unexplored potential for the study of diluted systems, allowing the simultaneous determination of the electronic and magnetic configuration of the impurity states.

References

- [1] G. van der Laan and B.T. Thole, *Phys. Rev. B* **43**, 13401 (1991).
- [2] H. Beckmann and G. Bergmann, *Phys. Rev. Lett.* **83**, 2417 (1999); *ibid.* **85**, 1584 (2000).

Principal Publication and Authors

P. Gambardella (a), S.S. Dhesi (b), S. Gardonio (c),

C. Grazioli (c), P. Ohresser (d) and C. Carbone (c), *Phys. Rev. Lett.* **88**, 047202 (2002).

(a) EPF Lausanne (Switzerland)

(b) ESRF

(c) CNR-ISM, Trieste (Italy)

(d) LURE, Paris (France)

Resonant X-ray Scattering

Introduction by L. Paolasini (ESRF)

The research field of Resonant X-ray Scattering (RXS) is relatively new, with the first experiments only fifteen years ago. Tremendous progress has been achieved since its introduction and RXS is now rapidly becoming a crucial complementary technique to neutron scattering for investigating the subtleties of microscopic magnetism. This is especially true in systems where the ground state properties reflect a delicate balance between several different correlated processes, including coupling to the lattice, selective occupation of atomic orbitals and charge order. The element and shell specificity and the extremely high resolution in reciprocal space makes RXS truly complementary to neutron diffraction, as demonstrated recently by joint experiments on the historically controversial magnetic ground state of CeFe_2 [1]. The ability to study very small volume samples is a further attractive characteristic of the RXS technique, which has proved particularly useful

in the study of thin films, as demonstrated in the case of U/Fe multilayers [2], and other actinide systems.

Over the last few years, polarisation and azimuthal angle analysis have developed into standard tools, opening the experimental avenue to a whole new range of studies, including the physics of ordered multipole states. The dependence of the diffracted beam polarisation on the azimuthal angle, in the framework of anisotropic tensor susceptibility formalism, gives unique information on orbital occupancy order. This is a key issue in, for example, the physics of transition metal compounds, as shown in the investigation of the interplay between orbital and magnetic order for the model system KCuF_3 [3], or the direct observation of charge order at the metal-insulator transition in NdNiO_3 films [4].

A second classic application, presented below, has been its contribution to unravelling the microscopic nature surrounding the mysterious heat-capacity anomaly in neptunium dioxide [5]. This work exploits not only the combined power of the polarisation and azimuthal angle analysis technique, together with a detailed symmetry analysis of the azimuthal dependence, but also the intense synchrotron flux which enables microgram quantities of transuranic elements to be examined.

As a complement to these developments in RXS techniques, further progress is now planned for the sample environment. Measurements down to dilution-refrigeration temperatures, hydrostatic pressures up to 25 kbar and magnetic fields up to 10 Tesla will be available in the near future, and one can be confident that these novel opportunities will prove to be exceedingly fertile and of great scientific value in the field of strongly correlated electron systems.

References

- [1] L. Paolasini *et al.*, *Phys. Rev. Lett.*, in press (2003) and ILL Annual Report 2002.
- [2] S.D. Brown, submitted to MMM conference, to be published in *J. Appl. Phys.* (2003).
- [3] L. Paolasini *et al.*, *Phys. Rev. Lett.* **88**, 106403 (2002); R. Caciuffo *et al.*, *Phys. Rev. B* **65**, 174425 (2002).
- [4] U. Staub *et al.*, *Phys. Rev. Lett.* **88**, 126402 (2002).
- [5] J. A. Paixao, *Phys. Rev. Lett.* **89**, 87202 (2002).

Triple- \vec{q} Octupolar Ordering in NpO_2

For half a century the low temperature properties of NpO_2 have mystified theorists and experimentalists alike. Upon cooling from room temperature, a *single* phase transition is observed at $T_0 \approx 25.5$ K. However, earlier experiments gave (apparently) contradictory indications about the nature of this phase transition. While magnetisation and muon spin rotation experiments suggested an antiferromagnetic (AFM) nature of this phase transition, Mößbauer spectroscopy and neutron diffraction effectively ruled out AFM order by establishing an upper limit of $\approx 0.01 \mu_B$ for the ordered magnetic moment. Santini and Amoretti [1] pointed out the possibility of explaining the whole body of experimental evidence assuming magnetic-octupole

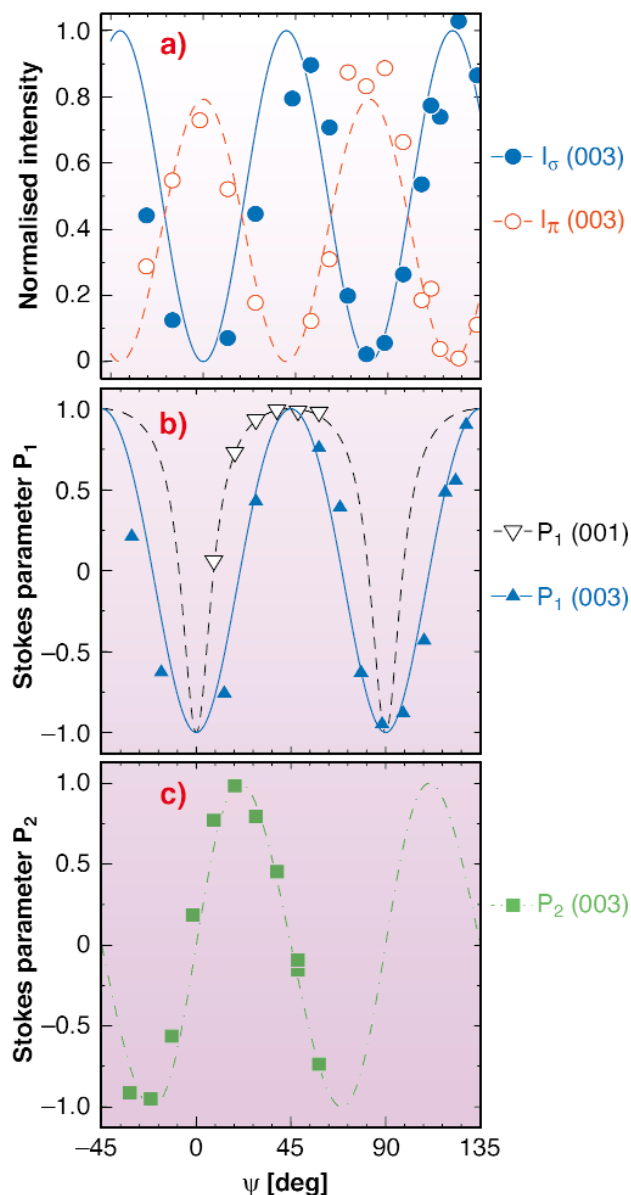


Fig. 55: Dependence of the scattering on the azimuthal angle ψ , with incident polarisation σ : (a) Intensity (b, c) Stokes parameters. The lines represent model calculations based on the orientation of quadrupoles shown in Figure 56.

order instead of magnetic dipole order. Furthermore, recent resonant X-ray diffraction (RXS) experiment [2] observed superstructure reflections with $\vec{q} = (0\ 0\ 1)$, similar to those found in the iso-structural AFM UO_2 . These reflections were assumed to be of magnetic origin and seemed to contradict the aforementioned neutron and Mößbauer findings. The absence of distortions [2] suggested a triple- \vec{q} nature of the order.

To clarify the above confusion, we have undertaken a new RXS experiment at **ID20**, the magnetic-scattering beamline. We performed polarisation analysis of the diffracted radiation and measured the dependence of the Np M_4 resonant scattering on the azimuthal angle ψ (the angle describing the rotation of the crystal about the scattering vector). Our results (see **Figure 55**) show that the superlattice peaks in NpO_2 are not due to a magnetic dipolar polarisation but rather to the asphericity of the vacant Np $5f$ orbitals. Indeed, the superlattice peaks signal the occurrence of electric quadrupole (EQ) long range order below T_0 , with the configuration shown in **Figure 56**.

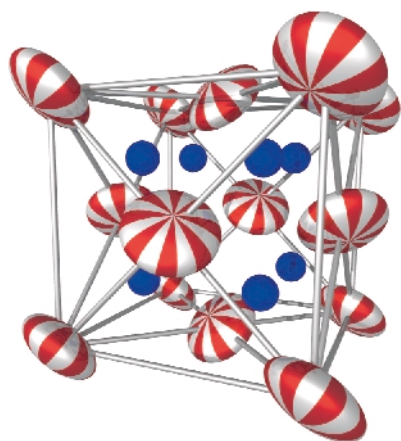


Fig. 56: Crystal structure of NpO_2 in the antiferroquadrupolar state with space group $\text{Pn}\bar{3}\text{m}$. The ellipsoids represent the orientation of the local symmetry axis at the Np position, not the actual charge distributions. The O atoms are shown as spheres.

However, quadrupolar order *alone* is not a sufficient ingredient, as it cannot explain the absence of a disordered magnetic moment and the breaking of invariance under time reversal. The lowest-rank multipolar order parameter consistent with the experimental findings is a magnetic octupole (MO) [1]. Indeed, triple- \vec{q} order of octupoles with Γ_5 symmetry would induce the observed quadrupoles as secondary order parameter, and is thus compatible with all present and earlier experimental observations.

Whilst no *direct evidence* for a triple- \vec{q} MO structure is available, the model does make testable predictions. Notably the energies of the crystal field levels can be estimated and experimentally investigated both directly through inelastic neutron scattering and indirectly through thermodynamic properties such as the specific heat.

References

- [1] P. Santini and G. Amoretti, *Phys. Rev. Lett.* **85**, 2188 (2000).
- [2] D. Mannix *et al.*, *Phys. Rev. B* **60**, 15187 (1999).

Principal Publication and Authors

J.A. Paixão (a), C. Detlefs (b), M.J. Longfield (c), R. Caciuffo (d), P. Santini (e,f), N. Bernhoeft (g), J. Rebizant (c), and G.H. Lander (c), *Phys. Rev. Lett.* **89**, 187202 (2002).

(a) Departamento de Física, Universidade de Coimbra (Portugal)

(b) ESRF

(c) European Commission, JRC, Institute for Transuranium Elements, Karlsruhe (Germany)

(d) INFM, Dipartimento di Fisica ed Ingegneria dei Materiali, Università di Ancona (Italy)

(e) Oxford Physics, Clarendon Laboratory (UK)

(f) Present address: INFM, Dipartimento di Fisica, Università di Parma (Italy)

(g) DRFMC, CEA Grenoble (France)

High Resolution and Resonance Scattering

Introduction

The beamlines of the High Resolution and Resonance Scattering Group cover a wide variety of scientific topics and applications, which range from the investigation of static and dynamical magnetic and electronic properties to vibrational dynamics with energy transfers in the neV to eV and μs to fs regime. Investigations of vibrational dynamics are carried out at beamline ID16 and ID28, measuring phonon dispersion relations. The (partial) phonon density of states is determined at the beamlines ID18 and ID22N. Electronic and geometrical structure is studied by X-ray absorption and emission spectroscopy at ID16 and ID26, where information is also gathered about magnetic properties. Magnetic and electric properties, both static and dynamic, are also actively studied by nuclear resonance techniques developed at ID18 and ID22N.

Development of the beamline instrumentation and sample environment continues alongside the scientific programme. On the machine side this comprises optimised undulators for highest brilliance ($1 \cdot 10^{20}$ photons/s \cdot 0.1% bw \cdot mm² \cdot mrad²) from three undulators with a 11 mm magnetic gap. On the beamline side, the most important developments were made in crystal optics in collaboration with the Optics Group on high-resolution monochromators, analysers, and advanced focusing schemes. Fast detector systems based on avalanche photo diodes

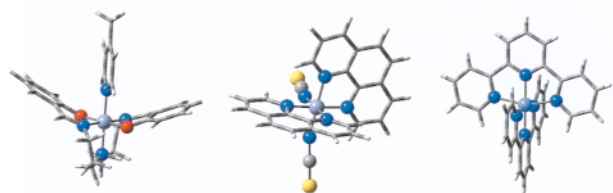
and position sensitive detectors based on multi-element drift diodes are other fields of development and application. Finally, a variety of sample environments has been developed and made available to users, such as furnaces, cryostats, superconducting cryomagnet systems, and high-pressure equipment.

The wide range of applications does not permit a full presentation here. Nonetheless, we will mention some scientific fields that are significant activities for the group. One example is the investigation of surface and interface magnetism such as exchange-coupled spring layered systems as Fe/FePt [1] and coarsening of the domain structure in antiferromagnetic Fe/Cr multilayers [2]. Another emphasis is put on the study of matter under extreme conditions. Here we mention the work on the valence-electron structure of liquid germanium and collective dynamics of liquid water [3]. Furthermore, the elucidation of dynamical properties of disordered systems remains an important field [4,5].

In this chapter we present examples of investigations of strongly correlated electron systems. By exploiting the different techniques at our beamlines we aim to contribute to the understanding of electronic, magnetic and dynamic properties of condensed matter.

References

- [1] R. Röhlsberger *et al.*, *Phys.Rev.Lett.* **89**, 237201 (2002).
- [2] D.L. Nagy *et al.*, *Phys.Rev.Lett.* **88**, 157202 (2002).
- [3] M. Krisch *et al.*, *Phys.Rev.Lett.* **89**, 125502 (2002).
- [4] C.A. Burns *et al.*, *Phys.Rev.Lett.* **89**, 236404 (2002).
- [5] T. Scopigno *et al.*, *Phys.Rev.Lett.* **89**, 255506 (2002).



Strongly-correlated Systems

Review by J.P. Sanchez (CEA-Grenoble, Département de Recherche Fondamentale sur la Matière Condensée, SPSMS, Grenoble, France)

Most of the properties of simple metals like copper (Cu) can be accounted for by models where the conduction electrons can wander freely through the sample. In some systems, however, one cannot ignore the Coulomb interaction between electrons and the effect of exchange on their motion. These interactions lead to correlations between particles. This is best exemplified either by *f*-electron systems called heavy fermions, where the interactions are so strong that the effective mass of the quasiparticles amounts to several orders of magnitude higher than that of the bare electron mass, or by a class of transition metal compounds, called Mott insulators, where the on-site Coulomb energy (the cost of putting two electrons on the same lattice site) is so huge that it localises the *d*-electrons on each lattice site leading to vanishing electrical conductivity. The study of these strongly-correlated electron systems (SCES) is the foremost area of research in contemporary condensed-matter physics. The challenge is double, the correlations can be very difficult to deal with theoretically and the experimental advances require extreme conditions (very low temperature, high pressure, and/or high magnetic field). The interplay and competition between spin, orbital, and charge order in these materials was shown to lead to a rich variety of behaviours. Besides the traditional branches of SCES such as the non-magnetic Kondo many body singlet, valence fluctuations or heavy fermions, new topics have emerged over the years [1]. Among them one may mention:

- the study of rare earth or actinide-based heavy fermion superconductors with focus on compounds where unconventional superconductivity coexists with magnetic order (e.g. UPt_3 , UPd_2Al_3 , ...).
- the tuning of the Kondo coupling through quantum-critical points (QCP) either by doping, application of pressure or external magnetic field with possible observation of non-Fermi liquid (NFL) behaviour and emergence of superconductivity when T_m (Néel or Curie temperature) goes to zero (e.g. CeIn_3 , UGe_2). It is worthwhile emphasising that the mechanisms which describe the QCP in rare earth or actinide compounds may control the physics over a much wider domain (e.g. the high temperature superconductors close to the optimal doping).
- the continuous interest in cuprate superconductors (high T_s , ruthenates like Sr_2RuO_4) or in "new" transition metal oxides such as the vanadates (NaV_2O_5) or the spin ladders ($\text{Sr}_{14}\text{Cu}_{24}\text{O}_{41}$).
- the organic metals which offer the possibility of tuning the transition between superconductors and

antiferromagnetic insulators by changing the ratio U/W between on site Coulomb correlation energy (U) and the bandwidth (W).

- the general class of manganites based on the perovskites parent compound LaMnO_3 , which, beside colossal magnetoresistance, exhibits a plethora of different behaviours (metal insulator transition, charge or orbital ordering associated with lattice distortions, ferromagnetism, etc.) by changing the chemical composition or by varying an external parameter such as pressure or magnetic field.

The selected highlights presented here are devoted to studies on a variety of compounds. Some have been intensively studied in the past and are now revisited such as YbInCu_4 and YbAgCu_4 – the mixed-valent heavy fermions, SmS – the so-called Kondo insulator, and the $\text{U}(\text{In}_{1-x}\text{Sn}_x)_3$ series. There is also one new subject, MgB_2 , which although known for a long time was only recently shown to be a new superconductor.

Mixed valence phenomena occurring in rare earth compounds attracted considerable attention in the seventies and early eighties [2]. Such effects arise when two *4f* shell configurations $4f^n$ and $4f^{n-1}$ have nearly degenerate energies or in other words when the *4f* levels are close to the Fermi energy. The ground state of a mixed-valence compound is a quantum mechanical mixture of two (or more) electronic configurations as explained phenomenologically by the valence fluctuation model (or theoretically by the one-impurity Anderson model) and shown experimentally by e.g. photoemission measurements (characteristic time 10^{-17} s) which present features due to both $4f^n$ and $4f^{n-1}$ configurations. The leading interaction in such systems is the Kondo temperature $T_K \propto \exp(-1/JN)$, where J is the exchange coupling (hybridisation strength) between the *4f* and the *5d* conduction electrons, N is the *4f* density of states at the Fermi level. The most elegant way to tune T_K is the application of pressure (P). T_K decreases (increases) with P for mixed valent Yb or Sm (Ce) compounds and drives the materials towards a trivalent (tetravalent) state. The rare earth valence is generally determined either from Vegards – law analysis of the lattice parameters or from magnetic susceptibility or spectroscopy methods. The latter techniques (e.g. photoemission, X-ray absorption) led in the past to controversial results owing either to their high surface sensitivity or to complex deconvolution of poorly-resolved spectra. Dallera *et al.* have overcome all these pitfalls by using resonant inelastic X-ray scattering (RIXS) which was proven to be a bulk-sensitive method to trace rare earth valency with unprecedented accuracy.

The interest of SmS started with the discovery that this compound undergoes a first order isostructural (NaCl -type) pressure-induced semiconductor (black phase) to metal (gold phase) transition at the incredibly

low pressure of 6.5 kbar and that the metallic state is mixed valent while the Sm ions in the black phase are divalent or nearly so. At the critical pressure $P_c \sim 6.5$ kbar the Sm 5d and 4f bands overlap as a result the 4f electrons spill into the 5d band leaving a $4f^5$ state. Nowadays it appears that the temperature-pressure phase diagram of SmS (Figure 57) is much more intricate, particularly concerning the nature of the golden phase. At low temperature (below T_Δ) and up to 20 kbar the high pressure SmS phase actually behaves like a semiconductor but with a small energy gap (several meV) often named hybridisation gap, Δ . Trivalent Sm ions are expected to be stabilised above 20 kbar in the metallic phase and band structure calculations predict the occurrence of a magnetic ground state at T_m although all attempts have failed to find magnetic order and thus a QCP. The valence transition at P_c also manifests itself in lattice dynamics, investigated in the past by neutron scattering in a restricted pressure range (up to 7 kbar) and extended to 80 kbar by Raymond *et al.* using inelastic X-ray scattering (IXS). These measurements enabled the characterisation of novel phonon anomalies in the longitudinal acoustic mode.

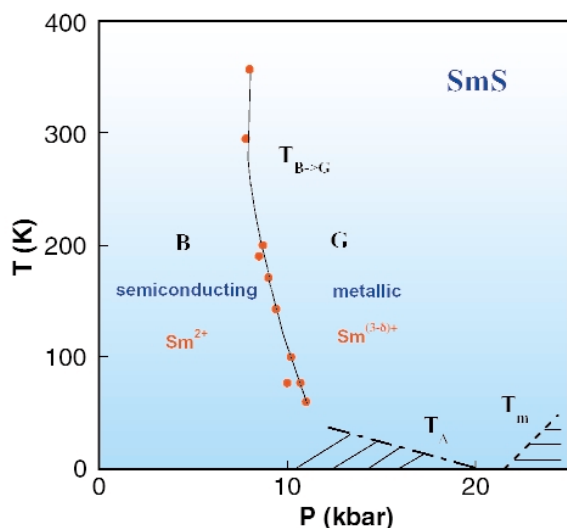


Fig. 57: (T, P) phase diagram of SmS showing the phase boundary between the black (B) and golden (G) phases. The lines T_Δ and T_m which represent, respectively, the crossover temperatures to a low temperature semiconducting phase and a magnetically-ordered state need still to be determined.

When the valence of the f -ion is an integer (or close to) and the corresponding total angular momentum of the ion is non-zero (*i.e.* the ion is "magnetic"), the ground state of the system is determined by a delicate balance between the Kondo effect, which screens the local f -moment towards a singlet state, and the Ruderman-Kittel-Kasuya-Yosida (RKKY) interaction ($T_{\text{RKKY}} \propto J^2$) responsible for the magnetic exchange coupling (Figure 58). For small J values, $T_{\text{RKKY}} \gg T_K$ and the compound can sustain magnetic order but with somewhat reduced magnetic moment. The most interesting situation occurs in the heavy fermion regime where the compound is near a magnetic

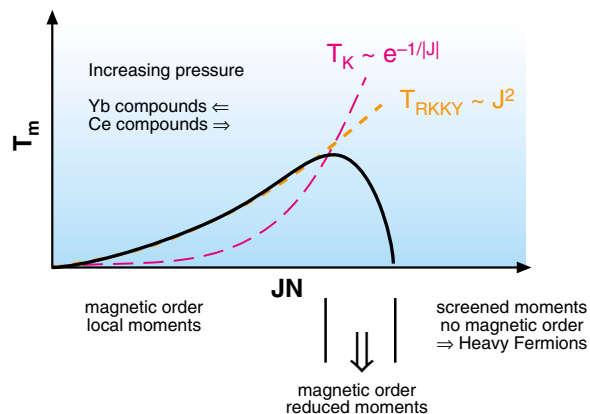


Fig. 58: Possible ground states resulting from the competition between the Kondo and RKKY interactions. T_m is the ordering temperature and JN is the f -d exchange coupling times the f density of states at the Fermi energy.

instability, *i.e.* close to the phase transition between magnetically ordered (MO) and non-magnetic (NM) ground states. In these systems the strong interaction between electrons leads to a very large effective mass of the quasiparticles (hence the term heavy fermion) and the large spin fluctuations which develop at the QCP can induce a breakdown of the conventional Fermi liquid (FL) theory (*e.g.* a linear T dependence of the electrical resistivity is found instead of the T^2 Fermi liquid dependence) and the onset of unconventional superconductivity at T_s . Such behaviour is exemplified in the (T , P) phase diagram (Figure 59) of the antiferromagnetic (AFM) CeIn_3 [3]. The MO to NM crossover in the $\text{U}(\text{In}_{1-x}\text{Sn}_x)_3$ series was observed at $x \sim 0.45$. The effect of pressure was investigated by Barla *et al.* using ^{119}Sn nuclear forward

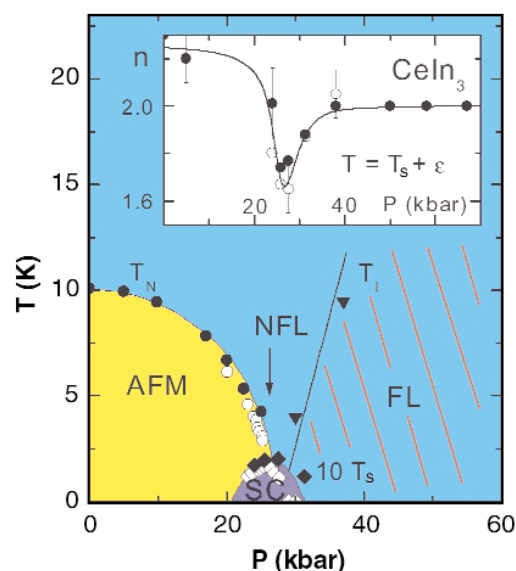


Fig. 59: (T, P) phase diagram of the antiferromagnet CeIn_3 . T_N and T_I are respectively the Néel temperature and the crossover temperature to the FL regime. The full symbols are CEA Grenoble data, the open ones the Cambridge results [3]. The inset shows the pressure variation of the exposant n derived from the low temperature fitting of the electrical resistivity, $\rho = \rho_0 + A_n T^n$. NFL behaviour ($n \neq 2$) is observed just at P_c .

scattering (NFS). They showed that $\text{U}(\text{In}_{0.8}\text{Sn}_{0.2})_3$ behaves as a nearly-localised system and concluded from the behaviour of $\text{U}(\text{In}_{0.6}\text{Sn}_{0.4})_3$ that the MO to NM transition is driven by the 5f-ligand hybridisation which delocalises the 5f electrons.

The superconductivity observed in heavy fermions is unconventional in the sense that the pairing mechanism of the Cooper pairs cannot be explained by the standard Bardeen-Cooper-Schrieffer (BCS) theory, which involves an attractive interaction between the electrons mediated by lattice vibrations. Nowadays it is generally accepted that the superconductivity in heavy fermions arises from magnetically-mediated pairing. Moreover, when the magnetic correlations are ferromagnetic (UGe_2 , URhGe [4]), pairing must result from electrons with parallel spin orientation (triplet superconductivity). The 39 K superconductivity discovered in MgB_2 seems to require a phonon mediated pairing mechanism [5]. This new superconductor differs in several important ways from ordinary metallic superconductors (e.g. the observation of two energy scales associated with the formation of charge carrying pairs, referred to as the superconducting gap; inconsistency between the value of T_s and the isotopic effect, etc.). The determination of the phonon dispersion and lifetimes in MgB_2 by Shukla *et al.* using inelastic X-ray scattering is an important step towards a better understanding of the fascinating properties of this new superconductor.

References

- [1] H. von Löhneysen, *Physica B* **281-282**, 1031 (2000).
- [2] P. Watcher, in *Handbook on the Physics and Chemistry of Rare Earths*, K.A. Gschneidner Jr., L. Eyring, G.H. Lander and G.R. Chopin (Eds), North Holland, Amsterdam, 177-382 (1994).
- [3] N.D. Mathur, F.M. Grosche, S.R. Julian, I.R. Walker, D.M. Freye, R.K.W. Haselwimmer and G.G. Lonzarich; *Nature* **294**, 39 (1998).
- [4] J. Flouquet, A. Buzdin, *Physics World* **15**, 41 (2002).
- [5] H.J. Choi, D. Roundy, H. Sun, M.L. Cohen, S.G. Louie, *Nature* **418**, 758 (2002).

Intermediate Valence and Kondo Energy-scale probed by Resonant Inelastic X-ray Scattering

Mixed valence arises in strongly-correlated solids from the conflict between the natural tendency of electrons to form extended bands, and the opposing tendency to

occupy atomic-like, localised states. This leads to spectacular physical properties including Kondo and heavy fermion behaviour as well as unconventional magnetism and superconductivity.

A typical manifestation of such many-body interactions in solids are small energy scales. In intermediate valence systems, like many cerium and ytterbium compounds, the characteristic scale is the energy separation between the hybrid singlet ground state and the first excited magnetic states, which defines the *Kondo temperature* T_K . Photoemission could directly probe the Kondo scale, but is severely limited by its surface sensitivity, and results are highly controversial. In contrast, resonant inelastic X-ray scattering (RIXS) in the hard X-ray energy range is a truly bulk probe of electronic states. Like other resonant core-hole spectroscopies it is also element-specific and sensitive to the electronic configuration. These advantages are clearly demonstrated by a RIXS study of the typical Kondo system YbAgCu_4 .

The principle of the measurement is summarised in **Figure 60**. The ground state $|\Psi_G\rangle$ of YbAgCu_4 is a coherent superposition of the Yb^{2+} ($4f^{14}$, $n_h = 0$) and Yb^{3+} ($4f^{13}$, $n_h = 1$) configurations. At $T = 0$, the estimated number of 4f holes is $n_h = 0.87$, and the valence is $v = (2 + n_h) = 2.87$, but excited magnetic states ($n_h = 1$) lying at an energy $\delta - k_B T_K$ above the ground state are thermally populated. As a consequence n_h , and the valence, vary with temperature as a characteristic function of T/T_K reflecting the existence of a Kondo scale [1]. Photon absorption at the Yb L_3 edge (8.95 keV) leads to intermediate states of mainly $2p^5 4f^{14} d^{n+1}$ and $2p^5 4f^{13} d^{n+1}$ character, separated by 7 eV by the strong 4f-core hole Coulomb interaction. These states can decay radiatively to the $L\alpha_1$ RIXS final states $3d^9 4f^{14} d^{n+1}$ ($2+$) and $3d^9 4f^{13} d^{n+1}$ ($3+$). At beamline **ID16**, we measured these decay channels for excitation energies varying through the Yb L_3 ($2p_{3/2}$) absorption edge. The emitted radiation was analysed by a Si (620) Rowland circle spectrometer.

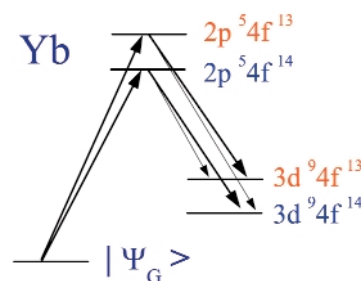


Fig. 60: Total energy level scheme for an Yb ion in YbAgCu_4 . The arrows indicate the relevant XAS and RIXS transitions.

Distinct 2+ and 3+ features are observed both in absorption (XAS) and RIXS spectra (**Figure 61**). They are resonantly and separately enhanced when the excitation energy $h\nu_{in}$ is swept through the Yb L_3 absorption edge. When the excitation energy is tuned to the 2+ XAS

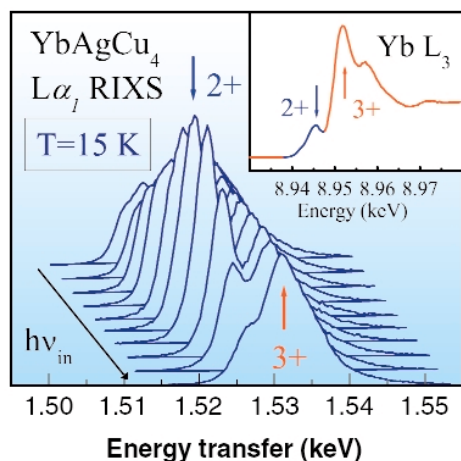


Fig. 61: RIXS spectra of YbAgCu_4 , excited along the Yb^{2+} feature of the XAS (inset). The 2+ feature is resonantly enhanced in the RIXS spectra.

feature, the signal from the minority Yb^{2+} configuration dominates the spectrum. We followed continuously the temperature evolution of this signal. Its intensity, proportional to $(1 - \langle n_h(T) \rangle)$, exhibits a 100% variation from 0.13 at 15 K to 0.065 at 300 K (Figure 62), revealing the existence of the underlying Kondo scale. The experimental curve is accurately reproduced by a calculation performed within the non-crossing approximation (NCA) for the Anderson Impurity Model (AIM). The fit yields a Kondo temperature $T_K = 70$ K, which agrees well with indirect estimates from magnetic and thermodynamic data. For comparison, we show in the same figure the results of an analogous RIXS measurement on the isoelectronic compound YbInCu_4 . This material exhibits a first-order valence transition (from 2.96 to 2.83) at $T_C = 42$ K, and therefore is not a typical Kondo system. As expected, the intensity of the 2+ signal suddenly drops at T_C .

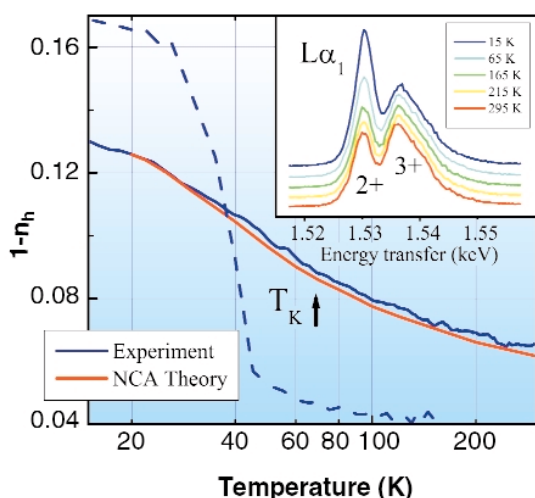


Fig. 62: Temperature dependence of the 2+ RIXS intensity in YbAgCu_4 , compared with an NCA calculation for $T_K = 70$ K. Selected spectra show the temperature dependence (inset). The case of YbInCu_4 (dashed line), which exhibits a valence transition at 42 K, is shown for comparison.

The correspondence between bulk-sensitive RIXS results and thermodynamic properties confirms that the AIM is applicable to spectroscopic properties. It is remarkable that spectral changes, which are controlled by the small Kondo energy scale (~ 6 meV), are readily observed by RIXS in spite of the much larger excitation energy (~ 9 keV) and energy resolution (~ 1 eV). RIXS appears to be an extremely interesting probe of electronic configuration and strong correlations, with possible extension to studies of the electronic properties of solids under extreme conditions of pressure and magnetic fields.

Reference

[1] N.E. Bickers *et al.*, *Phys. Rev. B* **36**, 2036 (1987).

Principal Publication and Authors

C. Dallera (a), M. Grioni (b), A. Shukla (c), G. Vankó (c), J. Sarrao (d), J.-P. Rueff (e), D.L. Cox (f), *Phys. Rev. Lett.* **88**, 196403 (2002).

(a) INFN - Politecnico di Milano (Italy)

(b) Ecole Polytechnique Fédérale de Lausanne (Switzerland)

(c) ESRF

(d) Los Alamos National Laboratory (USA)

(e) Université Pierre et Marie Curie, Paris (France)

(f) University of California, Davis (USA)

Magnetic Instability in $\text{U}(\text{In}_{1-x}\text{Sn}_x)_3$ under High Pressure

The variety of ground state properties of strongly correlated $5f$ electron systems, such as those of the family UX_3 (X being an element of the groups IIIA or IVA of the periodic table), are determined by a competition between the indirect exchange interaction between the localised $5f$ electrons and the conduction electrons and their strong hybridisation with the conduction electrons of the ligands. This is well demonstrated by the broad spectrum of magnetic properties of the compounds UX_3 . Within this family of compounds, the series $\text{U}(\text{In}_{1-x}\text{Sn}_x)_3$, crystallising in the cubic AuCu_3 structure, is particularly interesting because the substitution of Sn for In practically does not alter the unit cell volume, but determines the strength of the f -ligand hybridisation. The phase diagram of $\text{U}(\text{In}_{1-x}\text{Sn}_x)_3$ [1] shows that upon increasing the Sn concentration a transition occurs from long-range antiferromagnetic order ($0 \leq x \leq 0.45$) to a non-magnetic state ($x \geq 0.45$), in which the system exhibits heavy fermion behaviour.

In order to gain more information on the nature of $5f$ magnetism, the role of f -ligand hybridisation, as well as

the formation of the heavy fermion state, external pressure can be used, with the result of changing the unit cell volume without altering the electronic configuration of the ligand. We have therefore performed high-pressure experiments using ^{119}Sn nuclear forward scattering (NFS) of synchrotron radiation in a diamond anvil cell. Using such a technique the effect of pressure on the magnetic properties of the system can be investigated through the transferred magnetic hyperfine field (B_{thf}) at the ^{119}Sn nuclei, which is determined by the magnitude of the U 5f moment, ordering temperature and the spin structure of the system.

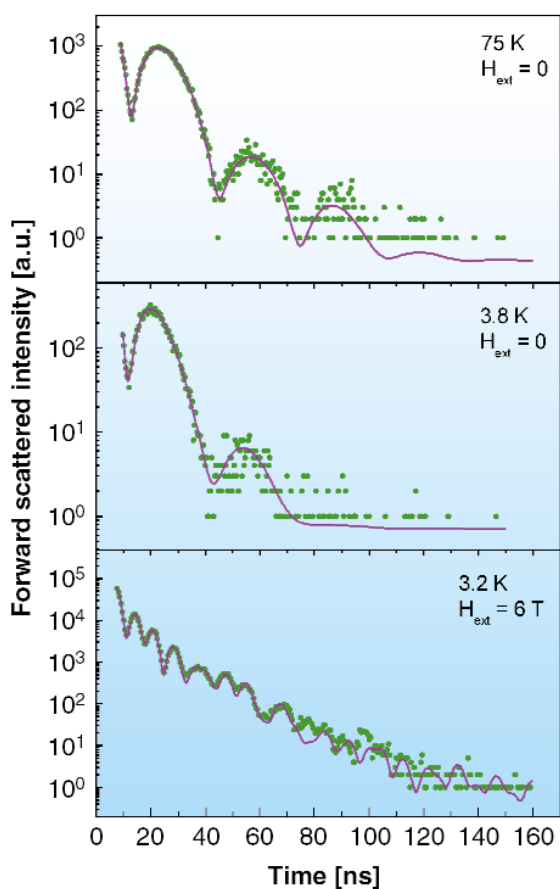


Fig. 63: Measured NFS spectra of $\text{U}(\text{In}_{0.6}\text{Sn}_{0.4})_3$ at 25 GPa (dots) and corresponding fits (lines) in the paramagnetic (75 K) and in the antiferromagnetic phase (3.8 and 3.2 K), with and without an externally-applied magnetic field.

The measurements were performed at beamline **ID18** in the 16-bunch mode of operation of the storage ring. **Figure 63** shows typical NFS spectra. **Figure 64** shows the volume dependence of B_{thf} (at $T \leq 5.6$ K) and the Néel temperature T_N for the two compounds with $x = 0.2$ and 0.4 . For $x = 0.2$, B_{thf} shows almost no dependence on pressure up to 15 GPa while T_N shows a monotonic increase with pressure. Whereas when $x = 0.4$, B_{thf} decreases monotonically with increasing pressure and reaches its lowest value, corresponding to a U 5f moment of $\leq 0.1 \mu_B$, at 25 GPa, while T_N first increases

with pressure, reaches a maximum at $P \approx 14$ GPa and then starts decreasing for $P > 14$ GPa.

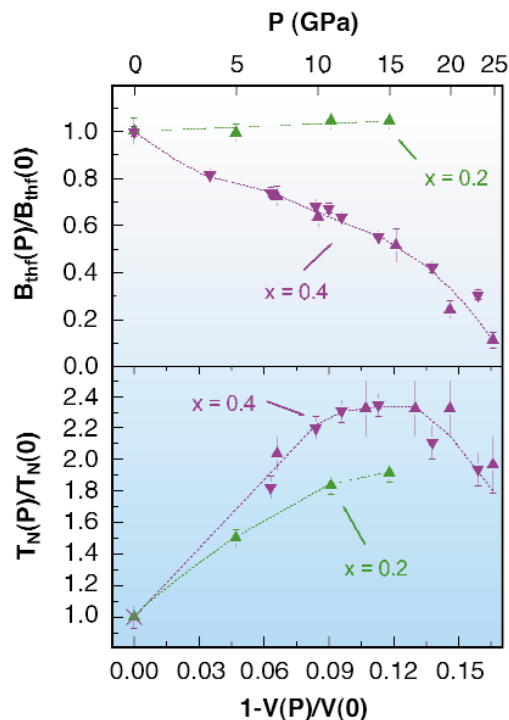


Fig. 64: Volume dependence of the transferred magnetic hyperfine field (B_{thf}) and of the Néel temperature (T_N) for $x = 0.2$ and 0.4 . The lines are guides for the eye.

The results of our measurements can be interpreted in terms of the model developed by Sheng and Cooper [2]. The increase of the hybridisation between the 5f electrons and the band states, as a result of the decrease of the interatomic distance caused by pressure, leads to the reduction of the local moment on the one hand and to the enhancement of the exchange coupling (i.e. of the magnetic order via the RKKY interaction) on the other. The pressure dependences of B_{thf} and T_N are therefore determined by the change of the relative strength of these two effects with pressure. In the case of $\text{U}(\text{In}_{0.8}\text{Sn}_{0.2})_3$, the very weak dependence of B_{thf} on pressure and the increase of T_N with pressure suggest that the moment is nearly localised. On the contrary, the monotonic decrease of B_{thf} with pressure and the decrease of T_N above 14 GPa in $\text{U}(\text{In}_{0.6}\text{Sn}_{0.4})_3$ indicate that here the U magnetic moment is strongly delocalised. Measurements at 25 GPa and 3.2 K in applied fields of up to 6 T show the presence of a large induced magnetic hyperfine field at the ^{119}Sn nuclei in $\text{U}(\text{In}_{0.6}\text{Sn}_{0.4})_3$. This clearly points towards the presence of large dynamical spin correlations in the high-pressure state of this compound.

References

- [1] L.W. Zhou, C.L. Lin, J.E. Crow, S. Bloom, R.P. Guertin, S. Foner, *Phys. Rev. B* **34**, 483 (1986).
- [2] Q.G. Sheng, B.R. Cooper, *J. Appl. Phys.* **75**, 7035 (1995).

Principal Publication and Authors

A. Barla (a), J.P. Sanchez (b), B. Ni (c), B.P. Doyle (a), P. Vulliet (b), O. Leupold (a), R. Ruffer (a), D. Kaczorowski (d), J. Plessel (c) and M.M. Abd-Elmeguid (c), *Phys. Rev. B* **66**, 094425 (2002).

(a) ESRF

(b) Département de Recherche Fondamentale sur la Matière Condensée, CEA-Grenoble (France)

(c) II. Physikalisches Institut, Universität zu Köln, Cologne (Germany)

(d) W. Trzebiatowski Institute for Low Temperature and Structure Research, Polish Academy of Sciences, Wrocław (Poland)

Phonon Anomalies at the Valence Transition of SmS: An Inelastic X-ray Scattering Study Under Pressure

The interplay between charge, lattice and magnetic degrees of freedom is at the heart of modern condensed matter research. Pressure is a unique tool to tune the different couplings between these quantities. The recent advances in research on pressure-induced superconductivity near a quantum critical point stresses the significance of the role of spin fluctuations [1]. Here we are going to concentrate on the role of charge fluctuations, about which very little is actually known. For this we have reinvestigated intermediate-valence compounds where these fluctuations are at their strongest, in particular the case of SmS. At ambient pressure, SmS is a semiconductor with a divalent Sm^{2+} ionic configuration (black phase). It undergoes a first order isostructural phase transition to a metallic phase (gold phase) at 0.65 GPa. In this phase, the Sm ion has an intermediate valence achieved by promoting a $4f$ electron into the conduction band, schematically written: $\text{Sm}^{2+} \leftrightarrow \text{Sm}^{3+} + 5d$. This leads to a volume reduction of 15% at the transition, and to strong anomalies in the phonon spectrum. These anomalies are reported by inelastic neutron scattering (INS) studies performed under pressure [2].

The combination of the diamond anvil cell (DAC) technique and inelastic X-ray scattering (IXS) permitted us to extend the previous INS study to much higher pressure while keeping good crystal quality. The IXS measurements were carried out on a single crystal platelet of SmS placed in a DAC on the beamline **ID28** using the constant final energy 17.794 keV (given an energy resolution of 3 meV). The spectra measured on

both sides of the valence transition at $P = 0.1$ and 0.9 GPa at the [111] zone boundary (ZB) are shown in **Figure 65**.

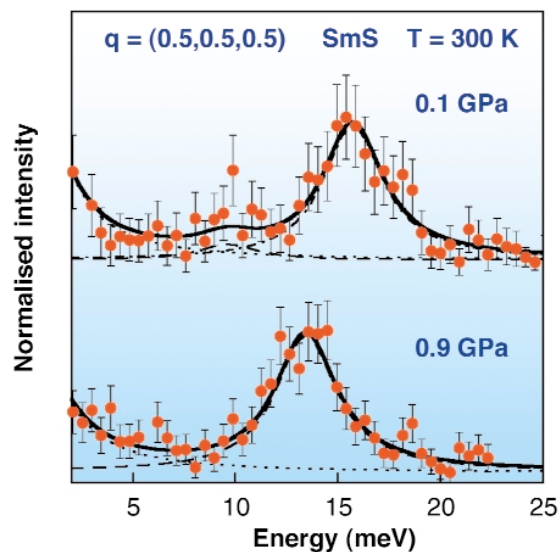


Fig. 65: IXS phonon spectra of SmS measured at $q = (0.5, 0.5, 0.5)$ at $P = 0.1$ and 0.9 GPa. The lines are fits to the data. The dotted line corresponds to the central diffuse peak, the dot-dashed line to the transvers acoustic modes and the dashed one to the longitudinal acoustic (LA) modes.

A clear softening of the mode is observed from 15.7 to 13.4 meV. The overall dispersion curves of the LA [111] modes as a function of pressure are shown in **Figure 66**.

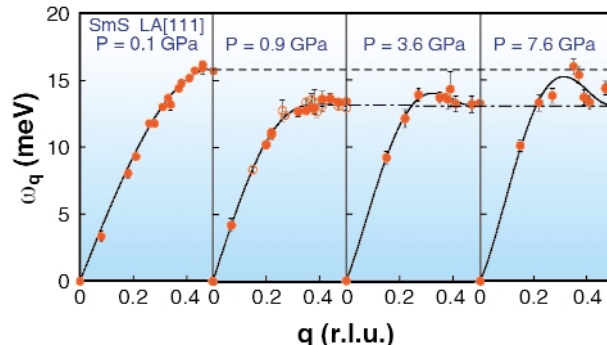


Fig. 66: Dispersion relation of the LA [111] branch of SmS for several pressures.

A softening of the LA [111] mode from halfway and up to the ZB is observed when entering the metallic phase. The anomalous phonon softening effects observed are attributed to the electron-phonon interaction occurring at the valence transition of SmS: the conversion of the $4f$ electron into the conduction band induces a breathing of the Sm atom that couples resonantly to lattice vibrations. Our IXS study also shows that the ZB LA [111] phonon energy does not evolve further up to 7.6 GPa while a gradual hardening of the low and intermediate q modes occurs in parallel. The fact that the ZB value does not follow the hardening expected when pressure increases is probably linked to an increasing density of states (DOS) at the Fermi level at high pressure in parallel to (or in cooperation with) the change of valence. In this respect, the phonon spectra of SmS at 7.6 GPa is

qualitatively similar to the one of the isostructural superconducting compound YS, where a high DOS of d electrons at the Fermi level produces a phonon softening at the ZB. It is well known from the strong coupling theory of superconductivity that soft phonon modes and high electronic DOS at the Fermi level favours superconductivity.

Future studies aimed at finding pressure-induced superconductivity in SmS are encouraged by our results: the large phonon anomalies persist up to high pressure where the Sm has reached its trivalent state (Sm^{3+}). In view of recent works on pressure-induced superconductivity, this superconducting phase may also appear cooperatively or in competition with a pressure-induced magnetically-ordered phase.

References

- [1] N.D. Mathur *et al.*, *Nature* **294**, 39 (1998).
- [2] H.A. Mook, D.B. McWhan and F. Holtzberg, *Phys. Rev. B* **25**, 4321 (1982).

Principal Publication and Authors

S. Raymond (a), J.P. Rueff (b), M. D'Astuto (c), D. Braithwaite (a), M. Krisch (c), J. Flouquet (a), *Phys. Rev. B* **66**, 220301(R) (2002).

(a) *Département de Recherche Fondamentale sur la Matière Condensée, CEA-Grenoble (France)*

(b) *Laboratoire de Chimie-Physique, CNRS, Paris (France)*

(c) *ESRF*

Phonon Dispersion in the New Superconductor MgB_2

The discovery of 39 K superconductivity in MgB_2 [1] has led to in-depth study of the material and a picture has emerged of a phonon-mediated superconductor described by conventional theory, in contrast to high-temperature superconductors. The unusually high transition temperature mainly finds a justification in the high energy vibrational modes of the light B atoms. Additional peculiarities of this material, such as strong electron-phonon coupling (EPC) and anharmonicity, have been noted by various authors. Measurement of phonon dispersion and the evolution of phonon lifetimes over the Brillouin Zone (BZ) would shed more light on these aspects but has been impeded by the absence of large single crystals. This problem was circumvented by the use of inelastic X-ray scattering of a focused and intense X-ray beam at ID28. This technique is now routinely used in small ($\sim 100 \mu\text{m}$) single crystalline samples and is well adapted for the measurement of high-energy optical

modes. In this work we present the first measured phonon dispersion curves and linewidths in MgB_2 along three major directions in the BZ, Γ -A, Γ -M and A-L and at a temperature of 300K. We also calculate phonon dispersion and the contributions of EPC and anharmonicity to the linewidth using Density Functional Theory in the generalised gradient approximation.

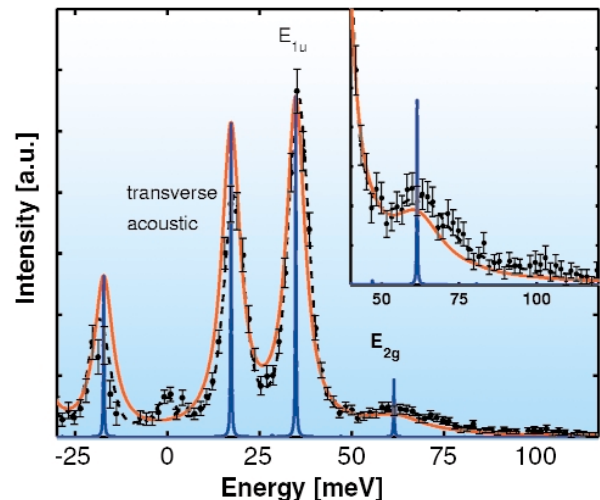


Fig. 67: Energy loss scan in almost transverse geometry measured at 0.6 Γ -A. The data (dots), normalised to the incident flux, are shown with the least-squares fit (dashed black line) and the calculated spectrum with (red line) and without (blue line) the broadening due to experiment and electron-phonon coupling. The broad peak corresponding to the damped E_{2g} mode is shown in greater detail in the inset.

Figure 67 shows the energy loss scan at 0.6 Γ -A. The acoustic mode as well as the lower energy E_{1u} optical mode are visible as resolution-limited (6.1 meV FWHM) peaks. Most importantly, a broad peak is observed at higher energy loss, corresponding to the E_{2g} optical mode in which the B atoms vibrate in-plane in opposite directions while the Mg atoms are stationary. By measuring similar energy loss scans over three directions in the BZ and extracting the linewidth of the E_{2g} mode where possible, we map the phonon dispersion of all modes and the E_{2g} linewidth variation shown in **Figure 68**. Also shown is the theoretical dispersion. Calculated structure factors and energies show excellent quantitative agreement with our measured data. The measured as well as calculated linewidth of the E_{2g} branch, shown in the top panel of **Figure 68**, is strongly anisotropic in the BZ. Along Γ -A it is particularly large signifying short lifetimes or heavy damping. In the other directions the linewidth is more difficult to extract due to unfavourable structure factor or overlap with other modes. However, we could determine that near the M and L points it is below the experimental resolution, *i.e.* at least 5 times smaller than along Γ -A. This is also borne out by calculations which further attribute the damping almost exclusively to EPC (the contribution shown in **Figure 68**) since the anharmonic contribution is much smaller.

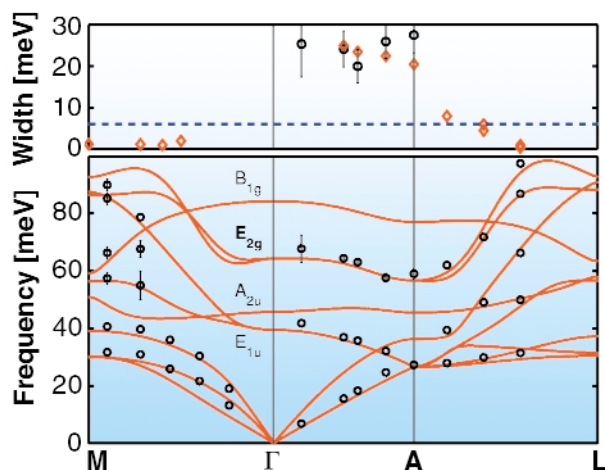


Fig. 68: (Bottom) Experimental (circles) and theoretical phonon dispersion (red line). The optical modes are labelled according to the symmetry at the Γ point. (Top) Linewidth of the E_{2g} mode. The experimental linewidth (circles) is large along Γ -A and below the experimental resolution (dashed blue line) near the M and L points. The theoretical result (red diamonds) for the electron-phonon coupling contribution to the linewidth is also shown.

In conclusion we have shown that the E_{2g} optical mode is strongly damped in certain regions of the Brillouin Zone in MgB_2 . Calculations attribute this behaviour exclusively to electron-phonon coupling as a consequence of Fermi surface nesting. In MgB_2 this points to the possibility of directly determining the contribution of this mode to electron-phonon coupling from the measured linewidth.

Reference

[1] J. Nagamatsu, N. Nakagawa, T. Muranaka, Y. Zenitani, and J. Akimitsu, *Nature* **410**, 63 (2001).

Principal publication and Authors

A. Shukla (a), M. Calandra (a), M. d'Astuto (b), M. Lazzeri (a), F. Mauri (a), C. Bellin (a), M. Krisch (b), J. Karpinski (c), S.M. Kazakov (c), J. Jun (c), D. Daghero (d), and K. Parlinski (e), *Phys. Rev. Lett. (cond-mat/0209064)*, accepted (2003).

(a) LMCP, Université Pierre et Marie Curie, Paris (France)

(b) ESRF

(c) Solid state Physics Laboratory, ETH, Zürich (Switzerland)

(d) INFM-Dipartimento di Fisica, Politecnico di Torino (Italy)

(e) Institute of Nuclear Physics, Cracow (Poland)

Nano-structured Material

Nano-structured materials become more and more important in various fields such as nano-electronics, magnetic storage technology, etc. On such a length scale properties might change compared to bulk properties. These might become beneficial for new applications. As an example, investigations on the magnetic properties of nano-structured material (about half a monolayer of 2 nm iron islands on a tungsten substrate) have been carried out. The results show that the magnetic properties are highly temperature dependent and have an unexpected perpendicular spin alignment with respect to the surface [1]. In another example the vibrational dynamics of pure nano-crystalline iron has been investigated. These results are presented hereafter.

Reference

[1] R. Röhlisberger *et al.*, *Phys. Rev. Lett.* **86**, 5597 (2001).

Scale Effects on the Vibrational Properties of Nanocrystalline Iron

The investigation of vibrational dynamics in low-dimensional and nanostructured solids is a rapidly growing research field, powered by the interest in thermodynamic, conductive, and optical properties of mesoscopic systems [1]. A wealth of novel phenomena, such as phonon folding, phonon confinement, and vibrational interface states have been revealed in the last few years. A key role in this respect is played by the vibrational density of states (VDOS), $g(E)$. In the VDOS of nanocrystalline (NC) materials, *i.e.*, polycrystals with an ultrafine grain size d , both finite-size effects and interface-related phenomena due to the large fraction of disordered interfaces are expected. In particular, two basic questions are extremely relevant: (i) how does the VDOS scale with d , and (ii) is there a deviation from the usual Debye law $g(E) = aE^2$ at low energies?

Nuclear inelastic scattering (NIS) of synchrotron radiation was applied to the determination of the VDOS in NC iron samples with different grain size, prepared by inert gas condensation. The oxidation degree of the samples (1-X) is defined as the atomic fraction of oxidised Fe atoms,

obtained from X-ray diffraction and Mössbauer spectroscopy. NIS experiments were carried out on **ID18**, tuning the incident radiation in the ± 90 meV range around the transition energy of ^{57}Fe (14.412 keV). A final bandwidth of 0.6 meV was achieved using a high-resolution monochromator, consisting of two (975) Si crystals in a dispersive (+,+) energy setting.

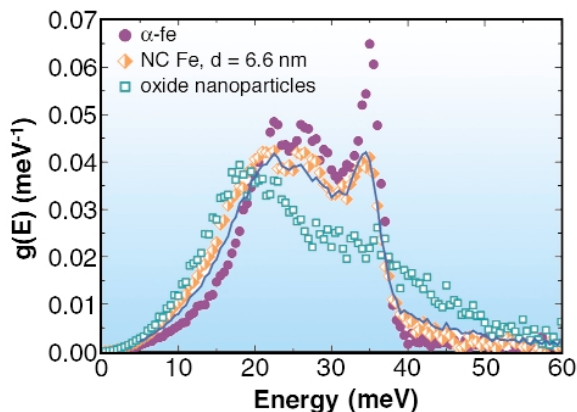


Fig. 69: VDOS of NC iron ($d = 6.6$ nm), iron oxide nanoparticles, and reference $\alpha\text{-Fe}$. Solid line: linear combination $Xg_{\alpha\text{-Fe}} + (1-X)g_{\text{oxide}}$ after convoluting $g_{\alpha\text{-Fe}}$ with a 1.1 meV FWHM Lorentzian in order to represent phonon damping.

In the NC samples, in comparison with a reference $\alpha\text{-Fe}$ foil, an enhanced population of low-energy modes and a broadening of the longitudinal peak at about 36 meV were observed (**Figure 69**). This softening can be explained only partially by oxidation of the grain interfaces: a linear combination $Xg_{\alpha\text{-Fe}} + (1-X)g_{\text{oxide}}$ does not fully account for the low-energy intensity. Here g_{oxide} is the VDOS measured for totally oxidised nanoparticles. The remaining excess modes are most likely ascribable to vibrations of atoms at the grain interfaces, with modified local environment and softened force constants. Most notably, the low-energy VDOS exhibits a $g(E) = aE^2$ dependence over the whole range 1.5–15 meV for all measured samples (**Figure 70a**), and the coefficient a increases with decreasing d (**Figure 70b**).

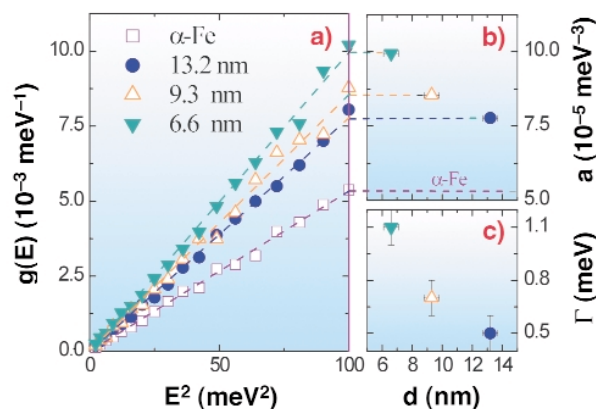


Fig. 70: (a) low-energy VDOS vs. energy square of NC samples with different grain size. Dashed lines: best fits according to $g(E) = aE^2$; (b)-(c) coefficient a and damping parameter Γ vs. grain size, respectively.

Turning now to the broadening, we attribute it to the damping of phonons due to confinement in nanocrystals. A damping parameter Γ was determined by first convoluting the experimental $\alpha\text{-Fe}$ VDOS with a Lorentzian (with $\text{FWHM} = \Gamma$) and then fitting the longitudinal peak of the NC VDOS through the aforementioned linear combination (solid line in **Figure 69**). The d -dependence of the parameter Γ (**Figure 70c**), indicates that phonon lifetime $\tau \approx 2\hbar/\Gamma$ and mean free path $\lambda \approx v\tau$ (with v the phonon velocity) decrease with decreasing grain size. Assuming a reasonable value of $v \approx 2500$ m/s, a mean free path $\lambda \approx 3$ nm is estimated for the sample with $d = 6.6$ nm.

In conclusion, a d -dependent VDOS softening was revealed, and the Debye-like character of the soft modes was clearly demonstrated. This finding should clarify controversies recently emerged in the literature [2]. In addition, phonon confinement in nano-sized grains was observed, the damping parameter being correlated and consistent with the grain size. Both achievements were only possible thanks to the high-energy resolution of the experimental setup, which allowed us to investigate the VDOS at very low energies and to measure broadening features in the meV energy range.

References

- [1] M.A. Strocio, M. Dutta, *Phonons in Nanostructures*, Cambridge University Press, Cambridge, England, (2001).
- [2] A. Kara, T.S. Raman, *Phys. Rev. Lett.* **81**, 1453 (1998).

Principal Publication and Authors

L. Pasquini (a), A. Barla (b), A.I. Chumakov (b), O. Leupold (b), R. Rüffer (b), A. Deriu (c), E. Bonetti (a), *Phys. Rev. B* **66**, 073410 (2002).
 (a) Department of Physics, University of Bologna and INFM (Italy)
 (b) ESRF
 (c) Department of Physics, University of Parma and INFM (Italy)

New Techniques and Applications

Besides technical developments, methodological developments are also ranked highly. Examples are the nuclear lighthouse effect [1], 'K β ' spectroscopy, deep inelastic scattering and synchrotron radiation based perturbed angular correlation (SRPAC) spectroscopy. The latter three techniques will be presented and discussed in the following contributions.

Reference

[1] R. Röhlberger *et al.*, *Phys. Rev. Lett.* **87**, 47601 (2001).

Molecular Spin Transitions Studied with X-ray Emission Spectroscopy (XES)

Making use of isolated molecules in electronic devices is expected to bring major advances to information technology. Photoswitchable molecular magnets, for example, have potential applications in data storage and display devices. The most promising candidates are the so-called spin transition complexes, which are coordinate compounds of transition metal ions with medium ligand-field strength and an electronic configuration between d^4 and d^7 . In these systems, the spin state of the molecules can be switched back and forth between the low spin (LS) and the high spin (HS) states by triggering a redistribution of the $3d$ electrons on the t_{2g} and e_g orbitals with external perturbations such as variation in the temperature or pressure, as well as irradiation with light [1].

Recent research work on these materials is concerned with systems containing two or more different metal sites and their behaviour under extreme conditions like high pressure. With such experiments, new challenges are to be faced due to the possible presence of different metal ions and sample environments with limited access to standard techniques. Therefore, the field would certainly profit from element-sensitive spectroscopic probes of the local (atomic) magnetism and the electronic state, which make use of penetrating radiation. We have studied spin transition complexes of Fe^{3+} , Fe^{2+} and Co^{2+} (well below and above their transition temperatures) on ID26 to demonstrate that techniques based on X-rays emitted after $1s$ core ionisation of the metal ions [2] have these attributes.

The studied compounds, which cover almost the entire d^4 to d^7 range, have unambiguous spin states and

show diverse spin transitions. These thermally-induced transitions were found to affect all features of the X-ray emission spectra; nevertheless, the largest variations were observed on the K β lineshapes, which arise from the $3p$ to $1s$ transition. In Figure 71 we show that the intensity of the satellite peak on the low energy side of the main line follows the variations in the spin state of the molecule. In fact, the satellite intensity is related to the local magnetic moment on the $3d$ orbitals, through the exchange interaction of the latter and the $3p$ core hole of the final state. Theoretical calculations were also made, and the calculated lineshapes were in agreement with the experimental data. The K β spectra reflect the variation of the spin states of different transition metal ions of well-defined $3d$ configurations with preserved chemical environment and valence state. They can be regarded as benchmark measurements in studying magnetism with XES.

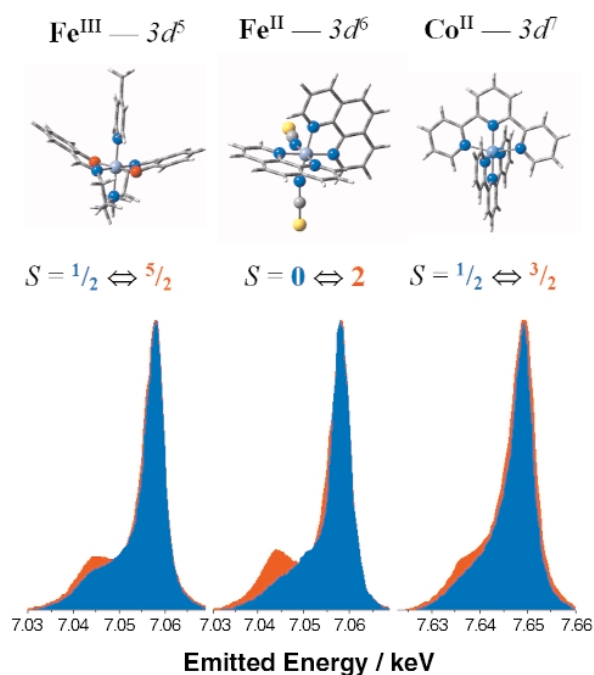


Fig. 71: Electronic configuration, structure, spin states and K β spectra of the studied complexes. The intensity of each spectra is normalised to its maximum. The peaks are shifted for better comparison. (Colour code for the spectra: blue — LS, red — HS).

As the rearrangement of the electrons at the spin transition affects the electronic structure and the molecular geometry, X-ray absorption spectroscopy (XAS) can also be used to follow the transition. However, better separation of XAS spectral features can be achieved by selective detection of emitted X-rays using a high-resolution spectrometer with the analyser energy fixed to a maximum of the emission spectra. We applied this detection technique, called partial fluorescence yield (PFY) with the analyser energy fixed to the K α_1 emission line, to record the X-ray absorption near edge structure (XANES) spectra for the different spin states. In the case of Fe^{2+} the variations of the molecular geometry are dramatic and completely alter the X-ray absorption

spectra (Figure 72a). On the other hand, the Co^{2+} compound is known for having the smallest changes in the bond length among all spin transition molecules. Accordingly, the PFY-XANES spectra show relatively small changes as displayed in Figure 72b. However, the variation of the pre-edge structure, where contributions from $1s$ to $3d$ quadrupolar transitions are expected, is remarkable due to the differences of the electronic distribution on the $3d$ orbitals.

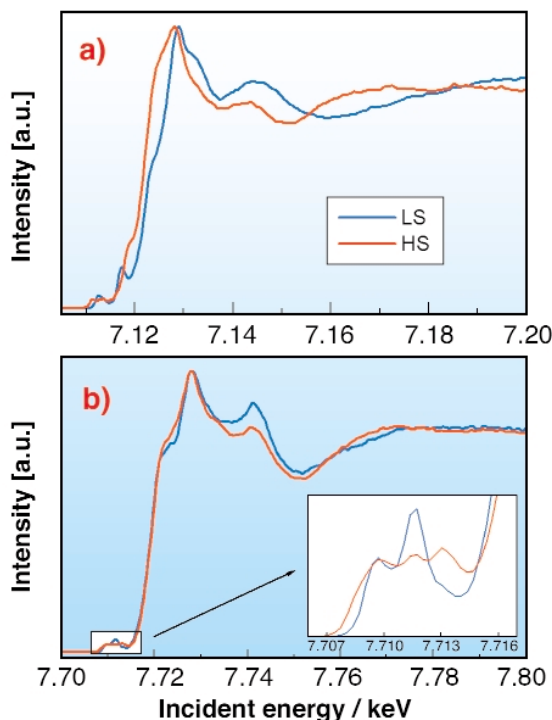


Fig. 72: Partial fluorescence yield XANES spectra (taken on the $K\alpha_1$ emission line) of a) the $[\text{Fe}(\text{phen})_2(\text{SCN})_2]$ and b) the $[\text{Co}(\text{terpy})_2]^{2+}$ complexes. The inset shows the pre-edge region.

Furthermore, in the transition regime both the $K\beta$ and the pre-edges of the PFY-XANES spectra were shown to be superpositions of the HS and LS states. This allows convenient determination of the HS fraction and thus the monitoring of the spin transition by either technique. This work should stimulate the use of XES and PFY-XANES in numerous chemical studies, particularly in the field of molecular magnetism.

References

- [1] P. Gütllich, A. Hauser, H. Spiering, *Angew. Chem. Int. Ed. Engl.* **33**, 2024–2054 (1994), and references therein.
- [2] F.M.F. de Groot, *Chem. Rev.* **101**, 1779–1808 (2001), and references therein.

Authors

- G. Vankó (a), T. Neisius (a), F. Renz (b), S. Kárpáti (c), A. Shukla (d), A. Mirone (a), F. de Groot (e).
 (a) ESRF
 (b) Gutenberg Univ., Mainz (Germany)
 (c) Eötvös Loránd Univ. Budapest (Hungary)
 (d) LMCP, Univ. Pierre et Marie Curie, Paris (France)
 (e) Utrecht University, Utrecht (The Netherlands)

Deep Inelastic Atomic Scattering of X-rays in Liquid Neon

Deep inelastic scattering experiments are used in many research areas of physics and are based on the following argument. If the energy, E , and the momentum, q , which are transferred in a scattering experiment from the probe particle to the target particle are very high compared to the characteristic energy and momentum of the target particle, the latter can be considered to recoil freely from the collision, and the scattered probe particle carries information on the initial momentum distribution of the target particles. If the probe is an X-ray beam, the natural deep inelastic scattering regime is the usual Compton limit where the electronic momentum distribution is experimentally accessed. The low energy part of the spectrum of the scattered X-rays reflects - via the adiabatic approximation - the atomic dynamics. The question to be addressed here is whether it is possible to select an appropriate energy and momentum transfer range where the scattering of X-rays can also be used to obtain information on the atomic momentum distribution, which to date was only accessed in high- q neutron scattering experiments.

The experiment has been carried out at beamline **ID16** using the vertical arm spectrometer for the scattered energy analysis with an instrumental energy resolution of 6.9 meV (FWHM). Inelastic X-ray scattering spectra of liquid Neon were collected for several q values between 1.0 and 16.0 \AA^{-1} . The sample was kept at a temperature of 27.6 ± 0.1 K and at a pressure of 1.4 ± 0.2 bar. The spectral intensities (Figure 73) appear as structureless peaks that, with increasing q , shift towards higher energies and broaden. On approaching the impulse

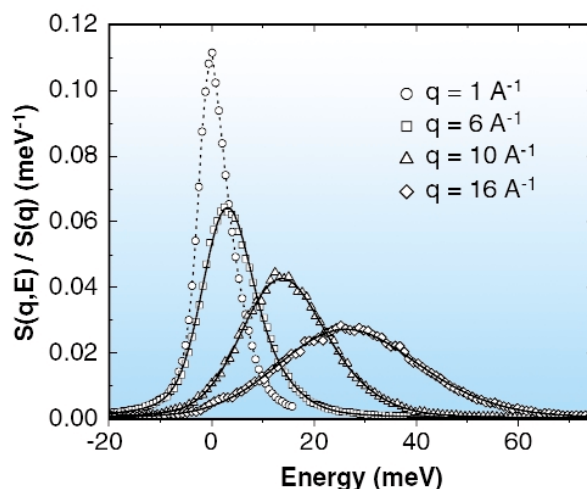


Fig. 73: Normalised spectral intensities of liquid neon at selected values of the exchanged momentum, q . The full lines correspond to the additive approach model of Ref. [1]; the dashed line superimposed on the $q = 1 \text{ \AA}^{-1}$ spectrum is a guide for the eye.

approximation regime, the dynamic structure factor $S(q,E)$ (proportional to the inelastic X-ray scattering cross-section) is expected to shift in energy as q^2 and to broaden as q . The spectra in Figure 73 do present such behaviour, and this shows that the impulse approximation regime is being reached. Clearly, the impulse approximation regime found here corresponds to the scattering of the X-rays from the neon core electrons with an effective mass given by the atomic mass.

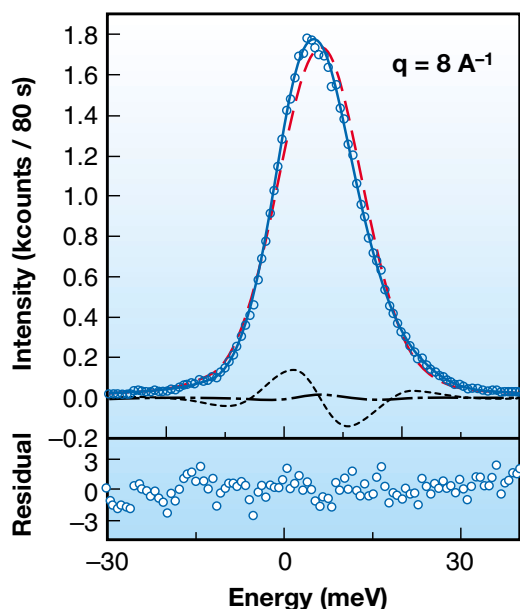


Fig. 74: Upper part: the spectrum of liquid neon at $q = 8 \text{ \AA}^{-1}$ is reported together with the best fit of the model of Ref. [1] to the data (full line). Here, the model line is the sum of three contributions: a dominant Gaussian contribution (dashed red line) and two correction terms (dashed and dotted-dashed black lines). Bottom part: Residuals of the fit, in standard deviation units.

For a quantitative description of the spectra, the so-called additive approach model [1] has been followed here, which amounts in approximating the dynamic structure factor as the sum of a dominant Gaussian contribution to describe the momentum distribution plus corrective terms to describe the final state effects. These latter effects are due to the fact that the impulse approximation is reached only asymptotically: the struck atom cannot be considered to recoil completely freely from the collision, and the effects coming from the interaction of the struck atom with the neighbouring atoms have to be taken into account. On adjusting this model to the experimental data (Figure 73 and Figure 74) it is possible to determine quantities as the mean atomic kinetic energy which, for this moderately quantum liquid, comes out to be $E_k = 51 \pm 3 \text{ K}$, in agreement with neutron scattering determinations [2]. This shows that deep inelastic atomic scattering of X-rays is indeed achievable, which might be of particular interest in cases as that of ^3He , a system of broad interest but irksome for neutron scattering due to its large absorption.

References

- [1] H.R. Glyde, *Phys. Rev. B* **50**, 6726-6742 (1994).
- [2] R.T. Azuah, W.G. Stirling, H.R. Glyde, P.E. Sokol, S.M. Bennington, *Phys. Rev. B* **51**, 605-608 (1995).

Principal Publication and Authors

G. Monaco (a), A. Cunsolo (b), G. Pratesi (c), F. Sette (a), R. Verbeni (a), *Phys. Rev. Lett.* **88**, 227401 (2002).

(a) ESRF

(b) Università di Roma Tre, Rome (Italy)

(c) Università di Firenze, Florence (Italy)

Synchrotron Radiation-based Perturbed Angular Correlation

Research based on nuclear resonant scattering of synchrotron radiation (SR) has increased greatly in the last few years. The intense, spatially-coherent channel of Nuclear Forward Scattering (NFS) has been used to determine static and dynamic hyperfine interactions as well as slow and fast spatial dynamics of Mössbauer atoms in the solid state. The spatially-incoherent channel of Nuclear Inelastic Scattering (NIS) has been employed to measure the partial densities of phonons coupling to the Mössbauer atoms in soft and hard condensed matter. Both methods excel when applied to small samples under extreme conditions given e.g. by combinations of high pressure, low temperature, strong magnetic fields, etc. With increasing intensity of the beamlines a third method, SR-based Perturbed Angular Correlation (SRPAC), pioneered at ESRF six years ago [1], has now become accessible for applications in soft matter. The techniques described above are compared in Figure 75.

SRPAC is basically a scattering variant of Time-Differential Perturbed Angular Correlation (TDPAC), a method well known in nuclear solid state physics (see e.g. [2]). In SRPAC the intermediate nuclear level is not excited from above via a cascade originating from the decay of a radioactive parent like in TDPAC, but from below, i.e. from the groundstate, during spatially incoherent, single-nucleus resonant scattering of SR. This scattering channel avoids, in contrast to TDPAC, any chemical or electronic after-effects. Directional selection and timing by the first detector in TDPAC are replaced in SRPAC by the direction and the timing of the incident SR flash. In both methods the interference of indistinguishable paths via an intermediate nuclear level split by magnetic dipole and/or electric quadrupole interaction allows one to investigate hyperfine interactions and rotational dynamics of the nuclear probes.

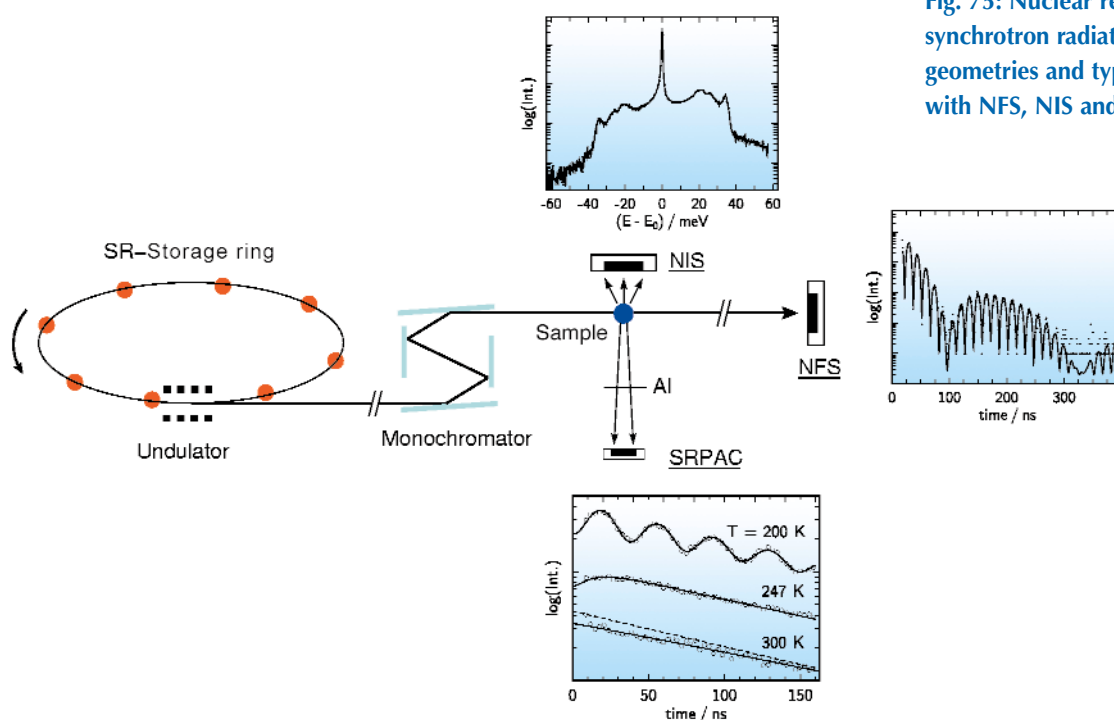


Fig. 75: Nuclear resonant scattering of synchrotron radiation: Scattering geometries and typical measurements with NFS, NIS and SRPAC.

The lower panel in Figure 75 shows an example, where SRPAC has recently been applied at beamline ID18 to study the rotational dynamics of the molecular glass former 5%ferrocene/dibutylphthalate above the glass transition. At 200 K the time evolution is characterised by a natural decay with lifetime of ~ 141 ns, modulated by a pronounced quantum beat which corresponds to the quadrupole splitting of ferrocene. The beat exhibits only a weak damping, indicating still very slow relaxation. At 247 K the beat is largely overdamped due to medium relaxation. At 300 K the slow approach of the natural decay (dotted line) is characteristic of fast relaxation (Abragam-Pound limit).

The potential of SRPAC relies on the fact that single-nucleus scattering depends neither on recoil-free emission and absorption, nor on translational motion. Therefore, SRPAC allows one to continue Mössbauer investigations of hyperfine interactions and rotational dynamics into regions where the Lamb-Mössbauer factor vanishes, i.e. in soft matter and viscous liquids.

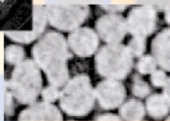
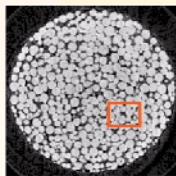
It is expected that SRPAC using the ^{57}Fe -resonance can cover a dynamic range of relaxation times of five orders of magnitude, from ~ 10 ps up to $1 \mu\text{s}$. Furthermore, SRPAC enables one to investigate pure rotational dynamics in hard-condensed matter as well. In combination with Mössbauer spectroscopy or NFS, translational and rotational dynamics can be separated.

References

- [1] A.Q.R. Baron *et al.*, *Europhys. Lett.* **34**, 331 (1996).
- [2] T. Butz, *Z. Naturforsch.* **41a**, 396 (1996).

Principal Publication and Authors

I. Sergueev (a,b), U. van Bürc (a), A.I. Chumakov (b,c), T. Asthalter (d), G.V. Smirnov (c), H. Franz (e), R. Ruffer (b), W. Petry (a), *to be submitted to Phys. Rev. Lett.*
(a) TUM Physik E13, Garching (Germany)
(b) ESRF
(c) RRC, Moscow (Russia)
(d) Univ. Stuttgart, Physikal. Chemie (Germany)
(e) DESY, HASYLAB, Hamburg (Germany)



Materials Science

Introduction

The Materials Science group now comprises the beamlines ID09A and B, ID11, ID15A and B, ID30 and ID31. The major news from the group is the transfer of the Powder Diffraction Beamline BM16 to an undulator source located at ID31. The new powder beamline provides superior flux and resolution giving a much improved production capability. New and improved microfocussing capabilities using flexible refractive lenses have been implemented on ID11 and ID15. It is now possible to obtain microfocus beams up to energies in excess of 130 keV and down to a few micrometres in spot size. Early tests show flux increases under these conditions of two orders of magnitude and a much simplified alignment procedure. ID30 has successfully implemented a laser-heating facility for high-pressure work. The temperatures reached so far are in excess of 4000°C. ID09A and B have installed new superior mirrors and a more flexible undulator to further improve the useable flux. ID15 has finished a major refurbishment of the shielding and experimental flux capability. The Materials Science group actively participates in FaME38, which is a project aimed at encouraging engineering research throughout Europe. FaME38 is a joint venture between the ESRF, ILL and British Universities.

Materials science research plays a major role at the ESRF and spans a wide range of applications from metals to novel materials for electronics applications. It is thus impossible to cover all areas in a short highlight presentation.

The tendency in the field is to utilise the unique properties of the X-ray source *i.e.* the high brilliance, the microfocussing capability and coherence. Many of the experiments thus deal with time-resolved studies, non-ambient conditions such as high temperatures and pressures and studies of relationships between structure and material properties in bulk materials. A few representative studies are given below.

Fundamental studies in materials science deal with development of microstructure as a function of processing conditions. The microstructure plays an important role for the properties of materials and detailed information is needed on the mechanisms guiding the development of specific microstructures. This knowledge will be used to obtain new models that will form the basis for the production of novel materials. One article describes a new area, where the 3D high-energy microscope is used for microstructure characterisation. A specific example of the use of this instrument is given in the article on

grain nucleation and growth during phase transformations in carbon steel. Another article describes a study of sintering of copper powder by rapid *in situ* tomographic imaging at high energies.

A promising development in the electronics field is the manipulation of matter by light on picosecond to femtosecond timescales. Examples of studies in this area are given by a study of lattice relaxed exciton strings in organic compounds. A second study addresses ferroelectric structural ordering by picosecond diffraction.

Novel development in high-pressure research has opened up the field of studies of liquids at high pressure. A pioneering study of first-order liquid-liquid phase transitions of phosphorus illustrates the possibilities of direct determination of the local structure of liquids by X-ray diffraction.



Highlights 2002

Fundamental Studies in Materials Science: Microstructure Development in 3D

A longstanding problem in materials research is the lack of any robust quantitative modelling to predict a material's microstructure after processing. For example this may consist of mechanical deformation, heat treatments, and other often complex processing steps that have been developed by years of educated trial and error. The relationship between microstructure and physical properties is better understood. For example, the strength, ductility, and electromagnetic properties of materials are strongly dependent on the microstructure such as grain size, grain boundary morphology, and orientation distribution of grains (texture). For this reason, a more fundamental understanding of the development of microstructure during thermo-mechanical processing is of great importance in order to facilitate the development of future generations of engineering materials.

New developments in the understanding and modelling of microstructure evolution have, in general, followed directly from the emergence of new experimental techniques. New developments in optical microscopy led to the first confirmation of slip along preferred crystallographic planes as a mechanism for plastic deformation. Further developments came with the availability of electron microscopy. For the first time microstructure could be observed from the grain to the dislocation level. The result of these new experimental techniques was an explosion of theoretical work on the dynamics of dislocation motion and the kinetics of grain nucleation and growth. Although these techniques have brought materials science from a black art to a true scientific discipline, a number of problems are still associated with the currently available characterisation techniques, which have prevented the next breakthrough in microstructural development modelling. The major disadvantage of the traditional microscopy methods (optical, SEM, TEM, etc.) is that they are primarily surface measurements unable to probe microstructure deeply embedded within bulk materials. It is well known that the surfaces of materials are non-representative of the bulk due to stress relaxation at the surface and dislocation migration. Serial sectioning can provide 3D data but being a destructive technique does not allow direct studies on the dynamics.

What is needed then is a technique that is able to provide non-destructive 3D information on the microstructure of materials. The penetrating power of high energy X-rays (> 50 keV) allows for bulk sampling (from mm to cm

depending on the material). This has been routinely used for bulk strain and texture measurements at neutron and synchrotron facilities. These techniques, though, rely on powder diffraction methods, and therefore give only average information of ensembles of grains. More advanced models need a finer microstructural map as they incorporate interactions between neighbouring grains. Powder average measurements are unable to address such issues.

The second hutch of ID11, the materials science beamline, has been built as a dedicated instrument for the development of techniques for measuring the microstructure of individual grains (and sub grains in certain cases) within bulk 3D volumes. In general, we refer to this instrument as the three-dimensional X-ray diffraction (3DXRD) microscope. Currently a number of techniques have been developed which allow for measurements of grain morphology (a 3D equivalent of an SEM micrograph), individual grain orientations, strain tensors of individual grains, and structural refinement of individual grains. About 100-1000 grains can be measured simultaneously, either statically or as a function of applied stress or temperature. Increasing statistics at the individual grain level have already invalidated a number of traditional models. Further statistics should allow us to reach the proper constraints necessary for the next generation of models.

The basic design of the 3DXRD is shown in **Figure 76**. The optics consists of a bent Laue crystal, which acts as a monochromator and vertical focusing element, and a bent multilayer, which focuses horizontally. This provides a minimum spot size of $2 \times 5 \mu\text{m}$ at energies between 50 and 90 keV.

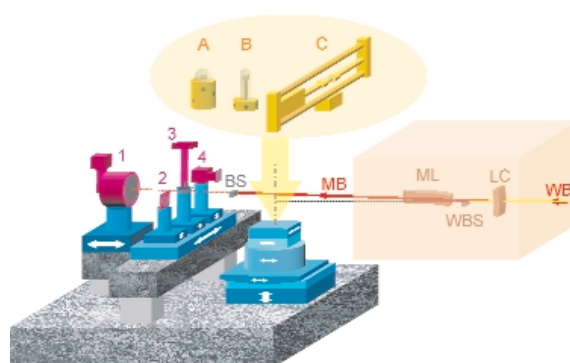


Fig. 76: Optics: WB: White beam; LC: Bent Laue crystal; ML: Bent multilayer; WBS: White beam stop; MB: 2-dimensionally micro-focussed monochromatic beam; BS: Monochromatic beam stop. **Sample environment (yellow):** A: Cryostat; B: Furnace; C: 25 kN stress rig. **Detectors / slits (purple):** 1: Large area detector; 2: Conical slit system; 3: High-resolution area detector; 4: Optional detector.

The sample stage provides for x-y-z translations with a $1 \mu\text{m}$ precision and a rotation table with a sphere of confusion of less than $1 \mu\text{m}$. The sample stage has been

designed to allow for a wide variety of sample environments including furnaces, cryostats, and stress rigs. Finally we have a number of detector systems, which may be translated in order to allow for a variety of measurements on the same sample. A brief description of the major techniques will be given with a short example of experimental results.

The most basic detector configuration of the 3DXRD utilises a large area detector (FRELON coupled to an image intensifier). In this configuration the full thickness of the sample is probed. If the illuminated volume contains up to several hundreds of grains then each individual grain can be indexed simultaneously as to its orientation and volume. The indexing is automated by software developed specifically for the instrument [1]. In order to define a gauge volume within the sample, a conical slit cell may be inserted between the sample and detector. This cell has 7 conically-shaped openings of 20 μm (corresponding to cubic reflections). With the conical slit in place, a 250–300 μm gauge length is defined along the beam direction [2]. The focal point of the conical slit then acts as a fixed position in 3D space with which to locate grains positions. This system is ideal for measuring the kinetics during thermo-mechanical processing. A tensile stress rig can be mounted on the sample stage and the orientation of individual grains can be measured as a function of applied load. The rotation pathway of individual grains can then be compared directly to texture models, which previously had only been tested by measurements on ensembles of grains (which inherently assumes no grain-grain interactions). Current results on 100 grains show significant deviations from classical models [3]. The kinetics of nucleation and grain growth may also be examined on the level of individual grains for the first time. By mounting a furnace on the sample stage the nucleation and growth of grains can be monitored *in situ*. Figure 77 shows growth curves

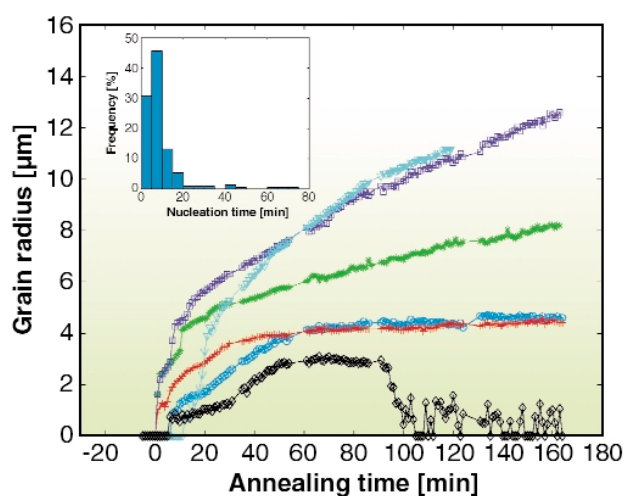


Fig. 77: Growth curves for 6 random grains are shown to illustrate the large spread in growth kinetics. The inset shows the distribution of nucleation times given a threshold of 1.3 μm .

for a number of grains [4]. Again the results are in disagreement with classical models (Avrami). In particular, growth rates can vary by an order of magnitude and individual grains may have varying incubation time. Statistics on the order of 1000 grains have been measured to date and correlations between growth rate and orientation are being used to modify existing models. Similar measurements have been recently done on the kinetics of phase transformations of steels and further information is given in a later highlight (Offerman *et al.*).

A high-resolution camera (5 μm point spread) is also mounted on the detector arm. This camera is used to create 3D grain maps with a spatial resolution limited by the resolution of the camera. The technique is in essence a virtual 3D detector. In this case only vertical focusing is used so that a single layer is illuminated. The detector is placed close to the sample (5 mm) so that the shape of the diffraction spots are projections of the grains shape and not dominated by divergence. The detector is then translated along the beam direction in order to track each reflection back to the sample plane [5] (Figure 78). Translating the sample height then allows a full 3D map of the grain boundaries and grain orientations to be reconstructed.

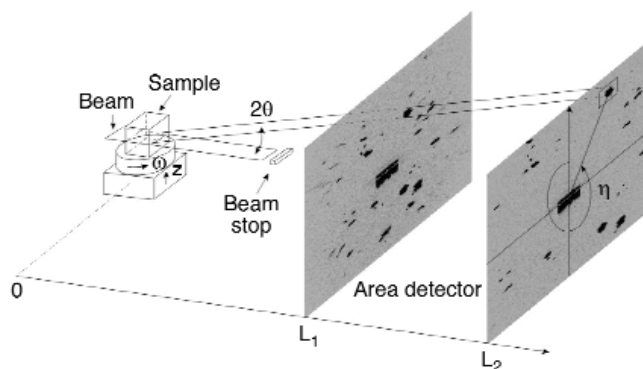


Fig. 78: Illustration of the tracking technique. When the detector is translated away from the sample the diffraction spots will move outwards on the detector. The positions of the diffracting grains in the sample are determined by linear fits. The fits also provide the 2θ and η values for grain indexing.

By combining the various techniques outlined above it is possible to follow the microstructural development by measuring the boundary morphology, size, orientation, and elastic strain tensor of each grain within the volume of interest during thermo-mechanical processing. As the spatial resolution is tunable, it is also possible to zoom out in order to perform materials engineering studies of the local stress and texture. Although the examples given here have focused on thermo-mechanical processing of metals it should be emphasised that this is a general technique which has already been applied to a variety of problems including high temperature superconductor processing, texture development in polymers, and a large variety of

phase transformations. With the introduction of the 3DXRD technique it is hoped that theoretical development will follow suit and a better understanding of the fundamental processes which govern microstructure development will lead not only to a firmer understanding of basic materials science but also lead to a new generation of materials with improved physical properties.

References

- [1] E.M. Lauridsen, S. Schmidt, R.M. Suter and H.F. Poulsen, *J. Appl. Cryst.* **34**, 744-750 (2001).
- [2] S.F. Nielsen, A. Wolf, H.F. Poulsen, M. Ohler, U. Lienert, and R.A. Owen, *J. Synch. Rad.*, **7**, 103-109 (2000).
- [3] L. Margulies, G. Winther and H.F. Poulsen, *Science* **291**, 2392-2394 (2001).
- [4] E.M. Lauridsen, D.J. Jensen, H.F. Poulsen and U. Lienert, *Scripta matter* **43**, 561-566 (2000).
- [5] S.F. Nielsen, W. Ludwig, D. Bellet, E.M. Lauridsen, H.F. Poulsen and D.J. Jensen, (Eds) N. Hansen, X. Huang, D.J. Jensen, E.M. Lauridsen, T. Leffers, W. Pantleon, T.J. Sabin and J.A. Wert, *Proc. of 21st Risø International Symposium on Materials Science*, Risø 4-8 September, 473-478 (2000).

Authors

L. Margulies (a,b), D.J. Jensen (a), E.M. Lauridsen (a), R.V. Martins (a), S.F. Nielsen (a), H.F. Poulsen (a) and S. Schmidt (a).

(a) Risø National Laboratory, Roskilde (Denmark)

(b) Risø Scientist in Residence at the ESRF

Grain Nucleation and Growth during Phase Transformations

Grain nucleation and growth are important phenomena in polycrystalline materials like metals and most ceramics. They govern the kinetics of many phase transformations and recrystallisation processes that take place during processing. The final average grain size after the transformation is directly related to the strength of the material. In general a smaller average grain size results into a stronger material. Despite the various transformation models that have been proposed in the last 60 years, the kinetics of these phase transformations are still poorly understood. Most of these models are based upon the Classical Nucleation Theory (CNT) [1] and the law of parabolic grain growth as derived by Zener [2], which describe the behaviour of individual grains in the bulk of the material.

The experimental techniques which have been available to verify these nucleation and growth models are either

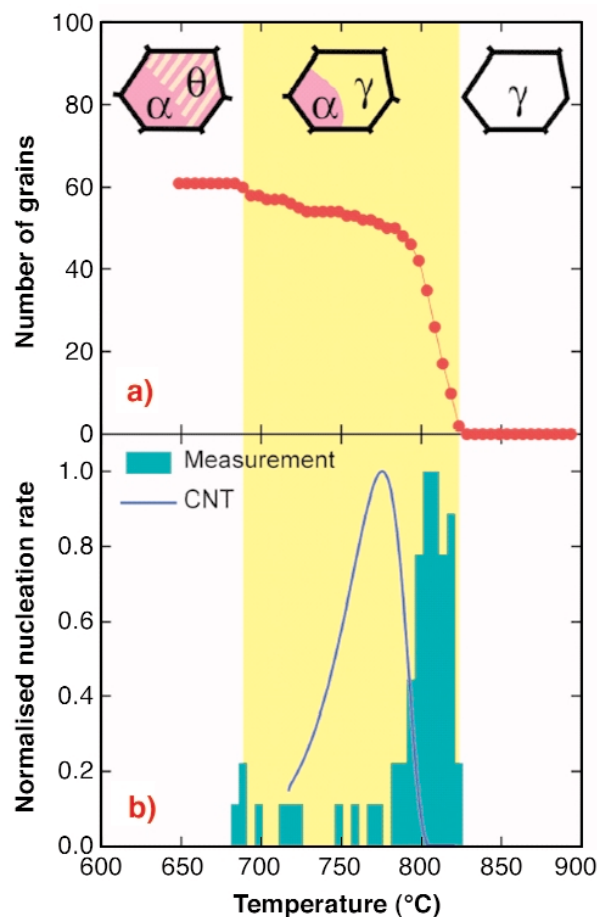


Fig. 79: Nucleation as a function of temperature: (a) the total number of valid ferrite reflections; (b) the normalised experimental nucleation rate (bars) compared to the classical nucleation theory (line). The different stages during the phase transformations in steel are schematically drawn at the top of the figure, which shows the three phases: Austenite (γ), ferrite (α), and cementite (θ).

limited to observations at the surface or the determination of the average grain growth behaviour in the bulk. The development of the 3DXRD microscope at beamline ID11 has created the opportunity to study individual grains in the bulk of a material [3]. These measurements give unique information about the grain nucleation and growth during the phase transformations. Thanks to a combination of fundamental scientific interest and technological importance the phase transformations in steel have been investigated more extensively than in any other material.

Carbon steel consists of iron and carbon (up to 2 wt.%) with small quantities of alloying elements, and exists in three stable crystalline phases: austenite (above 822°C), ferrite (below 822°C), and cementite Fe_3C (below 685°C). In the experiments we continuously cooled the steel from 900°C to 600°C in 1 hour. In order to study the time evolution of individual grains during the phase transformations, a relatively small volume of steel is illuminated with a monochromatic beam of hard X-rays (80 keV). A number of individual grains give rise to diffraction spots on a 2D-detector. From the standard

diffraction theory it can be shown that the intensity of each spot is proportional to the volume of the grain it originates from. By repeated acquisition of images, the nucleation and growth of the individual grains are studied with a typical time resolution of 10 seconds.

Our measurements show that the activation energy for grain nucleation is at least two orders of magnitude smaller than that predicted by the CNT (Figure 79). The observed growth curves of the newly formed grains confirm the parabolic growth model, but also show three fundamentally different types of growth. On the level of individual grains we can distinguish four types of grain growth as shown in Figure 80. There are grains that do not interact with neighbouring grains, grains that continue to grow with the same crystallographic orientation into another phase, grains that indirectly interact, and grains that directly interact with neighbouring grains.

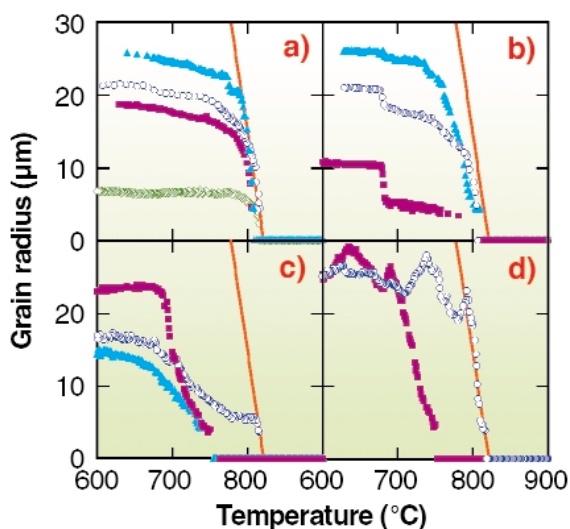


Fig. 80: Particle radius of individual ferrite grains as a function of temperature: (a) no interaction with neighbouring ferrite grains; (b) ferrite grains, which continue to grow with the same crystallographic orientation during the pearlite formation as part of a pearlite colony; (c) ferrite grains that indirectly interact; (d) ferrite grains that directly interact with neighbouring grains. The solid line indicates the classical Zener theory.

We conclude that the current models do not accurately predict the phase transformation kinetics in polycrystalline materials. From a technological perspective these new insights are of importance to the modern materials production process, which relies heavily on grain nucleation and growth models to produce tailor-made materials.

References

- [1] J.W. Christian, *The Theory of Transformations in Metals and Alloys*, Pergamon Press, Oxford, (1981).
- [2] C. Zener, *J. Appl. Phys.* **20**, 950-953 (1949).
- [3] E.M. Lauridsen, D.J. Jensen, H.F. Poulsen, U. Lienert, *Scripta Mater.* **43**, 561-566 (2000).

Principal Publication and Authors

S.E. Offerman (a), N. H. van Dijk (a), J. Sietsma (a), S. Grigull (b), E.M. Lauridsen (c), L. Margulies (b,c), H.F. Poulsen (c), M.Th. Rekveldt (a) and S. van der Zwaag (a), *Science* **298**, 1003-1005 (2002).

(a) Delft University of Technology (The Netherlands)

(b) ESRF

(c) Center for Fundamental Research: Metal Structures in 4D, Risø National Laboratory, Roskilde (Denmark)

In situ Microtomography Study of Metallic Powder Sintering

Sintering is a thermal treatment, below the melting temperature of the main constituent material, that transforms a metallic or ceramic powder (or a powder compact) into a bulk material containing, in most cases, residual porosity. This is the final step of an industrial powder metallurgy process that allows mass production of complex-shape components. Despite a consistent research activity over the decades, several questions remain open in the field of metal powder sintering (for example the role of particle rearrangement in the densification process, or the causes of anisotropic shrinkage during sintering) [1]. Thanks to the recent development of high-resolution X-ray microtomography, significant advances in the understanding of the phenomena occurring during sintering can now be expected. To investigate highly absorbing materials such as copper or steel and to follow *in situ* the structural evolution during thermal treatment, we have used the ultra fast micro-tomography setup recently developed at ID15, the High Energy X-ray Beamline. This setup allows one to collect a full 3D dataset in less than one minute. In the present study, the microstructural evolution of a loose copper powder and of a steel powder compact was studied. Both materials were sintered in a furnace in which a mixture of helium and hydrogen (4 at.%) was used to prevent oxidation.

Copper powder was poured in a 1 mm-diameter, 20 mm-high quartz capillary. Four reconstructed slices representing the same section of the sample before sintering and at three different moments of the thermal cycle are shown in Figure 81. The microstructural evolution during sintering can be clearly observed. Initial bonding between particles and neck formation appears at 1000°C but the main evolution occurs between 1000°C and 1050°C when, because of fast neck growth, the particles get closer to each other and the porosity is highly reduced. Finally pore channel closure, rounding,

and shrinkage terminate the densification process. The neck growth is better observed in the magnified images.

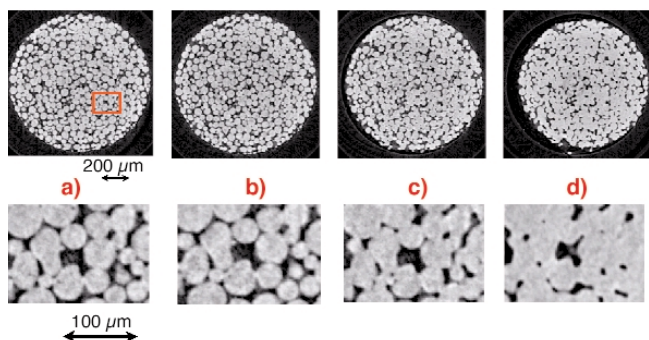


Fig. 81: 2D reconstructions (virtual slices) perpendicular to the cylindrical axis showing Cu particles at different stages of the sintering process: (a) before sintering, (b) after sintering at 1000°C, and (c) after sintering at 1050°C. Identical regions (inside the rectangle of (a)) are shown at a higher magnification below.

Steel compacts have been obtained by pressing samples into a close die of commercial Distaloy AE powder. Several microtomography scans were recorded at room temperature before and after sintering (see **Figure 82**). A small (about 1%) and anisotropic shrinkage was observed. Small pores located at the interfaces between particles can be observed before sintering, but disappear afterwards. Since the direction of such visible interfaces is preferentially horizontal, *i.e.* perpendicular to the direction of compaction, the disappearance of such interfaces during sintering could be the origin of the anisotropic shrinkage observed here.

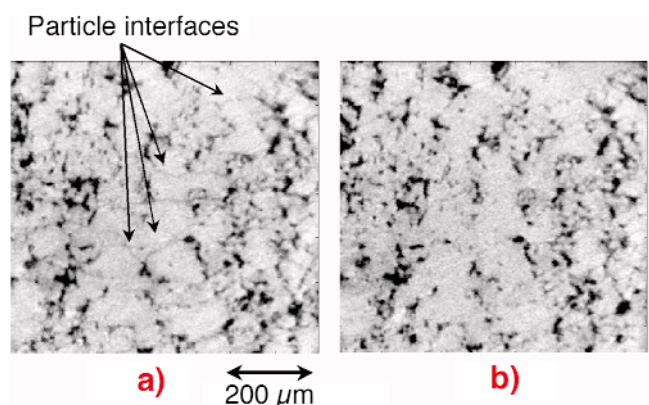


Fig. 82: Reconstructed slices of a compacted Distaloy sample before (a) and after (b) sintering at 1130°C. The direction of prior compaction is along the vertical direction in the paper plane.

This non-destructive method provides the 3D microstructural evolution of metal powder during sintering. Local and statistical information can be obtained, and will be used in the future for modelling the sintering process. Special attention will be given to the anisotropy induced by prior compaction and to its evolution through sintering.

Reference

[1] R.M. German, *Sintering Theory and Practice*, John Wiley and Sons, New York, 1996.

Principal Publication and Authors

O. Lame (a), D. Bellet (a), M. Di Michiel (b) and D. Bouvard (a), European Materials Research Society 2002 Proceedings, to be published in *Nuclear Instruments and Methods in Physics Research B*.
(a) Laboratoire Génie Physique et Mécanique des Matériaux, Institut National Polytechnique de Grenoble, CNRS UMR 5010, Saint Martin d'Hères (France)
(b) ESRF

Photo-induced Ferroelectric Structural Order Evidenced by 100 Picosecond Diffraction

A new type of manipulation of matter by light, in the picosecond (ps) or femtosecond (fs) timescales, has recently emerged by virtue of optically-controlled phase transitions. In some materials, molecular multistability between degenerate or quasi-degenerate states involves changes in the molecular identity, such as charge and/or spin. The structural relaxations of the electronic excited states following the absorption of photons are not independent processes, as in conventional excitonic or photo-chemical ones, but entail a photo-induced phase transformation towards a new lattice structure and electronic order. It is exemplified in some mixed-stack

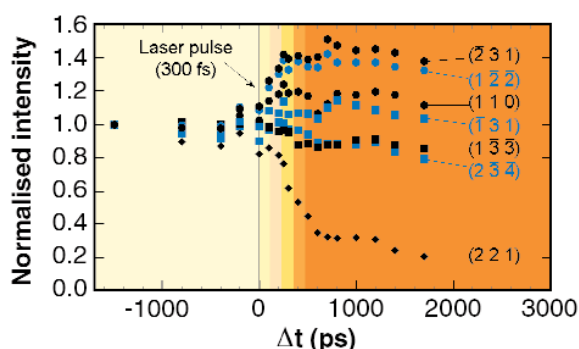


Fig. 83: Relative intensity of some Bragg reflections, measured at 0.753 Å, vs the delay between the laser pump and the X-ray probe. 11 K above the phase transition, a large structural reorganisation associated with the neutral-to-ionic transformation follows the laser irradiation. After 500 ps the light-driven metastable state is established. The delay dependence of the colour of the background reflects the change of reflectivity associated with the change in electronic state [1].

charge-transfer molecular materials that are readily tuned between competing neutral and ionic ground states. The sequence of alternating donor (D) and acceptor (A) molecules stimulates cooperative electron transfer, giving rise to a chain multistability and phase transition between regular neutral state ... $D^0 A^0 D^0 A^0 D^0 A^0 D^0 A^0 \dots$ and polar dimerised ionic state ... $(D^+ A^-) (D^+ A^-) (D^+ A^-) (D^+ A^-) \dots$. Structural and electronic changes are strongly coupled, as in the prototype compound TTF-CA (tetrathiafulvene-p-chloranil). The photoinduced neutral-ionic transformation takes place on the 100 ps time scale [1], whereas the life time of the photoinduced metastable state is in the range of few nanoseconds to a few microseconds. These phenomena are highly non-linear, since the efficiency, as large as a few hundreds of DA pairs transform per photon, is not simply proportional to the total absorbed photon energy. The advent of time-resolved photo-crystallography based on recent instrumentation developments gives an outstanding opportunity to observe directly the photoinduced structural changes with the appropriate time resolution.

The 100 ps time-resolved crystallography experiments on the neutral to ionic photo-induced transformation were performed at beamline **ID09TR**, using the optical pump and X-ray probe method [2]. An optical infra-red femtosecond pulse switches the material from a neutral to a metastable ionic state, followed by the recovery to the stable state. It is then possible to probe the sample stroboscopically by recording the diffraction pattern, for different delays between the X-ray and the laser pulses. Following laser irradiation, drastic changes are observed in the intensity of several Bragg reflections (Figure 83), some decreasing and others increasing. These intensity changes are a direct signature of a strong structural reorganisation in the photo-induced state, characteristic of a phase transformation (coherent three-dimensional domains) and not of independent local photo-induced distortions as in photosensitive proteins. The transformation is completed in less than 500 ps, in good agreement with optical studies [1]. One of the most salient features is the direct observation from the diffraction patterns of the symmetry lowering in the photo-induced state. Indeed, new weak Bragg peaks characteristic of a photo-induced ferroelectric organisation is observed as shown in Figure 84 +1 ns after the laser pulse. These new reflections are a direct signature of the 3D long-range ferroelectric order nature of the photo-induced state, similar to the low temperature one, also confirmed by preliminary refinement of the structures before and after laser irradiation which indicate photo-induced changes at the molecular level.

Still a dream only a decade ago, the success of 100 picosecond-scale crystallography on **ID09TR** gives outstanding possibilities to study photo-induced phase transformations. Moreover it stimulates future

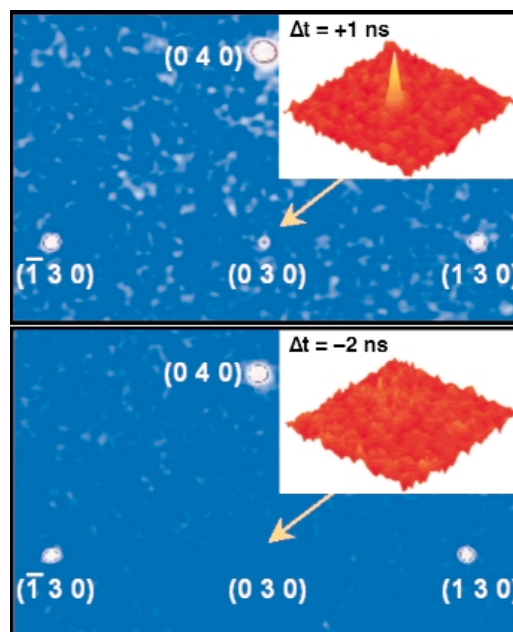


Fig. 84: Intensity in the reciprocal (a^* , b^*) planes before ($\Delta t = -2$ ns) and after ($\Delta t = +1$ ns) laser irradiation. The appearance of the (030) reflection establishes the ferroelectric nature of the three-dimensional ordered photoinduced state.

research towards photo-induced precursor cooperative phenomena such as the formation of nanoscale 1D charge-transfer domains, as successfully done at thermal equilibrium.

References

- [1] S. Koshihara, Y. Takahashi, H. Sakai, Y. Tokura, T. Luty, *J. Phys. Chem. B* **103**, 2592 (1999).
- [2] S. Techert, F. Schotte, M. Wulff, *Phys. Rev. Lett.* **86**, 2030 (2001), and citations within.

Principal Publication and Authors

E. Collet (a), M.H. Lemée-Cailleau (a), M. Buron (a), H. Cailleau (a), S. Techert (b), M. Wulff (c), T. Luty (d), S. Koshihara (e), M. Meyer (f), L. Toupet (a), P. Rabiller, *submitted*.

(a) *Groupe Matière Condensée et Matériaux, Université de Rennes1 (France)*

(b) *Max Planck Institut for Biophysical Chemistry, Göttingen (Germany)*

(c) *ESRF*

(d) *Institute of Physical and Theoretical Chemistry, Wrocław (Poland)*

(e) *Department of Materials Science, Tokyo Institute of Technology (Japan)*

(f) *Oxford Diffraction Poland, Wrocław (Poland)*

X-ray Diffraction of High-Pressure Fluids in Diamond-anvil Cells

The study of the structure of liquids at high pressure and temperature has been a long-standing goal in high-pressure research. With the maturation of third-generation synchrotron sources this goal is now attainable as demonstrated by the recent observation of a first-order liquid-liquid phase transition in phosphorous in a large-volume press [1]. We have successfully extended X-ray diffraction measurements in liquids to diamond-anvil cell (DAC) experiments.

Most of the recent work on the structure of liquids at high pressure and temperature has been done on solids (at ambient conditions) like phosphorous [1]. It was our desire to study liquids and gases (at ambient conditions) such as argon, H_2O , O_2 , and CO_2 . These samples can be easily loaded into a DAC but are very difficult to load in large volume presses. In order to analyse our DAC liquid diffraction data we found it possible and necessary to directly determine the density from the diffraction measurements. Thus, our experiments yielded both structural and equation-of-state information.

The thick diamond cells comprising the pressure vessel, the small sample size in DAC experiments, and the small scattering intensity of low-Z materials make these studies extraordinarily difficult. Thus, we developed a self-consistent, corrective procedure that addressed problems associated with the normalisation of the diffraction intensity, variations of the molecular form factor, and temperature diffuse scattering. Adequate attention must be paid to all of these uncertainties in order to obtain quantitative measurements of the structure factor of high-pressure fluids. A necessary component of our analysis is the determination of the density.

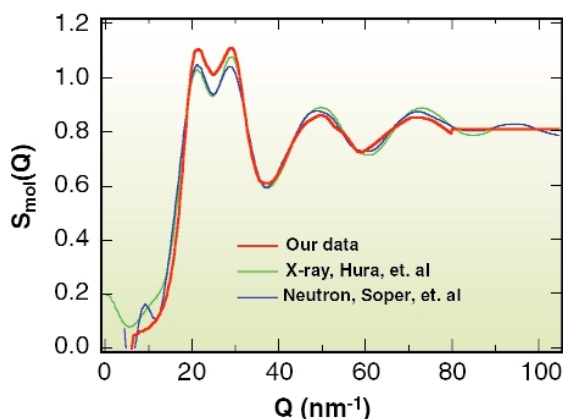


Fig. 85: Determination of the molecular structure factor of water at ambient conditions in a DAC compared to other ambient condition experiments.

In order to ensure that the results of our experiments represented accurate results, we performed an extensive comparison of our method with high-quality determinations of the structure factor of water at ambient conditions by X-ray and neutron diffraction. This comparison is shown in **Figure 85**. All of the peak positions are in good agreement and the peak intensities are very nearly so. The small discrepancy in the relative and total intensities of the primary doublet at 20 and 30 nm^{-1} is entirely consistent with a small (< 0.05 GPa) residual pressure according to extensive high-pressure experiments.

In **Figure 86** we plot our determination of the density for liquid water at 295 K versus pressure. The excellent agreement between our measurements and the Saul and Wagner equation of state (shown by the red line) suggests that our analysis rests on a sound foundation, and that it is possible to measure the density of low-Z liquids by X-ray diffraction to $\sim 3\%$ accuracy in diamond-anvil cells. This is the first time that high-pressure density measurements of liquids have been measured by X-ray diffraction, and it opens exciting new possibilities for directly measuring the equation of state of liquids.

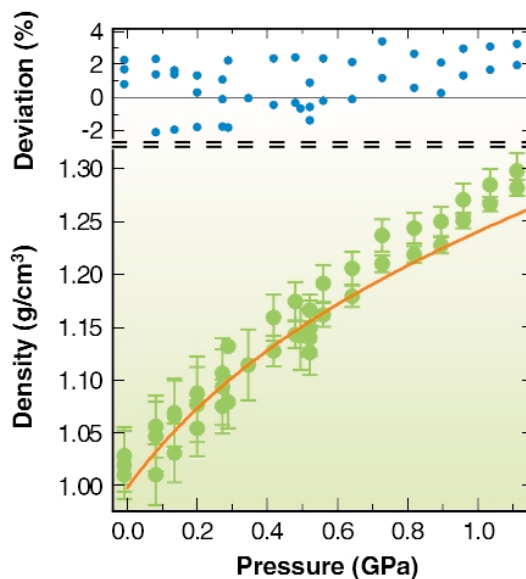


Fig. 86: Determination of the density of water at 295 K up to the freezing pressure. The Saul and Wagner EOS is shown by the red curve and the deviation shows that we achieve about 3% accuracy.

In conclusion, we have measured the structure factor of liquids at high pressure in a diamond anvil cell for the first time. We have also measured the density of a liquid at high pressure by diffraction for the first time. We compared our results with high-accuracy measurements at ambient condition and to a well-known equation of state and found very good agreement.

Reference

[1] Y. Katayama, T. Mizutani, W. Utsumi, O. Shimomura, M. Yamakata, and K. Funakoshi, *Nature* **403**, 170 (2000).

Principal Publication and Authors

J.H. Eggert (a), G. Weck (b), P. Loubeyre (b), M. Mezouar (c),
Phys. Rev. B **65**, 174105 (2002).

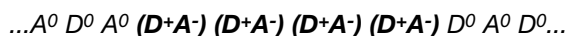
(a) LLNL (USA)

(b) CEA (France)

(c) ESRF

Direct Evidence of Lattice-relaxed Charge-transfer Exciton-string

Many novel low-dimensional electronic materials exhibit a high tunability between competing ground states. Interactions between charge, spin and lattice degrees of freedom are enhanced in the low-dimensional systems and cause cooperative phenomena and broken symmetries. The structure-function relationships are thus determined by self-trapped non-linear excitations. Besides well-known examples such as high- T_c superconductors, manganite oxide perovskites, conducting polymers or mixed-valence chains, the mixed-stack charge-transfer (CT) organic compounds undergoing neutral-ionic (N-I) transition appear as other promising materials and can serve as a model system to study the physics of non-linear excitations. In those quasi one-dimensional systems, the alternation of electron donor (D) and acceptor (A) molecules along stacks gives rise to chain multistability between a regular neutral (N) state ... $D^0 A^0 D^0 A^0$... and dimerised polar ionic states ... (D^+A^-) (D^+A^-)... This unusual electronic-structural transition is governed by the formation of CT exciton-strings, theoretically discussed by Nagaosa [1]. A chain is then inhomogeneous with the formation of lattice-relaxed CT (LR-CT) strings, sequences of I dimers within a N chain:



New physical properties originate from these non-linear excitations, such as photo-induced phase transformations, a new type of ferroelectric phenomena or negative resistance effects. The excitation of CT exciton-strings has been observed by optical spectroscopy [2]. However, direct evidence of their lattice-relaxed state, which may be thermally activated, had not been found. Here we report on such a fundamental observation by X-ray diffuse scattering in different CT complexes. The size and concentration of these LR-CT strings have been determined by diffuse scattering measurements taking advantage of the X-ray flux and high resolution at **BM2**, the D2AM CRG beamline. The LR-CT exciton-strings extending along the stacking axis **a** are directly evidenced by diffuse (**b***, **c***) planes as shown in

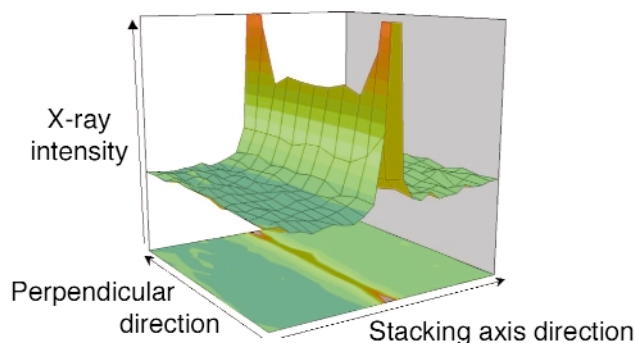


Fig. 87: Diffuse plane perpendicular to the stack showing the 1D nature of the fluctuating CT nanodomains.

Figure 87. Scans in reciprocal space makes it possible to extract precisely the intrinsic correlation lengths which characterise the mean size of these fluctuating nanodomains, and from the intensity at maximum (I_M), the temperature evolution of susceptibility. The results obtained for a compound presenting a continuous phase transition are plotted in **Figure 88**.

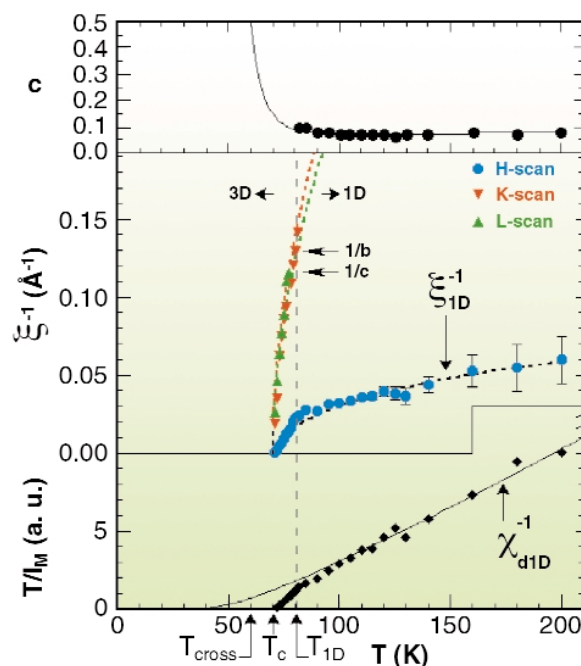


Fig. 88: High-resolution measurements of the inverse X-ray intensity T/I_M (squares, bottom), inverse correlation lengths (middle) along a^* (blue), b^* (red) and c^* (green), and concentration in I species c (dots, top). T_c is the phase transition temperature and T_{1D} is the lower limit of 1D fluctuations. The dotted lines (bottom) represents the 1D susceptibility, while the dashed lines for the transverse correlations (middle) correspond to the mean field approach for weakly coupled chains.

The almost equal perpendicular correlation lengths ξ_{b^*} and ξ_{c^*} reach the inter-stack distances at T_{1D} , 10 K above the 3D phase transition. At the same temperature, anomalies of the intra-chain correlation length, ξ_{a^*} , and of the susceptibility are observed. This clearly indicates a crossover from a 3D to a pronounced 1D regime for the

fluctuations. The important cooperativity inside the stack is reflected in the size of the strings extending around 100 Å at T_{1D} , giving direct evidence of 1D LR-CT fluctuations. The comparison of I_M and ξ_{a^*} makes it possible to deduce the concentration of thermally-activated excitations (Figure 88). Another aspect of these systems is that the size and also the concentration of these nanoscale non-linear excitations can be triggered by pressure, temperature or light irradiation.

This kind of investigation, actually pursued to understand the photo-induced and quantum fluctuation effects, is fundamental with regards to the universality of the equilibrium and out of equilibrium multi-scale phenomena in these novel low-dimensional electronic materials.

References

- [1] N. Nagaosa, *J. Phys. Soc. Jap.* **55**, 3488 (1986).
- [2] M. Kuwata-Gonokami *et al*, *Nature* **367**, 47 (1994).

Principal Publication and Authors

E. Collet (a), M.H. Lemée-Cailleau (a), M. Buron (a), H. Cailleau (a), S. Ravy (b), T. Luty (c) J.F. Bérar (d), P. Czarnecki (e), and N. Karl (f), *Europhys. Lett.* **57**, 67-73 (2002).

(a) *Groupe Matière Condensée et Matériaux, Université de Rennes1 (France)*

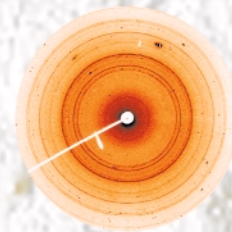
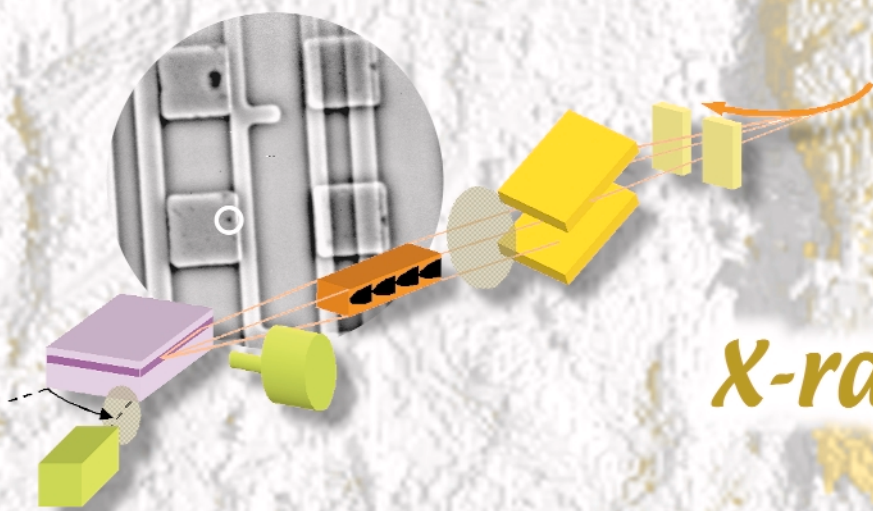
(b) *Laboratoire de Physique des Solides, Université Paris-sud, Orsay (France)*

(c) *Institute of Physical and Theoretical Chemistry, Wrocław (Poland)*

(d) *D2AM CRG, ESRF*

(e) *Institute of Physics, Adam Mickiewicz University, Poznan (Poland)*

(f) *Physikalisches Institut, Universität Stuttgart (Germany)*



X-ray Imaging

Introduction

A considerable development in X-ray imaging techniques has taken place over the last few years at the ESRF. This has associated optimal source characteristics with new detectors and computers. These developments may be characterised using keywords such as “high spatial resolution”, “three-dimensional”, “coherent beams”, “*in situ*”, “real-time”, and “combination of techniques”. The main aims of the X-ray Imaging Group are to enhance imaging techniques and to apply these techniques to a range of topics, including physical, biomedical, materials and engineering science. New subject areas such as geophysics, the environment, archaeology and biology are constantly appearing.

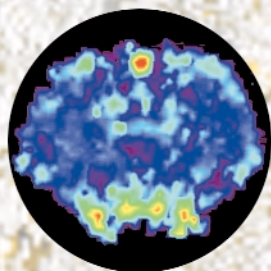
Three short general papers introduce important aspects of the development of these techniques and their applications. The first highlights the increasing use of microtomography for the investigation of a wide variety of problems. Microtomography

provides three-dimensional information and, by making full use of the ESRF's capabilities, can also provide high spatial resolution and quantitative measurement. The second describes how synchrotron radiation is currently being used in state-of-the-art medical applications. The main themes of this research are the combination of imaging for diagnosis with radiation therapy in its various forms coupled with work on small animals. The third paper shows the importance of microanalysis to environmental studies.

These general papers are supported by short illustrative contributions. The *in situ* visualisation by diffraction imaging (X-ray topography) of the migration of a grain boundary provided the data required to determine the basic characteristics of this process (Polcarova *et al.*). The high spatial resolution now available in microtomography allowed the investigation of an important but complex problem, the quantification of fatigue crack closure (Khor *et al.*).

Fiedler *et al.* present the latest developments at the ESRF of Diffraction Enhanced Imaging (DEI), which could constitute an important diagnostic tool for mammography. The first *in vivo* assessment of cerebral blood volume and blood flow was made using highly-accurate synchrotron radiation tomography: this new tool to investigate cerebral physiopathology, coupled with radiotherapy, could help to treat brain tumours (Adam *et al.*).

Microanalysis has been used to study the role of metals in processes leading to neurodegenerative disorders, such as Parkinson's disease (Lankosz *et al.*), and to extract information about the sulphur-metabolising activities in archean bacteria, which could give clues about the mechanisms involved in the origin of life (Philippot *et al.*). Two technical enhancements open new scientific possibilities. First the standing-waves technique coupled with a microbeam permitted the identification of polarity-inverted regions of a GaN film (Drakopoulos *et al.*) and second, Zernike-type phase contrast was used to improve the possibilities of X-ray microscopy at energies of about 4 keV (Neuhausler *et al.*).



Highlights 2002

Synchrotron-radiation Microtomography

Review by P. Cloetens and J. Baruchel (ESRF)

Microtomography is the three-dimensional (3D) reconstruction, via a numerical process, of the structure of a sample from a set of two-dimensional images, with a resolution of a few micrometres or less. Synchrotron radiation microtomography is now routinely used on several beamlines to perform investigations on a wide range of topics. Like other imaging techniques, it can provide information on samples from physical, medical, materials science and engineering subjects. Furthermore, the technique is also able to innovate in new areas like geophysical, environmental, paleontological and biological studies. This technique occupies now most of the beam time on ID19, and a substantial fraction on ID15, ID17 and ID22 and demand is clearly increasing. The three-dimensional data provided by microtomography is essential for the understanding of a wide range of phenomena [1,2].

When considering the present situation, we could be surprised that this use was not foreseen at the early stages of the ESRF, only 15 years ago (the “Red book”). The reason resides in the fact that microtomography not only requires the very brilliant sources provided by the ESRF, but also adapted detectors and very high computer power both in terms of calculation speed and memory. Indeed one 3D image represents about 2 Gigabytes of data, which is presently recorded in, typically, 10 minutes. This has to be compared with the total central memory foreseen for the ESRF at the time of the Red book, *i.e.* 3 Gigabytes. The effort devoted at the ESRF to implement high-resolution X-ray detectors based on a CCD camera exhibiting simultaneously a high dynamic range and a fast readout (the FReLoN camera), together with the general progress of the computers, when coupled with the ESRF beams, resulted in the microtomographic possibilities we have today.

Intensity is the first quantitative feature that has made progress in microtomography possible. It allows either the use of a monochromatic beam, which makes the quantitative evaluation of the results possible, and eliminates artefacts from the reconstructed image, or the implementation of fast tomography, which has been for instance used to follow the sintering of copper spheres.

In addition, when working at the ESRF, the physical effect that leads to image formation is not only the attenuation of the beam, essentially through photo-electric absorption, but also its phase shift suffers on going through a specimen. Contrast from phase features can be obtained with high instrumental simplicity through mere propagation over finite distances. A quantitative 3D reconstruction of

the phase shift (corresponding to the local electron density) is now routinely achieved, based on images recorded at several distances (“holotomography”) [3].

The ESRF is the place where the most significant progress of the relatively young synchrotron radiation microtomography technique has been achieved. This is why representative results indicating the developments that have emerged can be found in previous issues of the ESRF Highlights. Among them let us mention:

- the quantitative analysis of bones, which showed the actual effect of drugs used to treat osteoporosis,
- the observation of Uranium particles from Chernobyl soils, where cavities and channels reflect the formation of fission products during reactor operation,
- the holotomographic investigations of semisolid alloys, which allows one to visualise phases which display less than 2% difference in density, and of the seed of *Arabidopsis thaliana*, a favourite among plant geneticists, which is imaged in the damp state, without any specimen preparation.

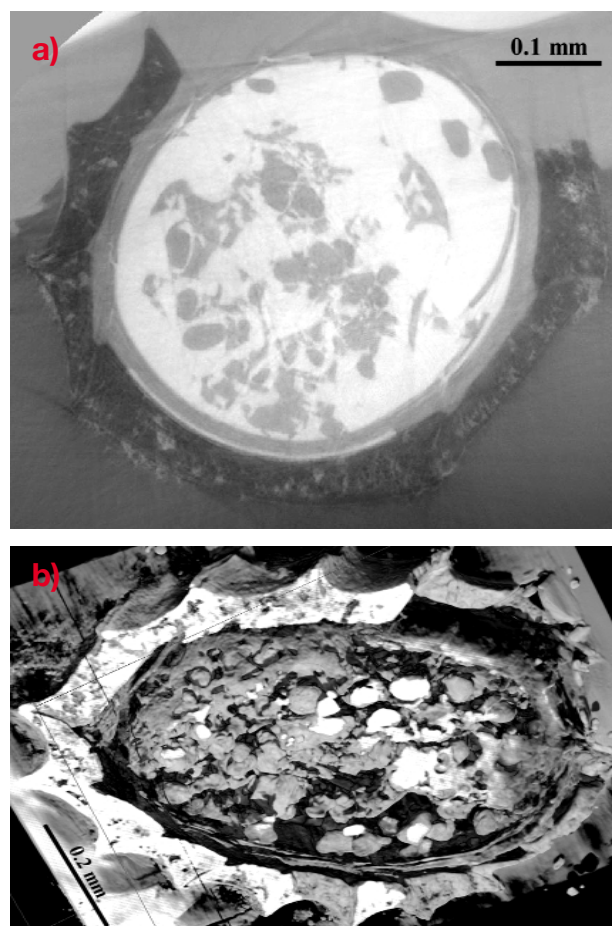


Fig. 89: (a) Reconstructed holotomographic slice through a charophyte plant and (b) three-dimensional rendering of a calcified fossil of charophyte fertile elements (inside) and sheath (outside); the scans were performed at 23 keV and the resolution was about 1.5 μm , pixel size = 0.7 μm (courtesy of M. Feist, P. Tafforeau and S. Zabler).

A recent result showing the state of the art is the one on charophytes, which are members of the green algae group. They are supposed to play an important role in the evolution towards vascular plants. Their fertile elements are well conserved in a calcified state (typically calcite) and fossils are often found in limestones and marls, deposited in brackish or freshwater environments. The analysed fossil consists of an inner structure and an outer protective sheath, formed by the growth of elongated spiral cells around the core. The observation of contrast between the sample that is mineralised in calcite and the limestone bulk necessitates a complete holotomographic reconstruction (Figure 89).

The future progress in microtomography is foreseen along various ways, which include the combined technique approaches, fast tomography and magnified tomography.

The possibilities of combined approaches, in which tomography cooperates e.g. with topography ("topo-tomography") or fluorescence have already been implemented and demonstrated in a few cases. In this last case, the local character observed by fluorescence implies the use of a microbeam, and tomography is obtained by recording a scanned image for each orientation, and recording the fluorescence associated with each point in the map. The chemical state of an element can, alternatively, be visualised through the combination with X-ray absorption near-edge structure (XANES).

Fast tomography is very important to be able to follow evolving phenomena. One example application is given in Figure 90, which shows a liquid foam (a) and its evolution over 35 minutes through the subtraction of two successive images (b): this last image indicates that coarsening tends to increase the volume of the large bubbles at the expense of the small ones.

The emergence of magnifying devices is another exciting area, which allows us to perform 3D images with sub-micrometre spatial resolution. Presently there is no X-ray magnification of the image so the resolution limit of microtomography is set by the detectors used. A very promising approach allowing this magnification is based on the use of curved mirrors and multilayers in the Kirkpatrick-Baez (KB) geometry. X-ray focusing to about $10^{-2} \mu\text{m}^2$ spot size with 5.10^{11} ph/s at a photon energy of 20 keV has been very recently demonstrated using a KB device. A magnified image is obtained when the detector is placed further from the specimen than the focus to sample distance (projection microscopy). The extension to microtomography is not straightforward in a routine mode, because it implies mechanical precision and stability, which are at the very limit of what is presently achievable, and therefore requests substantial technical developments.

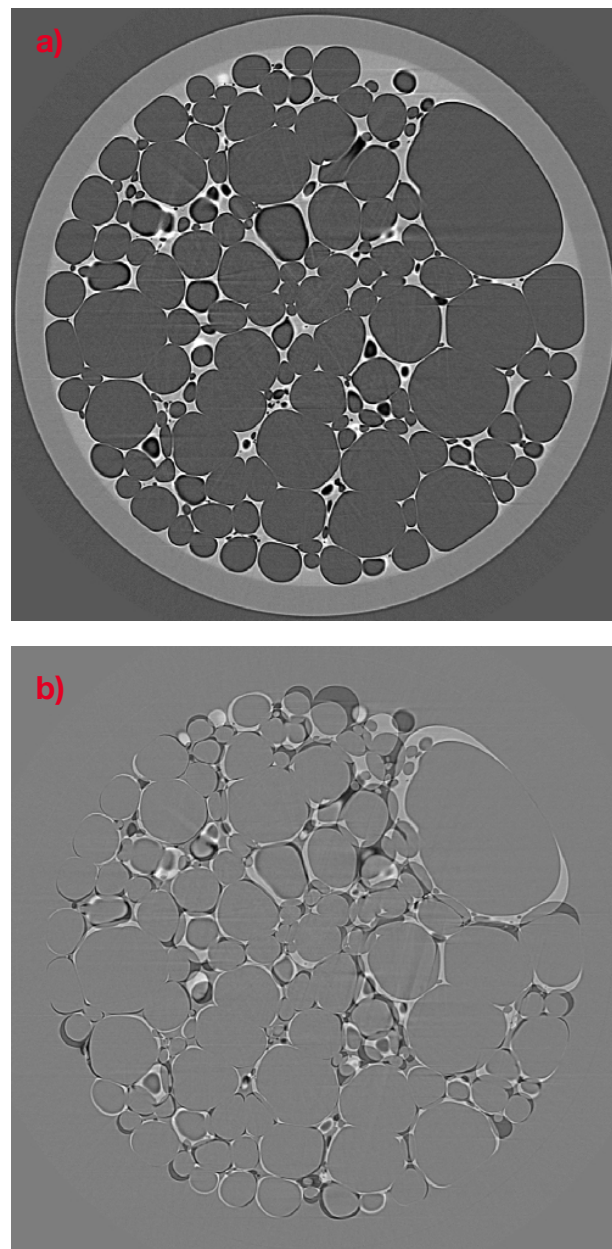


Fig. 90: a) image of a liquid foam and b) its evolution over 35 minutes (subtraction of two successive images) (courtesy of F. Graner).

Let us note, to conclude, that the use of microtomographic data is evolving. In addition to its industrial interest, the major scientific point to note is the emergence of imaging from taking 'snapshots' or 'videos' to extracting quantitative data from images suitable for model building or evaluation.

References

- [1] Developments in X-Ray Tomography III, U. Bonse, editor, *Proceedings of SPIE* **4503** (2002).
- [2] P. Cloetens, W. Ludwig, E. Boller, F. Peyrin, M. Schlenker, and J. Baruchel. *Image Anal. Stereol.* 21(Suppl 1), S75-S85 (2002).
- [3] P. Cloetens, W. Ludwig, J. Baruchel, D. Van Dyck, J. Van Landuyt, J. P. Guigay, and M. Schlenker, *Appl. Phys. Lett.*, **75**:2912-2914 (1999).

Synchrotron Microtomography of Fatigue Crack Closure

The incidence of fracture surface contact in the wake of fatigue cracks, and the associated attenuation of cyclic displacements, is known to be critical to crack propagation resistance. Whilst such surface contact (or 'closure') has been widely investigated over the last 20-30 years, measurement methods remain the subject of ongoing controversy, with the most widely established methods (compliance based) offering little micromechanical insight, or indeed any direct information on the active crack tip region. Synchrotron microtomography has been identified as a uniquely powerful method to obtain *in situ* understanding of plane strain crack tip behaviour [1]. Resolution levels have however been limited to date ($\sim 6 \mu\text{m}$), requiring sub-voxel interpolation to be used in the crack tip region. Recent work has demonstrated the ability of high-resolution synchrotron microtomography to image the fine details of fatigue cracks together with surrounding microstructural features in Al-alloys with a $0.7 \mu\text{m}$ resolution [2]. This resolution has been used in the present work to image crack closure in a 2024 alloy, carried out on beamline ID19. Work has been particularly carried out using the damage tolerant airframe aluminium alloy, AA2024-T351. By extracting relatively small tomography samples from the crack tip of conventional fatigue test coupons, results representative of aerospace engineering performance have been obtained. *In situ* straining facilities have been used to assess the progressive loading and unloading process.

Tomography results have been used for both direct imaging of crack paths and 3D image analysis to extract

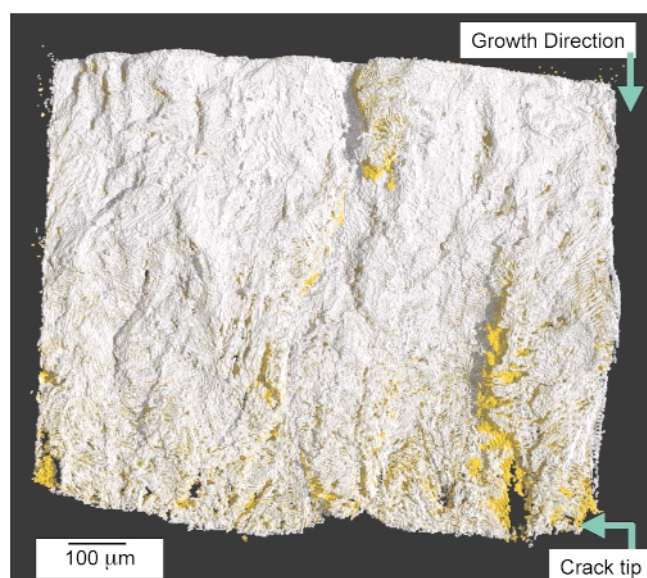


Fig. 91: Thresholded crack volumes obtained at maximum and minimum loads.

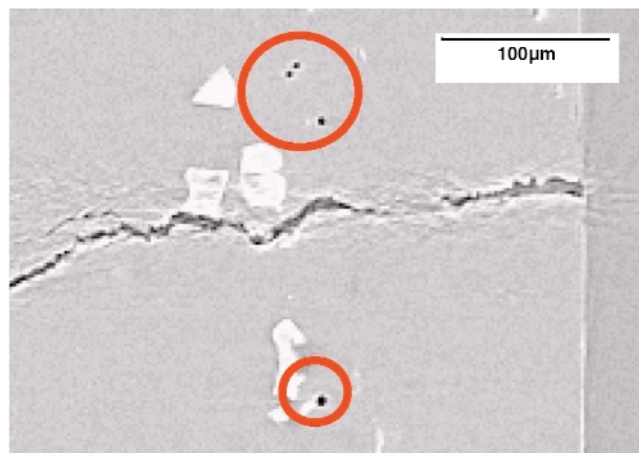


Fig. 92: Two-dimensional slice of a tomographic reconstruction showing crack and fine porosity used to quantify local deformations.

the crack volume. Figure 91 shows 3D crack volumes extracted in the loaded and unloaded conditions, rendered and viewed perpendicular to the crack plane. The white layer represents the unloaded crack, superimposed over the same crack at maximum load in yellow. As representations of the crack volume in each case, discontinuities in the surfaces represent either unbroken ligaments in the crack wake, or regions of fracture surface contact. The regions appearing in yellow clarify areas in the crack wake that have gone from a closed to open condition on loading. Such results identify distributed, relatively small points of contact close to the crack tip (of the order of $10 \mu\text{m}$ across), and large contact areas (of the order of $100 \mu\text{m}$) occurring to greater distances behind the crack tip. The larger contact areas and their apparent association with ridges running parallel to crack growth direction is consistent with previous reports, whilst the distribution of small contact points approaching the crack

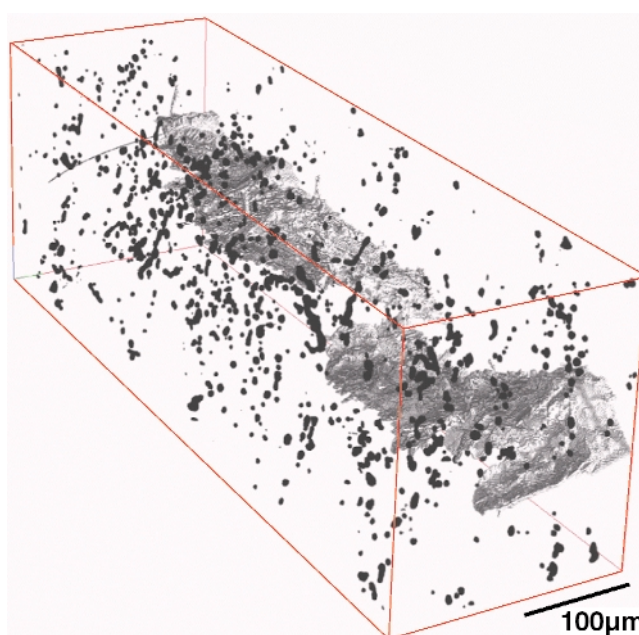


Fig. 93: Three-dimensional arrangement of particle and microvoid locations about the crack tip used for stress intensity calculations.

tip has not been seen previously. Quantitative assessment of contact areas has confirmed the progressive nature of closure processes during crack loading and unloading. This highlights the intrinsic simplification and deficiency involved in the widespread use of a single valued closure point to quantify crack driving forces.

Given the available spatial resolution, a unique feature of the present work has been the quantitative use of micro-porosity and intermetallic particles associated with the underlying material for compliance/displacement measurements at a microstructural scale (Figure 92) [3]. Figure 93 highlights the three-dimensional distribution of such features around the crack tip, as have been used to measure local stress intensity factors around the crack tip, providing explicit information on changes in crack driving force as a function of location within the bulk sample.

References

- [1] A. Guvenilir, T.M. Breunig, J.H. Kinney and S.R. Stock, *Phil. Trans. R. Soc. Lond. A*, **357**, 2755-2775 (1999).
- [2] W. Ludwig, J-Y. Buffière, S. Savelli and P. Cloetens, *Acta. Materialia* **51**(3), 585-598 (2003).
- [3] H. Toda, I. Sinclair, J-Y. Buffiere, E. Maire, T. Connolly, M. Joyce, K.H. Khor, and P.J. Gregson, *Phil. Mag.*, submitted.

Authors

K.H. Khor (a), M. Joyce (a), T. Connolley (a), H. Toda (b), I. Sinclair (a), E. Maire (c), J.-Y. Buffiere (c).
 (a) Southampton University (UK)
 (b) Toyohashi University (Japan)
 (c) INSA (France)

Visualisation of Grain Boundary Migration

Traditional methods for quantitative measurement of grain boundary (GB) migration consist of consecutive *post-mortem* observations of a migrated branch of the boundary on the surface of a bicrystal by light microscopy [1]. Recent progress in the study of this problem is represented by an application of synchrotron radiation (SR) offering many advantages for *in situ* observation. [2].

For our study of GB migration by *in situ* synchrotron radiation diffraction topography, a specimen 4 mm wide and 1 mm thick was prepared of a bicrystal with the {130} GB [3]. The boundary was perpendicular to the largest specimen surface (001) and made an angle of 45° with both side surfaces. The measurements at 965°C were done at beamline ID19, using a special high-temperature vacuum

stage. At this temperature, the boundary migrates towards the centre of its curvature to reduce its energy (= area). Transmission topographs were taken using monochromatic beam ($\lambda = 0.0207$ nm, 420 symmetrical reflection for both grains, $\vartheta = 9.44^\circ$). The diffracted beam was recorded by a FReLoN camera [4]. As the bicrystal contained sub-grains misoriented up to tens of minutes, the sample was rocking over this angle while the topograph was recorded. The recording time, approximately 1 minute, was comparable to the exposure time for photographic plates, but the records could be taken in shorter intervals without interrupting the experiment. This fact is very important when fast changes

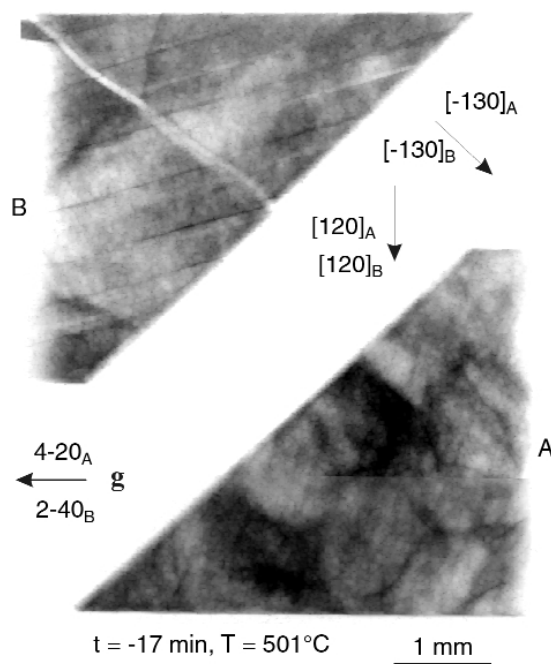


Fig. 94: SR topograph characterising planar boundary before start of grain boundary migration. Fine details in the structure are magnetic domains and a sub-boundary in grain B, g is the diffraction vector.

have to be registered. It is apparent from characteristic topographs that both branches of the originally planar GB (Figure 94) curve and migrate towards the centre of their curvature (Figure 95). The time dependence of the migrating distance, $a = Ct^{1/2}$, on the side surface for each branch of the boundary provides the parameter C important for quantification of temperature and orientation dependent GB migration [1].

The *in situ* observation showed that the GB is circular with a right angle to the side surface at the beginning of migration. Later it tends to become straight with an angle of $\sim 70^\circ$ to the side surface and so, parallel to the [110] direction of the grain A of the bicrystal (Figure 95). The boundary is not exactly perpendicular to the largest sample surface but nearly parallel to the $(\bar{1}10)$ plane as can be deduced from the width of its image on the transmission topographs and from *post-mortem* observation. Finally, good agreement was found between the data measured by SR topography and by light microscopy technique [1].

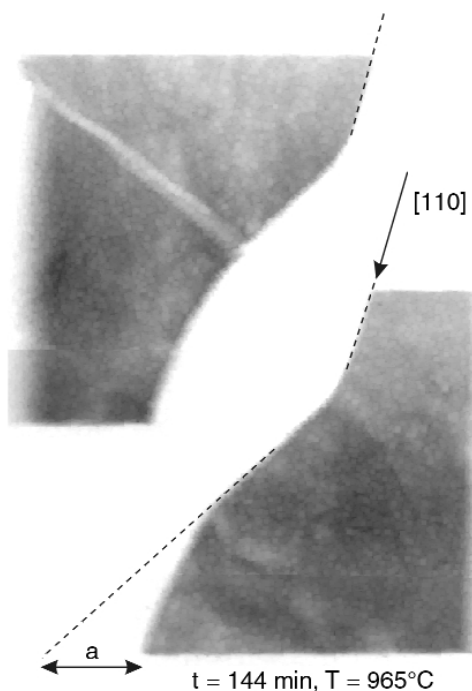


Fig. 95: SR topograph showing migrating boundary after 144 min. at 965°C. *a* is the migrated distance of the GB. The $(\bar{1}10)$ facet (surface GB trace parallel to the $[110]$ direction) is clearly apparent.

The described results were achieved thanks to the high energy and intensity of synchrotron radiation, and the high sensitivity and good resolution of the FReLoN camera. The method is capable of providing the data necessary for the determination of basic characteristics of dynamical processes. Much more data can be collected in this way than using repeated annealing experiments. In addition, the *in situ* measurements may reveal many details elucidating the mechanism of GB migration and interaction of moving interface with lattice defects.

References

- [1] P. Lejcek, V. Paidar, J. Adánek and S. Kadecková, *Interface Sci.* **1**, 187 (1993).
- [2] S. Tsurekawa, T. Ueda, K. Ichikawa, H. Nakashima, Y. Yoshitomi and H. Yoshinaga, *Mater. Sci. Forum* **204–206**, 221 (1996).
- [3] S. Kadecková, P. Toulá and J. Adánek, *J. Crystal Growth* **83**, 410 (1987).
- [4] M. Polcarová, J. Brádlér, J. Gemperlová, A. Jacques and A. George, *J. Phys. D: Appl. Phys.* **32**, A109 (1999).

Principal Publication and Authors

M. Polcarová (a), J. Brádlér (a), A. Jacques (b), P. Lejcek (a), A. George (b), O. Ferry (b), *J. Phys. D: Appl. Phys.*, accepted.

(a) *Institute of Physics, AS CR, Praha (Czech Republic)*

(b) *LPM, Ecole des Mines, Nancy (France)*

Medical Research with Synchrotron Radiation: Present and Future

Review by S. Fiedler and G. Leduc (ESRF), and F. Estève (Equipe d'accueil RSRM-CHU Grenoble, France)

From the very beginning the synchrotron radiation-based medical research programme has involved both imaging for diagnosis and irradiation for therapy, for pre-clinical and potentially clinical application [1].

A big effort was devoted to angiography, which aims at visualising coronary arteries. At beamline **ID17** dual-energy images are acquired during the bolus passage of an iodine contrast agent after an intravenous infusion. At the moment studies have been performed on 51 volunteer patients (32 right coronary arteries, 19 left coronary arteries). This protocol should end up with 62 patients and might be continued by clinical trials like human kidney perfusion studies, follow up after arterial stent implantations or test of contrast agents [2].

Asthma is a disease from which more and more people suffer in our industrial societies. This motivated programme to use the possibilities of synchrotron radiation to image the lung (Functional Lung Imaging Programme). Dynamic measurements of xenon concentrations in the airways are used to obtain maps of regional lung ventilation. We have studied local specific lung ventilation using tomographic and projection images. Recently, volume-rendering spiral computed tomography of rabbit lungs after an asthma crisis has been performed. This tool is particularly valuable in the experimental study of small airway pathophysiology of the role of local mediators and that of pharmaceutical agents, and to develop experimental models of obstructive lung diseases such as asthma or emphysema [3].

Another disease which is very common and where the early diagnosis is definitely very important is breast cancer. The Diffraction Enhanced Imaging (DEI) modality is especially interesting for radiation sensitive, soft-tissue imaging in mammography. The method is based on the use of highly-monochromatised radiation, passing through an analyser crystal in order to obtain an edge enhancement, at the interfaces of regions with different refractive indices. Excellent correspondence between tomographic slices and histological cuts of the same layer of cancerous tissue samples has been established. DEI offers a new kind of contrast for soft-tissue imaging based on the fact that each tissue species has its own characteristics with regards to small-angle scattering. Thanks to the low X-ray dose delivered in the

experiments, a significant step towards clinical use of this method has been achieved (page 81).

Cerebral perfusion studies at the ESRF are made by temporal subtraction after the first passage of a contrast agent in the tomography mode. The accuracy and the precision of the synchrotron radiation computed tomography (SRCT) has been studied on the beamline. Direct measurement of the concentration of the contrast agent allows us to obtain functional parameters such as Cerebral Blood Volume or Flow and Permeability Coefficient (**Figure 96**). Such parameters are essential for the analysis of the physiopathology of brain diseases (mainly tumour processes), for therapy efficiency and for studying novel contrast agents issued from pharmaceutical companies (following article).

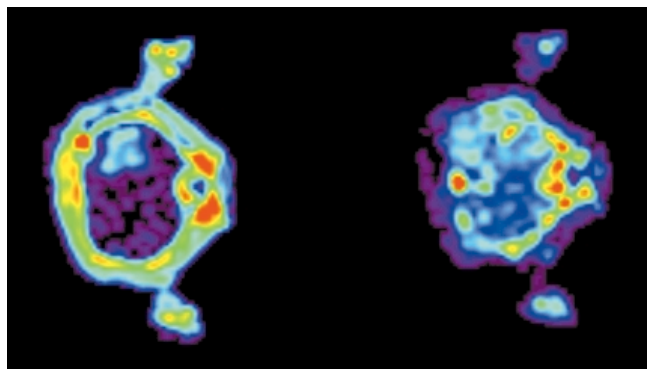


Fig. 96: From left to right: permeability and blood volume map obtained on a rat brain tumour.

The other important activity performed at the beamline is radiotherapy. Three radiation therapy techniques are currently under development on rats bearing cerebral tumours:

- Micro Beam Radiation Therapy is very promising for the treatment of cerebral tumours. It consists of a spatially fractionated beam, which allows the delivery of lethal doses to the tumour while sparing surrounding healthy brain tissues. Important steps from the pre-clinical phase towards the treatment of human tumours have been achieved [4].
- Another method is known as Tomotherapy. It consists of loading the tumour with a contrast agent in association with low energy X-ray irradiation (50-100 keV) during a rotation of the sample into the beam. The agent passes through the impaired blood brain barrier of the tumour vasculature. When using an iodinated contrast agent, the dose delivered to the tumour is enhanced thanks to the energy absorbed by the heavy element.
- Photon Activation Therapy is the irradiation of tumoural cells after introduction of cis-platinum in the cell culture medium. Cis-platinum is a widely used chemotherapy agent, it enters the nucleus and causes direct DNA damages when it produces photo-electrons under irradiation. Trials on rats bearing gliomas were carried out in various conditions of associated chemotherapy or

contrast agent infusion and overall X-ray dose delivery. Outstanding increased survival rates were obtained with cis-platine infused directly in the tumour location before the irradiation in tomographic mode. Such results were the best ever obtained on pre-clinical trials aimed to cure the F98 model of brain glioma, and better than all others radiation therapy modalities. Moreover, basic studies dedicated to the analysis of the DNA damages and repair process on human cells incubated with cis-platinum showed the radiation damage depends on the wavelength when using a quasi-monochromatic beam.

The programmes developed on the ESRF medical beamline **ID17** are the result of fruitful collaborations with different institutions located in different countries. The involvement of a team of the Grenoble university hospital allowed clinical protocols to become a reality.

The trends for medical research at the ESRF for the near future covers a wide range, which goes from basic studies up to clinical trials. This programme involves a lot of pre-clinical work, which clearly is not to be done on human beings. This implies work on small animals, and the ESRF has invested in facilities which allow experimentation in good conditions, both scientifically and ethically. The combination of imaging for diagnosis and radiotherapy remains the main axis of the work to be performed.

References

- [1] W. Thomlinson, P. Berkvens, G. Berruyer, B. Bertrand, H. Blattmann, E. Brauer, T. Brochard, A.-M. Charvet, S. Corde, M. DiMichiel, H. Elleaume, F. Estève, S. Fiedler, J.A. Laissue, J.-F. Le Bas, G. Le Duc, N. Lyubimova, C. Nemoz, M. Renier, D.N. Slatkin, P. Spanne and P. Suortti, *Cell. and Mol. Biol.* **46**(6), 1053-1063 (2000).
- [2] H. Elleaume, S. Fiedler, B. Bertrand, T. Brochard, F. Estève, J.F. Le Bas, G. Le Duc, C. Nemoz, M. Renier, P. Suortti and W. Thomlinson, *Phys. Med. Biol.* **45**, L39-L43 (2000).
- [3] S Bayat, G. Le Duc, L. Porra, G. Berruyer, C. Nemoz, S. Monfraix, S. Fiedler, W. Thomlinson, P. Suortti, C.G. Standertskjold Nordenstam and A.R.A. Sovijarvi, *Phys. Med. Biol.* **46**(12) 3287-3299 (2001).
- [4] A. Laissue, H. Blattmann, M. Di Michiel, D.N. Slatkin, N. Lyubimova, R. Guzman, W. Zimmermann, S. Birrer, T. Bley, P. Kircher, R. Stettler, R. Fatzer, A. Jaggy, H.M. Smilowitz, E. Brauer, A. Bravin, G. Le Duc, C. Nemoz, M. Renier, W. Thomlinson, J. Stepanek and H-P. Wagner, in *Medical Applications of Penetrating Radiation*, H.B. Barber, H. Roehrig, F.P. Doty, R.C. Schirato, E.J. Morton (Eds.), *Proceedings of SPIE* **4508**, 65-73, (2001).

Absolute Cerebral Blood Volume (CBV) and Blood Flow (CBF) Measurements Based On Synchrotron Radiation Quantitative Computed Tomography

CBV and CBF are important perfusion parameters related to cerebral haemodynamic changes such as those observed in brain tumours, stroke or ischemia. Most of the medical imaging methods have been used to quantify these parameters *in vivo* and to build functional maps of the brain. All of these methods have major drawbacks for an acute tracer concentration quantification, which is the basis of perfusion assessment (poor spatial resolution for PET, non-linearity for MRI, beam hardening and scattering for CT scanners). Synchrotron Radiation Computed Tomography (SRCT) opens new fields by using monochromatic (avoiding beam hardening effects) and parallel X-ray beams allowing the sample to be placed far from the detector (thus avoiding scattering effects). This technique allows measuring absolute contrast agent concentrations with high accuracy and precision [1] with a good spatial resolution (0.35 mm for the ID17 germanium detector). A relative error on the measured concentrations less than 1% is found for the range 0.35 to 1 mg mL⁻¹ of iodine, which corresponds to the usual concentrations measured in the brain tissue. A relative error less than 3% is found for the range 2 to 25 mg mL⁻¹ of iodine, which corresponds to usual

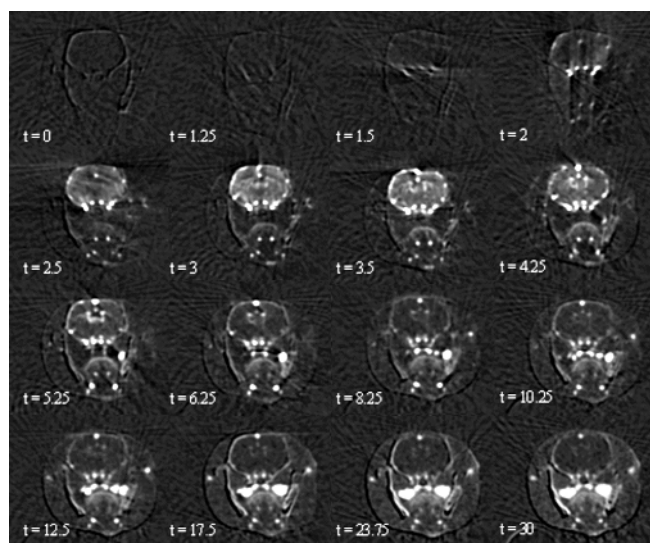


Fig. 97: Head axial time course of iodine concentration maps (mg mL⁻¹) on a healthy rat obtained by SRCT, after a bolus infusion (only 16 images amongst 125 are displayed). Time (t) is expressed in s, the infusion starts at t = 0. Iodine enters the brain vasculature via the arterial inputs, passes through the brain microvasculature and is washed out by the intracerebral and extracerebral venous outputs.

concentrations measured in the blood vessels. A noise equivalent to 55 µg mL⁻¹ of iodine is observed in the SRCT measurements.

Absolute CBV or CBF measurements are based on the method employed in dynamic computed tomography [2]. It uses the time course changes in the iodine concentration after the infusion of a bolus of iodinated contrast agent in each voxel of the brain tissue in comparison of the same changes in an arterial input of the brain. In this model, the CBV, CBF and Mean Transit Time (MTT) calculations are theoretically derived from the non-diffusible tracer kinetic theories applied to dynamic CT bolus tracking methods, since the contrast agent remains intravascular.

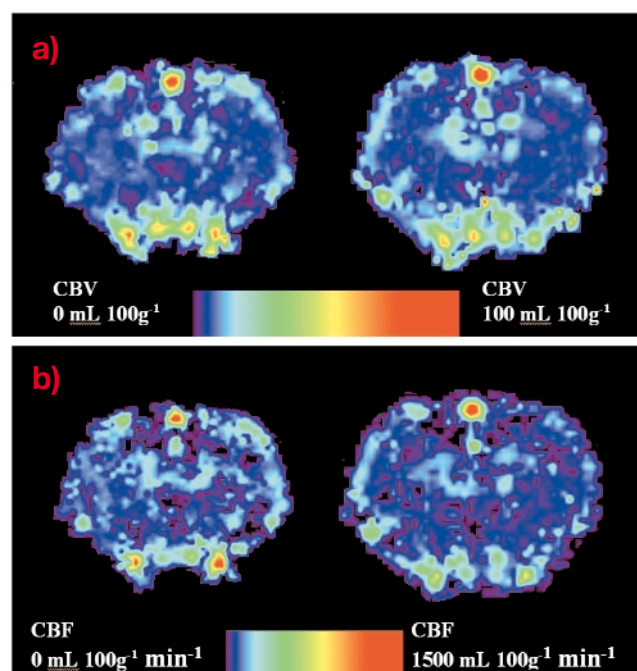


Fig. 98: a) Transverse CBV maps of two healthy rat brains. From purple to red the CBV increases from 0 to 100 mL 100 g⁻¹. b) Transverse CBF maps of the same rat brains than the ones used for figure 98a. From purple to red the CBF increases from 0 mL 100 g⁻¹ min⁻¹ up to 1500 mL 100 g⁻¹ min⁻¹. Black pixels inside the brain slices indicate voxels where the CBF cannot be determined.

The experiments are performed on healthy rats. After the intravenous injection of a bolus of an iodinated contrast agent, Computed Tomography (CT) images are acquired every 2 seconds. The first image acquired before iodine infusion is subtracted from the others in order to get CT slices expressed in absolute iodine concentrations (Figure 97). Each pixel of the slice provides a curve representing the iodine time course in the corresponding brain voxel. These curves are fitted by gamma-variate functions in order to avoid the recirculation phenomenon. CBV and CBF maps (Figure 98a and b) are then computed by using these fits in the tracer kinetics models. A correction for partial volume effects in the chosen arterial input is necessary for a good quantification. Mean CBV and CBF values (n = 7) are

found equal to $2.1 \text{ mL } 100 \text{ g}^{-1} \pm 0.38$ and $129 \text{ mL } 100 \text{ g}^{-1} \pm 18$ in the parietal cortex; $1.92 \text{ mL } 100 \text{ g}^{-1} \pm 0.32$ and $125 \text{ mL } 100 \text{ g}^{-1} \pm 17$ in the caudate putamen. These values are in good agreement with the reported ones in the literature.

This is the first *in vivo* assessment of the CBF and the CBV based on synchrotron radiation quantitative computed tomography. It is a new tool for studies in cerebral physiopathology hemodynamic changes, such as those observed in brain tumours or in cerebrovascular diseases. This method could be useful especially in the domain of novel attempts to treat brain tumours as far as these therapies induce changes in the brain perfusion. Various modalities of radiation therapy using synchrotron radiation are under active development in different synchrotron facilities, including the ESRF. The possibility of assessing brain perfusion reinforces the potential of these programmes.

References

- [1] H. Elleaume, A.M. Charvet, S. Corde, F. Estève and J.F. Le Bas, *Phys Med Biol* **47**, 3369-3385 (2002).
- [2] L. Axel, *Radiology* **137**, 679-686 (1980).

Principal Publication and Authors

J.-F. Adam (a), H. Elleaume (a), G. Le Duc (a, b), S. Corde (a), A.-M. Charvet (a), I. Troprès (a, b), J.-F. Le Bas (a), F. Estève (a), *J Cereb Blood Flow and Metab.*, in press.
 (a) Équipe d'Accueil RSRM, MRI Department, CHU Grenoble (France)
 (b) ESRF

Characterisation of Cancerous Breast Tissues by the Diffraction-enhanced Imaging (DEI) Technique

Early detection and characterisation of breast abnormalities like small mass lesions and microcalcifications is crucial to a positive prognosis of breast cancer as they may indicate malignant tumours. The absorption contrast of such signatures in radiographs obtained by standard mammography is limited by the acceptable radiation dose that can be given to the breast. The size of the details that still can be visualised is limited also by dose and by diffuse scattering from the breast tissue.

The DEI technique can reduce considerably these limitations. It can sense phase gradients in the diffraction

plane of the analyser crystal that is introduced behind the tissue sample. Since such phase effects can be strong for low Z elements, spectacular contrast enhancements have been achieved in mammograms obtained with this technique [1,2]. In addition, diffuse scattering is intrinsically rejected by the analyser crystal and the possibility for significant dose reduction is offered due to the weaker energy dependence of phase in comparison with absorption [3].

However due to the different nature of the phase dependent contrast process, DEI mammograms differ greatly in appearance and are more complex than conventional images. In order to facilitate the interpretation of DEI images and in particular to identify malignant lesions and differentiate them from normal tissue, we performed a comparison between DEI- and conventional images and the histology of the sample.

A detailed analysis of the samples is based on computed tomography (CT) images taken by the DEI method at slices that are prepared for histo-pathology after X-ray imaging, so that there is an approximate one-to-one correspondence of positions. This also ensures a better identification of details than for planar projection images where different structures in the projection direction can be superimposed. However projection images are used as reference material to make a connection to conventional mammography.

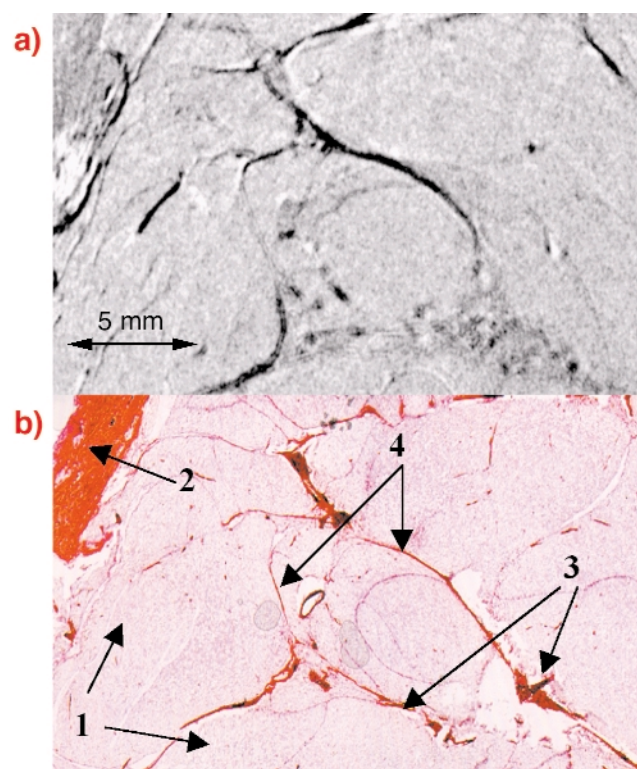


Fig. 99: a) DEI-CT image of cancerous breast tissue showing excellent correspondence with the histological section b) taken at the same position. Arrows 1 indicate adipose tissue, arrow 2 skin and muscular tissue, arrows 3 cancer cells embedded in collagen, and arrows 4 collagen strands.

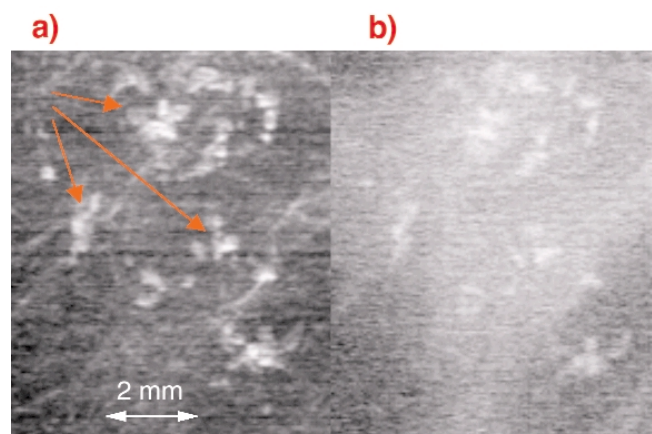


Fig. 100: a) DEI planar projection of a ductal carcinoma with malignant microcalcifications (indicated by arrows); b) conventional radiograph of the sample imaged with the same detector and dose at 33 keV.

An example for a DEI-CT image of breast tissue invaded by a malignant tumour is shown in **Figure 99a** and the corresponding stained histological section in **Figure 99b**. Fine details of the different tissue structures found in the histology can be identified in the DEI image. In particular, the histological examination reveals collagen strands along which cancer cells penetrate into the adipose tissue. Such strands are difficult to visualise in conventional mammography but they are clearly distinguishable in the DEI images.

In many cases microcalcifications constitute only benign lesions. Nonetheless, they can be the most important radiological indicator for early breast cancer. In order to distinguish between malignant and benign microcalcifications they have to be classified according to their size, number, morphology, location and distribution. A typical cluster of malignancy indicating microcalcifications, which have variable size and shape and irregular margins, is shown in **Figure 100**. The analyser-based planar projection image (**Figure 100a**) allows a much better characterisation than the conventional radiograph (**Figure 100b**) recorded under the same conditions.

In connection with this work, standard mammographic phantoms have been imaged with doses lower than 0.1 mGy (mean glandular dose). The potential for low-dose imaging together with the additional diagnostic information obtainable with the DEI method make an extension to human studies envisageable.

References

- [1] E.D. Pisano, R.E. Johnston, D. Chapman, J. Geradts, M.V. Iacocca, C.A. Livasy, D.B. Washburn, D.E. Sayers, Z. Zhong, M.Z. Kiss, W.C. Thomlinson, *Radiology* **214**, 895-901 (2000).
- [2] F. Arfelli, V. Bonvicini, A. Bravin, G. Cantatore, E. Castelli, L. Dalla Palma, M. Di Michiel, M. Fabrizioli, R. Longo, R.H. Menk, A. Olivo, S. Pani, D. Pontoni, P. Poropat, M. Prest, A. Rashevsky, M. Ratti, L. Rigon,

G. Tromba, A. Vacchi, E. Vallazza, F. Zanconati, *Radiology* **215**, 286-293 (2000).

[3] A. Bravin, S. Fiedler, W. Thomlinson; *Medical Imaging 2002; Proceedings of SPIE* **4682**, 167-173 (2002).

Authors

S. Fiedler (a), A. Bravin (a), J. Keyrilainen (b), M. Fernandez (a), P. Suortti (c), W. Thomlinson (d), P. Tenhunen (b), P. Virkkunen (b), M.-L. Karjalainen Lindsberg (b), *submitted to Applied Radiology*.

(a) ESRF

(b) Helsinki Central University Hospital (Finland)

(c) University of Helsinki (Finland)

(d) Canadian Light Source (Canada)

Waste Incineration: Why is a Synchrotron-based Multidisciplinary Approach Needed?

Review by A. Somogyi (ESRF) and M.C. Camerani Pinzani (Dep. of Inorg. Environm. Chem., Chalmers Univ. of Technology, Göteborg, Sweden)

Finding alternative sources of energy for the decreasing stocks of fossil fuels and dealing with the increasing amount of waste which pollutes the environment are serious problems of our times. Waste incineration appears to be a potential solution for both problems since it has the advantage of transforming the wastes stored chemical energy into electricity or heat while reducing its volume and destroying the chemical reactivity of its organic compounds.

However incineration, as with the combustion of other fuels, creates large quantities of ash containing concentrated amounts of potentially toxic trace metals (*i.e.* Pb, Ni, Cu, Cd). Thus heat and power technologies based on combustion of such complex fuels require the development of routines for intelligent ash management that make thorough knowledge of the chemical properties of the ash material essential.

The complex study of heavy metal distribution, concentration, speciation and of matrix composition and morphology within individual fly ash particles are of great importance for the evaluation of the possible environmental impact of ash material. This is a valuable complement to the usual bulk analytical methods. The investigation of individual particles is the only possible

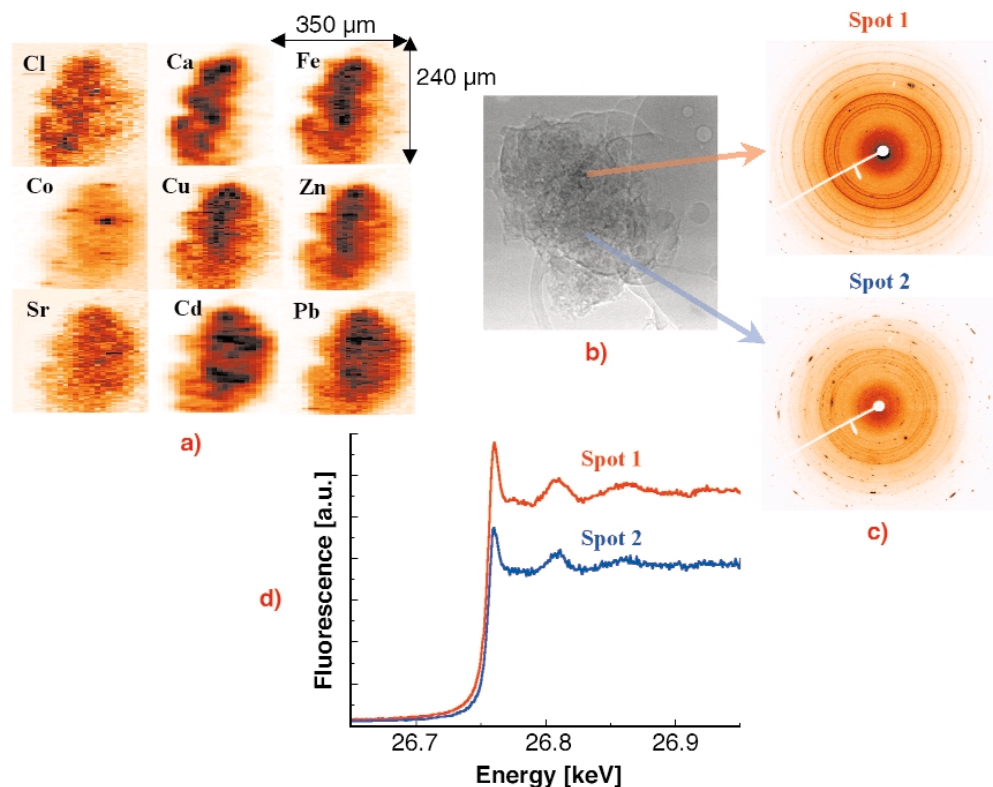


Fig. 101: Investigation of a single municipal waste fly ash particle by different micro X-ray analytical methods. (a) 2D X-ray fluorescence maps, step size: H x V: 2 x 10 mm²; (b) absorption image registered by a high-resolution CCD camera; (c) X-ray diffraction patterns registered by a large area CCD; (d) Extended XANES spectra measured in the chosen spots of the particle.

method to check and develop theoretical models of potential fly ash forming processes during combustion. This might lead to the improvement of the combustion procedure itself through a better control of the transport of heavy metals.

The **ID22** multipurpose X-ray microprobe beamline is well-suited for the microscale investigation of such complex materials. The energy of the X-ray beam can be tuned in the 6–70 keV range in order to obtain optimal excitation conditions for the elements to be studied. With the help of different focusing devices e.g. Kirkpatrick-Baez (KB) mirrors ($E < 18$ keV) and refractive lenses ($E > 15$ keV), the X-ray source can typically be demagnified to a V x H: 1.5 x (3–10) μm² spot with 10¹⁰–10¹¹ ph/s intensity in the $E < 30$ keV energy region. Several routinely-available micro-analytical techniques, such as micro X-ray fluorescence analysis (μ-XRF), micro X-ray absorption spectrometry (μ-XAS), micro-diffraction (μ-XRD) and absorption/phase contrast imaging and tomography, make the complex analysis of the sample possible.

The investigation of individual fly ash particles was performed at 27 keV excitation energy in order to excite the characteristic X-ray lines of heavy metals up to Cd [1,2]. The beam was focused by compound refractive lenses (CRL) to a V x H = 2 x 10 μm² spot. In order to investigate the spatial elemental distribution and inter-elemental correlation within single particles and the dependence of the heavy metal content on the particle size, several particles of different sizes were raster scanned in the focused beam while registering the XRF spectra in each voxel. The obtained 2D characteristic X-ray intensity

maps of a large particle can be seen in **Figure 101a**. The variation of the crystalline structure of the matrix was measured simultaneously in each voxel by collecting XRD WAXS spectra using a large area CCD detector (see **Figure 101c**) in order to study the possible attachment of the investigated elements to a given crystalline structure.

The dissolution and transport of metal ions from the ash matrix to soil water are key steps because dissolved ions are available for biological uptake and ground water contamination. Thus the toxicity of ash strongly depends on the chemical speciation of the different potentially toxic elements. The chemical speciation of a given element in a voxel chosen on the basis of the 2D XRF/XRD maps can be investigated by micro-XAS. The extended XANES spectra of the element to be investigated (see **Figure 101d**) is obtained by changing the energy of the monochromatic excitation X-ray beam in the vicinity of the absorption edge while registering the intensity of its characteristic X-ray intensity (fluorescence mode). The obtained XAS spectra provide information about the oxidation state and first shell neighbours of the element.

The eventual fate of heavy metals is also influenced by their position within the particle: on the surface they are more prone to leaching while at some depth within the matrix they might be more shielded from chemical attack by water. Due to the large penetration depth of high energy X-rays the 2D intensity maps (see **Figure 101a**) only reflect the variation of the overall concentration among the irradiated voxels but do not give any information about the internal elemental distribution.

These internal elemental distributions can be reconstructed by appropriate mathematical algorithms from X-ray sinograms obtained by successive linear scans and rotations of a slice of the sample (X-ray fluorescence tomography). X-ray absorption tomography can be used to obtain information about the particle morphology (3D linear absorption coefficient distribution), usually determined from light, non-detectable elements.

Some important conclusions can be drawn from the study of waste fly ash particles about the chemical properties of their Cd-content [3]. In most of the cases the main Cd-bearing phase was the Ca-containing matrix. Cd identified in this study was found to be evenly distributed throughout all the particle sizes investigated. X-ray fluorescence tomography showed that Cd was distributed not only on the surface but also within the matrix of the investigated slices. Comparing XAS spectra of fly ashes and reference compounds showed that in the particles studied Cd is present in the oxidation state +2. Analysis of linear combinations of standard spectra allows us to estimate the fly-ash composition as an admixture of CdSO_4 , CdO and CdCl_2 in all the analysed spots.

From an environmental perspective, these results are of particular importance when considering the short-term leaching potential of fly ashes. The fact that Cd appears in an easily soluble form in a soluble particle matrix (Ca) can make the direct dumping of fly ashes problematic but on the other hand it might allow a leaching medium to concentrate Cd-containing phases before dumping the major fraction of ash material. It is expected that the knowledge of the spatial elemental distribution and speciation of different heavy metals, as obtained in the present study for Cd, would allow formulation of models for the formation of fly ash particles during the combustion process. These models may be used as a basis to improve Fluidised Bed Combustion processes by including the control of the transport of heavy metals.

The technique presented here is applicable to fly ash from all sorts of fuel, like coal, sludges, biomass, peat and their mixtures, as well as from municipal solid wastes.

References

- [1] M.C. Camerani, A. Somogyi, M. Drakopoulos, B.-M. Steenari, *Spectrochimica Acta Part B* **56**, 1355-1365 (2001).
- [2] M.C. Camerani Pinzani, A. Somogyi, B. Vekemans, A.S. Simionovici, B.M. Steenari, I. Panas, *submitted to Environmental Science and Technology* (2002).
- [3] M.C. Camerani Pinzani, A. Somogyi, A. Simionovici, S. Ansell, B.M. Steenari and O. Lindquist, *Environmental Science and Technology* **36** (14), 3165 – 3169 (2002).

Phase Contrast X-ray Microscopy at 4 keV Photon Energy with 60 nm Spatial Resolution

Recent progress in nanotechnology makes it possible to fabricate high aspect ratio Fresnel zone plates with nearly theoretical diffraction efficiency. For the multi-keV photon energy range, such zone plates are made of gold and are used as condenser and objective lenses. They permit X-ray imaging with high spatial resolution and short exposure times. Similar to conventional light microscopy, the resolution of an X-ray microscope is best when illuminating the object with a condenser, whose aperture is matched to the aperture of the imaging objective. The full-field X-ray microscope installed at the **ID21** beamline, operating at 4 keV photon energy with condenser and objective zone plates of matched apertures and 50 nm outermost zone width, currently achieves 60 nm spatial resolution. It was realised that many scientifically-relevant samples provide only weak absorption contrast in the multi-keV photon energy range, whereas much higher contrast could be achieved in the phase contrast mode of an X-ray microscope [1].

According to Zernike, phase contrast images are obtained in a full-field microscope by inserting a phase plate in the objective's back focal plane, which only shifts the undiffracted light's phase. In the novel Zernike-type phase contrast mode of the X-ray microscope, a ring-shaped condenser in combination with a central beam stop (see **Figure 102**) provides a hollow-cone illumination of the object. This also creates an image field free of zero order radiation from the zone plate objective and allows the introduction of a ring-shaped phase plate matched to the location of the undiffracted light, while light diffracted by sample structures remains nearly unaltered. Thereby, the phase information of the object is transformed into an

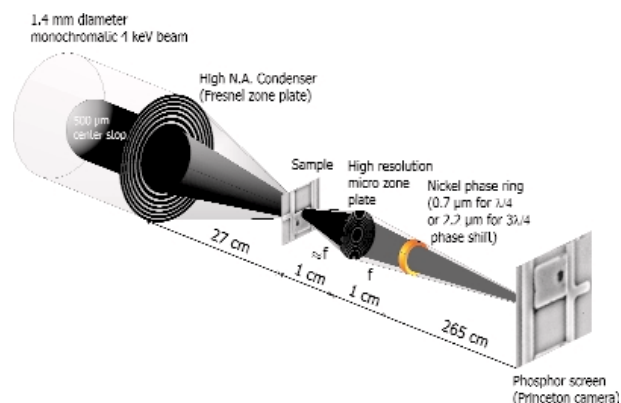


Fig. 102: Schematic of the optical setup of the X-ray microscope (TXM) in Zernike phase contrast mode. A zone plate condenser focuses the monochromatised undulator beam onto the object and a micro zone plate objective forms a magnified image on a phosphor-coupled CCD camera. The phase ring selectively phase shifts the undiffracted light of the object.

intensity modulation in the image plane. In the Zernike-type phase contrast setup, even the image contrast of weakly phase-shifting samples can be tuned to almost any value by employing optimised phase rings, which also strongly attenuate the undiffracted light [2].

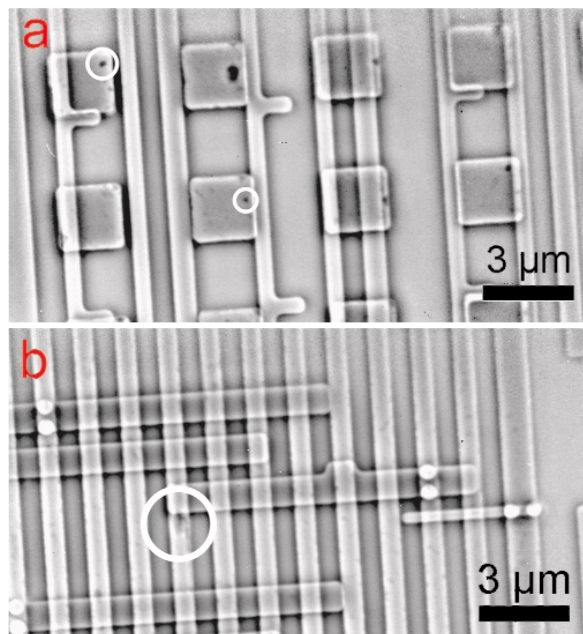


Fig. 103: Different copper interconnect structures, imaged in positive phase-contrast mode in the ID21 transmission X-ray microscope. Irregularities in the square structures (as indicated by the white circles) can be seen in image 103(a). Furthermore, an irregularity within a conducting copper line is indicated by the white circle in image 103(b).

In the multi-keV photon energy range, phase-contrast X-ray microscopy is a new tool for investigations in biology, materials and environmental sciences. As an example for high-resolution phase contrast imaging in the Zernike mode, we apply this technique to integrated circuits. State-of-the-art microprocessors, which operate at frequencies in the GHz range, require the integration of more than 100 million transistors which have to be connected by metal lines buried in dielectrics. As the line width of the interconnects continue to shrink, the formation of voids in interconnects induced by high current densities (electromigration) during integrated circuit operation can cause an open circuit or an increase in resistance, resulting in malfunction or speed degradation. Phase-contrast X-ray micrographs of advanced microprocessor test structures with copper interconnects and vias are shown in **Figure 103** and **Figure 104**. As demonstrated with these images, phase-contrast X-ray microscopy is a powerful new technique for integrated circuit process parameter control and defect analysis.

Future perspectives for this technique include the development of new phase-contrast microscopes operating at higher energies, driven by the possibility to study weakly-absorbing structures in thick samples with high spatial resolution. In addition, due to the large depth of field of X-ray objectives operating in the keV photon

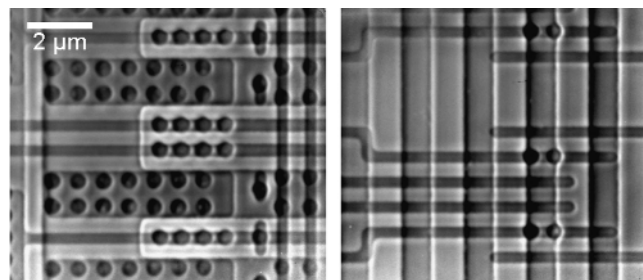


Fig. 104: Negative phase-contrast images of microprocessor structures from different regions on a chip, imaged with the ID21 transmission X-ray microscope. Note that the contrast is reversed compared to the X-ray micrographs taken in positive phase contrast shown in Figure 103(a) and (b).

energy range, high-resolution tomography based on X-ray microscope images is possible.

The authors are indebted to E. Anderson and B. Harteneck from the Center for X-ray Optics, LBNL, Berkeley, for fabricating the phase rings.

References

- [1] U. Neuhausler, G. Schneider, W. Ludwig, D. Hambach, *Proceedings of the 7th International Conference on X-ray Microscopy, Journal de Physique IV, in press*
- [2] G. Schneider, U. Neuhausler, W. Ludwig, D. Hambach, *submitted*

Principal Publication and Authors

U. Neuhausler (a), G. Schneider (b), W. Ludwig (a,c), M.A. Meyer (d), E. Zschech (d), D. Hambach (e), *J. Phys. D, in press.*

(a) ESRF

(b) Center for X-ray Optics, Lawrence Berkeley National Laboratory (LBNL), Berkeley (USA)

(c) now with INSA de Lyon, Villeurbanne (France)

(d) AMD Saxony LLC & Co. KG, Dresden (Germany)

(e) Institut für Röntgenphysik, Universität Göttingen (Germany), now with EPO, Munich (Germany)

Imaging Sulphur-metabolising Activities in Individual Filamentous Bacteria and Microfossils

Microbially-mediated oxidation and/or reduction of sulphur and iron emanating at deep-sea hydrothermal vents are known to be important globally. Because of their morphological similarities with modern S- and Fe-oxidising bacteria producing filamentous sulphur and

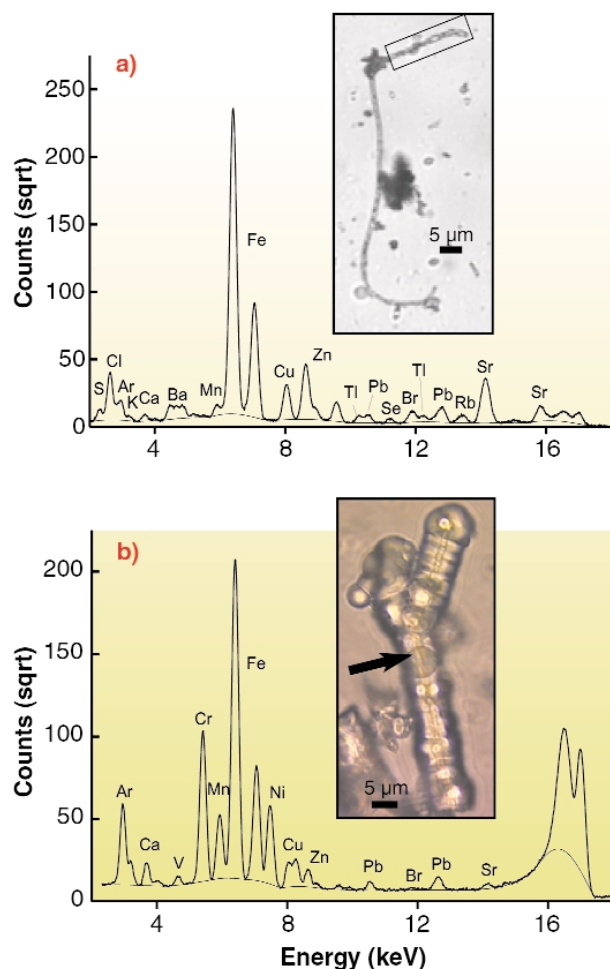


Fig. 105: X-ray microfluorescence spectra of (a) individual filamentous bacteria from the Mid-Atlantic Ridge (the delimited area corresponds to the zone analyzed for its sulphur redox distribution (Figure 106b) and (b) iron-oxide filament (arrowed) of putative biogenic origin encapsulated with amorphous silica from the East Pacific Rise.

hydrous ferric oxides, a putative microbial origin has been proposed for filamentous microfossil remains in fossil hydrothermal vent sites as well as other ancient environments. The oldest record is that of Rasmussen [1], who reported pyritic filaments in deep-sea volcanic rocks that are some 3,200 million years old, thus providing support for proposals in favour of a thermophilic origin of life (*i.e.*, non-photosynthetic microbes utilising inorganic matter in their environment as the energy source and which lived at or near 100°C at depths far below the light-penetration zone on the sea floor). Morphological resemblance, however, is not sufficient for discriminating between true microbial fossils and nonbiogenic microstructures, specifically considering their minute size and incomplete preservation in geological material. Hence, an important challenge for microbiologists, geochemists and exobiologists is to extract unequivocal biogenic information from individual microfossils using high-resolution, non-destructive and sensitive techniques.

Here, we use combined synchrotron micro-XANES (ID21) and X-ray micro-fluorescence (SXRF; ID22) analyses to

illustrate the spatial distribution on a μm-scale of a variety of potential biogenic markers (major and trace elements and sulphur-oxidation states) in individual filaments. Two types of filaments were analysed. 1) Sulphur- or iron-rich filaments of most likely ϵ -Proteobacteria organisms collected from a micro-coloniser device exposed for 15 days to a fluid source vent of the Mid-Atlantic Ridge [2] (Figure 105a) and 2) fossilised iron-oxide filaments of putative biogenic origin encapsulated with amorphous silica from a fragment of an inactive chimney of the East Pacific Rise [3] (Figure 105b).

SXRF spectra of filamentous bacteria and microfossils contain X-ray peaks of Ca, Ba, Mn, Fe, Cu, Zn, Pb, Br and Sr. In addition to these, Cr and Ni has been detected in the fossil microfilament and S, K, Ti, Se and Rb in the microbial filament. Owing to the high absorbance of the siliceous envelope, only a weak X-ray peak of sulphur was identified in the fossil filament. The origin of S, Ti and Se and possibly that of Mn, Fe, Cu and Zn, may be attributed to the microbe metabolic activity. In contrast, Cl, K, Ca, Ba, Br, Rb and Sr are most likely derived from seawater.

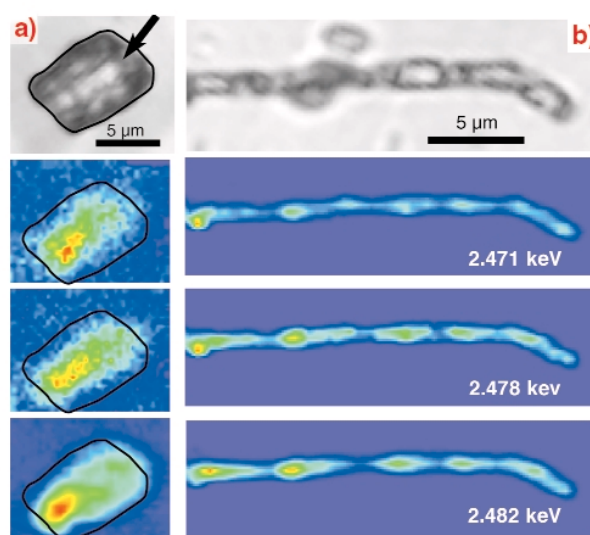
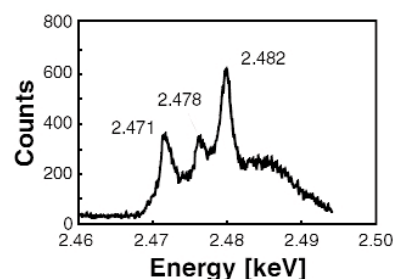


Fig. 106: Micro-XANES spectrum of sulphur in individual filaments showing three peaks at 2,482 eV (sulphate), 2,471 and 2,478 eV (sulphide and -SH radicals). Associated maps show the distribution of sulphate, sulphide and SH-radicals within (a) a fragment of filamentous microfossil from the EPR (the arrow points to the trace of the filament embedded in the siliceous envelope) and (b) a microbial filament from MAR (note that sulphur distribution mimics the shape of individual microbes).

Micro-XANES spectra (Figure 106) show three main types of sulphur with X-ray peaks at 2,471, 2,478 and 2,482 eV. The marked peak at 2,482 eV is characteristic of sulphate. The peaks at 2,471 and 2,478 eV are typical of sulphide or –SH amino acid groups, or both. Mapping of the different forms of sulphur performed at energies of 2,471, 2,478 and 2,482 eV revealed different distributions of sulphates, sulphides and amino acid-SH groups. Recognition of a heterogeneous overlap of sulphides and SH-radicals strongly suggests that the two sulphur components are present in the same filament. In both types of filaments, the occurrence of three main sulphur species showing heterogeneous distribution on a filament scale and locally underlining the shape of individual bacteria (microbial filament), strongly suggests that the original microorganisms were actively metabolising sulphur. Despite uncertainties on the metabolic capability of the bacteria that produced the filaments studied here, these results show the potential of combining high-resolution SXRF and micro-XANES techniques for extracting unequivocal biogenic information from fossilised hydrothermal systems or extraterrestrial material.

References

- [1] B. Rasmussen, *Nature* **405**, 676-679 (2000).
- [2] P. Lopez-Garcia, H. Philip, F. Gaill, D. Moreira, *PNAS*, *in press*.
- [3] S.K. Juniper, Y. Fouquet, *Can. Mineral.* **26**, 859-869 (1988).

Principal Publication and Authors

P. Philippot (a), J. Foriel (a), J. Cauzid (a, b), J. Susini (b), B. Menez (a), A. Somogyi (b), submitted to *PNAS*.

(a) *Laboratoire de Géosciences Marines, Institut de Physique du Globe, CNRS, Paris (France)*

(b) *ESRF*

Topographic and Quantitative Elemental Analysis of Human Central Nervous System Tissue

Though well-characterised, the pathogenesis of neurodegenerative disorders *i.e.* Parkinson's disease (PD) and amyotrophic lateral sclerosis (ALS) is still unknown. There is strong evidence that processes leading to degeneration and atrophy of nervous cells can be promoted by abnormal biochemical reaction catalysed by selected metal ions [1,2]. The main goal of this study is a better understanding of the role of metals in PD and ALS. The microbeam synchrotron X-ray fluorescence (μ -SXRF) technique was used to obtain topographic and quantitative analysis of selected elements in central nervous system (CNS) tissue from PD, ALS and control cases. Two areas of CNS, *i.e.* substantia nigra (SN) of brain and thoracic spinal cord were sampled. Nonstained, cryomicrotome slices were investigated.

The measurements were carried out on beamline ID22. The polychromatic pink beam mode excitation was used at a final beam spot of 5 μ m x 2 μ m (horizontal x vertical). The elements such P, S, Cl, K, Ca, Fe, Cu, Zn, Se, Br, Rb and Sr were identified in CNS tissue. Two-dimensional maps of elemental distribution were compared with the microscopic view of the histopathological sections. The results showed that significantly higher intensities of selected elements in μ -SXRF images correspond to the position of the neurons in the tissue slices. Particularly, in the control group, neurons of *substantia nigra* revealed higher accumulation of S, Cl, K, Ca, Fe, Zn, Se and Rb when compared to the surrounding area. Figure 107 shows

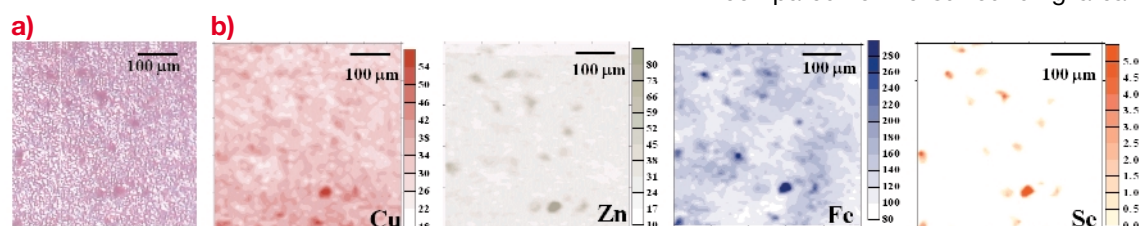


Fig. 107: *Substantia nigra* – the control case: (a) microscopic view of scanned area of the tissue; and (b) distribution of selected elements. The neurons are seen on the optical image as the dark points. The values on the scales represent intensities in relative units.

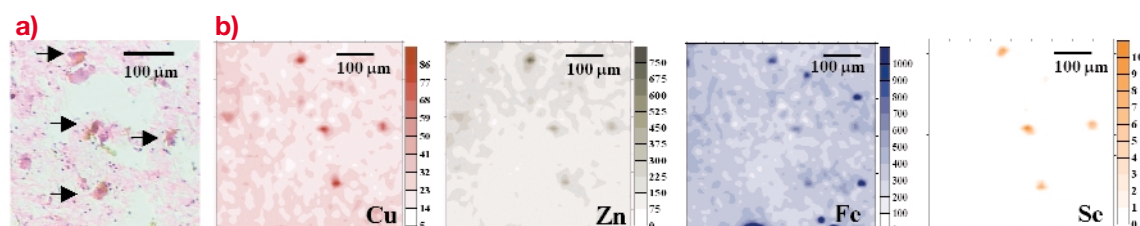


Fig. 108: *Substantia nigra* – the PD case: (a) microscopic view of scanned area of the tissue; and (b) distribution of selected elements. The arrows show neuron localisation. The values on the scales represent intensities in relative units.

the distribution of Cu, Zn, Fe and Se together with the optical image of the scanned area of the control tissue.

The elemental maps obtained from the tissue slices of spinal cord show, in the control case, a correlation between neuron bodies positions and increased content of S, Cl, K, Ca, Zn, Br and Rb. Such correlation is not observed for Fe and Cu, whereas P is accumulated to a lower degree inside the perikarial part of the neuron. The topographic results obtained for ALS tissue slices of spinal cord are in good agreement with those observed for the control group excluding S.

The distribution of selected elements in PD tissue is presented in **Figure 108**. The quantitative analysis indicated that SN neurons of the PD samples show a strong accumulation of Cu and Fe and a significantly higher accumulation of S, Ca, Zn, Se and Br in comparison with the control case. For the same part of the brain, an increased content of Cl, Ca, Zn, and Br was noticed for the ALS case. The quantitative analysis reveals a decreased level of Zn in the degenerated motor neuron of spinal cord in the ALS cases studied.

The present study indicated that μ -SXRF is a very powerful tool for the study of abnormalities in elemental concentrations, in thin CNS tissue sections at the single cell level. These abnormalities may promote biochemical reactions leading to pathological changes in CNS tissue especially to the degeneration and atrophy of neurons. Our results are in good agreement with existing hypotheses concerning the neurodegenerative role of trace elements, which are based on *in vitro* investigations or experiments on animals. These results should help us gain some information on metal function in the central nervous system tissue for neurological disorders. Particularly interesting is the perspective of using this tool for the investigation of chemical states of metallic elements in tissues from sites of degeneration.

References

- [1] L.M. Sayre, G. Perry, M.A. Smith, *Current opinion in Chemical Biology* **3**, 220-225, (1999).
- [2] J.S. Bains, C.A. Shaw. *Brain Res. Rev.* **25**, 335-358, (1997).

Principal Publication and Authors

M. Lankosz (a), M. Szczerbowska-Boruchowska (a), J. Ostachowicz (a), D. Adamek (b), A. Krygowska-Wajs (b), B. Tomik (b), S. Bohic (c), A. Simionovici (c).

(a) Faculty of Physics and Nuclear Techniques, University of Mining and Metallurgy, Krakow (Poland)

(b) Institute of Neurology, Collegium Medicum, Jagiellonian University, Krakow (Poland)

(c) ESRF

X-ray Standing Wave Microscopy: Chemical Microanalysis with Atomic Resolution

Today's technology and technology-driven research are closely linked to the development of 1-, 2-, and 3-dimensional solid-state structures with length scales ranging from several nanometres for electronic quantum wells to several micrometres for optoelectronic devices, photonic crystals, or micro electro-mechanical systems.

Our development of X-ray Standing Wave (XSW) technique [1] should contribute towards the determination of such structures. XSW is a microscopic technique where we are able to determine the crystalline

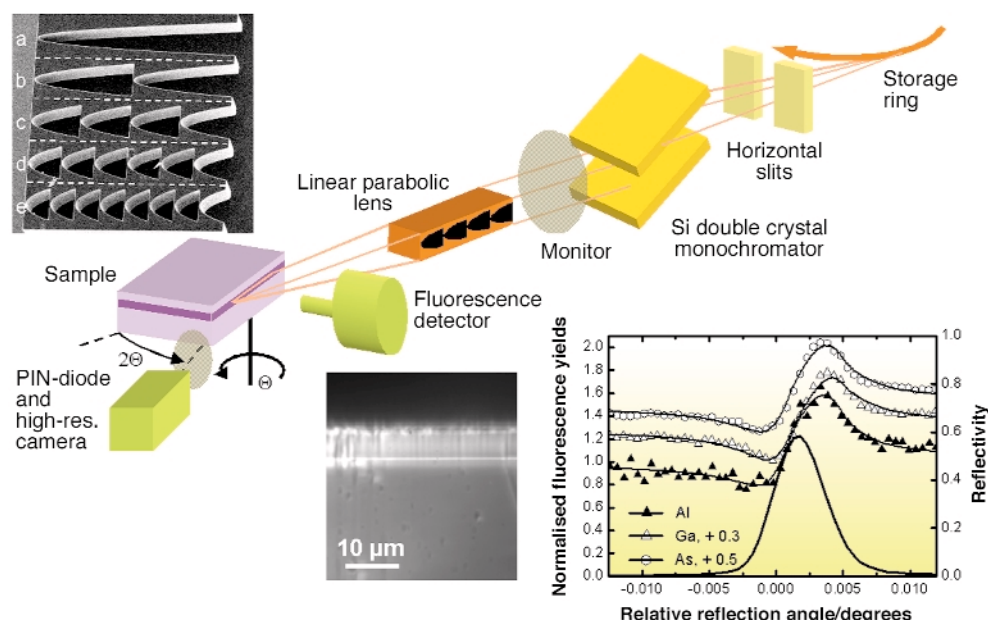


Fig. 109: X-ray standing wave setup for microscopic resolution. The upper left inset shows a set of linear refractive lenses; for this experiment type (c) was used. The high-resolution topogram (lower left inset) reveals the AlGaAs layer, which has a slightly different lattice constant than the GaAs substrate. The micro-XSW measurement on the AlGaAs-layer is shown in the right inset. Reflectivity, fluorescence yields and XSW-fits to the fluorescence yields are displayed as a function of the reflection angle.

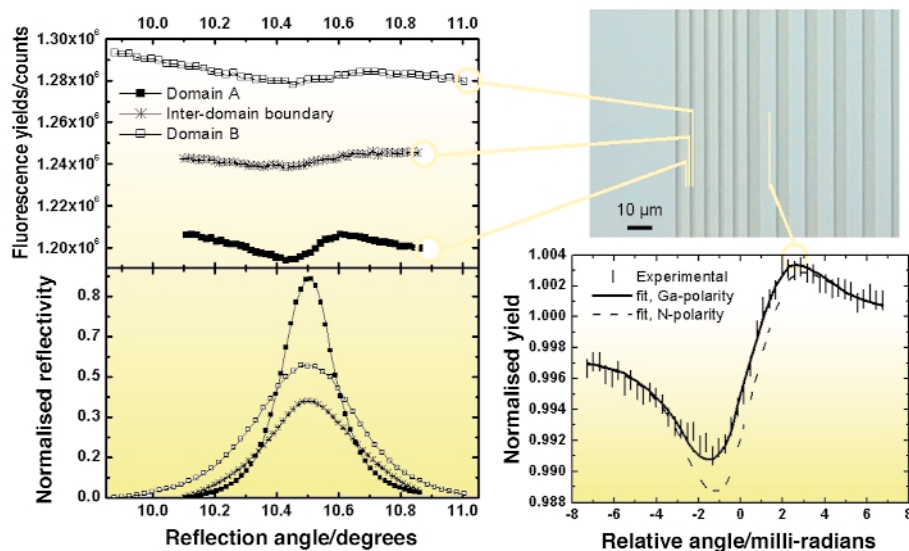


Fig. 110: Micro-XSW on polarity inverted GaN thin films (upper right). Reflectivity and Ga-fluorescence yields for two adjacent domains and the boundary in-between are shown in the left graph. A fitted XSW curve is shown in the lower right.

organisation with subatomic resolution and chemical sensitivity. Moreover, we can exploit its phase sensitivity to characterise materials that exhibit microscopic heterogeneity of their crystallographic polarity.

A micro-XSW setup was realised at beamline **ID22** (Figure 109). Both, the low angular beam divergence (10 μ rad vertically and 20 μ rad horizontally) and the small angular source size (2 μ rad vertically by 40 μ rad horizontally) are necessary conditions to create a monochromatic beam with a low dispersion which can be further focussed by means of a linear refractive lens [2]. With this, an X-ray beam was produced having the dimensions of 1.5 micrometres vertically and 100 micrometres horizontally, with low horizontal divergence.

We analysed a GaAs/AlGaAs/GaAs(001) multilayer structure, nowadays important for quantum-well systems with various applications. Via molecular beam epitaxy, a GaAs buffer layer was grown onto the (001) oriented GaAs-wafer surface, followed by a 4 μ m layer of AlGaAs (10% Al), and a 4 μ m cap layer of GaAs doped with Si. We studied the adjacent layers in cross-section, after cleaving the wafer along the (110) planes (Figure 109). The micro-XSW scans inside the AlGaAs layer and a fit to the measured fluorescence yields (Al K-lines, Ga and As L-lines) reveals the coherent positions P and coherent fractions F of the constituents relative to the AlGaAs (220) planes with $F_{\text{Al}} = 0.71 \pm 0.14$, $P_{\text{Al}} = 0.08 \pm 0.04$, $F_{\text{As}} = 0.62 \pm 0.06$, $P_{\text{As}} = 0.06 \pm 0.02$, $F_{\text{Ga}} = 0.59 \pm 0.04$, and $P_{\text{Ga}} = 0.98 \pm 0.02$. The positions are in agreement with an undistorted lattice of GaAs-type. However, the coherent fractions differ significantly from their ideal value, which would be about 0.94 owing to thermal vibrations indicating some random displacement of the atoms from their ideal lattice positions.

To prove the possibility of polarity determination on the microscopic scale we studied GaN thin films, which exhibit periodic domains of lateral polarity inversion with a

periodicity of a few micrometres. The Ga polarity is achieved by the presence of a prior deposited AlN nucleation layer between the film and the Sapphire substrate. The thickness of the GaN-film was around 800 nm. We found these films being of relatively poor crystalline quality, with rocking curve widths between 0.5° and 1° , and with very low reflectivity of about 1% or less (Figure 110). Because of this large angular acceptance we could replace the 1-dimensional focusing lens by a 2-dimensional focusing compound refractive lens [3] and thus reduce the focal spot to 10 μ m horizontal by 1.5 μ m vertical.

Micro-XSW scans were performed through adjoined polarity domains with a step size of 1.5 μ m. From our data we can distinguish the two different polarity domains. The domains which have been grown on an AlN nucleation layer exhibit Ga-polarity. This finding is in agreement with XSW-measurements of large GaN films grown directly on sapphire, which have the opposite, i.e. have N-polarity.

References

- [1] B.W. Batterman, *Phys. Rev.* **133**, A759 (1964); B.W. Batterman, *Phys. Rev. Lett.* **22**, 703 (1969).
- [2] V.V. Aristov, M.V. Grigorev, S.M. Kuznetsov, L.G. Shabelnikov, V.A. Yunkin, M. Hoffmann, E. Voges, *Opt. Comm.* **177**, 33 (2000).
- [3] B. Lengeler, C. Schroer, J. Tümmeler, B. Benner, M. Richwin, A. Snigirev, I. Snigireva, and M. Drakopoulos, *J. Synchrotron Rad.* **6**, 1153 (1999).

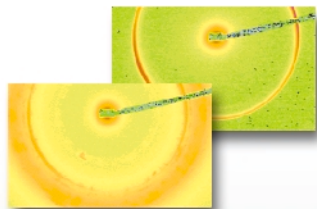
Principal Publication and Authors

M. Drakopoulos (a), J. Zegenhagen (a), A. Snigirev (a), I. Snigireva (a), M. Hauser (b), K. Eberl (b), V. Aristov (c), L. Shabelnikov (c), and V. Yunkin (c), *Appl. Phys. Lett.* **81**, 2279 (2002).

(a) ESRF

(b) Max-Planck-Institut für Festkörperforschung, Stuttgart (Germany)

(c) Institute for Microelectronics Technology RAS, Chernogolovka (Russia)



Industrial and Applied Research

Introduction

The ESRF's effort in industrial and applied research is rewarded by a steady growth of activities in this area. The constantly expanding proprietary research activity in macromolecular crystallography represents the major component of our commercial actions. At a world-wide level the high expectations generated by the progress in genome sequencing and structural genomics initiatives are pushing both large pharmaceutical companies and small start-up enterprises to expand in this field of research. The continuous improvements in automation of the hardware and software tools have led to a steady increase of the beamline throughput. All the Macromolecular Crystallography Group beamlines are involved in industrial research with each beamline dedicating around 20% of beam-time to this activity.

One example of research specifically aimed at identifying new therapeutic treatments is the investigation of the structures of small molecule inhibitors in a complex with Aurora-2, an oncogenic serine threonine kinase. This protein could be a good target for a series of drugs that would disrupt cell cycle and proliferation. It is hoped that information gathered from current investigations will help in the design of inhibitors that can bind more specifically to Aurora-2.

The creation of a centre of excellence in structural biology will boost current research in macromolecular crystallography. Starting in 2003, the Partnership for Structural Biology (PSB) will combine the skills and know-how of

the ESRF, the EMBL, the ILL and the IBS to develop an integrated European programme in which they will pool their resources in structural genomics studies focussing on proteins of medical interest. A number of companies have joined this initiative as Associate Partners and will thus benefit from preferred access to facilities at the ESRF.

Pharmaceutical companies also use Synchrotron Radiation for quality control assessment. The powder diffraction beamline (ID31) is routinely used for identifying the different polytypes present in the active compounds.

Transmission microtomography allows three-dimensional imaging of samples with micrometre or submicrometre resolution. Its application spans large fields of applied research. The 3D rendering at 10 micrometre resolution of a sandwich loaf in [Figure 111](#) is a typical example of this activity. The limit of transmission microtomography is the low sensitivity for low Z elements and the low contrast in distinguishing neighbouring elements. This limit can be overcome using the recently-developed technique of phase microtomography. This exploits the

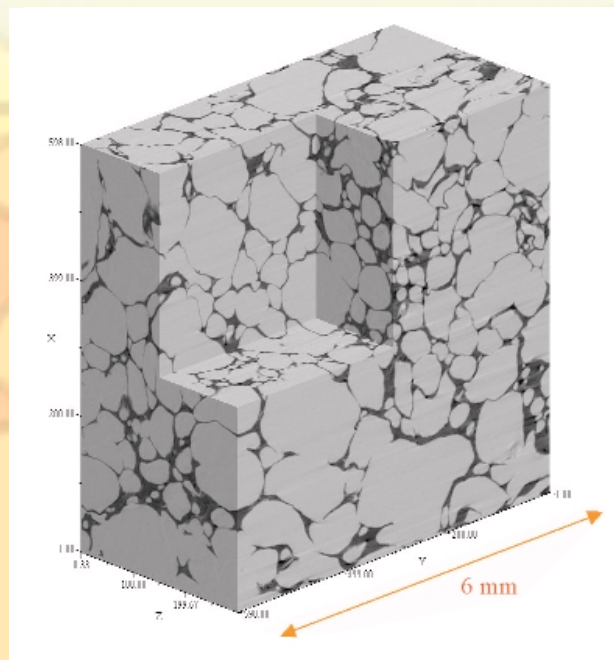


Fig. 111: Tomography of a sandwich loaf. [FreLoN camera 1024*1024 pixels of 10.13 micrometre size]. Courtesy of INRA Nantes GPM2 INPG.

spatial coherence of the ESRF beams, allowing a holographic reconstruction of the sample investigated. The image of the felt in [Figure 112](#) has been obtained using this technique. More details and images recorded using phase contrast can be found in the chapter "X-ray Imaging".

These are difficult times for the semiconductor industry. Nevertheless, the TXRF station ID27 has enabled a number of Japanese companies to map the trace element distribution on the surface of silicon wafers with a remarkable sensitivity of 10^8 atoms/cm², equivalent to 10^{-7} monolayers. This unique facility will remain available for industrial customers, while its long-term future is considered.



Highlights 2002

The dispersive EXAFS beamline ID24 is the reference installation for time-dependent studies of catalytic reactions. For example, the study of the catalyst $\text{CuCl}_2/\gamma\text{-Al}_2\text{O}_3$ used in the production of 1,2-dichloroethane, a basic ingredient in the production of vinyl chloride is extensively reported in the chapter "Absorption and Magnetic Scattering". The analysis of the XANES spectra of the basic catalyst and of its mixture with KCl has identified the rate-limiting step of the reaction and pinpointed the role of the K-dopant as a moderator of the catalytic process.

While proprietary research is easy to identify, the border between applied and fundamental research appears less clear. We estimate that some 30% of the research proposals considered by the ESRF review committees have significant industrial relevance and involve collaboration between industrial and academic partners.

A new service, the Industrial and Commercial Unit (ICU), has been created within the ESRF Directorate for a better management of industrial and commercial issues. The ICU integrates all the functions needed to enhance industrial relations and the efficiency of the different ESRF services available to industry. The new unit will be the "hub" for all initiatives related to beam time sales, and for all the ancillary services, collaborations, contracts and agreements with academics or industry.

Two examples of applied research follow: the first shows how high-energy X-rays are used to map out the residual stress field in a worn railroad rail, and the second describes how studies of the phase diagram of mixtures can help improve fabric-washing products.

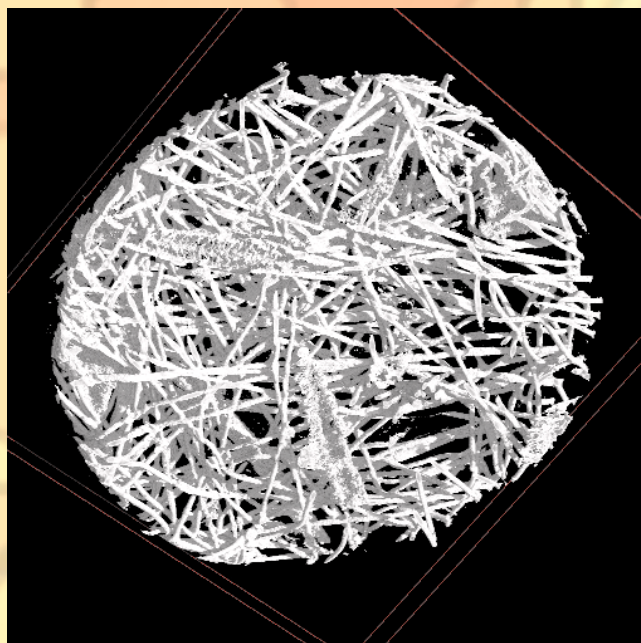


Fig. 112: Phase reconstruction of a FELT sample. [FreLoN camera 2048*2048 pixels of 1.4 micrometre size]. Courtesy of Fraunhofer Institut.

Residual Stresses in Railway Rails – The FaME38 Project

A number of serious incidents, including fatal derailments, have been attributed to rail fractures resulting from rolling-contact fatigue cracking. Many of the various mechanisms of rail failure are related to the relationship between defects and the 'residual' stress field in the rail. Typically a rail fracture is the result of a progressive defect, the propagation of which is related to the inherent residual stresses in the rail.

Residual stresses are generated in railway rails first as a result of manufacturing processes. These may include hot-rolling, roller-straightening and head-hardening. Then, in service, the running surfaces of rails are subjected to repeated rolling-contact stresses through contact with the train wheels. These stresses are usually high and they can cause plastic deformation around the contact surface and modify the stress field near the running line and internally in the railhead [1]. There will also be wear caused by sliding friction near the running band and at the gauge corner side of the head when contact is made by the flange, as often happens in curved track. The head of the rail may be ground periodically as a maintenance procedure to restore the correct head profile, to remove surface cracks before they grow too big, or to move the wheel-rail contact position across the head in order to extend the life of the rail. Although grinding is a costly procedure, it can, in appropriate circumstances, prolong rail life.

A number of techniques are used to determine residual stresses in engineering components, but diffraction techniques are particularly suited to the non-destructive mapping of complex stress fields. Traditionally neutron diffraction has been used to determine residual stresses internally in denser materials such as steel. Now that intense beams of high-energy synchrotron radiation are available, it has become practicable to obtain comparable, and very high spatial resolution, stress maps using X-rays.

Figure 113 shows maps of the internal residual stresses in a worn US rail, derived from measurements of strain made on a matrix of over 6000 points using beamline ID11 operating at 60 KeV. The 'banana'- and 'T'-shaped tensile (red) regions that are observed are characteristic of many transverse and vertical railhead residual stress patterns respectively [2]. In each of these patterns there are asymmetrical pointed features where the internal tensile regions extend towards the surface. These features are related to discontinuities at the surface, at the side where the flange-rail contact ends and on the top where the tyre-rail contact ends. It is in these regions, where there are tensile residual stresses near

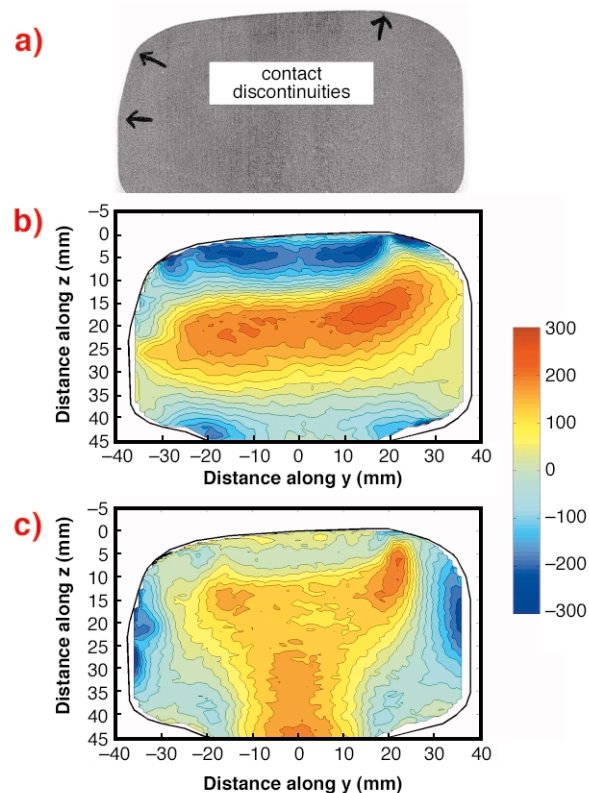


Fig. 113: a) cross-section of a worn railhead. b) Maps of transverse and c) vertical residual stress (in MPa).

the surface, that fatigue cracks are most likely to propagate from defects. Detailed maps such as these should enable railway engineers to model and to better understand how residual stress fields are generated and to determine the most appropriate rail maintenance and replacement schedules for safe and economic operation.

The work was performed in collaboration with the FaME38 project that is designed to develop and to provide on- and off-line facilities and support, in collaboration with beamline staff, to enable materials engineering research to become a routine activity at ILL-ESRF.

References

- [1] P.J. Webster, X. Wang and G. Mills, in *Proc. NATO Advanced Research Workshop on Measurement of Residual Stress using Neutron Diffraction*, Oxford, Kluwer Academic Publishers, 517-524 (1992).
- [2] P.J. Webster, *Neutron News* **2**, 19-22 (1991).

Principal Publication and Authors

P.J. Webster (a,b), D.J. Hughes (a,b), G. Mills (a), G.B.M. Vaughan (c), *Materials Science Forum* **404-407**, 767-772 (2002).
 (a) Institute for Materials Research, University of Salford, Manchester (UK)
 (b) FaME38 at ILL-ESRF
 (c) ESRF

Small-angle X-ray Scattering Studies on Concentrated Surfactant Mixtures

For any company whose business performance is assessed by sales growth, the drive to improve products is paramount to satisfy both the increasingly complex consumer demands and the need to grow market share. However the introduction of a new ingredient to a complex mixture such as a fabric-washing product necessitates a detailed understanding of the interplay between different components. For example the use of two different surfactants leads to a synergistic benefit in "Detergency" as derived by the ability to remove an oil from a substrate (Figure 114), where the mixed surfactant is more efficient at removing oily soil than either of the individual ingredients alone.

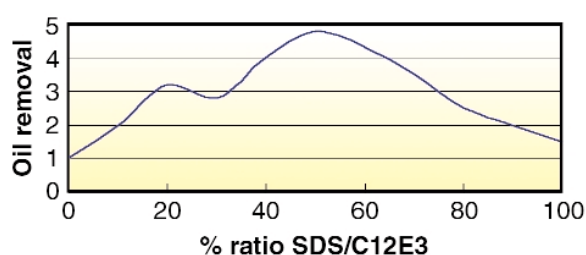


Fig. 114: Example of Synergistic detergency in a mixed anionic nonionic surfactant system.

Understanding how the surfactants mix/compete at interfaces is very important and detailed adsorption and adsorbed layer structural studies in the dilute state have been made by combinations of neutron reflectivity and small-angle neutron scattering in order to probe the role of non-ideal mixing in this synergistic effect [1,2].

Ultimately though a company like Unilever must put the ingredients in concentrated form into a product. It is here and also during processing that issues can arise as hot concentrated surfactants exhibit high bulk viscosities via formation of complex mesophases. Data in Figure 115 show how a well-ordered (but low viscosity) lamellar phase can invert to a complex multiphase mixture including a micellar and very viscous cubic phase at high temperature.

Although these high-temperature data are at a glance quite complicated, the scattering expert is able to resolve features which indicate the presence of different coexisting microstructures. Knowledge of the phase diagram is therefore a prerequisite for processing and this in turn demands accurate measurements at a variety of concentrations, compositions and temperatures. It is here that we value the facilities offered at the ESRF. Specifically, the beamline ID02 offers the necessary sensitivity/contrasts and q-range, combined with well-controlled sample temperature. When we add source reliability, the sheer speed of data acquisition available on ID02 together with the added benefit of the wide-angle scattering capability, the beamline fulfills and needs. In fact, we have found that we can effectively map out the detail on a complex phase diagram in a single shift of 8 hours.

References

- [1] E.J. Staples, L. Thompson, I.M. Tucker, J. Penfold, R.K. Thomas, J.R. Lu, *Langmuir* **9**, 1651, (1993).
- [2] E.J. Staples, J. Penfold, I.M. Tucker, *J. Phys. Chem. B* **104**(3), 606-614, (2000).

Authors

I.M. Tucker, P. Carew, M. Cooke, N. Lewkowicz.
Unilever Research and Development Port Sunlight,
Bebington (UK)

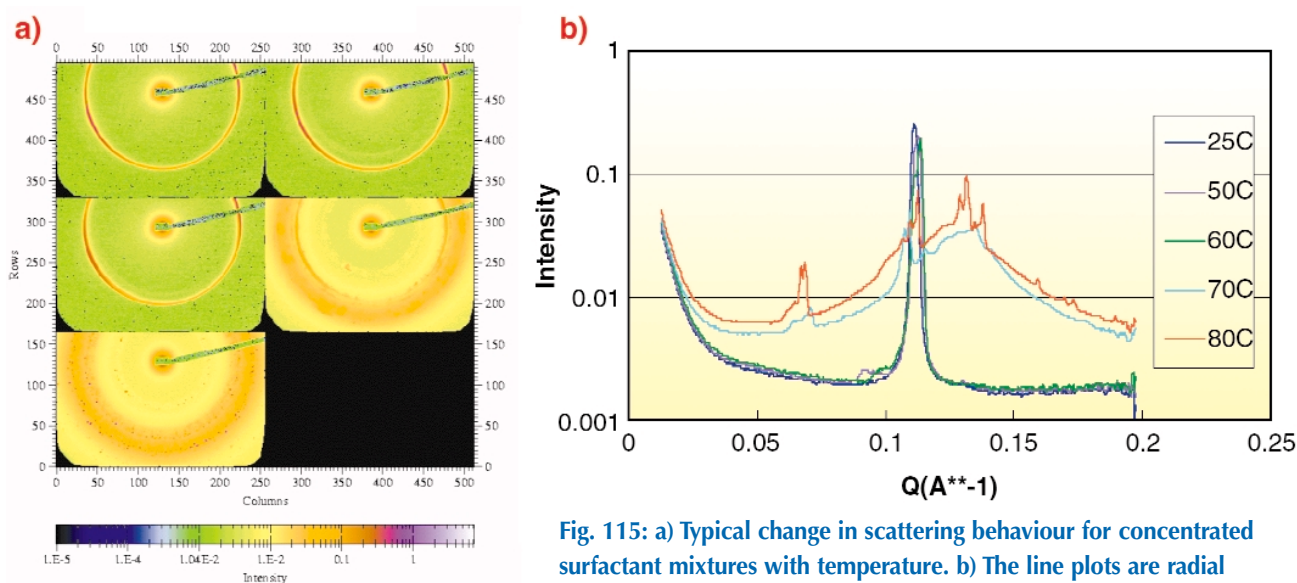


Fig. 115: a) Typical change in scattering behaviour for concentrated surfactant mixtures with temperature. b) The line plots are radial averages of the 2D images shown in a). Data obtained during commercial beam time on ID2 (June 2002).

Introduction

In the never ending quest for better adapted and more efficient beamline instrumentation, optical devices for focusing X-ray beams have always had a very important place. Adapted means that the instrumentation must be tailored to given experimental requirements with the guideline "as simple as possible and as sophisticated as reasonably achievable". This is the reason why we have developed a great variety of focusing optics and why the activities in this field will always continue. Efficiency is closely related to the quality of the optical elements used, such as the figure and finish of surfaces, the accuracy of microfabrication, the quality of crystals and the mechanical precision and stability of supports, in particular for bending.

The first part of this chapter contains a series of reports on recently developed optics for focusing, starting off with two major systems, the famous Kirkpatrick-Baez (KB) double mirror device and the well-known compound refractive lenses (CRLs). In both areas impressive

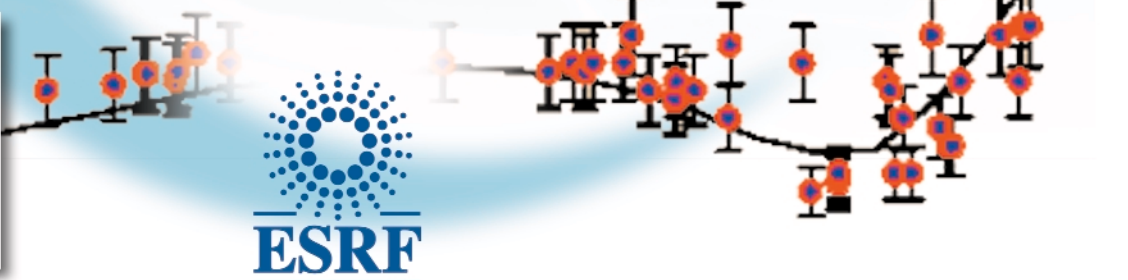
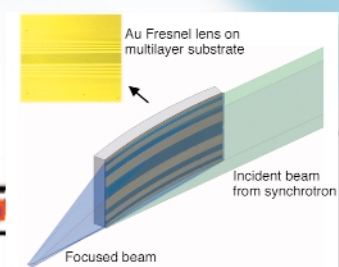
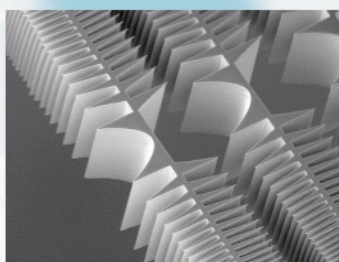
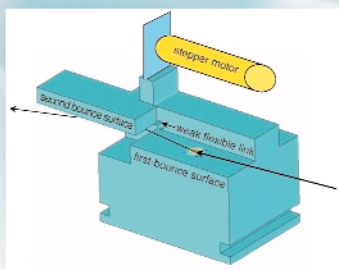
progress has been seen over the past year. Both devices permit to produce a spot size below the micron level and the so-called diffraction limit that is the ultimate performance is almost reached. Whereas the mirror based KB system is achromatic, the CRLs are not. The second contribution reports on the most recent results obtained with a two-dimensional waveguide, which is new, because until now this device concentrated the beam in only one direction. This device functions as predicted by theory and can be applied to many techniques, for example coherent imaging. The last but not least report describes a multilayer based Bragg-Fresnel optic that double focuses a hard X-ray beam to a not so small spot, but produces a focus size that is well adapted to the requirements from a protein crystallography beamline.

What can be done in visible light optics is often also possible in the X-ray domain. This has been proven many times and the shearing interferometer described in the following contribution is a beautiful example of this observation. The differential phase contrast seen in the pictures demonstrates the high quality of the manufacturing and allows us to use this device for wavefront evaluation, which is useful for following the quality of the X-ray beam before and after conditioning in a beamline.

The amount of flux that can be concentrated on the sample also depends on the amount of photons that can be digested by the first

optical element of a beamline, very often a crystal monochromator. At the ESRF we have plans to increase the current from 200 to 300 mA. Will our cryogenic cooling technique of silicon crystals be capable of preserving the quality of beams generated by in-vacuum undulators? This question has been addressed in the last contribution where theoretical predictions from finite element analysis are compared to results from high heat load experiments. The excellent agreement even in detail - the dip in the rocking curve width where the crystal temperature corresponds to the zero thermal expansion point of silicon - show that we can have full confidence in the calculations. They also show that the power limit of about 450 W should not be exceeded for indirect cooling and that we therefore have to envision to use direct cooling in the future.

The detector is the last component in a beamline and it can be a limiting factor for the final data output rate of an experiment. It is therefore very important to dispose of high count-rate detectors that have to meet other needs as well, such as low noise, wide dynamic range and linearity. 2D pixel detectors are currently being developed and an example of this activity is presented in the last contribution. The results show that up to six orders of magnitude in intensity can be covered by such a detector allowing the 2D detection of diffuse scattering from quasicrystals.



Recent Progress in Focusing X-ray Beams

A major goal in the field of X-ray optics development has always been to concentrate more X-ray photons into a smaller area and thus gain in flux. Of course, this gain in flux, measured in photons per unit time and area, is accompanied by an equivalent increase in beam divergence. Therefore, the gain is limited by the maximum divergence that can be tolerated by an experiment. Fortunately, the X-ray beams generated by a third-generation source such as the ESRF are well collimated in angle, typically a few tens of micro-radians, so that four or more orders of magnitude of flux can be gained without jeopardising the quality of the experiment. Another limit is set by the survival of the sample under such high-flux conditions. Once the experimental parameters have been defined, the practically achievable gain depends on the type and quality of the optical element used. The same holds true for the minimum spot size. Further limits are given by the source size S and the magnification $M = q/p$, where p is the source-to-optics distance and q is the optics-to-focus (i.e. to the sample) distance. So the working distance (q) and thus the overall length of the beamline must also be considered. For perfect optics the focus size F is then given by $M \times S$. However there is a fundamental limit called the *diffraction limit* (DL): the DL spot size is proportional to the wavelength and the focal length divided by the beam width. Apart from the maximum gain – minimum spot size criteria, other arguments such as availability, simplicity of use and cost influence the final choice of the optics.

In recent years, quite substantial progress has been made in the field of microfocusing as shown in previous ESRF Highlights articles and specialised literature such as various proceedings of SPIE and SRI conferences (see some references below). Here we want to present the most recent achievements made at the ESRF, often in collaboration with other laboratories and institutes. They focus on two techniques: reflective optics based on specular reflection by mirrors and multilayered structures and on refractive optics based on beam deviation by refraction like in an optical lens.

Microfocusing by Curved Mirrors and Multilayer Structures

Focusing hard X-rays with the help of grazing-incidence, reflecting surfaces is probably the method mostly used on synchrotron beamlines. A typical example is a toroidal mirror that gives spots several hundreds of micrometres wide. The goal to decrease the spot size to a micrometre or less has triggered technological developments of a specific reflecting system, the so-called Kirkpatrick-Baez system (KB). Two orthogonal mirrors focus the

beam successively in the horizontal and in the vertical planes. The system can be either static, with mirrors polished according to the figure optimised for a given incidence angle and focus. Or it can be dynamic, with actuators bending flat mirrors into the elliptical shapes required by the experiment. **Figure 116** shows an example of a complete dynamic system consisting of two 170 mm long mirrors with integrated motors for adjustment of bending and positioning.

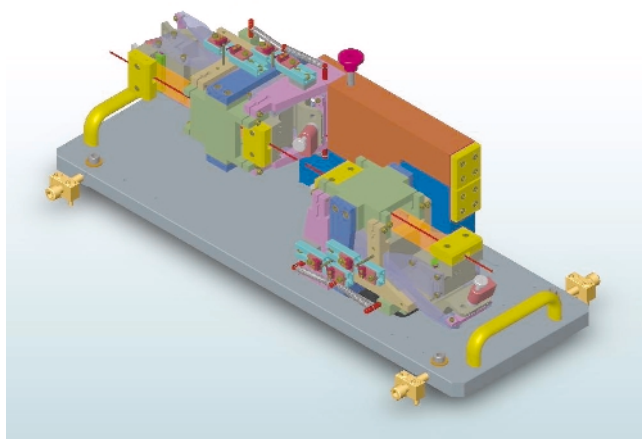


Fig. 116: Kirkpatrick-Baez system.

The reflection by a single layer is achromatic: a wide range of X-ray wavelengths or energies are reflected at a given angle, typically a few milli-radians. Therefore, experiments requiring energy tuning can be performed without any readjustment of the optics. The transmission can be as high as 70%, with only a small amount of light scattered outside of the central spot when super-smooth polished surfaces are used. A combination of different metal and multilayer coatings makes it possible to cover the range from 2 keV to 90 keV. Multilayers with a graded layer spacing can have an energy bandwidth as high as 6%. They can accept wider beams, up to several mm, due to their ten times larger angles of reflection.

With eight degrees of freedom to be tuned to sub-micrometre precision, the alignment procedure of a dynamic system is relatively complex. To this end automated sequences based on linear optimisation with the help of CCD position sensors have been developed at the ESRF [1]. The vibration level has to be controlled to within a few micro-radians and the figure accuracy of the elliptical mirrors to within a few nanometres. This is technologically challenging. The reflected beam is deflected with respect to the incoming beam. These constraints can all be managed, but have to be taken into account when selecting the most appropriate microfocusing technology.

The final spot size is determined by a convolution of four parameters: the source size (geometrically demagnified), the mirror imperfections, the vibrations and ultimately by the diffraction limit set by the X-ray wavelength. If the source is sufficiently small and distant,

it is seen by the optical system as a "star", which means that the optical system cannot resolve its angular width [2]. The synchrotron source then behaves like a laser: it is "coherent". This is already the case on long beamlines such as ID19, where we are approaching the diffraction limit: a record spot size close to 100 nanometres and a gain of up to five orders of magnitude were obtained. Non-conventional polishing processes have been developed for ultra-precise figuring, for example ion-beam figuring. Diffraction-limited conditions have also been obtained at Spring-8 in Japan.

To date, the ESRF Optics Group has produced 38 bent mirrors, most of them assembled as KB pairs, and several more are planned for 2003. Three standard dimensions (300 mm, 170 mm, 90 mm) and the multilayer-coating capability allow us to tackle a wide range of applications [3].

Microfocusing by Refractive Optics

Other types of microfocusing devices for hard X-rays are based on refraction. Although they function in the same way as visible light optics, there are some differences. Firstly, the X-ray refractive index of a material is smaller than in vacuum or air and, therefore, an X-ray focusing lens has a double concave shape. Secondly, because the refractive index of all materials is very close to unity for hard X-rays, the deflection is usually very small and many lenses have to be placed in series to achieve reasonably short focal lengths. In order to keep absorption to a minimum, these compound refractive lenses (CRLs) should be made from low-Z materials such as beryllium, carbon, aluminium, silicon, etc. CRLs with parabolic shapes made from polycrystalline aluminium by a pressing technique have proven to be well suited for microanalysis and full field microscopy applications for 20-120 keV X-rays [4]. These lenses for two-dimensional focusing were developed in collaboration with Aachen Technical University and are now extensively used as a standard tool in experiments at ID11, ID15 and ID22/18F. The advantages of CRLs are their small size, robustness, and ease of alignment and operation. Their focal length and size is adjustable by adding or removing individual lenses and the lenses can withstand high heatload.

Recently, microelectronics planar fabrication technology has been applied to obtain silicon-based devices. One-dimensionally focusing, parabolic refractive lenses have been manufactured in collaboration with the Institute of Microelectronics Technology (Chernogolovka, Russia) and Dortmund University using lithography and highly anisotropic plasma etching techniques. This type of planar lenses is well suited for high-resolution diffraction experiments including those involving the standing-wave technique [5]. It is possible to make a composite lens consisting of a set of parallel parabolas with different

focal distances. To change the focal distance or the desirable working energy, one can switch from one array to another by moving the composite lens. Figure 117 shows planar parabolic lenses made of silicon, fabricated by RWTH in Aachen [6]. They have a focal distance in the range of a few millimetres at hard X-ray energies. At ID22, two lenses were used in a crossed geometry to generate a microbeam with a lateral size of 380 nm by 210 nm at 25 keV. The planar technology is being transferred to materials like diamond that have low X-ray absorption, low thermal expansion and high heat conductivity [7]. These lenses are mechanically robust and can withstand the high heatload of the white beam produced by ESRF in-vacuum undulators.

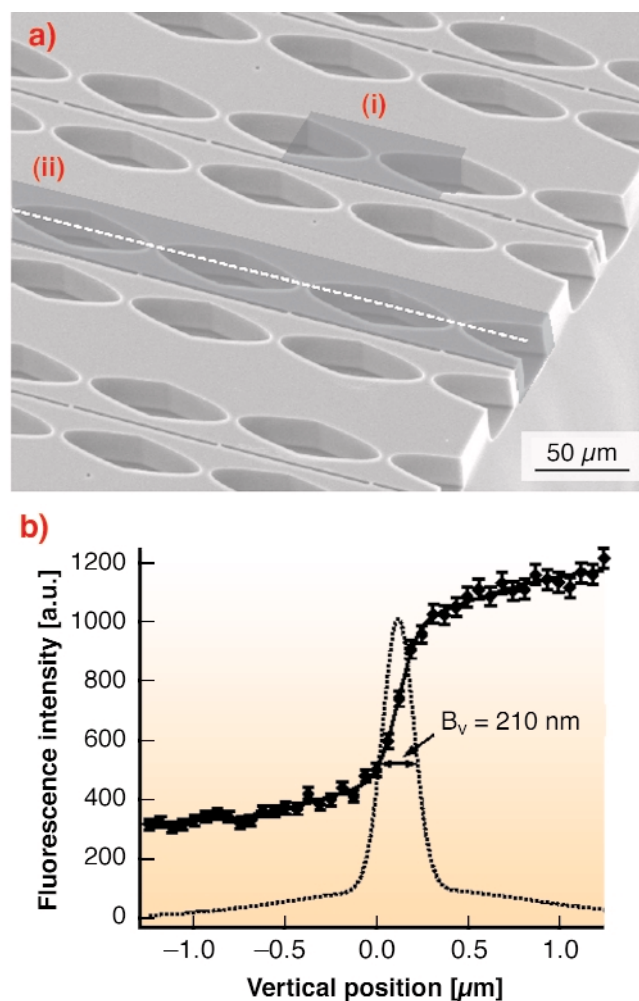


Fig. 117: Scanning electron micrograph of an array of parabolic refractive X-ray lenses made of silicon. (a) The shaded areas (i) and (ii) delimit an individual and a compound nanofocusing lens, respectively. The optical axis of the NFL is shown as a white dashed line. (b) Vertical scan of a gold knife-edge through the microbeam.

Recently, holographic or kinoform optical elements with the combination of refractive and diffractive properties have been manufactured. With this method we eliminate drawbacks of purely diffractive or refractive elements and combine advantages like high transmission, absence of zero-order, high efficiency, etc. The ability to manipulate the local amplitude and phase of the

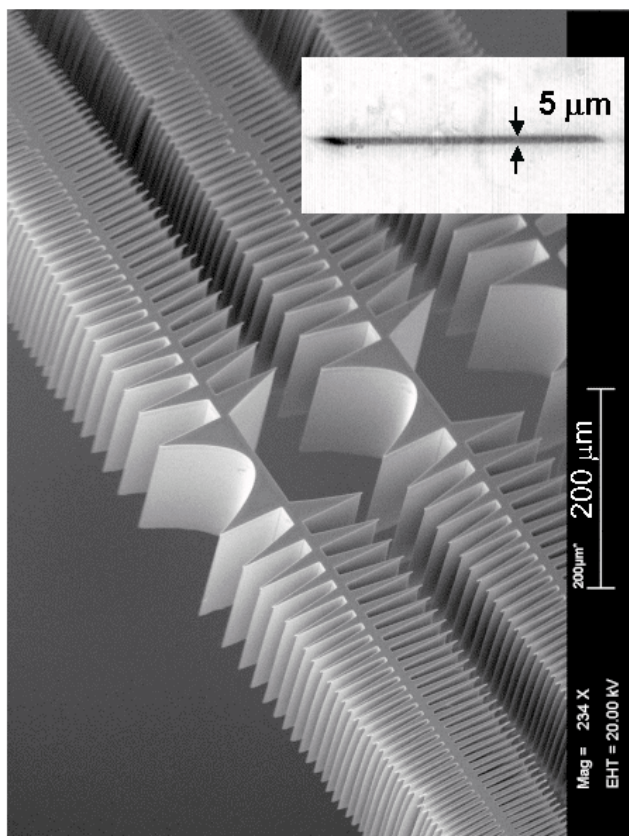


Fig. 118: Scanning electron micrograph of a Ni kinoform lens with 140 single elements, each 300 μm high and 1500 μm wide. The lens is designed for 4.5 m focal distance at 212 keV X-ray energy. The insert (upper right) shows a 5 μm wide focus line measured at ID15A using monochromatic 212 keV X-rays.

incoming wave opens the perspective to make a new class of beamshaping X-ray optics for coherent synchrotron radiation. 300 μm -thick, identically focusing elements with a kinoform profile were made of nickel by the Institute for Micro-Technology (Karlsruhe) using a lithographic process (LIGA) [8]. In these refractive lenses, passive parts of the material that cause multiples of 2π in phase shift are removed thereby reducing absorption (**Figure 118**). At ID15A, these planar kinoform lenses focused 212 keV X-rays to a focal line 5 micrometres-wide with a 10-fold gain.

Among the various applications of microfocused X-ray beams we can mention:

Projection microscopy (see **Figure 119**): a magnified image of an object placed close to the focus plane is projected onto a fast CCD detector with a resolution corresponding to the spot size. The efficiency of the set up permits us to obtain a 2000 x 2000 pixel image in a fraction of a second and to perform fast tomography at the sub-micrometre level.

Microfluorescence: the information of the chemical content of an object is obtained by scanning the sample in front of a fluorescence detector. Results have been obtained in materials science and cell biology.

Microdiffraction: this is needed at the sub-micrometre level and microfocus systems are widely used for high pressure and surface science.

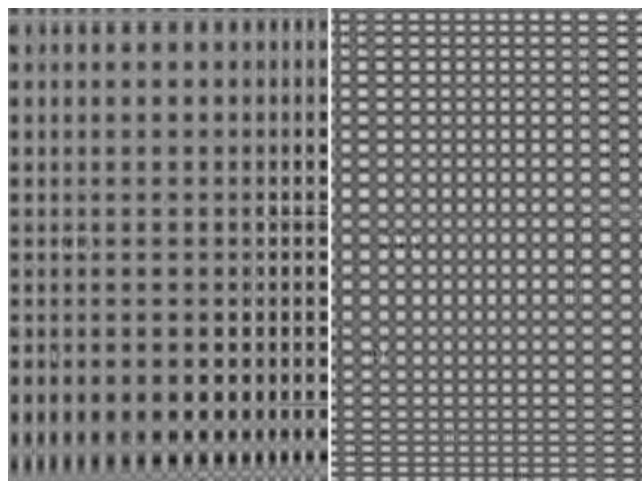


Fig. 119: Two projection images of a 2 x 2 μm dot phase structure at 20.5 keV, with different contrast conditions, obtained with a KB system [9].

References

- [1] O. Hignette, G. Rostaing, P. Cloetens, W. Ludwig and A.K. Freund, *SPIE Proceedings* **4499**, 105-116 (2001).
- [2] O. Hignette, P. Cloetens, W. Ludwig and G. Rostaing, *XRM 2002 Proceedings*, Grenoble, 2002, in press.
- [3] Y. Dabin, G. Rostaing, A. Rommeveaux and A.K. Freund, *SPIE Proceedings* **4782**, 235-245 (2002).
- [4] C.G. Schroer, J. Meyer, M. Kuhlmann, B. Benner, T.F. Günzler, B. Lengeler, C. Rau, T. Weitkamp, A. Snigirev, I. Snigireva, *Appl. Phys. Lett.* **81** (8), 1527-1529 (2002).
- [5] M. Drakopoulos, J. Zegenhagen, A. Snigirev, I. Snigireva, M. Hauser, K. Eberl, V. Aristov, L. Shabelnikov, and V. Yunkin, *Appl. Phys. Lett.* **81**, 2279 (2002).
- [6] C.G. Schroer, M. Kuhlmann, U. Hunger, T.F. Günzler, O. Kurapova, S. Feste, F. Frehse, B. Lengeler, M. Drakopoulos, A. Somogyi, A. Simionovici, A. Snigirev, I. Snigireva, C. Schug, A. Schroeder, *Appl. Phys. Lett.* (2003), *to be published*.
- [7] A. Snigirev, V. Yunkin, I. Snigireva, M. Di Michiel, M. Drakopoulos, S. Kouznetsov, L. Shabelnikov, M. Grigoriev, V. Ralchenko, I. Sychov, M. Hoffmann, E. Voges, *SPIE Proceedings*, **4783**, 1-9, (2002).
- [8] A. Snigirev, I. Snigireva, M. Di Michiel, V. Honkimiaki, V. Nazmov, E. Reznikova, J. Mohr, V. Saile, M. Grigoriev, L. Shabelnikov, *to be published*.
- [9] P. Cloetens *et al.*, *to be published*.

Authors

O. Hignette, A. Snigirev, A. Freund.
ESRF

Two-dimensional X-ray Waveguides

We have carried out a proof of principle experiment demonstrating that resonant coupling of synchrotron beams into suitable nanostructures can be used for the generation of coherent X-ray point sources. To this end, a rectangular, two-dimensionally (2D) confining X-ray waveguide structure has been fabricated by electron-beam lithography. Shining a parallel undulator beam onto the structure, a discrete set of resonant modes can be excited in the dielectric cavity, depending on the two orthogonal coupling angles between beam and the waveguide interfaces. The resonant excitation of the modes is evidenced from the characteristic set of coupling angles as well as the observed far-field pattern. The device thus delivers a coherent X-ray beam of 68.7 nm x 33.0 nm cross-section (horiz. and vert. FWHM) at the exit of the cavity.

Planar X-ray waveguide structures have been demonstrated as new tools to produce coherent and divergent X-ray beams with cross-sections in the sub-micrometre range in one dimension [1-3]. However, for many nanomicroscopy and nanospectroscopy applications, a two-dimensionally-confined point beam instead of one-dimensional line beam is needed.

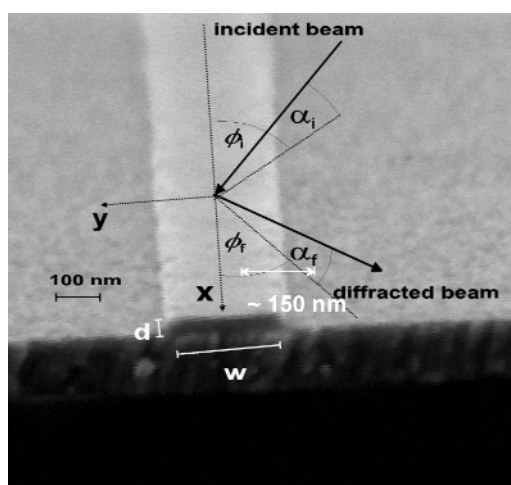


Fig. 120: Scanning electron micrograph of a two-dimensional waveguide consisting of an electron-beam patterned PMMA-core coated with Cr (cladding).

In recent experiments carried out at undulator beamline **ID13** we have demonstrated for the first time that a two-dimensional beam compression using the resonant beam coupling principle can be achieved. Applying state-of-the-art electron-beam lithography techniques, we have fabricated laterally and vertically patterned nanostructures, where the beam is channelled in two-dimensions. **Figure 120** shows a schematic of such an 'X-ray fibre' consisting of a spin-coated, rectangular patterned PMMA core coated with evaporated Cr metal on silicon substrate. In the experiments, waveguides of cross sections down to 33 nm x 68 nm were measured.

Just like in the optical analogue, the resonantly-enhanced electromagnetic field distribution of an X-ray waveguide can be described by a set of discrete and precisely-defined modes (at the respective angles α_i and ϕ_i), which are determined by the geometry of the structure and the choice of materials. Accordingly, the guided modes are excited by shining a parallel beam onto the waveguide at grazing incidence at a set of angles $\alpha_{i,n}$ and $\phi_{i,m}$. A coherent beam exists and the structure at the side has a cross-section corresponding to the thickness of the guiding layer and a divergence in the range of some mrad.

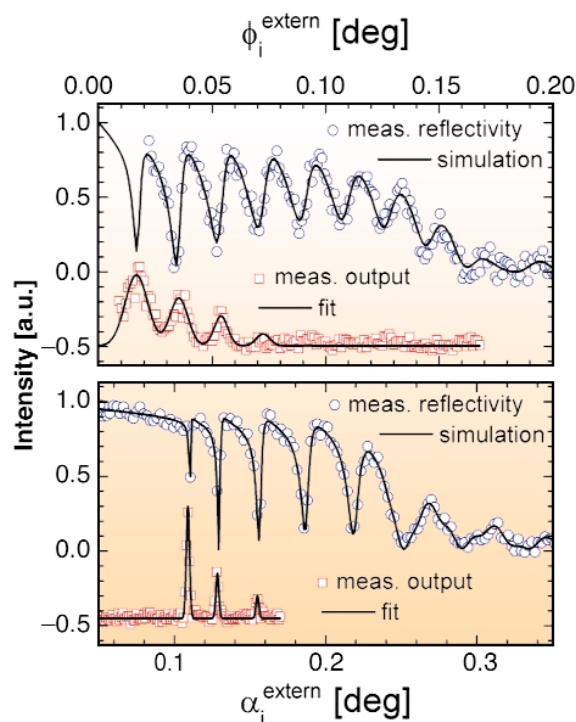


Fig. 121: Reflectivity (1:2) and mode scans (1:1) in the two orthogonal directions of the approximately rectangular fibre. The characteristic cusps in the reflectivity curves correspond to peaks in the mode scans, where the intensity in the forward direction along the fibre axis is collected.

Experimentally, the resonant waveguide effects were evidenced in several ways: (i) The measured reflectivity curves of the nanostructure both as a function of α_i ($\phi_i = \text{const.}$, $\alpha_f = 2\alpha_i$) and ϕ_i ($\alpha_i = \text{const.}$, $\phi_f = 2\phi_i$) show the characteristic cusps, see **Figure 121**. Waveguide effects readily manifest themselves in the reflectivity curve as cusps in the plateau of otherwise total external reflection. (ii) The far field pattern of the lowest lying mode was measured with a high-resolution CCD camera and showed the expected distribution. (iii) The excitation characteristics were measured, *i.e.* the integrated far-field intensity was measured in a mesh scan of (α_i / ϕ_i) . (iv) Additionally, the 'point source' character of the recorded beam was evidenced by translating a knife-edge in the divergent waveguide beam, resulting in the geometrically expected cross-section.

Possible future applications of 2D X-ray waveguides include phase-contrast projection microscopy, as

already demonstrated in the case of the 1D counterpart [3]. Apart from microscopy and imaging, all conventional X-ray applications that would benefit from coherent beams of sub-micrometre cross-sections, can be addressed, in the field of imaging, scattering and photon correlation spectroscopy.

References

- [1] Y.P. Feng *et al.*, *Phys. Rev. Lett.* **71**, 537 (1993),
M.J. Zwanenburg *et al.*, *Phys.Rev.Lett.* **82**, 1696 (1999).
[2] F. Pfeiffer, T. Salditt, P. Høghøj and I. Anderson, *SPIE Proceedings* **4145**, (2001).
[3] S. Lagomarsino, A. Cedola, P. Cloetens, *et al.*, *Appl. Phys. Lett.* **71**, No. 18 (1997).

Principal Publications and Authors

F. Pfeiffer (a), C. David (b), M. Burghammer (c), C. Riekel (c),
and T. Salditt (a,d), *Science* **297**, 230 (2002).

(a) Universität Saarbrücken (Germany)

(b) Paul-Scherrer Institut Villingen (Switzerland)

(c) ESRF

(d) now at: Institut für Röntgenphysik, Universität Göttingen (Germany)

2D Focusing Multilayer Bragg-Fresnel Optics

Bragg Fresnel lenses (BFLs) have been used extensively at third-generation synchrotron sources for hard X-ray microscopy and microdiffraction applications [1,2]. We have developed a new 2D focusing X-ray lens by combining a linear thin-film Fresnel lens and a multilayer mirror. In the multilayer Bragg-Fresnel lens (MBFL), the Fresnel zones focus the X-ray beam vertically by diffraction, whereas the multilayer mirror is bent to focus X-rays horizontally. This unique combination eliminates the need for a second mirror in conventional Kirkpatrick-Baez mirror-based microprobes.

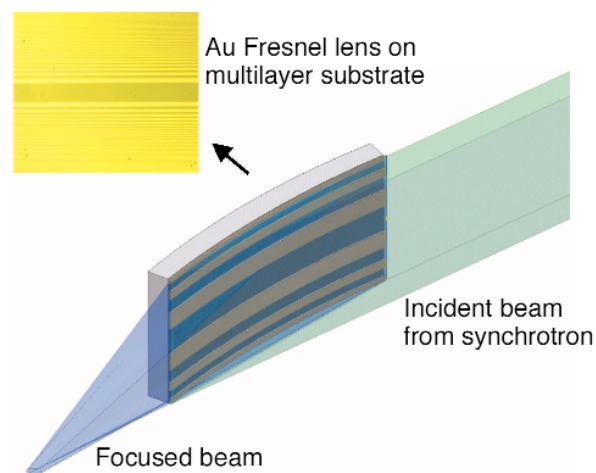


Fig. 122: Illustration of a multilayer Bragg-Fresnel lens made of Au Fresnel zones deposited on a multilayer substrate, which is bent to produce horizontal focusing; (inset) an optical micrograph of the Au Fresnel zones on the prototype lens.

The structure of a multilayer BFL is illustrated in **Figure 122**. The linear Fresnel zones are made of a thin Au layer deposited on a multilayer substrate after patterning by electron beam lithography. (An optical micrograph of the Au Fresnel zones is shown in the inset of **Figure 122**). For the prototype lenses that we fabricated, the multilayer consists of 200 layers of Mo/Si on a float glass substrate. The multilayer was fabricated by Xenocs, Grenoble. The layer spacing increases over the length of the substrate away from the source with a 4% gradient to maintain a large acceptance angle. The thickness of the Au layer is chosen such that the radiation going through the metallised zones are phase-shifted by π to ensure high focusing efficiency. The thickness, which depends on the layer spacing of the multilayer, is about 12 nm for the test lenses. The length of the Fresnel zones is 20 mm, with an outermost zone width of 200 nm. An array of six lenses with different focal lengths was made on a single 15 mm x 60 mm substrate.

X-ray characterisation of the prototype multilayer BFLs was conducted at the optics beamline **BM5**. The focusing properties of the lenses were measured using

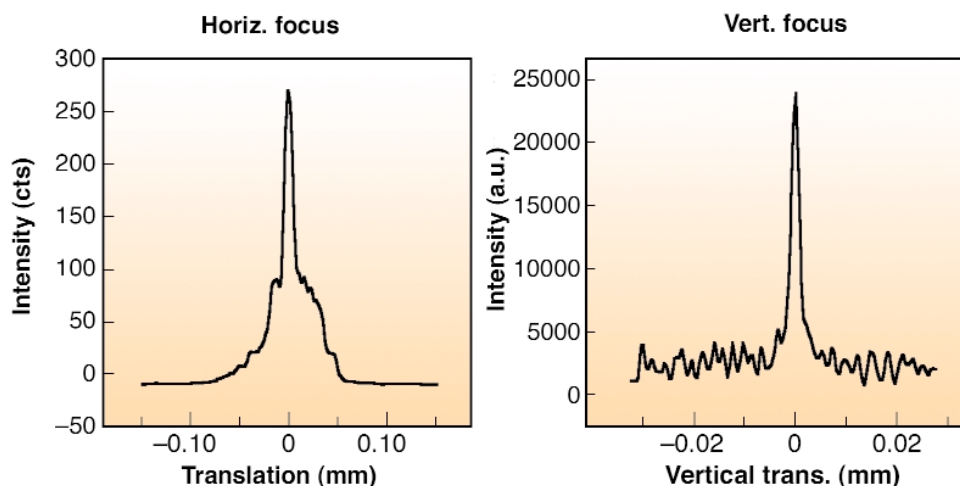


Fig. 123: Horizontal (left) and vertical (right) intensity profiles across the focused beam. The horizontal focus was measured with a 5 μ m aperture whereas the vertical focus profile was derived from a knife-edge scan.

10 keV and 12.4 keV radiation. **Figure 123** shows the measured horizontal and vertical intensity profiles of the beam at the focal plane of the MBFL. The focus size is approximately $2\ \mu\text{m}$ (vertical) \times $12\ \mu\text{m}$ (horizontal) from an incident beam size of $250\ \mu\text{m}$ (V) \times $200\ \mu\text{m}$ (H). The vertical focus is close to the demagnified source size, but the horizontal focus was broader than expected, which we attribute to geometric figure errors caused by the simple mirror bender used in the experiment. Submicrometre spot sizes should be achievable with improvement in the bender and by choosing a larger demagnification ratio.

In conclusion we have demonstrated an X-ray focusing optic that combines diffraction and geometric focusing in one single device. The multilayer Bragg Fresnel lens requires only one binder to produce two-dimensional focusing and will be useful in a wide range of applications.

References

- [1] Y. Hartman, A.K. Freund, I. Snigireva, A. Souvorov, A. Snigirev, *Nucl. Instr. and Met. Phys. Res. A*, **385**, 371-375, (1997).
- [2] Y. Li, G.C.L. Wong, C.R. Safinya, E. Caine, E.L. Hu, D. Haefner, P. Fernandez, and W. Yun, *Rev. Sci. Instrum.* **69**, 2844-2848 (1998).

Authors

Y. Li (a), M. Yasa (a), C.R. Safinya (a), J. Als-Nielsen (b), C. Mammen (b), A. Freund (c), J. Hozowska (c), C. Mocuta (c).

(a) University of California, Santa Barbara (USA)

(b) Niels Bohr Institute, Copenhagen (Denmark)

(c) ESRF

Differential X-ray Phase-contrast Imaging Using a Shearing Interferometer

The phase-shift cross sections of light elements are much larger than the absorption cross-sections in the hard X-ray region. Therefore, the acquisition of X-ray micrographs with sufficient amplitude contrast requires a significantly higher radiation dose than phase-contrast micrographs. To analyse the phase shift caused by an object placed into an X-ray beam, we have developed an interferometer for hard X-rays, which is known from visible light optics as shearing interferometer. The main optical components consist of silicon transmission gratings with a period of $1\ \mu\text{m}$, which we fabricated by electron-beam lithography and wet chemical etching [1].

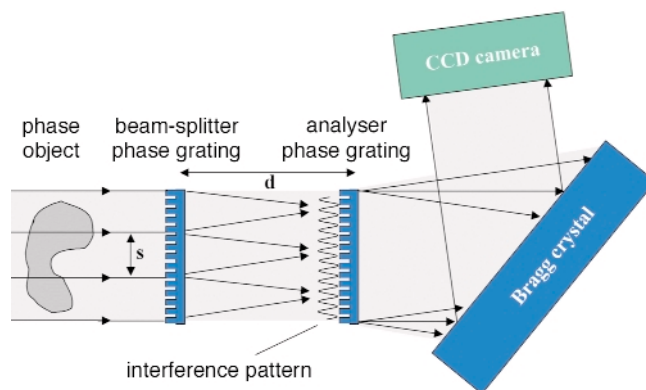


Fig. 124: Schematic view of the shearing interferometer setup consisting of two gratings and a Bragg-crystal.

The interferometer setup is depicted in **Figure 124**. The first grating splits the incoming wave into the $+1^{\text{st}}$ and -1^{st} diffraction orders. The interference of these two wavefronts results in a pattern of interference lines, which is analysed by the second diffraction grating. The relative phase of the two interfering beams determines how the incoming intensity will be distributed over the analyser's diffraction orders. We used a Bragg crystal to select the zeroth diffraction order for imaging. Through a slight angular misalignment of the two gratings one obtains an interferogram of Moiré-lines. Any distortions of the incoming wavefront - e.g. those caused by a phase shifting object placed upstream of the setup - will result in a deformation of this Moiré-pattern.

In the shearing interferometer, the incoming light is not split into separate object and reference beam as it is the case in a Mach-Zehnder type interferometer [2]. In our case, both beams pass through two closely-spaced regions of the

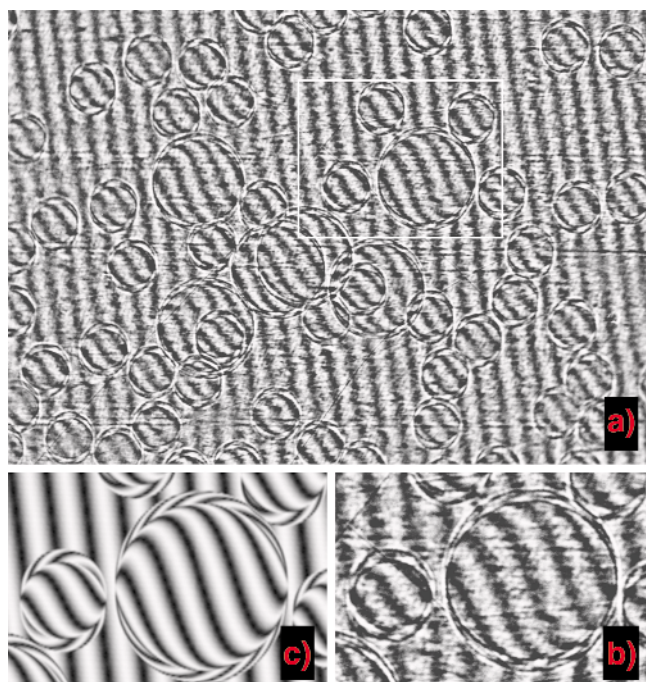


Fig. 125: Shearing interferograms of 100 and 200 μm polystyrene spheres for 12.4 keV photon energy. Experimental results (a, b) and simulations (c).

phase object. The intensity transmitted through the analyser will therefore depend on the difference in phase shift introduced by two closely spaced regions of the sample, *i.e.* the gradient in phase shift. Thus, the resulting interferograms are differential phase-contrast micrographs. The main advantage of this type of interferometer lies in the fact that the setup is insensitive to mechanical vibrations and drift, as the optical components do not have to be stable within a fraction of a wavelength, but only within the fraction of a grating period.

We tested this interferometer on **BM5** for several photon energies between 12.4 and 24.8 keV. Polystyrene spheres with 100 and 200 μm diameter were used as well defined phase objects. As can be seen in the interferogram shown in **Figure 125a**, a change of the orientation of the Moiré-lines is observed, which is directly linked to the difference in phase of the two interfering beams. The obtained interferograms are in excellent agreement with numerical simulations based on a wave propagation algorithm (see **Figure 125b, c**). This shows that a reconstruction of unknown phase objects from such images is possible.

As the interferometer is sensitive to any kind of wave front distortion other applications besides phase-contrast imaging can be envisioned. We plan to use the shearing interferometer to map out the quality of optical components such as mirrors situated upstream of the interferometer in the near future.

Reference

- [1] C. David, E. Ziegler, B. Nöhammer, *J. Synchrotron Rad.* **8**, 1054 - 1055 (2001).
- [2] U. Bonse and M. Hart, *Appl. Phys. Lett.* **6**, 155-157 (1965).

Principal publication

C. David (a), B. Nöhammer (a), H.H. Solak (a), E. Ziegler (b): *Appl. Phys. Lett.* **81**(17), 3287-3290 (2002).
 (a) Laboratory for Micro- and Nanotechnology, Paul Scherrer Institut (Switzerland)
 (b) ESRF

Performance of a Cryogenic Monochromator in the Beam from an In-vacuum Undulator

The brightest X-rays beams at the ESRF are produced by in-vacuum undulators that have their magnets inside

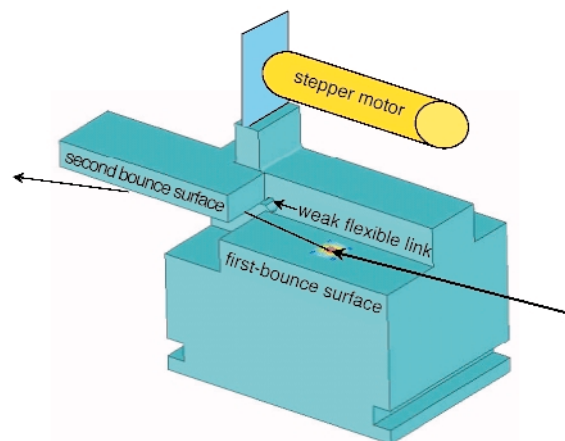


Fig. 126: The channel-cut monochromator on ID09. The Bragg angle of the second crystal is adjusted by a stepper motor that pushes (or pulls) against a blade attached to the second crystal.

the vacuum vessel of the storage ring. In these undulators, the distance between the magnets and the electron beam can be as small as 2.5 mm (5.0 mm gap) as compared to 5.5 mm for conventional undulators. That boosts the Lorentz force on the electrons, which increases the brightness of the emitted X-rays. The gain in brightness is a factor of 3 at 15 keV and 9 at 60 keV. The emitted power in the central cone varies, depending on the undulator period, between 350-650 watt and the power density, 30 m from the source, is between 70-165 watt/mm². At these levels silicon-based monochromators need to be cooled with liquid nitrogen. We will shortly describe the test of a new monochromator that was installed on beamline **ID09** at the end of 2001. It is a so-called channel-cut monochromator, machined from a monolithic block of silicon, see **Figure 126**. This geometry was chosen for its stability and ease of alignment. The overall length is 140 mm and the (perpendicular) distance between the two diffracting surfaces is 4.0 mm. The diffracting planes are oriented along (111) and the monochromator can be tuned between 4 to 50 keV. The monochromator is the first optical element in the beamline and it receives the direct beam from the in-vacuum undulator U17 (magnetic period 17 mm). The fundamental energy of this 2.0 m-long undulator is 15.0 keV; the deflection parameter K is 0.835; the power in the central cone is 350 watt and the power density is 70 W/mm² at the monochromator position 31.4 m from the source. The spectrum of the U17 is dominated by its first harmonic and that keeps the heatload relatively low. The absorbed heat is extracted by two liquid nitrogen-cooled copper blocks that are clamped onto the sides of the first diffracting surface. The nitrogen is held at 80 K at a pressure of 3 bars. In the test, the two undulators U17 and U46 were used in tandem with the U17 as a (gap) variable heat source. The monochromator was set to 8.0 keV and the gap of the U46 was lowered to 16.9 mm where its fifth harmonic emits at 8.0 keV. The intensity of the monochromatic beam was measured by a PIN diode

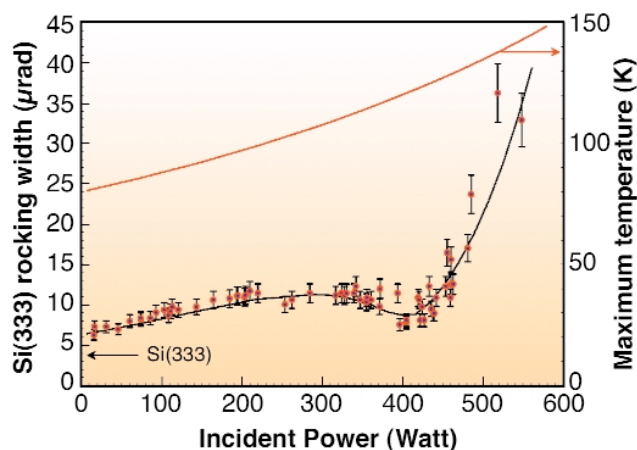


Fig. 127: The efficiency of the cooling system is determined from the broadening of the rocking-curve of the second crystal. At the local minimum at 410 W, the thermal coefficient of silicon is zero.

with a 2.0 mm-thick Al-sheet in front of it. The detected beam was therefore dominated by the 333 and 444 reflections that are more sensitive to thermal deformation. The deformation was determined by rocking the second crystal and recording the FWHM-width as a function of power. The power dependence of the rocking curve is shown in [Figure 127](#). The rocking width of Si (333) at 24.0 keV is 3.3 μrad , which is smaller than the observed cold-limit of 6.3 μrad . This discrepancy is attributed to strain from the clamping of the Cu-absorbers (5.3 μrad). The rocking width increases to a local maximum at 280 watt, which is followed by a local minimum at 410 watt. At higher powers, the rocking width increases dramatically. The fitted curve was calculated by finite-element-analysis (FEA). The rather surprising local minimum in the FWHM-width around 410 watt is explained in the following way. As the heatload is raised from 0 watt, the crystal temperature starts to increase above 80 K. At 410 watt, the temperature reaches 125 K in the centre of the X-ray footprint. At that temperature, the thermal expansion-coefficient of silicon is zero. Therefore small temperature gradients associated with the flow of heat do not perturb

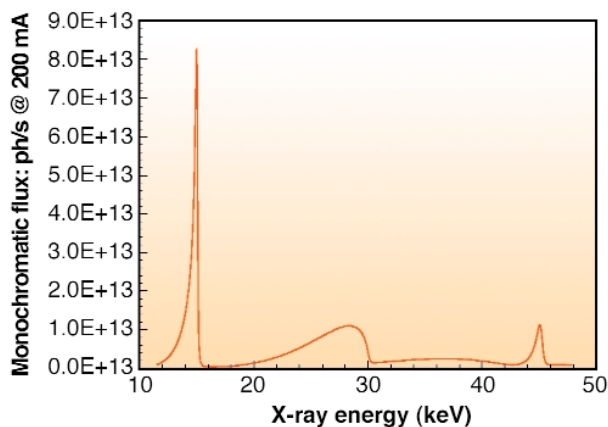


Fig. 128: The spectrum of the U17 undulator at 6.0 mm gap measured with the channel-cut monochromator.

the planarity of the atomic planes in the centre of the beam. The conclusion from this work is that indirect cooling is sufficient below 450 watt. Above this level, which is reached with two in-vacuum undulators in tandem, one is forced to cool the silicon directly, *i.e.* having liquid nitrogen flowing inside the crystal. The measured spectrum of the U17 is shown in [Figure 128](#). Note that the flux at 15 keV attains the very high value of 8×10^{13} ph/s.

Principal Publication and Authors

L. Zhang (a), W.-K. Lee (b), M. Wulff (a), L. Eybert (a), to be published.

(a) ESRF

(b) APS, Argonne (USA)

A Pixel Detector with Large Dynamic Range for High Photon Counting Rates

The dynamic range of the X-ray diffracted signal is usually more than six orders of magnitude for material science studies. As these requirements cannot be satisfied by the available detectors, a new detector using hybrid pixel technology has been developed by the **BM2** beamline (D2AM/CRG) in collaboration with the CPPM/IN2P3, a laboratory participating in CERN detector development.

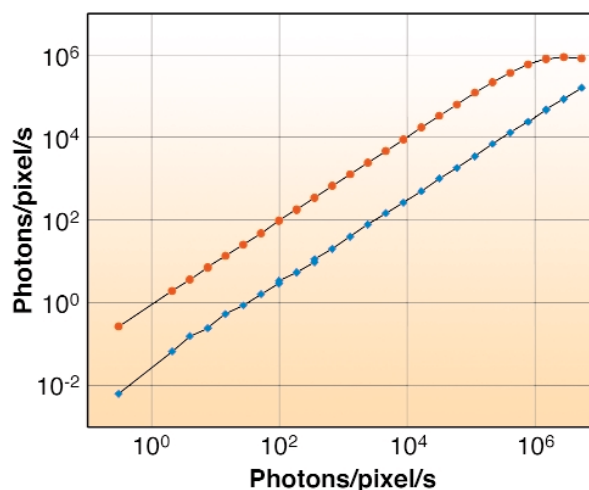


Fig. 129: Counted photons on 2 neighbouring pixels versus incident flux.

In the design of the X-ray Pixel chip with Adaptable Dynamics (X-PAD), we aimed for low noise, high dynamic range and fast read-out. The first prototypes were designed to use the diodes from the Delphi experiment leading to modules containing 6000 pixels of $330 \times 330 \mu\text{m}^2$. These have been tested using synchrotron radiation on the BM2 beamline.

The dynamic response measurement results are shown in **Figure 129**. Low count rates of about 0.01 photons/pixel/s have been measured and high count rates near 10^6 photons/pixel/s have been reached. It should be emphasised that neighbouring pixels are not disturbed by loss of linearity in one pixel, which is not the case for CCDs where blooming appears.

In SAXS experiments, most of the results arise from scaling laws. This requires a large dynamic range. **Figure 130** corresponds to a 400-second exposure of silver behenate. During the test of the XPAD detector, the beam stop used with the CCD settings was shifted upwards allowing us to record high intensities near the direct beam, *i.e.* at very low scattering vector. We measured up to 7 orders of diffraction with an intensity scale of 4 orders of magnitude. The white spots correspond to untunable pixels.

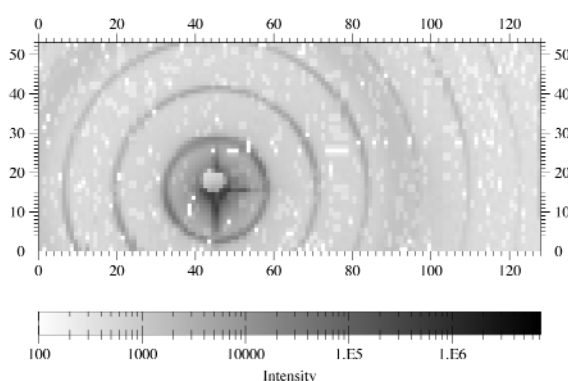


Fig. 130: SAXS on silver behenate recorded at 20 keV.

A test experiment using the diffraction high-resolution settings was also carried out: the reciprocal space zone around an intense five-fold axis of CdYb icosahedral quasicrystal was studied.

A small θ oscillation allowed integration of the Bragg peaks (**Figure 131a**) and the detection of some diffuse intensity. However the knowledge of the diffuse scattering requires mapping the reciprocal space obtained through fixed θ snap shots as shown in **Figure 131b**. The diffuse scattering associated with the out-of-Bragg condition peak in the middle is revealed and its extension in reciprocal space can now be defined.

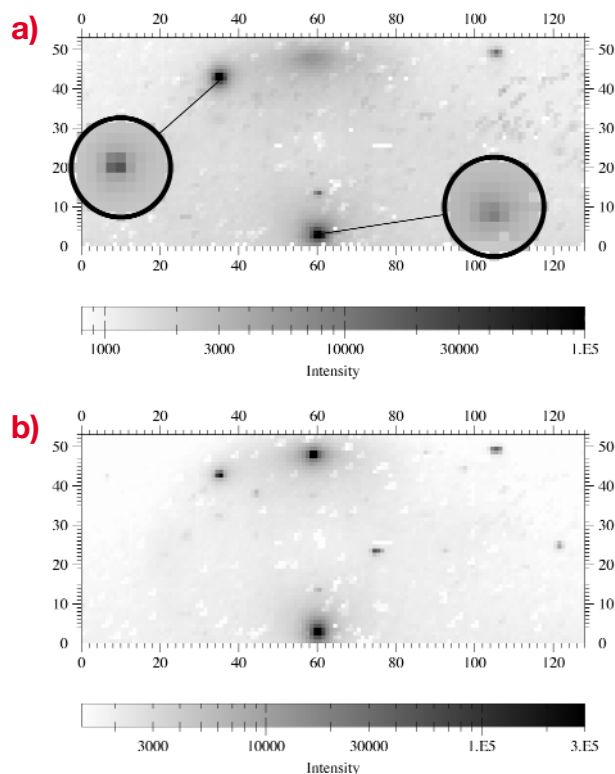


Fig. 131: Bragg peaks and diffuse scattering of CdYb icosahedral quasicrystal at 20 keV. a) θ oscillation, b) θ fixed, inserts are zooms using a gray scale shifted by 2 orders of magnitude.

As technological improvements enable us to reach 100-150 μm^2 with similar or enhanced performance, smaller pixel sizes will become available. Using modular technology, a large detector with a typical size of 10^6 pixels is expected for 2004.

Principal Publication and Authors

J.-F. Bérar (a,c), L. Blanquart (d), N. Boudet (a,c), P. Breugnon (b), B. Caillot (a,c), J.-C. Clemens (b), P. Delpierre (b), I. Koudobine (b), C. Mouget (c), R. Potheau (b) and I. Valin (b), *J. Appl. Cryst.* **35**, 471-476 (2002).

(a) D2AM-CRG, ESRF

(b) CPPM-IN2P3, Marseille (France)

(c) Laboratoire de Cristallographie, CNRS, Grenoble (France)

(d) LBNL, Berkeley (USA)



The X-ray Source



Highlights 2002

Introduction

Throughout 2002, the Machine Division continued its efforts to improve performance and carried out a number of developments, which are described below.

Machine Parameters

Table 2 presents a summary of the characteristics of the electron beam of the storage ring:

Energy	[GeV]	6.03
Maximum Current	[mA]	200
Horizontal emittance	[nm]	4
Vertical emittance		
(*minimum achieved)	[nm]	0.025 (0.010*)
Coupling (*minimum achieved)	[%]	0.6 (0.25*)
Revolution frequency	[kHz]	355
Number of bunches		1 to 992
Time between bunches	[ns]	2816 to 2.82

Table 2: Main global parameters of the electron beam.

Table 3 gives the main optics functions, electron-beam sizes and divergences at the various source points. For insertion device source points, the beta functions, dispersion, sizes and divergences are computed in the middle of the straight section. Two representative source points of bending magnet radiation have been selected, corresponding to an angle of observation of 3 mrad (9 mrad) from the exit, which corresponds to different fields. Electron-beam profiles are Gaussian and the size and divergence are presented in terms of rms quantities. The associated full-width half-maximum sizes and divergences are 2.35 times larger. Beam sizes and divergences are given for the uniform filling modes and apply to almost all filling patterns except for the single bunch for which a slightly larger size and divergence is reached due to the increased energy spread of the electron beam.

The lifetime, bunch length and energy spread depend on the filling pattern. These are given in the **Table 4** for a few representative filling patterns. It should be noted that in both the 16-bunch and single-bunch modes the energy spread and bunch length decay with the current (the value indicated in the table corresponding to the maximum current). The bunch lengths are given for the usual RF accelerating voltage of 8 MV.

Filling pattern		Uniform	16-bunch	Single bunch
Maximum current	[mA]	200	90	20
Lifetime	[h]	75	9	6
Rms energy spread	[%]	0.11	0.12	0.22
Rms bunch length	[ps]	20	48	73

Table 4: Current, lifetime, bunch length and energy spread in various representative filling modes.

Summary of Machine Operation

The figures of merit for 2002 (**Table 5**), namely the mean time between failure (MTBF) and availability, were maintained at the same level as in 2001. This confirms the high level of reliability. A total of 687 shifts (5495 hours) were scheduled for delivery to the Users. Seven shifts (56 hours) were dedicated to radiation tests or Personal Safety System checks. Out of these 5495 scheduled hours, 5319 hours were actually delivered, which represent an availability of 96.8% (to be compared with 96.4% in 2000 and 96.8% in 2001). The remaining hours are shared between the dead time for refills: 67 hours for 507 refills (i.e. 1.2% of USM time) and the time lost due to failures: 110 hours (i.e. 2% of USM time) for 95 beam interruptions. This gives a record MTBF of 57.8 hours (to be compared with 38 hours in 2000 and 46.1 hours in 2001). It is worth pointing out that these results, and in particular the low rate of failures, were maintained whilst a lot of development work was under way: in particular, the successful tests of the Soleil superconducting cavity installed throughout 2002. These

		Even ID Section (ID2,ID6...)	Odd ID Section (ID1,ID3 ...)	Bending Magnet 3 mrad	Bending Magnet 9 mrad
Field	[T]	Depends on ID	Depends on ID	0.4	0.85
Horiz. Beta Functions	[m]	35.2	0.5	1.41	0.99
Horiz. Dispersion	[m]	0.137	0.037	0.061	0.045
Horiz. rms e- beam size	[μm]	402	59	100	77
Horiz rms e- divergence	[μrad]	10.7	90	116	111
Vert. Beta Functions	[m]	2.52	2.73	34.9	34.9
Vert. rms e- beam size	[μm]	7.9	8.3	29.5	29.5
Vert. rms e- divergence	[μrad]	3.2	3	0.85	0.85

Table 3: Beta functions, dispersion, rms beam sizes and divergences for the various source points of the ESRF storage ring.

RUN NUMBER	TOTAL 2001	2002-01	2002-02	2002-03	2002-04	2002-05	TOTAL 2002
Start		18/01/02	22/03/02	31/05/02	23/08/02	25/10/02	
End		13/03/02	22/05/02	31/07/02	16/10/02	19/12/02	
Total number of shifts	845.9	162	183	183	162	165	855.0
Number of USM shifts	675	128	148	148.9	127	135	686.9
Beam available for users (h)	5224.6	1000.9	1131.1	1150.0	976.0	1061.0	5319.0
Beam availability*	96.8 %	97.7%	95.5%	96.5%	96.1%	98.2%	96.8%
Beam availability**		98.3%	98.4%	98.0%	97.4%	99.2%	98.0%
Dead time for failures	1.9 %	1.7%	1.6%	2.0%	2.6%	0.8%	2.0%
Dead time for refills	1.3 %	0.6%	2.9%	1.5%	1.3%	1.0%	1.2%
Average intensity (mA)	145	178	127	130	151	150	146.2
Number of failures	117	22	13	23	23	14	95.0
Mean time between failures (h)	46.1	46.5	91.1	51.8	44.2	77.1	57.8
Mean duration of a failure (h)	0.9	0.8	1.4	1.0	1.2	0.6	1.2

Table 5: Statistics of availability of the beam in 2002.

* Beam availability after subtraction of time lost for injection of the ring.
 ** Beam availability without subtraction of time lost for injection of the ring.

tests were performed without any change of the beam size, bunch length and with the same stability. Indeed, this was fully transparent to user operation. Another way to appreciate these figures is to bear in mind that there were 17 periods with more than 72 hours of delivery without a single failure, out of which 9 periods were greater than 120 hours.

better than 10^{-6} compared to the filled buckets) was, a long-standing difficulty that was solved by exciting the beam at a high frequency through the newly-installed stripline shaker. This filling mode will be tested in user time in 2003.

Filling Patterns

The Multibunch filling pattern which represents 67% of the total user time is now delivered mostly in uniform filling with a lifetime greater than 70 hours at 200 mA (provided that the GRAAL laser is not being powered). Despite a slightly lower lifetime, the 2*1/3 fill is still used for time-structure experiments. The remaining 33 % is shared between the 16 bunch, the single bunch and the hybrid-mode filling patterns (Figure 132).

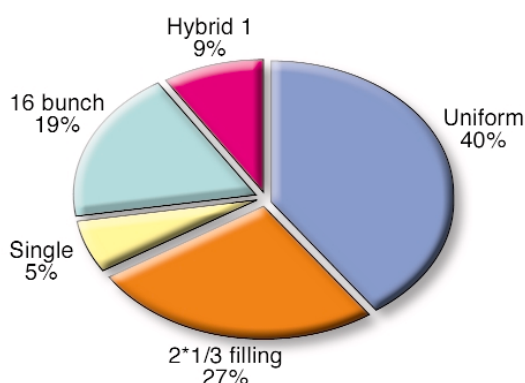


Fig. 132: Distribution of the 2002 user time in the various filling modes.

A new hybrid filling pattern based on groups of bunches was fully assessed during 2002 (24 groups of 8 bunches and a single bunch in the gap). The lifetime is in the order of 20 hours for a total current of 200 mA. The “cleaning” which removes electrons from the unwanted buckets (to a level

Undulators

Following the recent installation of several 10 mm-thick ID chambers on ID16, ID18 and ID28, the undulator segments of these beamlines were changed to a shorter magnetic period. These three beamlines now operate the equivalent of a 5 m-long undulator with a minimum gap of 11 mm. Figure 133 gives the brilliance reached in multibunch mode (uniform and 2 x 1/3 filling mode). A complete list of the installed insertion device segments is presented at the following address:

www.esrf.fr/Accelerators/Accelerators/InsertionDevices/IDs/

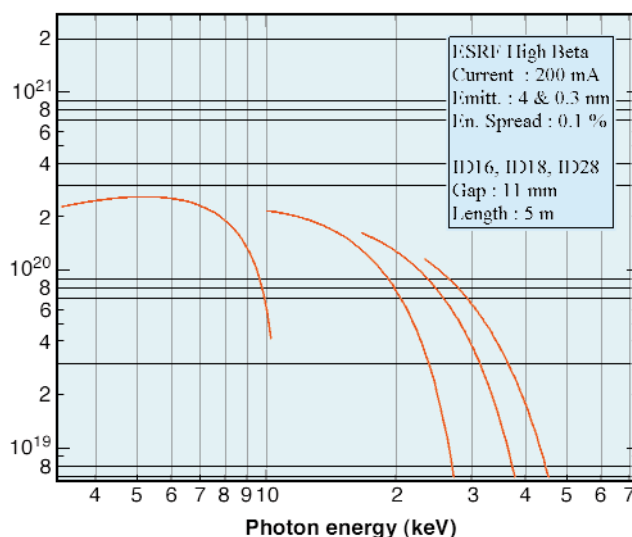


Fig. 133: Brilliance reached on ID16, ID18 and ID28 with three segments operated at a minimum gap of 11 mm.

SS	Period [mm]	Length [m]	Type of Magnet Array	Minimum Gap [mm]	Rms Phase Error [deg] @ 6 mm	Field Int. vs Gap [Gcm]	Operation
ID11	23	1.6	Hybrid	5	?	70	Jan 99
ID22	23	2	PPM	6	1.9	26	July 01
ID9	17	2	PPM	6	< 5	< 15	July 01
ID29	21	2	PPM	6	2.3	< 15	Dec 02
ID13	18	2	PPM	6	< 5	< 15	July 02
ID11	22	2	Hybrid	6			Dec 03
ID30	23	2 x 2	PPM	6			July 03

Table 6: Status of in-vacuum undulators.

Two additional in-vacuum undulators were installed in 2002. The status of the in-vacuum undulators is given in [Table 6](#).

Five beamlines operate with the combination of one in-vacuum undulator segment and one conventional open-air undulator. The short period U17 and U18 installed on ID9 and ID13 are intended to operate on either the fundamental or third harmonic, and consequently no particular attention was given to precise phase shimming. Whereas for ID22 and ID29, which are intended to be used at high energy, have been phase shimmed to around 2 deg rms. During the initial tests made on U17, beam loss occurred for gaps below 6.5 mm. Possible damage to the nickel copper sheet placed on the upper magnet assembly was immediately suspected and was confirmed during the May machine shutdown. Investigation showed that the sheet had been damaged by both the electron beam as well as by synchrotron radiation from the upstream dipole. As a consequence, the thickness of the nickel was increased from 25 to 50 micrometres and an improved fixation was designed. Since then the U17 has been operated at a gap of 6 mm without any further problems.

The removal of the SOLEIL super-conducting cavity, installed on the ID23 straight section, was carried out during the December 2002 shutdown. Three short dipoles made of permanent magnets have been installed in order to generate two undulator beams emitting at $\pm 750 \mu\text{rad}$ from the direction of the straight section. The first of these canted undulators (U35) is in place, the other undulator (U20.2), optimised to produce 14 keV X-rays, is being designed.

metre long 11 mm internal aperture aluminium insertion devices were installed on ID13 and ID29. One of them had to be re-activated in order to reduce the Bremsstrahlung radiation in the beamline's experimental hutch. A leak on the ceramic feed-through of the ion pump installed immediately upstream was later identified as the reason for the problem. A few days after re-activation, as the Bremsstrahlung was sufficiently reduced, the beamline ID13 was allowed to operate without further radiation safety constraints. A 5-metre long 11 mm aperture aluminium chamber was installed on ID2. This is working perfectly. The main development of 2002 was the production of a prototype followed by full tests of an 8 mm aperture 5m-long aluminium vessel (see [Figure 134](#)). The choice of aluminium instead of stainless steel was made to reduce both manufacturing costs and the excitation of the resistive wall instability. However, raw aluminium presents strong synchrotron radiation induced desorption compared to stainless steel. The conditioning of the prototype chamber installed in May 2002 was so slow and the Bremsstrahlung produced was so high that the chamber was removed immediately after installation. When the same chamber coated with NEG was re-installed in October 2002 a rapid conditioning was observed (half the nominal multibunch lifetime was obtained after 20 minutes of beam at full current). This confirmed, once again, the effectiveness of the NEG coating and the similar desorption of stainless steel and aluminium once a NEG coating is applied. The coating of the tiny 57 x 8 mm elliptical chamber was made at CERN by the EST-SM Group.

Progress with NEG Coated Insertion Device Vacuum Chambers

The installation of non-evaporable getter (NEG) coated vessels continued throughout the year. Two additional 2-

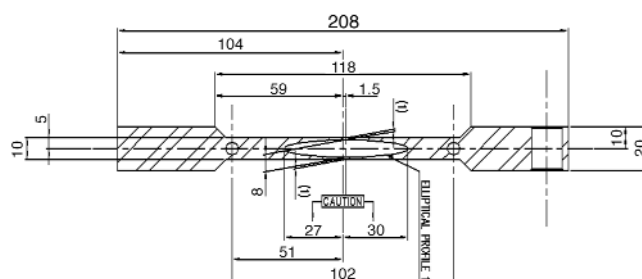


Fig. 134: Cross-section of the 8 mm aperture 5 m-long aluminium insertion device vacuum chamber.



Fig. 135: NEG coating facility. The 5 m-long insertion device vacuum chamber is placed vertically.

In 2002 a NEG coating facility was assembled which now allows the coating of 5m-long insertion device vessels (see [Figure 135](#)). The facility became operational at the end of 2002. In 2003, it is planned to manufacture several aluminium chambers, to NEG coat them in-house and to then install them on the ring.

Test of the SOLEIL Superconducting Cavity

A cryo-module housing two superconducting 352 MHz strongly HOM-damped cavities has been developed within the framework of the SOLEIL project design study phase, in a collaboration between CEA, CERN, ESRF and SOLEIL. In 2002 the prototype was installed in the ESRF storage ring ([Figure 136](#)) and tested with beam in the accelerating regime at 4.5 K with the cavities cooled by liquid helium poured from Dewars. Four such tests were carried out at the end of scheduled shutdowns at the ESRF. In order to avoid disturbing the ESRF machine performance during user mode operation, the cavities were maintained detuned at room temperature in a passive regime. The heat

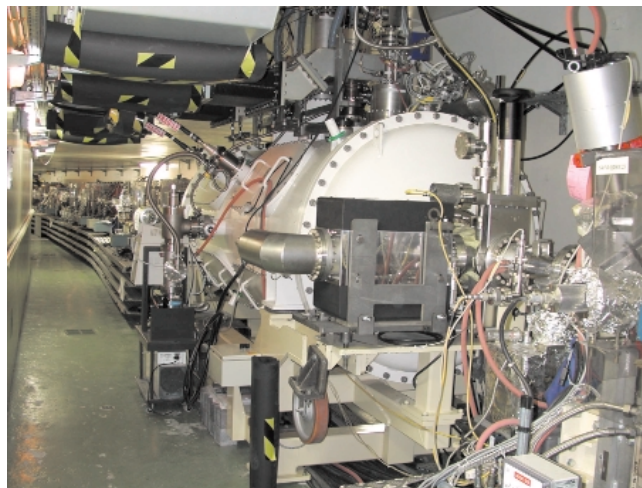


Fig. 136: Superconducting HOM-free SOLEIL cavity in cell 23 of the ESRF storage ring.

generated by the beam was then evacuated by means of a helium gas flow, cooled by a heat exchanger.

In passive operation at 300 K or 4 K, no instability was detected up to the maximum ESRF intensity of 200 mA: this demonstrated the validity of the concept of an effective damping of the Higher Order Modes (HOM). With the cavity at room temperature, the test arrangement provoked only three beam trips over one year and was therefore almost transparent to the normal ESRF operation.

The superconducting module was also tested successfully in the accelerating regime with 3 MV of accelerating voltage. A maximum power of 360 kW could then be transferred to 170 mA of beam. This power was limited by minor problems of spurious coupling of the dipolar HOM couplers to the fundamental accelerating mode. Corresponding modifications are therefore planned prior to the installation on the SOLEIL storage ring. The tests also showed that a cold shield could help to reduce the static cryogenic losses, thereby limiting the liquid helium consumption, which is presently above specifications. Nevertheless, the achieved performances of the prototype module are already sufficient for the first operation phase of SOLEIL. For long-term operation the production of a second improved module will be launched in parallel.

Due to the successful prototype test, the concept of this almost HOM-free superconducting cavity has been validated. Full evaluation of the beam tests at the ESRF will contribute to finalise the design. The tests have also shown that this cavity constitutes a valuable option for a possible future intensity upgrade at the ESRF.

Understanding the Non-linear Longitudinal Beam Dynamics with a Harmonic RF System

New numerical tools have been developed in the framework of a PhD thesis. These tools carried out, which have helped to improve our understanding of non-linear longitudinal beam dynamics in the presence of harmonic RF systems. Such systems are in operation on several low- and medium-energy machines in order to lengthen the bunches and thereby increase the Touschek lifetime. All the longitudinal issues have been addressed, such as transient beam loading with uneven fills, Robinson instabilities, Higher Order Modes (HOM) driven Longitudinal Coupled Bunch Instabilities (LCBI), as well as for high currents per bunch, the potential well and the microwave instability. Simulations have confirmed many experimental observations on various existing machines such as Landau damping of LCBI or strong phase transients with gaps in the fill pattern. They have also demonstrated the superiority of superconducting versus normal conducting harmonic cavities. This has very recently been confirmed by the commissioning of the superconducting Super3HC passive harmonic cavity at the Swiss Light Source. Taking into consideration all longitudinal effects, it transpires that an active superconducting third-harmonic cavity would constitute the only appropriate solution for the ESRF. It would be useful in single bunch and sixteen-bunch operation to improve the beam lifetime by a factor of 2 and 3, respectively.

Status of the Beam Loss Detection System

Monitoring and localising the electron beam losses has been a high priority over the last few years. Three networks of beam loss detectors are now in operation around the ring perimeter. Sixty-four neutron detectors are placed outside the shielding directly above each bending magnet. These detectors, which are part of the personnel safety system, give the most precise dose rates corresponding to the beam losses taking place during injection. However, due to their low sensitivity, they are not capable of monitoring the beam losses during a current decay. Two other networks of detectors based on ionisation chambers (Figure 137, lower graph) and glass scintillator coupled to a photomultiplier (upper graph) detect some shower residues generated by electron losses in every straight section of the storage ring. These detectors are extremely sensitive and allow, for example, the localisation of very small leaks or obstacles at an early stage when the induced losses are not yet sufficient to reduce the lifetime of the stored beam.

A new detector has been installed on the front-end of the

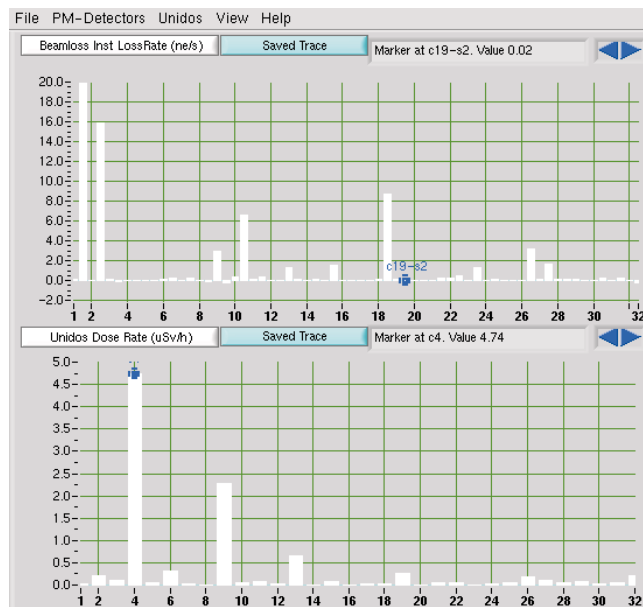


Fig. 137: Beam losses displayed along the ring's circumference (cells 1 to 32). The upper graph corresponds to the scintillator-photomultiplier detection. The lower one corresponds to the ionisation chamber type measurement.

ID6 beamline. Its role is to detect the amount of Bremsstrahlung passing down the beamline due to collisions between the electrons in the beam and the residual gas in the insertion device straight section. This diagnostic tool gives a relative measurement of the gas pressure integrated along the beam path in the small section ID vacuum chambers. It allows the monitoring of the vacuum conditioning of newly installed ID chambers and is non-destructive, allowing the measurement of the efficiency of the Non Evaporable Getter coating. Figure 138 shows the monitoring of Bremsstrahlung on ID6 normalised to the square of the current for a newly installed ID chamber. The sharp peaks correspond to high losses during injection. The higher losses in 16-bunch mode originate from the higher desorption induced by the high temperature of the chamber. In 200 mA uniform-filling mode, the signal decays with time following the reduction of desorption (vacuum conditioning).

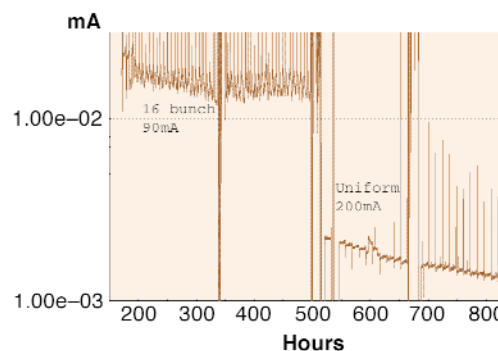


Fig. 138: Normalised gas pressure in ID6 chamber taken by dividing the Bremsstrahlung count rate by the current squared.

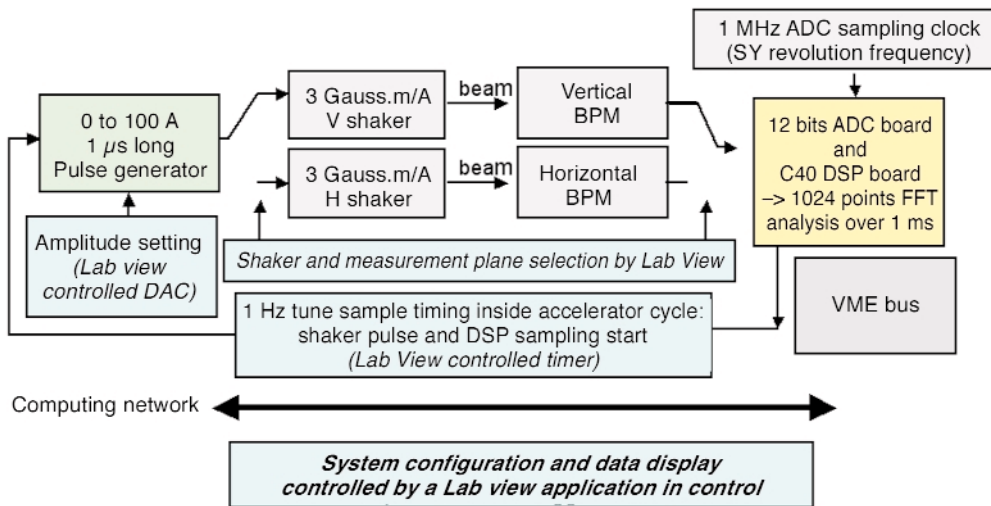


Fig. 139: Layout of the booster tune monitoring system.

A New Tune Monitoring System for the Booster

The booster tune monitor is a diagnostic tool used to measure the vertical and horizontal transverse resonant frequencies (or betatron tunes) of the electron beam accelerated in the booster. The beam is accelerated from 200 MeV to 6 GeV in 50 ms. To ensure optimum performance of the booster, the tunes must be kept constant during the acceleration cycle. To measure the tune, the beam is transversely excited by a 100A-1ms current pulse applied to the beam using a magnetic shaker. The beam position is recorded over 1024 turns (1ms). A FFT of the signal is performed on a DSP board and the resonant frequency is identified. The layout of this diagnostic is shown in Figure 139.

The front panel of the Labview application controlling the shaker and displaying the tunes is shown in Figure 140. This application now allows an automatic acquisition of the tunes throughout the acceleration cycle, making the booster tuning much easier.

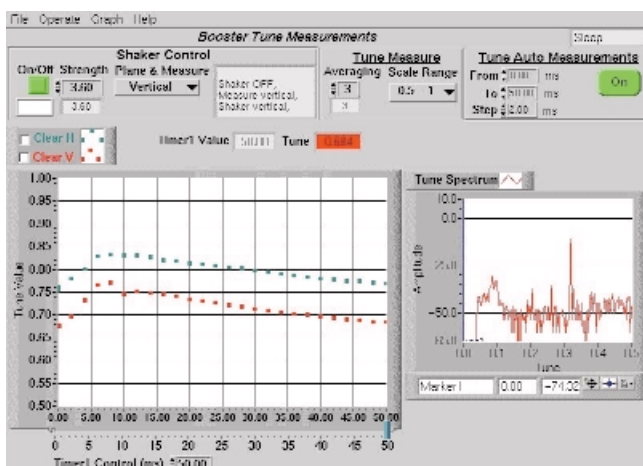


Fig. 140: Control panel of the Booster tune monitor. The left hand side gives the horizontal and vertical tunes as measured along the 50 ms ramping time. The right hand side shows the FFT of the signal measured on the beam position monitor.

Progress in the Evaluation of the Longitudinal and Transverse Machine Impedance

The installation of more and more chambers of irregular shape in the machine, in particular transitions to vessels of small vertical aperture, has detrimental effects on the beam. The consequences of these irregularities and lack of electrical conductance of the vacuum chamber are multiple. The tunes vary with the current (detuning), which complicates the single bunch operation and limits the current. Transverse instabilities are triggered above some current thresholds [1], which can be cured by increasing the chromaticity at the cost of a reduction in lifetime. The underlying effect is characterised by a deformation of the self-field of the beam (wake field). The effect is formally expressed in the quantities known as longitudinal and transverse machine impedance.

As the impedance of the vacuum chamber components is very difficult to measure, the wake field generated by each chamber has to be calculated in three dimensions with a dedicated computer algorithm [2]. These computations use a lot of resources (cpu time and memory), which push present-day computers to the limit. This task was started in 2000 [3] and is still progressing. In 2002 further critical elements were identified, in particular the gap between the flanges, which provides a large contribution to the total impedance. More than half of the vertical detuning (vertical tune variation vs current) can now be accounted for. The transverse impedance can be expanded in the frequency space and typically presents a broad peak at certain high frequencies (broad resonator model). The numerically derived impedance in the frequency space shows such a peak at a much lower frequency than the model used so far which was fitted from various tune measurements [4]. It has become clear that the important vertical detuning observed on the ESRF storage ring is a consequence of the large number of discontinuities generated by the RF fingers located on both sides of the dipole chamber where the vertical beta functions are large. The transition to the narrow aperture

insertion device chambers is less important than originally expected due to the low vertical beta function present there. As the evaluation of the transverse impedance budget in the vertical plane is now well advanced, its evaluation in the horizontal plane has just started. The flat nature of the ID chamber results in the presence of coherent and incoherent tune shifts which, in the horizontal plane, compensate each other for the fundamental head-tail mode ($m = 0$). This has been understood only recently and explains the very low horizontal detuning experimentally observed both in single bunch and multibunch. Nevertheless, following the recent installation of a large number of narrow gap chambers, a significant reduction of the current threshold of horizontal instability has been observed while such an effect was expected in the vertical plane instead. This is now better understood due to the very large horizontal beta functions in the even ID vessels and the horizontal impedance contribution.

References

- [1] J.L. Revol, R. Nagaoka, P. Kernel, L. Tosi, E. Karantzoulis, EPAC 2000 Vienna.
- [2] W. Bruns, GdfidL: A Finite Difference Programme with Reduced Memory and CPU Usage, PAC 97, Vancouver, p. 2651.
- [3] ESRF Highlights 2000.
- [4] T.F. Günzel, Evaluation of the vertical transverse impedance of the ESRF machine, EPAC 2002, Paris.

Facts and Figures



Highlights 2002

Member and Associate Countries

Members' share in contribution to the annual budget:

27.5%	France
25.5%	Germany
15%	Italy
14%	United Kingdom
4%	Spain
4%	Switzerland
6%	Benesync (Belgium, Netherlands)
4%	Nordsync (Denmark, Finland, Norway, Sweden)

Additional contributions (percentages refer to Members' total contribution):

1%	Portugal
1%	Israel
1%	Austria
0.38%	Czech Republic
0.2%	Hungary



The Beamlines

All thirty of the ESRF public beamlines have been operational since 1999. Two of these possess two end-stations, so there are thirty two end-stations in total, which can be run independently. An additional sixteen beamline branches, situated on bending magnets, are devoted to Collaborating Research Groups (CRG). Eleven of the CRG beamlines are now in operation (including GRAAL), the others are being commissioned or under construction. **Figure 141** shows the location of the beamlines in the experimental hall; a list of the public beamlines is presented in **Table 7**; and a list of the CRG beamlines in **Table 8**.

Following management proposals, in agreement with Council's decision of June 2000, the Powder Diffraction

beamline has been transferred from a bending magnet, BM16, to an insertion device, ID31. Similarly, BM14, the MAD beamline, was transferred to ID29 during 2000-2001. BM16 will become a Spanish CRG line with full MAD capability, and BM14 is now a British CRG, also dedicated to MAD studies in structural biology.

Additionally, there is an industrial beamline, ID27, which has been constructed for impurity analysis on silicon wafers. This line has capacity for further expansion to other fields of industrial interest, and different possibilities are currently under consideration.

Finally, a new beamline complex dedicated to protein crystallography is under construction on ID23 as part of the Partnership for Structural Biology (PSB).

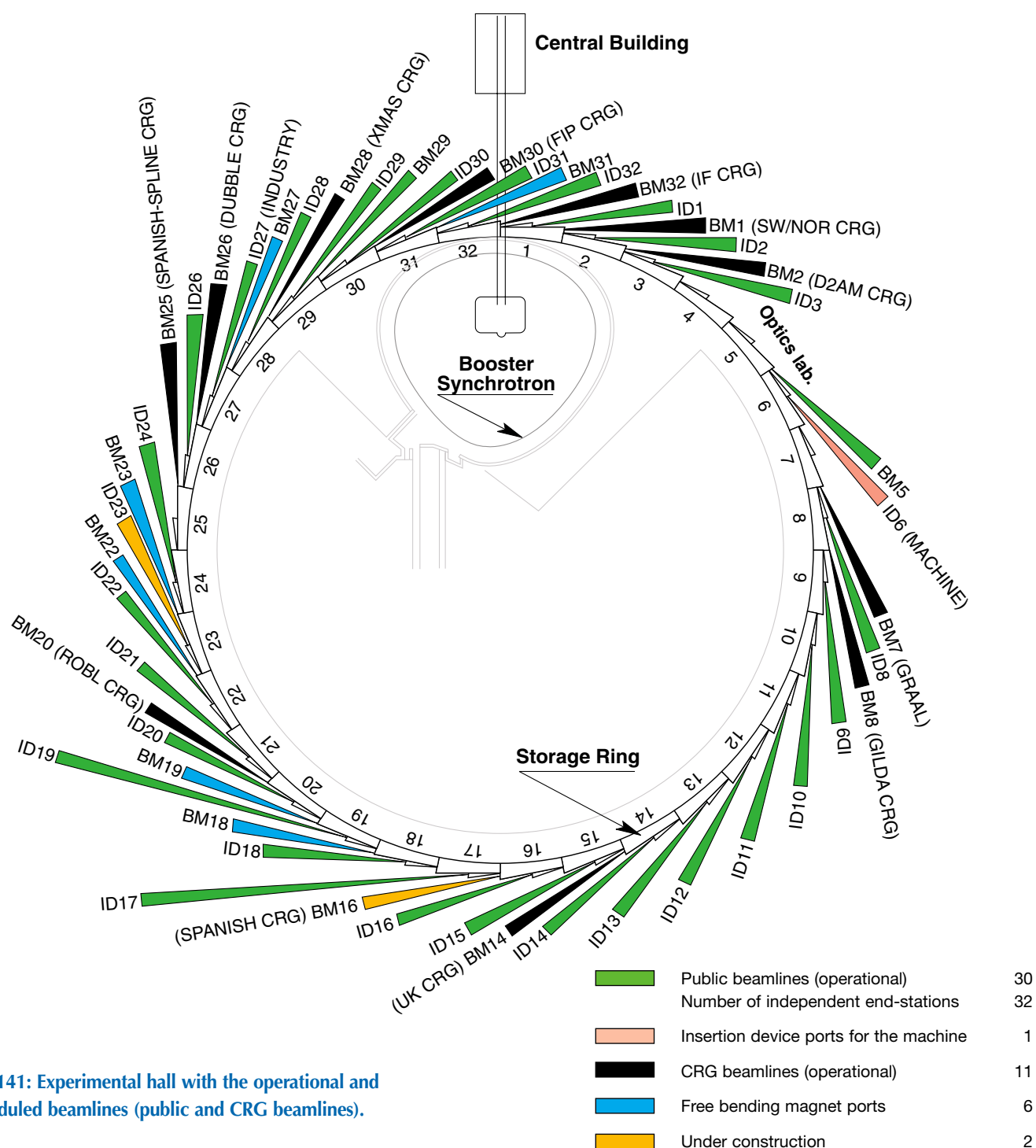


Fig. 141: Experimental hall with the operational and scheduled beamlines (public and CRG beamlines).

SOURCE POSITION	NUMBER OF INDEPENDENT END-STATIONS	BEAMLINE NAME	STATUS	
ID1	1	Anomalous scattering	Operational	since 07/97
ID2	1	High brilliance	Operational	since 09/94
ID3	1	Surface diffraction	Operational	since 09/94
ID8	1	Dragon	Operational	since 02/00 <i>Transferred from ID12</i>
ID9	1	White beam	Operational	since 09/94
ID10A	1	Troika I + III	Operational	since 09/94
ID10B	1	Troika II	Operational	since 04/98
ID11	1	Materials science	Operational	since 09/94
ID12	1	Circular polarisation	Operational	since 01/95
ID13	1	Microfocus	Operational	since 09/94
ID14A	2	Protein crystallography EH 1	Operational	since 07/99
		Protein crystallography EH 2	Operational	since 12/97
ID14B	2	Protein crystallography EH 3	Operational	since 12/98
		Protein crystallography EH 4	Operational	since 07/99
ID15A	1	High energy diffraction	Operational	since 09/94
ID15B	1	High energy inelastic scattering	Operational	since 09/94
ID16	1	Inelastic scattering I	Operational	since 09/95
ID17	1	Medical	Operational	since 05/97
ID18	1	Nuclear scattering	Operational	since 01/96
ID19	1	Topography	Operational	since 06/96
ID20	1	Magnetic scattering	Operational	since 05/96
ID21	1	X-ray microscopy	Operational	since 12/97
ID22	1	Microfluorescence	Operational	since 12/97
ID23	2	Macromolecular crystallography	Under construction	
ID24	1	Dispersive EXAFS	Operational	since 02/96
ID26	1	X-ray absorption on ultra-dilute samples	Operational	since 11/97
ID27	1	Industry	Operational	since 08/00
ID28	1	Inelastic scattering II	Operational	since 12/98
ID29	1	Multiwavelength anomalous diffraction	Operational	since 01/00 <i>Transferred from BM14</i>
ID30	1	High pressure	Operational	since 06/96
ID31	1	Powder diffraction	Operational	since 05/96 <i>Transferred from BM16</i>
ID32	1	SEXAFS	Operational	since 11/95
BM5	1	Optics - Open Bending Magnet	Operational	since 09/95
BM29	1	X-ray absorption spectroscopy	Operational	since 12/95

Table 7: List of the ESRF public beamlines in operation and under construction.

SOURCE POSITION	NUMBER OF INDEPENDENT END-STATIONS	BEAMLINE NAME	FIELD OF RESEARCH	STATUS
BM1	2	Swiss-Norwegian BL	X-ray absorption & diffraction	Operational since 01/95
BM2	1	D2AM (French)	Materials science	Operational since 09/94
BM7	1	GRAAL (Italian / French)	Gamma ray spectroscopy	Operational since 06/95
BM8	1	Gilda (Italian)	X-ray absorption & diffraction	Operational since 09/94
BM14	1	UK CRG	PX (MAD, SAD)	Operational since 01/01
BM16	1	SPANISH CRG	PX (MAD, SAX)	Operational in 2003
BM20	1	ROBL (German)	Radiochemistry & ion beam physics	Operational since 09/98
BM25	2	SPLINE (Spanish)	X-ray absorption & diffraction	Construction phase
BM26	2	DUBBLE (Dutch/Belgian)	Small-angle scattering & interface diffraction Protein crystallography + EXAFS	Operational since 12/98 Operational from 06/01
BM28	1	XMAS (British)	Magnetic scattering	Operational since 04/98
BM30	2	FIP (French) FAME (French)	Protein crystallography EXAFS	Operational since 02/99 Operational since 08/02
BM32	1	IF (French)	Interfaces	Operational since 09/94

Table 8: List of the Collaborating Research Group beamlines in operation and under construction.

User Operation

During the year 2002 the full complement of 30 public beamlines, together with 8 additional beamlines operated by Collaborating Research Groups (CRGs), were open for user experiments. **Figure 142** shows the increase in requests for beam time since 1997; this figure confirms that although the main beamline construction effort was complete by 1999, the number of applications for beam time continued to rise in 2000 and 2001, and remained at a high level in 2002.

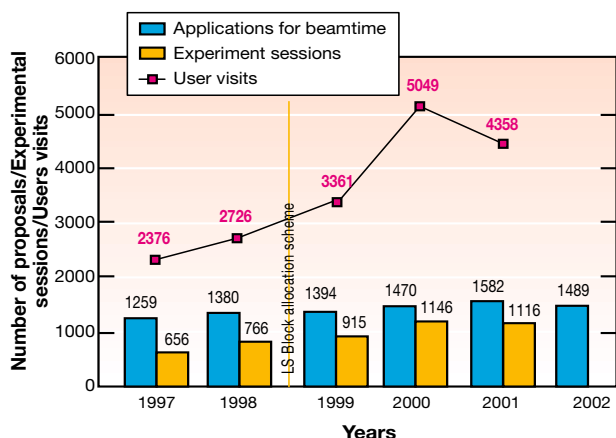


Fig. 142: Numbers of applications for beam time, experiments carried out, and user visits, 1997 to 2001. N.B. Final numbers of experiments and user visits for 2002 were not available at the time of going to press.

Proposals for experiments are selected and beam time allocations are made through peer review. Review Committees of specialists for the most part from European countries and Israel, have been set up in the following scientific areas:

- chemistry
- hard condensed matter: electronic and magnetic properties
- hard condensed matter: structures
- materials engineering and environmental matters
- macromolecular crystallography
- medicine
- methods and instrumentation
- soft condensed matter
- surfaces and interfaces

The Review Committees met twice during the past year, some six weeks after the deadlines for submission of proposals (1 March and 1 September). They reviewed a total of 1489 applications for beam time, and selected 748 (50%), which were then scheduled for experiments.

Features of this period have been

- the setting up of a Medical review committee, to assess research projects in medicine.
- increasing numbers of projects concerned more with applied than basic research in materials science, engineering and environmental matters. As shown in

Figure 143, experiments in these areas accounted for 10% of the total number of experiments carried out in the first half of 2002. A new facility on site, FaME38, will provide specific instrumentation and support to enable engineers to carry out materials and engineering research.

- the very successful operation of the Block Allocation Group (BAG) scheme for macromolecular crystallography users. This scheme, designed to encourage groups of users to block together their multiple requests for beam time, and the scheduling of their experiments, encompassed 37 groups from Europe and Israel in 2002.

Shifts scheduled for Experiments, Scheduling period 2002/I: Total: 6977

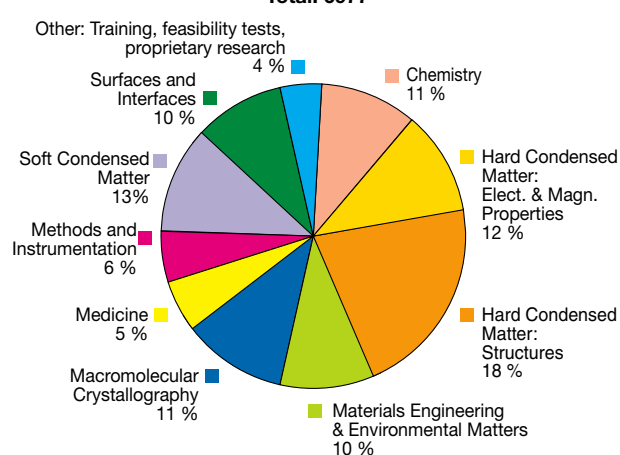


Fig. 143: Shifts scheduled for experiments, from February to July 2002, by scientific area.

Requests for beam time, which is scheduled in shifts of 8 hours, totalled 24 585 shifts or 196 680 hours in 2002, of which 11 759 shifts or 94 072 hours (48%) were allocated. The distribution of shifts requested and allocated, by scientific area, is shown in **Table 9**.

Scientific field	Total shifts requested	Total shifts allocated
Chemistry	2 854	1 390
Hard condensed matter:		
• Electronic and magnetic prop.	4 062	1 657
• Structures	5 476	2 104
Materials engineering & environmental matters	2 405	1 277
Macromolecular crystallography	2 563	1 413
Medicine	797	506
Methods & instrumentation	1 176	727
Soft condensed matter	2 998	1 365
Surfaces & interfaces	2 254	1 320
Totals	24 585	11 759

Table 9: Number of shifts of beam time requested and allocated for user experiments, year 2002.

The first half of 2002 saw 2482 visits by scientists to the ESRF under the user programme, to carry out 613 experiments. **Figure 142** shows the rapid rise in the number of user visits since 1997, the higher numbers in

recent years reflecting in part the multiple visits made by macromolecular crystallography BAG teams. The peak in 2000 is due to a somewhat longer scheduling period, and correspondingly higher overall number of experimental sessions and visits by users.

Overall, the number of users in each experimental team averaged 4 persons, and they stayed for some 4 days. Users responding to questionnaires indicate that they particularly appreciate the assistance they receive from scientists and support staff on beamlines, and smooth

administrative arrangements, in addition to the quality both of the beam and of the experimental stations. Facilities on site, such as preparation laboratories, a canteen and the Guesthouse, also make an important contribution to the quality of user support.

On the beamlines, beam time losses tended to occur because of occasional difficulties with samples or with the beamline components. Such beam time losses, however, remained below 5% of the total shifts scheduled for experiments during the period.

Administration and Finance

Expenditure and income 2001

		kEuro			kEuro
Expenditure			Income		
Machine			2001 Members' contributions		62,511.3
Personnel		4,400.0	Funds carried forward from 2000		379.0
Recurrent		2,093.8			
<i>Operating costs</i>	1,723.3		Other income		
<i>Other recurrent costs</i>	370.5		Scientific Associates		1,948.4
Capital		4,190.3	Sale of beam time		947.9
<i>Machine developments</i>	4,190.3		Other sales		279.0
Beamlines, experiments and in-house research			Funds from Slab settlement		1,218.0
Personnel		19,440.2	Scientific collaboration and Special projects		516.6
Recurrent		6,553.3	Income covering expenditure in connection with activities from 3rd parties		777.3
<i>Operating costs</i>	3,821.3		Financial discounts		6.0
<i>Other Recurrent costs</i>	2,732.0		Bank loans		11.0
Capital		6,472.9	Other		670.5
<i>Beamline developments</i>	4,277.8				
<i>Beamline refurbishment</i>	2,195.1				
Technical and administrative supports					
Personnel		13,736.4			
Recurrent		8,244.9			
Capital		4,133.2			
Unexpended committed funds					
Funds carried forward to 2002		0.0			
Total		69,265.0	Total		69,265.0

Revised expenditure and income budget for 2002

		kEuro			kEuro
Expenditure			Income		
Machine			2002 Members' contributions		63,946
Personnel		4,548	Funds carried forward from 2001		0
Recurrent		1,877			
<i>Operating costs</i>	1,514		Other income		
<i>Other recurrent costs</i>	363		Scientific Associates		3,522
Capital		4,433	Sale of beam time		1,070
<i>Machine developments</i>	4,433		Other sales		305
Beamlines, instruments, experiments and in-house research			Funds from Slab settlement		29
Personnel		19,816	Compensatory income		802
Recurrent		6,485	Scientific collaboration and Special projects		881
<i>Operating costs</i>	3,681		Income covering expenditure in connection with activities from 3rd parties		710
<i>Other Recurrent costs</i>	2,804		Financial discounts		5
Capital		7,575	Bank loans		250
<i>Beamline developments</i>	5,228		Other		195
<i>Beamline refurbishment</i>	2,347				
Technical and administrative supports					
Personnel		14,305			
Recurrent		8,555			
Capital		3,794			
Industrial and commercial activity					
Personnel		384			
Recurrent		143			
Total		71,715	Total		71,715

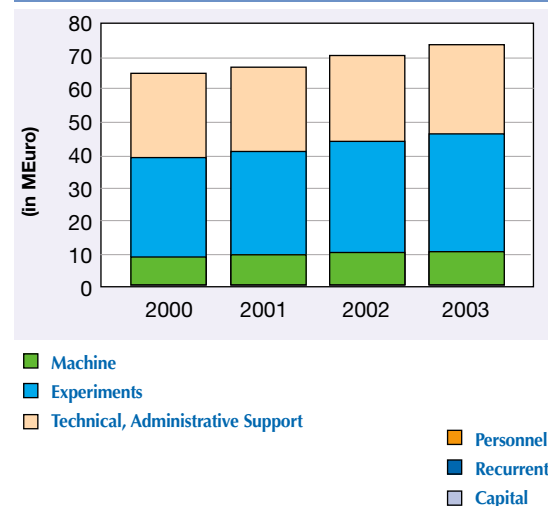
Expenditure 2001 by nature of expenditure	
	kEuro
PERSONNEL	
ESRF staff	36,121.7
External temporary staff	105.4
Other personnel costs	1,349.7
RECURRENT	
Consumables	6,359.7
Services	8,437.6
Other recurrent costs	2,094.6
CAPITAL	
Buildings, infrastructure	2,413.4
Lab. and Workshops	348.5
Machine incl. ID's and Fes	4,190.2
Beamlines, Experiments	6,472.9
Computing Infrastructure	1,239.2
Other Capital costs	132.1
Unexpended committed funds	
Funds carried forward to 2002	0
Total	69,265.0

Revised budget for 2002 by nature of expenditure	
	kEuro
PERSONNEL	
ESRF staff	37,399
External temporary staff	80
Other personnel costs	1,574
RECURRENT	
Consumables	6,045
Services	8,597
Other recurrent costs	2,227
CAPITAL	
Buildings, infrastructure	2,121
Lab. and Workshops	368
Machine incl. ID's and Fes	4,433
Beamlines, Experiments	7,566
Computing Infrastructure	1,160
Other Capital costs	145
Total	71,715

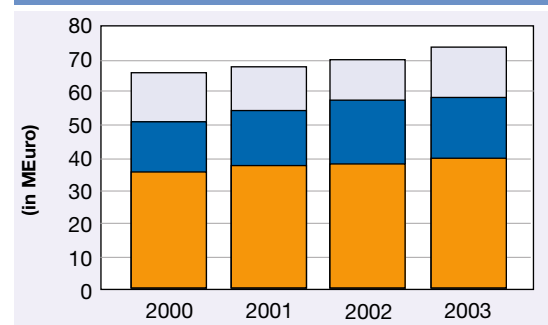
2002 manpower (posts filled on 31/12/2002)				
	Cadres	Non cadres	PhD students	Total
Staff on regular positions				
Machine	26	41	1	68
Beamlines, instruments and experiments*	184	68.8	24	276.8
General technical services	51.6	71.1		122.7
Directorate, administration and central services	22.3	54.6		76.9
<i>Sub-total</i>	<i>283.9</i>	<i>235.6</i>	<i>25</i>	<i>544.5</i>
Other positions				
Short term contracts	9.8	15.5		25.3
Scientific collaborators	7			7
Staff under "contrats de qualification" (apprentices)		14		14
European Union grants	3			3
Temporary workers	0.47			0.47
Total	304.1	265.1	25	594.2
Absences of staff (equivalent full time posts)	25.1			-25.1
<i>Total with absences</i>				<i>569.1</i>

* Including scientific staff on time limited contract.

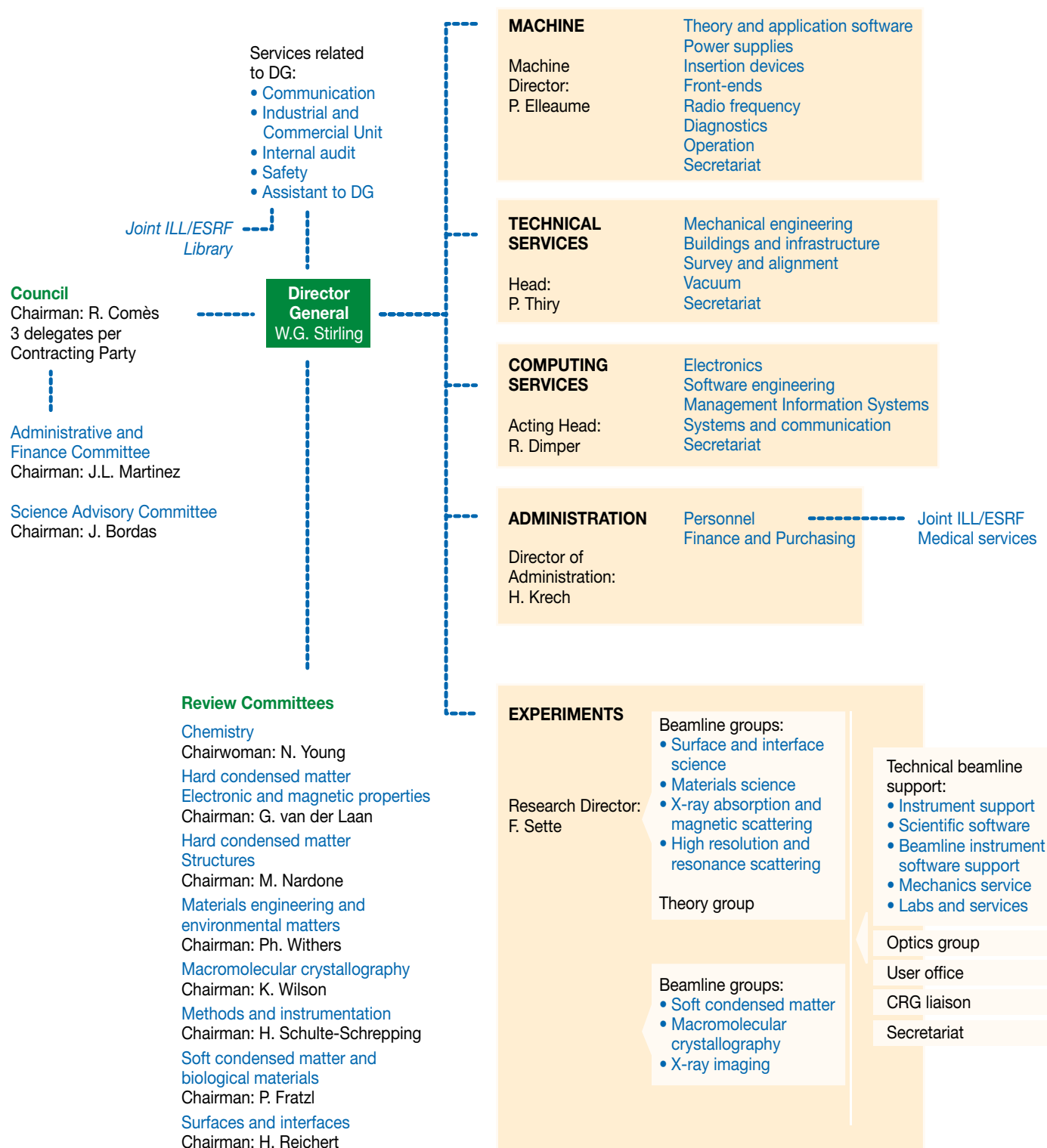
Financial resources in 2000, 2001, 2002 and 2003, by programme
(current prices in MEuro for the respective years)



Financial resources in 2000, 2001, 2002 and 2003, by nature of expenditure
(current prices in MEuro for the respective years)



Organisation chart of the ESRF (as of January 2003)



*We gratefully acknowledge the help of:
J. Baruchel, N. Brookes, F. Comin,
P. Elleaume, S. Ferrer, A. Freund, G. Grübel,
Å. Kvik, G. Leonard, R. Mason, R. Rüffer,
F. Sette, W.G. Stirling, McSweeney, K. Witte.*

Chief Editor

D. Cornuéjols, ESRF information officer

Editor

G. Admans, ESRF information officer

Layout

Pixel Project

Printing

Imprimerie du Pont de Claix

© ESRF • February 2003

Information Office

ESRF

BP220 • 38043 Grenoble • France

Tel. (33) 4 76 88 20 25 • Fax. (33) 4 76 88 24 18

<http://www.esrf.fr>